Improving the Performance of Electroanalytical Devices for Sensing and Energy Storage

A DISSERTATION
SUBMITTED TO THE FACULTY OF THE GRADUATE SCHOOL
OF THE UNIVERSITY OF MINNESOTA
BY

Seyedeh Moloud (Maral) Mousavi

IN PARTIAL FULFILLMENT OF THE REQUIREMENTS
FOR THE DEGREE OF
DOCTOR OF PHILOSOPHY

Philippe Bühlmann, Adviser

January 2016

Acknowledgements

First and foremost, I would like to acknowledge my adviser, Prof. Philippe Bühlmann, who supported and guided me in this journey, taught me the principles of scientific research and critical thinking, and patiently corrected my many mistakes. Prof. Bühlmann is a brilliant and dedicated scientist and his work and research resulted in major improvements and breakthroughs in many fields, especially in the field of electrochemistry and sensing. It has been a pleasure to work alongside him. I hope that I would be able to follow his footsteps and practice science in such a comprehensive, fundamental, and creative manner.

During the course of my doctoral work, I have received the assistance and support from collaborators, Professors Christy Haynes, Andreas Stein, and Marc Hillmyer, who are also part of my thesis committee and reviewed this thesis. Their advice and suggestions helped to broaden the scope of my knowledge and my research and I am truly grateful for their support. I would also like to thank the committee members of my preliminary exams, Prof. Pete Carr, Prof. Christopher Douglas, and Prof. Natalia Tretyakova.

I would like to thank the following people for their specific contributions to the work described in this thesis:

- Prof. Bill Smyrl for his insights and suggestion on development of high energy density electrochemical capacitors
- Prof. Satish Kumar for his advice and input on fundamentals of liquid flow through highly porous media
- Prof. Christopher Douglas for providing advice on synthesis of fluorophilic quaternary ammonium electrolytes.

- Prof. for Ana Vila Verde (Max Planck Institute of Colloids and Interfaces) for informative discussions on molecular dynamics of electron transfer in quaternary ammonium cations
- Dr. Aniko Nemes (Eötvös Loránd University) for her advice on the synthesis of the quaternary ammonium cations
- Sadra Kashefolgheta (Max Planck Institute of Colloids and Interfaces) for performing computational analyses for assessment of electrochemical stability of electrolytes and ionic liquids
- Dr. Melissa Maurer-Jone, Dr. Li Chen, and Ian Gunsolus who assisted me in projects involving application of fluorous-phase silver selective electrodes in assessment of toxicity and environmental hazards of silver nanoparticles
- Adam Dittmer for performing COMSOL simulations on electron transfer of supporting electrolyte in linear sweep voltammetry
- Benjamin Wilson for providing porous carbon films and carrying out analysis of double-layer capacitance of ionic liquids and Jinbo Hu for his help in fabrication of electrochemical cells with carbon films
- Evan Anderson for assisting with measurement of conductivity of ionic liquids and fluorophilic electrolytes
- Xin Sean Chen for his help in development of fluorous-phase pH sensors
- Stacey Saba for her help in development and characterization of porous materials for application in reference electrodes
- Dr. Letitia Yao, University of Minnesota Chemistry, NMR laboratories, for her assistance with NMR experiments

Moreover, I would like to express my gratitude to the Gleysteen family and University of Minnesota, Graduate School for providing partial funding for my research.

I would also like to thank the current and former members of the Bühlmann research group for their friendship and support. Specially, Dr. Eric Olson and Dr. Xu Zue who instructed me on several electroanalytical techniques and proper usage of instruments of

the Bühlmann research group. Also, I wanted to thank the undergraduate students whom I had the opportunity to mentor and work with, Carlos E Pérez De Jesús, Mitchell Lancaster, and Mai Moua. Working in this group with such supportive colleagues has made the years of my graduate research truly enjoyable.

Many thanks to Nancy Thao, Assistant to the Director of Graduate Studies, Department of Chemistry, University of Minnesota. Nancy was the first person who greeted me in the Chemistry Department and helped me get started in this program. She provided continuous support throughout the five years of my graduate studies.

Lastly, this journey would not have been possible without the help of my family and friends. I specifically want to thank Meisam Razviyayn, Zahra Sohrabpour, Sanaz Khosravani, and Fatemeh Sheikholeslami for their invaluable support and mentorship over the years. I cannot express my gratitude for my parents who always encouraged me to pursue education and knowledge, and for my sister, Maryam Mousavi, who always helped me navigate my path in life. Without their unconditional love and support, I would not be where I am today.

Dedication

To my family and friend

Table of Content

List of Tables

List of Figures

Chapter 1

Chapter 2

Chapter 3

Chapter 4

Chapter 5

Chapter 6

Chapter 7

Chapter 8

Chapter 9

Chapter 10

Chapter 11

List of Symbols and Abbreviations

3DOM	3-dimensionally ordered macroporous
A	area
a_x	activity of species x
CIM	colloid-imprinted mesoporous
CV	cyclic voltammogram
C_x	concentration of species x
$J_{cut\text{-}off}$	cut-off current density
DFT	density functional theory
NBu_4ClO_4	tetrabutylammonium iodide
EMI	1-ethyl-3-methylimidazolium
TFSI	bis(trifluoromethylsulfonyl)imide
$BuNMe_3$	butyltrimethylammonium
DSC	differential scanning calorimetry
D_x	diffusion coefficient of species x
E	electrical potential
E^o	standard reduction potential
$E^{o'}$	formal reduction potential
F	Faraday's constant
f	mole fraction
Fc	ferrocene
Fc^+	ferrocenium
PTFE	polytetrafluoroethylene
i	current
K_{Eq}	equilibrium constant
BP	Black Pearl 200
LUMO	lowest unoccupied molecular orbital
HOMO	highest occupied molecular orbital

l	length
n	number of electrons
NBu_4^+	tetrabutylammonium
NEt_4^+	tetraethylammonium
NHE	normal hydrogen electrode
$NHex_4^+$	tetrahexylammonium
$NPent_4^+$	tetrapentylammonium
PVC	poly(vinyl chloride)
z	charge
R	ideal gas constant
T	absolute temperature
t	time
TNT	2,4,6-trinitrotoluene
u_i	mobility of ion i
UME	ultramicroelectrode
XPS	X-ray photoelectron spectroscopy
z_i	formal charge of ion i
ΔG	Gibbs free energy
ΔG^o	standard Gibbs free energy
Γ	surface excess
α	transfer coefficient
EDLCs	electrochemical double-layer capacitors
GC	glassy carbon
η	viscosity
ν	scan rate
Bu_3MeN	tributylmethylammonium
EtMeIm	1-ethyl-3-methylimidazolium
PrMeIm	3-methyl-1-propylimidazolium

HexMeIm	1-hexyl-3-methylimidazolium
$EtMe_2Im$	1-ethyl-2,3-dimethylimidazolium
PrMePi	*N*-methyl-*N*-propylpiperidinium
BuMePyl	*N*-butyl-*N*-methylpyrrolidinium
TEOS	tetraethylorthosilicate
PF	phenol-formaldehyde
Ag NP	silver nanoparticle
ISE	Ion-selective electrode
TEM	transmission electron microscopy
DLS	dynamic light scattering
NOM	natural organic matter
DOM	dissolved organic matter
HA	humic acids
FA	fulvic acids
SRHA	Suwannee River humic acid II
SRFA	Suwannee River fulvic acid II
PLFA	Pony Lake fulvic acid
PPHA	Pahokee Peat humic acid standard
SRNOM	Suwanee River Aquatic NOM
HEPES	4-(2-hydroxyethyl)piperazine-1-ethanesulfonic acid
emf	Electromotive force
MOPS	*N*-morpholino-3-propanesulfonic acid
PVP	polyvinylpyrrolidone
LiOAc	lithium acetate
$Me_{10}Fc$	bis(pentamethylcyclopentadienyl)iron

List of Publications

The results presented in this thesis were adapted from the following publications ([†]equal contribution):

[†]Maurer-Jones, M. A.; [†]Mousavi, M. P. S.; Chen, L. D.; Bühlmann, P.; Haynes, C. L., Characterization of silver ion dissolution from silver nanoparticles using fluorous-phase ion-selective electrodes and assessment of resultant toxicity to Shewanella oneidensis. *Chem. Sci.* 2013, *4* (6), 2564-2572.

Mousavi, M. P. S.; Bühlmann, P., Reference Electrodes with Salt Bridges Contained in Nanoporous Glass: An Underappreciated Source of Error. *Anal. Chem.* 2013, *85* (19), 8895-8901.

Mousavi, M. P. S.; Dittmer, A. J.; Wilson, B.; Hu, J.; Stein, A.; Bühlmann, P., Unbiased Quantification of the Electrochemical Stability Limits of Electrolytes and Ionic Liquids. *J. Electrochem. Soc.* 2015, *162* (12), A2250-A2258.

Mousavi, M. P. S.; Gunsolus, I. L.; Pérez De Jesús, C. E.; Lancaster, M.; Hussein, K.; Haynes, C. L.; Bühlmann, P., Dynamic silver speciation as studied with fluorous-phase ion-selective electrodes: Effect of natural organic matter on the toxicity and speciation of silver. *Sci. Total Environ.* 2015, *537*, 453-461.

Gunsolus, I. L.; Mousavi, M. P. S.; Hussein, K.; Bühlmann, P.; Haynes, C. L., Effects of Humic and Fulvic Acids on Silver Nanoparticle Stability, Dissolution, and Toxicity. *Environ. Sci. Technol.* 2015, *49* (13), 8078-8086.

Saba, S. A.; Mousavi, M. P. S.; Bühlmann, P.; Hillmyer, M. A., Hierarchically Porous Polymer Monoliths by Combining Controlled Macro- and Microphase Separation. *J. Am. Chem. Soc.* **2015,** *137* (28), 8896-8899.

Mousavi, M. P. S.; Kashefolgheta, S.; Stein, A.; Buhlmann, P., Electrochemical stability of quaternary ammonium cations: An experimental and computational study. *J. Elec. Soc.* 2016, *163*, H74-H80.

Manuscripts submitted and in preparation:

†Mousavi, M. P. S.; †Wilson, B.; Kashefolgheta, S.; Anderson, E.; Bühlmann, P.; He. S. and Stein, A. Ionic Liquids as Electrolytes for Electrochemical Double-Layer Capacitors: Structures that Optimize Specific Energy, submitted to *ACS. App. Mater. Inter.* 2015.

Mousavi, M. P. S.; Saba, S. A.; Anderson, E.; Hillmyer, M. A.; Bühlmann, P.; Avoiding Errors in Electrochemical Measurements: Effect of Frit Material on the Performance of Reference Electrodes with Porous Frits. University of Minnesota. 2016. In preparation.

†Mousavi, M. P. S.; †Anderson, E.; Bühlmann, P.; Development of Electrolytes with High Solubility in Fluorous Media: Conductivity and Fluorophilicity. University of Minnesota. 2016. In preparation.

†Mousavi, M. P. S.; †Chen, X. S.; Bühlmann, P.; Application of Fluorophilic Amines as Ionophores in pH sensing Fluorous-Membrane Ion-Selective Electrodes. University of Minnesota. 2016. In preparation.

†Mousavi, M. P. S.; †Saba, S. A.; Hillmyer, M. A.; Bühlmann, P.; Reference Electrodes with Salt-Bridges Contained in Nano-porous Polymers: Improved Alternatives to Vycor. University of Minnesota. 2016. In preparation.

Abstract

My graduate research was focused on improving the performance and expanding the application of two categories electrochemical devices that are used in energy storage and sensing: electrochemical double-layer capacitors and ion-selective electrodes.

Energy storage is essential for sustainable use of renewable energies. Electrochemical capacitors store electrical charge in the double layer at the interface of an electrolyte and a surface, primarily porous carbon with high surface area. The energy density of such a capacitor is determined by ½ CV^2, where V is the potential difference between the plates of a capacitor and C is the capacitance density. Therefore, extending the operational voltage of such devices, which is limited by the electrochemical window of the electrolyte, can improve the device energy density. Optimizing the structure and improving electrochemical stability of electrolytes that can be utilized in electrochemical capacitors, was one of the goals of research presented in this thesis. Chapter 2 reviews the conventional methods for quantifying the electrochemical stability of electrolytes, and discusses their limitations. A new method for quantifying electrochemical stability of ionic liquids and electrolytes is suggested and several advantages of the proposed method is demonstrated for variety of systems.

The effect of electrolyte structure on its electrochemical stability and accessible potential window is discussed in Chapter 3. Results indicated that the cationic core has a significant effect on stability towards reduction. Quaternary ammonium cations were identified to provide the highest electrochemical stability. To further improve the cathodic stability of quaternary ammonium cations, several tetraalkylammonium cations with variations on the alkyl structure were synthesized. It was shown that the chain length, type branching, size, and steric hindrance of the substituents have only a minimal effect on the electrochemical stability. Chapter 4 investigates application of ionic liquids

as electrolytes in electrochemical capacitors. Ionic liquids maximize ion concentration and increase the capacitance density and thus can improve the energy density of the device. For device fabrication, mesoporous carbon electrodes with high accessible surface area (three-dimensionally ordered mesoporous carbon) were used to further improve the capacitance density, and develop high energy density double-layer capacitors. Effect of structure of ionic liquid on its electrochemical stability and double-layer capacitance is fully investigated and structures that optimize energy density are identified.

Ion-selective electrodes, ISEs, are electrochemical sensors that determine the concentration of a wide range of ions and are used for billions of measurements in clinical, environmental, and chemical process analyses every year. ISEs offer sensitive, selective, label-free, and non-destructive detection in complex media, which makes them appealing tools for in situ analysis and measurements in the complex biological media. However, two factors limit the application of ISEs in biological analyses: **(1)** Interference of biological molecules **(2)** Large sample volumes needed for ISE measurements. Recently, fluorophilic compounds have been applied in the ion-selective membrane of ISEs in an effort to reduce the interference of biological molecules. Fluorous compounds are organic molecules with high content of fluorine atoms within their structure and have much lower hydrophobicity compared to biological molecules. Fluorous-phase ISEs are shown to be more selective, and due to the lower membrane hydrophobicity are suggested to be less susceptible to the interference of biological molecules.

Chapters 5 to 7 discuss the reliability of sensing with fluorous-phase ion-selective electrodes in the environmental and biological samples. For this purpose, I assessed application of the silver-selective fluorous-phase ISEs in studying the silver nanoparticles, AgNPs, toxicity in biological and environmental conditions. The widespread use of AgNPs in many consumer products as antimicrobial agents has raised many concerns about their impact on the environment. Toxicity of AgNPs is mainly

imparted through ionization and release of Ag^+. Silver selective fluorous-phase ISEs were successfully used to monitor the extent and kinetics of Ag^+ release from AgNPs in the presence of the bacterium, *Shewanella oneidensis*, in the cell growth media where the sensors are exposed to a variety of interfering biological molecules. In addition to validating reliability of detection with fluorous-phase ISEs, AgNP ionization, and Ag^+ speciation was carefully quantified, providing critical information for the correct assessment of AgNP toxicity. Moreover, silver selective fluorous-phase ISEs were used to assess the effect of Natural Organic Matter, NOM, on Ag^+ and AgNP toxicity, the results of this project are presented in Chapters 6 and 7. NOM is a product of decomposition of living organisms, consists of large biological molecules, and is present in water, soil, and sediments. NOM can interact with the released Ag^+, resulting in silver ion speciation, decreased bioavailability, and altered toxicity. Fluorous-phase silver selective ISEs were successfully utilized to study Ag^+ release in the solutions containing NOM, and studied the extent of Ag^+ speciation and toxicity under various environmentally relevant conditions.

Even though fluorous-phase ISEs can be successfully used in complex biological and environmental media, the required large sample volumes required are still a drawback of these sensors. A part of my thesis research is focused on reducing the sample volume needed for detection with these sensors. This issue can resolved by reducing both the ISE and the reference electrode size. During my efforts to miniaturize the reference electrode, the well-established nanoporous glass plugs, which are widely used in commercial products, were utilized. During our experiments, deficiencies and sample dependent potential can cause up to 900% error in the determined concentration were noticed. The negative surface charge of the glass, electrostatic forces contribute to the deficiency of these reference electrodes. The findings are discussed in Chapter 8. Realizing the impact of the porous frit on the performance of reference electrodes, alternative frit materials to Vycor glass and the advantages and disadvantages of each material are discussed in detail in Chaper 9. Porous polymeric materials are appealing candidates for frit materials in

reference electrodes, because the pore size and surface chemistry can be well controlled and designed.

To miniaturize the ISEs, the tip diameter of ISEs (1–2 cm) can be decreased more than one thousand fold by developing ion-selective microelectrodes, μ-ISEs (tip diameter 1-5 μm). Yet, the increased thickness and decreased surface area of the μ-ISE membranes increases the electrical membrane resistance. To reduce the membrane resistance, a highly hydrophobic electrolyte salt is added to the membrane. Unfortunately, the currently available hydrophobic salts do not have sufficient solubility in fluorous phases to allow development of fluorous-phase μ-ISEs. Therefore, several structures for this electrolyte were designed (1,3-dialkylimidazolium or tetraalkylammonium cations paired with tetrakis[3,5-bis-(alkyl)phenyl]borate, where alkyl groups contain perfluorinated hydrocarbon chains of $(CH_2)_nC_mF_{2m+1}$ with $0 \leq n \leq 4$, and $6 \leq m \leq 10$) and the synthesis was carried out. Results show the designed electrolytes have good solubility in fluorous phases and can decrease the membrane resistance by more than six orders of magnitude. The design, synthesis, and conductivity of developed fluorophilic electrolytes are discussed in Chapter 10.

1 CHAPTER ONE

Introduction

1.1 Chapter Overview

The underlying theories behind experiments and analyses of the work presented in this thesis are described in this chapter. This work is heavily focused on ion-selective electrodes (ISEs) and electrochemical double-layer capacitors; thus, the history, response mechanism, and current limitations of these electrochemical devices are discussed. Since reference electrodes are an inevitable part of any electrochemical measurement, this chapter also briefly discusses the working mechanism and different types of reference electrodes. The foundation of electron transfer at an electrode and the concept of cyclic voltammetry are also briefly introduced.

The research presented in each chapter covers a wide range of topics, and in this introductory chapter, the general concepts and theories needed for interpretation of electrochemical experiments are discussed; specific details and backgrounds relevant to each research project are presented in the beginning of each chapter.

This introductory chapter only provides an overview of theoretical backgrounds and details of electroanalytical techniques; the author recommends the following references for a much more comprehensive introduction to electrochemistry, reference electrodes, and ion-selective electrodes:

Buhlmann, P.; Chen, L. D. In *Supramolecular Chemistry: From Molecules to Nanomaterials*; Steed, J. W., Gale, P. A., Eds.; John Wiley & Sons Ltd: Chichester, UK, 2012.

Bard, A. J.; Faulkner, L. R. *Electrochemical Methods Fundamentals and Applications*; 2nd ed.; John Wiley and sons: New York, 2009.

G. Inzelt; Lewenstam, A.; Scholz, F. *Handbook of Reference Electrodes*; Springer-Verlag Berlin Heidelberg: New York, 2013.

1.2 Introduction to Electrochemical Techniques

Shown below is the electron transfer reaction between O and R which are an Oxidized and Reduced species, respectively (*n* is the number of transferred electrons, and charge signs are omitted for simplicity).

$$O + n\,e^- \rightleftharpoons R \qquad (1)$$

In the electrochemistry terminology, O and R are commonly referred to as a *redox couple*. Reaction 1 can also represent a heterogeneous reaction occurring at the surface of an electrode and sample solution. Currents or potential pulses can be applied to the electrode to drive the reaction equilibrium to the desired direction. The reaction Gibbs free energy (ΔG) of this reaction can be written as:

$$\Delta G = \Delta G^o + RT \ln\left(\frac{a_R}{a_O}\right) \qquad (2)$$

where ΔG^o is the standard Gibbs free energy for Reaction 1, R is the ideal gas constant, T is the absolute temperature and a_x is the activity of species x. Equation 3, which is the famous Nernst equation, can be obtained by diving ΔG by "$-nF$", where F is Faraday's constant.

$$E = E^o - \frac{RT}{nF} \ln\left(\frac{a_R}{a_O}\right) \qquad (3)$$

Assuming a temperature of 25 °C, the constant values can be inserted into Equation 3 and activity coefficients can be extracted from the logarithmic term to give Equation 4:

$$E = E^{o'} - \frac{RT}{nF} \ln\left(\frac{C_R}{C_O}\right) = E^{o'} - 0.059 \log\left(\frac{C_R}{C_O}\right) \quad \{\text{For } T = 25\,^\circ\text{C}\} \qquad (4)$$

where C is the concentration of the species at the electrode and $E^{o'}$ is the formal reduction potential of the couple.

1.2.1 Electrochemical Cells

Most electrochemical measurements are performed in electrochemical cells that have as the main components a working electrode, a reference electrode, and a salt bridge. In many electrochemical measurements, a fourth element referred to as the auxiliary electrode or counter electrode is introduced in the system. Electrodes are electrically conducting materials that are inserted into the test solution, and are used for measuring electrical properties of test solution or perturbations of the system upon applying external voltages or currents through the system. An electrode inserted in a solution of O and R is referred to as a half-cell, and the potential of this half-cell is determined by the concentrations of O and R, as shown in Equation 3.

Electrical measurements can be performed only in closed circuits and, therefore, the potential of an electrode inserted in the test solution (working electrode) is measured with respect to a second half-cell with a known potential. The two half-cells are connected by a salt bridge, which provides a liquid junction between the two compartments. The purpose of the salt bridge is to allow ionic conductivity between the two half-cells while preventing the cross-contamination of the cells by slowing the transport of solutes across the junction. Examples of different experimental designs of salt bridges include liquid-filled capillaries, agar gel matrixes, or a piece of fritted glass. At the junction of any two liquids, a potential gradient known as the liquid-junction potential can be formed. The liquid-junction potential forms as the result of a non-equilibrium process that occurs at the interface of two miscible electrolyte solutions, and its magnitude can be predicted by the Henderson equation.[1-3] Utilizing cations and anions with similar mobilities and high concentrations in the salt bridge can minimize the liquid-junction potential.[4,5]

In real-life analyses, the electrical potential of only one of the half-cells is of interest; the electrode in this half-cell is labeled as the working electrode. Standard reference half-cells with defined interfacial potentials were introduced to be paired with the working electrodes; they are referred to in such experiments as the reference electrode.

1.2.2 Reference Electrodes

Reference electrodes are designed to provide a constant and sample-independent reference potential and are used in almost every electrochemical measurement, e.g., potentiometry, amperometry, voltammetry, etc.[1,3] The constant potential is achieved by employing a redox system with buffered concentrations for all the participating compounds in the redox reaction. A historical example of a redox system is a platinum wire inserted in an aqueous solution of protons with activity of one in contact with hydrogen gas with a pressure of 1.0 atmosphere. The potential of the resulting reference electrode (referred to as the normal hydrogen electrode, NHE) is defined as zero at all temperatures and is the basis relative to which the standard reduction potential of all other redox couples is reported.[3,6]

Because use of a NHE involves maintaining a partial pressure of H_2 of 1 atm, the experimental use of a NHE is complicated, and other redox systems were used for the development of reference electrodes. The common redox systems for reference electrodes used in aqueous media are $Ag/AgCl/Cl^-$ and $Hg/Hg_2Cl_2/Cl^-$, where the metal is in contact with the metal-chloride precipitate and is immersed in an aqueous solution of potassium chloride (usually 1-3 M) saturated with AgCl or Hg_2Cl_2.[1-3] Reference electrodes for organic media usually apply a Ag/Ag^+ redox system, i.e., an Ag wire is immersed in $AgNO_3$ solution of an organic solvent.[1,3] To allow an accurate electrical measurement, reference and sample solutions should be brought into contact at a junction with low electrical resistance.[2,7] To avoid the cross-contamination of sample and reference solutions, the intermixing of these solutions at the junction should also be minimized.[2]

Commercially available reference electrodes contain the salt bridge solution in two different junction types, as discussed in the next sections. It should be noted that reference electrodes without liquid junctions have been recently developed. These electrodes instead utilize current pulses to define the potential. By applying a current pulse, the transmembrane ion fluxes can be controlled to obtain a sample-independent reference electrode potential.[8]

Quasi-reference electrodes, or pseudo-reference electrodes, consist of a metal wire inserted into the test solution, and are used when proper reference electrodes are not available or are too cumbersome to use. Quasi-reference electrodes are suited for samples with small volumes and for samples with un-conventional solvents that are not compatible with existing reference electrodes.[1] Because the potential of a metal in a solution without an active redox couple is not well-defined, the potential of the quasi-reference electrode is calibrated against a well-known redox system, usually the ferrocene/ferrocenium (vs. Fc/Fc^{+}) redox couple.

1.2.3 Reference Electrodes with Free Flow Liquid Junctions

In this type of reference electrodes, the bridge electrolyte can flow into the sample, e.g., through a movable ground glass sleeve junction. These junctions allow a small amount (0.5-2 μL/h) of bridging solution to flow into the sample solution. The commonly used bridge electrolytes are potassium chloride and lithium acetate, for both of which the mobility of the cation and anion are similar, thus, minimizing the liquid junction potentials at the interface of bridge electrolyte and sample solution.[2] These electrodes are relatively easy to maintain and clean. The solution of the bridge electrolyte should regularly be re-filled. Common problems with these types of electrodes are clogging of the junction by proteins and lipids, and sample contamination by bridge electrolyte.[9]

1.2.4 Reference Electrodes with Porous Frit Junctions

The second common approach is separating the reference and sample solutions by a porous material filled with an electrolyte (usually the same electrolyte used in the reference solution).[10] First reported in 1955, porous glass plugs with a high density of nanopores (4.0 nm average pore size)[11] were made commercially available under the brand name Vycor and were recommended for use in reference electrodes.[12] Nanoporous Vycor offered the advantage of restricting excessive mass transfer of reference and sample components while providing a stable and low-resistance junction between the two.[7,12] Since then, Vycor has been widely used for fabrication of both in-house-prepared and commercially available reference electrodes.[7,10-12]

Unfortunately, systematic errors in measurements made with reference electrodes that contain nanoporous Vycor frits were reported recently.[10] It was shown that the reference potential in these electrodes is dependent on sample composition and can shift by as much as 50 mV during the measurement.[10] The variations in the reference potential were shown to be caused by the surface charge density on the glass surface of the nanoporous Vycor, and to be highly affected by the ionic strength of the sample solution.[10,13]

1.2.5 Application of External Voltages to Working Electrodes

The voltage of the working electrode can be controlled by an external voltage source. In that case, the concentrations of R and O in the test solution readjust eventually to satisfy the Nernst Equation. The change in concentration will be accommodated by reaction 1, which will result in passage of current either into or out of the working electrode. Under conditions where electrons pass *into* the electrode (R is being oxidized to O), the working electrode is considered an *anode* and the current is thus *anodic*. If electrons are passing from the working electrode into the solution (O is being reduced to R), the electrode is considered a *cathode* and the current is thus considered *cathodic.*

When large currents start to flow in the circuit consisting of working and reference electrodes, the potential of the reference electrode may change as a result of the passage of current. Of course, changes in the potential of reference electrodes are not desirable. To overcome this issue, a third electrode named auxiliary or counter electrode is introduced in the electrical circuit, see Figure 1. The three electrodes are connected to the potentiostat, which is an electrical device used for measurements of currents and potentials in electrochemical measurements. The potentiostat keeps the electrical resistance for current passing through the reference electrode high; thus, all the current passes between the working and auxiliary electrodes. This allows precise control of the potential of the working relative to the reference electrode. Usually, auxiliary electrodes are good conductors with high surface areas to allow passage of large currents without any polarization, e.g., a coil of Pt wire.

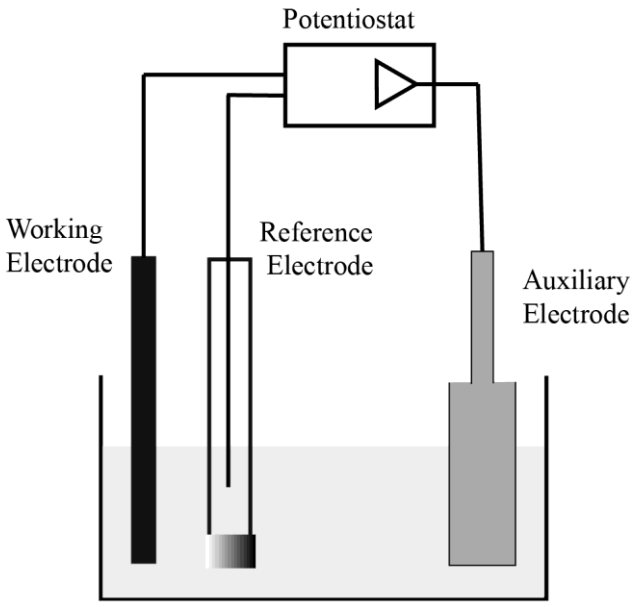

Figure 1. Simplified diagram of a three electrode setup used in electrochemical measurements.

Due to the resistance of the bulk solution, the potential at the interface of the working electrode and sample is lower than the applied potential by a term proportional to current and resistance of sample solution. The potential drop across the bulk solution can be minimized by addition of supporting electrolytes to the measuring solution.[1] If this bulk resistance is not compensated for in an electrochemical experiment, distortion of the measured current-potential relationship will be observed.

1.2.6 Cyclic Voltammetry

Cyclic voltammetry is one of the most commonly used electroanalytical techniques and can provide insights on mechanistic and kinetic aspects of electrode reactions.[1] Using this technique, the potential is swept in a linear manner with respect to time at the scan rate of ν, and the current is monitored during the potential sweep. See Figure 2 for a plot of applied potential with respect to time.

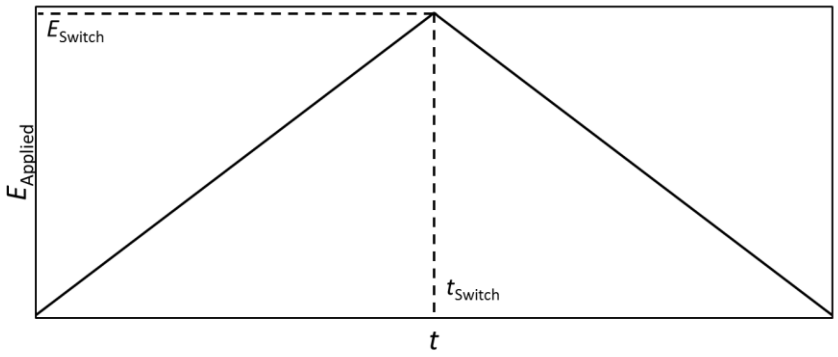

Figure 2. Profile of applied potential and time in a cyclic voltammetry experiment.

For a redox system of R and O during a cyclic voltammetry analysis, the Nernst equation must be rewritten as a time-dependent form.

$$E_{\text{Applied}} = E^{o'} - \frac{RT}{nF}\ln\left(\frac{C_{\text{R}}(0,t)}{C_{\text{O}}(0,t)}\right) \qquad (5)$$

In this notation, $C_x(y,t)$ refers to the concentration of species x a distance y from the surface of the electrode at time *t*. Since $E_{Applied}$ is a function of time, scan rate, and the initial starting potential, we can rearrange Equation 5 to:

$$E_{Initial} + \nu t = E^{o'} - \frac{RT}{nF}\ln\left(\frac{C_R(0,t)}{C_O(0,t)}\right) \qquad (6)$$

The concentrations of R and O at a given time are determined by rate of mass transport of these species from the bulk solution to the electrode surface. The total transport or flux of any chemical species to an electrode is described by the Nernst–Planck equation, which combines the individual contributions from diffusion (resulting from concentration gradients), migration (due to electric fields), and convection (caused by hydrodynamic velocity). For mass transport in one dimension only, the flux, *J*, of a species is given by[1]

$$J(x,t) = -\left[D\,\frac{\partial C(x,t)}{\partial x}\right] - \left[\frac{zF}{RT}DC(x,t)\right]\left(\frac{\partial \phi(x,t)}{\partial x}\right) + C(x,t)V(x,t)$$

where *D* and *C* are the diffusion coefficient and the concentration of the species in consideration, ϕ is the electrostatic potential, and *V* is the hydrodynamic velocity. Typically, voltammograms of redox-active molecules are measured in unstirred solutions and in the presence of high concentrations of supporting electrolyte; this minimizes convection and the migration of the redox-active molecules, making diffusion the main mode of mass transport.[1] Fick's second law must then be used to relate the mass transport rate to the concentration gradient of analyte from the electrode surface to the bulk solution. Because both the applied potential and diffusion are time-dependent variables, a discrete solution for Equation 6 is not available and numerical simulation are used to predict the CV of dissolved species.[1]

1.3 Electrochemical Capacitors

1.3.1 Overview and History

With the growing global population, the demand for energy increases rapidly, requiring utilization of renewable energy resources to address both energy and environmental concerns. However, the power obtained from renewable energies (e.g., solar and wind energy) is affected by environmental conditions, making energy storage technologies vital for assuring a more consistent and reliable power. Among electrical energy storage devices, batteries, electrochemical and hybrid battery/capacitor systems are the prevalent options. Even though batteries have low power, long charging times, limited cycling life times, and require maintenance, consumers adapted to the limitations of these devices due to lack of an alternative with comparable energy density. The recent advances in the design of nanostructured materials have resulted in improvements of the energy density of electrochemical capacitors, making them more compelling for energy storage applications.[14,15]

Electrochemical capacitors, also referred to as supercapacitors or ultracapacitors, store electrical charge in a double layer at the interface of an electrolyte and a surface, primarily porous carbon with high surface area. Interestingly, the concept of double-layer capacitance was first introduced in 1853 by a German physicist, Hermann von Helmholtz, yet, double-layer capacitors were not commercialized until 1957.[16] Unlike in batteries, this process does not involve chemical reactions of the electrolyte and, therefore, can be charged or discharged very quickly, resulting ideally in unlimited discharge cycle life and high specific power for the supercapacitor. The three parameters used to determine capacitor performance are the capacitance, energy, and power, defined by the following equations:

$$C = \frac{\varepsilon^* \varepsilon_0 A}{d} \qquad (7)$$

$$E = \frac{1}{2} CV^2 \quad (8)$$

$$P = \frac{V^2}{4R} \quad (9)$$

where C is the capacitance of the cell, ε^* is the dielectric constant of the electrolyte in the double layer, ε_0 is the dielectric permittivity of the vacuum, A is the accessible surface area for ion adsorption, d is the effective thickness of the double layer, E is the cell energy, V is the maximum potential the cell is cycled at, P is the power of the cell, and R is the resistance of the cell. The equations show that for a given mass or volume of a cell, the energy and power densities scale exponentially with the potential the EDLC is cycled at. Therefore, while improving the capacitance is important and can have a large effect on the cell performance, significant attention should be given to the voltage limits of the cell. Electrochemical capacitors have three main components, i.e., the electrode material, the electrolyte, and a separator.

1.3.2 Electrode Materials

Since double-layer capacitance occurs at the surface of the electrode and electrolyte solution, selection of the electrode material has a large impact on the properties of an electrochemical capacitor. A variety of materials such as are carbon, metal-oxides, and conducting polymers, were used as electrodes in electrochemical capacitors. Carbon (in the forms of foams, fibers, and nanotubes) has been particularly popular since it provides electrodes with a high surface-area per mass, and also has low cost, high availability, and long history of use.[16] The pore size of the electrode material must be chosen to suit the electrolyte used. Ions have different mobilities in the carbon pores than in bulk solution; ions cannot access very small pores, and thus cannot contribute there to the double-layer capacitance. Due to use of electrolyte solutions and porous electrode materials, electrochemical capacitors have capacitances per unit volume that are much larger than

electrostatic or electrolytic capacitors; this results in high energy densities for electrochemical capacitors. The electrodes in these devices can be symmetrical (same material for both cathode and anode) or asymmetrical.[16]

1.3.3 Electrolyte

The maximum accessible potential window of such devices is usually limited by electro-decomposition of the electrolyte or solvent, and these devices should not be charged beyond a voltage that can cause degradation of these components. Since electrolytes bear localized charges, they often have lower electrochemical stability than neutral solvent molecules. Therefore, the choice of electrolyte determines the potential window of electrochemical capacitors.[17] Four primary classes of electrolyte solutions have been used in electrochemical capacitors: aqueous,[18] organic,[19] polymeric,[20] and ionic liquid (IL) electrolytes.[21] Among these, ILs have the largest potential windows, exceeding 5 V,[22] compared to aqueous and polymer electrolyte solutions, which typically are limited to 1 V, and organic electrolyte solutions (typically based on acetonitrile or cyclic carbonates such as propylene carbonate) that are limited to 3.5 V due to decomposition of the solvent.[18,19] Additionally, ILs typically have a high decomposition temperature, allowing for a wider range of applications where high temperatures (exceeding 100 °C) are expected.[23,24] The magnitude of capacitance of an electrochemical capacitor is greatly influenced by the choice of electrolyte as well. The sizes of the ions affect the ability to store charge at the porous surface area; smaller ions allow higher ion packing at the surface and larger capacitances.[16]

1.3.4 Separator

The separator is an ion-permeable membrane that is placed in between the two electrodes of the electrochemical capacitor to avoid direct electrical contact between the electrodes. High ion conductance through the material and low thicknesses are preferred for

separators. Examples include polymers, paper, ceramic fibers, and glass-fiber separators.[16]

1.3.5 Electrochemical Stability of Electrolytes

The energy density (ED) of a charge capacitor is determined by ED = ½ CV^2, where V is the potential difference between the plates of a capacitor and C is the capacitance density. Therefore, because of the V^2 term in the energy density equation, extending the operational voltage of the device, which is limited by the electrochemical window of the electrolyte or solvent, is highly desirable. The electrochemical window is the potential range in which the electrolyte and solvent are chemically stable and do not get reduced or oxidized. Determination of the electrochemical stability limit of electrolytes is not well defined. Usually, a current–voltage polarization curve is measured, and the voltage at which a specific current density, *J*, is reached, is defined as the cathodic or anodic electrochemical limit of the electrolyte.[6] The choice of the cut-off current density, $J_{\text{cut-off}}$, is quite arbitrary, and a number of $J_{\text{cut-off}}$ values (0.01 to 5.0 mA/cm^2) have been used in the literature.[24-41] Unfortunately, the choice of $J_{\text{cut-off}}$ can influence the electrochemical limit of electrolytes by as much as 0.9 V.[24,41] In Chapter 2 of this thesis, a more reliable method for defining electrochemical stabilities is presented.

1.4 Ion-Selective Electrodes (ISEs)

1.4.1 Overview and History of ISEs

Ion-selective electrodes, ISEs, are electrochemical sensors that determine the concentration of a wide range of ions and are used for billions of measurements in clinical, environmental, and chemical process analyses every year.[42,43] The vast majority of laboratories quantify the concentration of sodium and potassium in blood using ISEs, i.e., in the United States alone, more than 200 million clinical analyses of these ions were reported to be performed with ISEs.[44] The first ion-selective electrode was developed for

detection of protons; Max Cremer discovered pH sensitive glasses in 1906, which resulted in development of the first commercial pH electrode in the 1930s.[42] Modifying the glass composition allowed detection of other ions such as Li^+ and Na^+ with limited selectivities.[45] The scope of ion sensing was soon expanded by introduction of crystalline compounds such as LaF_3, AgCl, or Ag_2S as sensing materials in the early 1960s.[43] However, the difficulty of designing crystalline materials with selectivities for ions of interest and the low conductivity of many of these materials restricted the development of ISEs for diverse ions.

This issue was overcome by application of ion-binding receptors (ionophores) in the ion-selective membrane of ISEs. One of the earliest ionophores used in ISEs was inspired by the work of Moore and Pressman, who in 1964 reported that the antibiotic valinomycin (structure shown in Figure 3) facilitates the uptake of K^+ into mitochondria.[42,46] This observation suggested strong host-guest chemistry between valinomycin and K^+. Soon after, antibiotics were used in thin water-immiscible films and ISEs, and it was shown that responses with similar selectivities to biological settings can be achieved.[47,48] Currently, the K^+ ISE based on the valinomycin ionophore is still one of the most successful commercial ISEs. The strong and selective binding of K^+ to valinomycin permits selective detection of K^+ in complex environments such as blood.[42] The experimental design of the original ionophore-based ISEs is very similar to pH glass electrodes, which contain inner-filling and outer filling solutions. Nowadays, ISEs cover a wide range of analytes and have diverse experimental designs, including ISEs with no inner-filling solution (referred to as solid-contact ISEs), ISEs with gas-permeable membranes for detection of volatile species, ISEs with enzyme-integrated membranes, paper-based and printable ISEs, etc.[49-52]

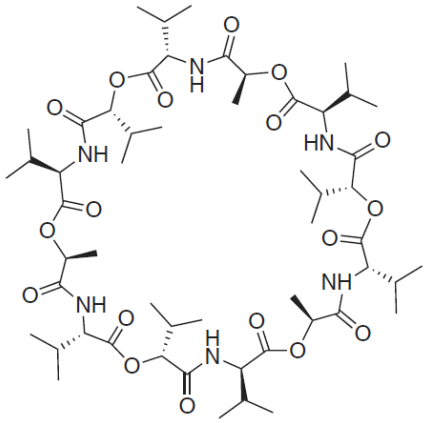

Figure 3. Structure of valinomycin, which is used as ionophore in K^+ ISEs.

1.4.2 Response Mechanism of ISEs

ISEs are potentiometric sensors (in potentiometry, analysis is performed under zero-current conditions) that selectively responds to the activity of specific ions in the sample solution. A typical setup consists of an ISE and an external reference electrode attached to a potentiometer, forming two galvanic half cells, see Figure 4.[42] The two half-cells are connected via a salt bridge housed in the body of the external reference electrode. A critical element in ISEs that enables detection of ions is the hydrophobic ion-selective membrane. The components of the ion-selective membrane are specifically designed to selectively bind to the ion of interest and develop a concentration dependent potential at the interface of the membrane and sample.[42] This potential is referred to as the electromotive force, emf, and is measured with respect to an additional electrode that provides a constant and sample independent potential, known as the reference electrode.

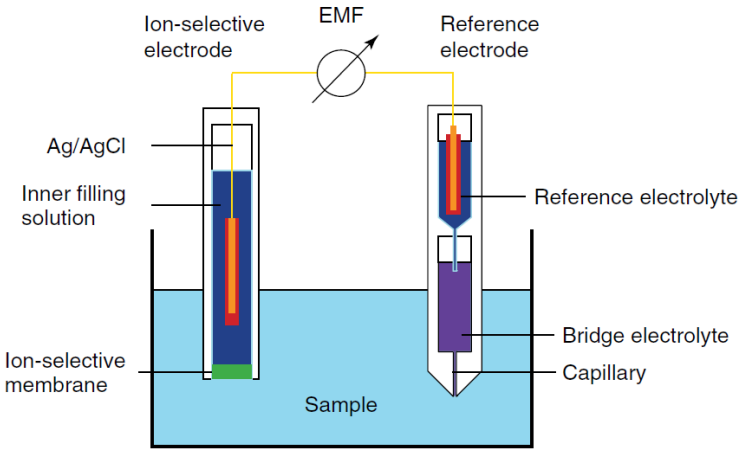

Figure 4. Diagram of a typical experiment setup with ion-selective electrodes.[42]

The ion-selective membrane is sandwiched between two different aqueous solutions—the sample solution and the inner filling solution. Inside the ISE, a Ag/AgCl wire contacts the inner filling solution creating an internal reference electrode that provides a well-defined potential. The total cell can be represented as follows:

Ag; AgCl; KCl (satd) | salt bridge | sample | membrane | internal solution; AgCl; Ag

E_1 E_2 E_3 E_J E_M E_4 E_5

Reference Electrode System Ion-Selective Membrane Electrode

Only E_M, the membrane potential, and E_J, the liquid junction potential at the sample/bridge electrolyte interface, are sample-dependent. Thus, the sample-independent phase boundary potentials E_1 to E_5 can be combined and represented by a constant value. The measured emf is usually expressed as:

$$emf = (E_1 + E_2 + E_3 + E_4 + E_5) + E_M + E_J = E_{const} + E_M + E_J \qquad (10)$$

The liquid junction potential, E_J, at the interface of the salt bridge and sample solution is the result of the difference of their ionic compositions.[2] Fortunately, in many

experiments, E_J can be kept very small, constant or can be estimated using the Henderson formalism.[1,2] This ensures that the major contribution to the emf is from the membrane potential, E_M. The membrane potential itself can be divided into three parts: the phase boundary potential at the membrane and inner-filling solution interface, the membrane diffusion potential, and the phase boundary potential at the membrane and sample solution interface. The membrane and inner-filling solution phase boundary potential can generally be assumed to be independent of the sample, and the diffusion potential can be neglected providing there is not a concentration gradient within the membrane.[53,54] This allows E_M from the previous equation to become

$$E_M = E_{const} + E_{PB} \qquad (11)$$

where E_{PB} is the phase boundary potential at the membrane/sample solution interface, which is determined by the activity of the sample ion in solution.[43] This phase boundary potential can be derived using thermodynamics. The electrochemical potential of an ion I in an aqueous phase can be expressed by:

$$\tilde{\mu}_I(aq) = \mu_I(aq) + z_I F\phi(aq) \qquad (12)$$

Where z_I is the charge of the ion I, F is the Faraday constant, ϕ (aq) is the electrical potential, and μ_I (aq) is the chemical potential of ion I in an aqueous phase. The μ_I (aq) can be defined as:

$$\mu_I(aq) = \mu_I^{\circ}(aq) + RT ln\, a_I(aq) \qquad (13)$$

where μ_I° (aq) is the chemical potential under standard conditions, R is the gas constant, T is the temperature, and a_I (aq) is the activity of ion I in the aqueous solution. Substituting equation 13 into 12 gives the expression:

$$\tilde{\mu}_I(aq) = \mu_I^{\circ}(aq) + RT ln\, a_I(aq) + z_I F\phi(aq) \qquad (14)$$

If the membrane is treated as the organic phase, the electrochemical potential for ion I in the membrane can be written as:

$$\tilde{\mu}_I(org) = \mu_I(org) + z_I F\phi(org) = \mu_I^{\circ}(org) + RT ln\, a_I(org) + z_I F\phi(org) \qquad (15)$$

It can be assumed that interfacial equilibrium between the two phases is reached, resulting in identical electrochemical potentials of the ion I in both phases. The E_{PB} can be calculated by combining equations 14 and 15:

$$E_{PB} = \phi(org) - \phi(aq) = -\frac{\mu_I^{\circ}(org) - \mu_I^{\circ}(aq)}{z_I F} + \frac{RT}{z_I F} ln \frac{a_I(org)}{a_I(aq)} \qquad (16)$$

Substitution of equation 16 into equation 11 gives an expression for E_M:

$$E_M = E_{const} + E_{PB} = E_{const} - \frac{\mu_I^{\circ}(org) - \mu_I^{\circ}(aq)}{z_I F} + \frac{RT}{z_I F} ln \frac{a_I(org)}{a_I(aq)} \qquad (17)$$

Combining the sample-independent parts into a constant E^0, equation 8 becomes the well-known Nernst equation:

$$E_M = E^0 + \frac{RT}{z_I F} \ln\, a_I(aq) \qquad (18)$$

Therefore at room temperature (298 K), an ISE would ideally display a so-called "Nernstian" response slope of 59.16 mV per 10-fold change in the activity of a monocation.[42] Figure 5 shows a representative response curve of an Ag^+ ISE measured at room temperature. The emf of the Ag^+ ISE increases as the Ag^+ concentration increases in the measuring solution.

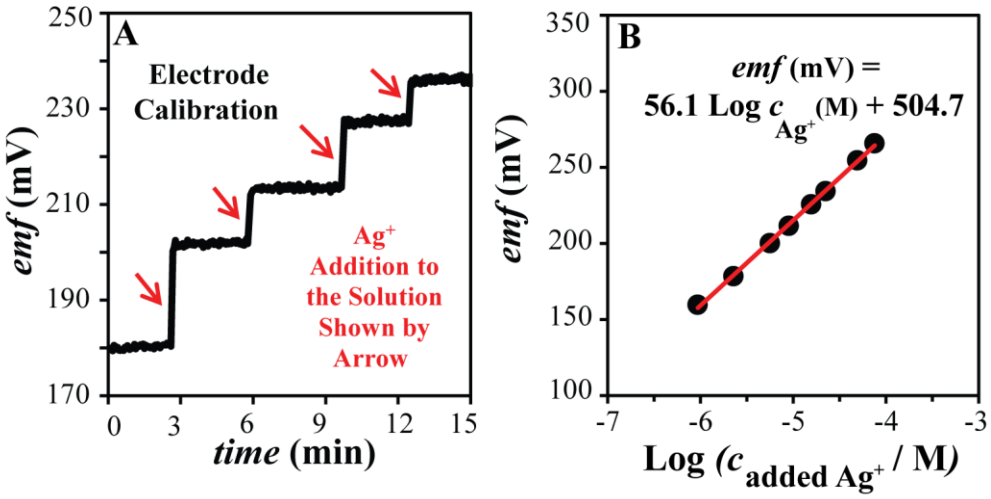

Figure 5. (A) The arrows indicate additions of $AgCH_3COO$ aliquots to the measuring solution. The emf of the Ag^+ ISE increases after each rise in Ag^+ concentration. (B) The linear relationship between the emf and Log c_{Ag^+} can be used as the calibration equation for converting emf values to Ag^+ concentrations.

1.4.3 Components of ISE Membrane

Most ISE membranes consists of four main parts: the polymer matrix, plasticizer, ionic site and ionophore; the role of each component is discussed below.[42]

1.4.3.1 The Polymer Matrix

The main component of the membrane is the polymer matrix. The main purpose of the polymer is to provide the mechanical support for the membrane. Polyvinylchloride (PVC) is the most popular polymer for use in ISE membranes due to its stability. Examples of other polymers used as polymer matrixes in ISE membranes include polyurethanes, silicone rubber, and polyacrylates; see Figure 6 for structures.[55-58] For proper functioning of ISEs, there should be sufficient ion conductivity in the sensing membrane. Therefore, the glass transition temperature (T_g) of the ISE polymer matrix should always be below the temperature at which the ISE will be operated.[42,45] At or below the glass transition

temperature (T_g), the polymer is hard, rigid and amorphous. Above this temperature the polymer is soft and flexible and has enough fluidity to allow the movement of ionic species through the membrane. Polymers such as high molecular weight PVC (T_g ~ 80°C) require a plasticizer to meet the fluidity requirements.[42]

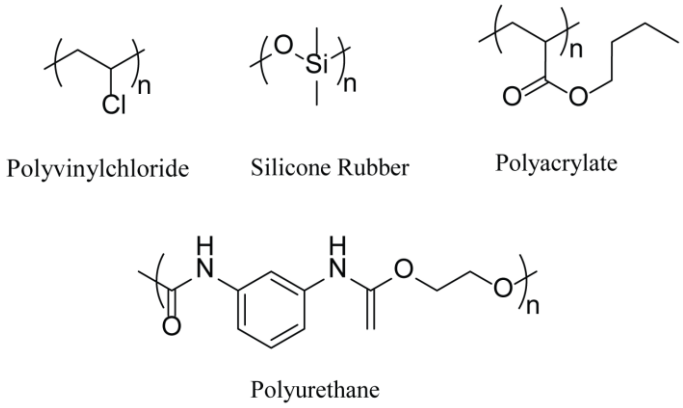

Figure 6. Structure of polymers (polyvinylchloride, polyurethanes, silicone rubber, and polyacrylates) used in ISE membranes.

1.4.3.2 Plasticizer

If the T_g of the pure polymer is too high, a plasticizer should be used to lower the polymer T_g. Plasticizers make up the majority of the membrane weight by solubilizing the chains of the polymer support. The plasticizer should have a high boiling point to prevent evaporation, as well as high hydrophobicity to discourage leaching into the sample solution. It has been shown that the polarity of the plasticizer can affect the selectivity of the ISE and the susceptibility to biofouling, so this should also be taken into account when choosing a plasticizer.[43] Figure 7 shows examples of plasticizers that are commonly used in ISEs.

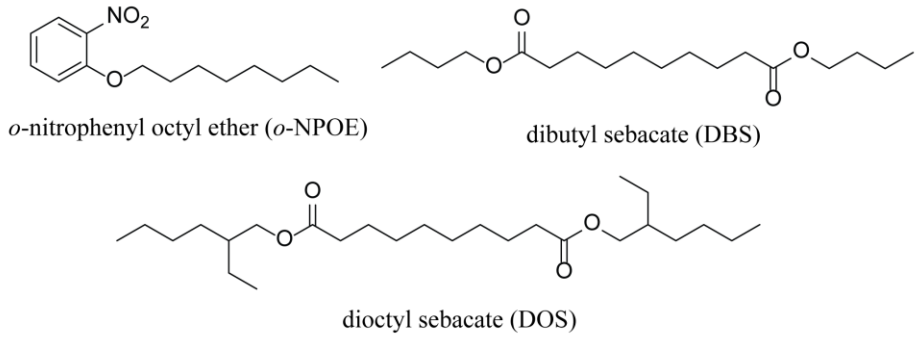

Figure 7. Structure of plasticizers that are commonly used in ISEs.

1.4.3.3 Ionic Sites and Ionophores

Ionic sites play an important role in the performance of the ISE. Anionic sites are used to create ISEs that are selective to cations and they consist of a highly hydrophobic anion paired with a hydrophilic cation; when the membrane is exposed to the test solution, the cations present in the sample can exchange with the cations in the membrane. However, due to the large free energy of transfer (from the membrane to the aqueous phase) of the hydrophobic anionic site, anion exchange does not occur; see Figure 8A. Cationic sites are used to create ISEs that are selective to anions. Similarly, cationic sites consist of a highly hydrophobic cation paired with a hydrophilic anion; see Figure 8B. Structures of representative ionic sites are shown in Figure 9.

The ionic site facilitates ion exchange by serving as a counter-ion for the primary ions diffusing out of the sample solution and into the membrane. This process maintains the electroneutrality of the membrane and prohibits the movement of counter ions from the bulk solution to the membrane in significant quantities. Ionic site used in an optimized ratio to the ionophore improve the selectivity of the ISE.[43]

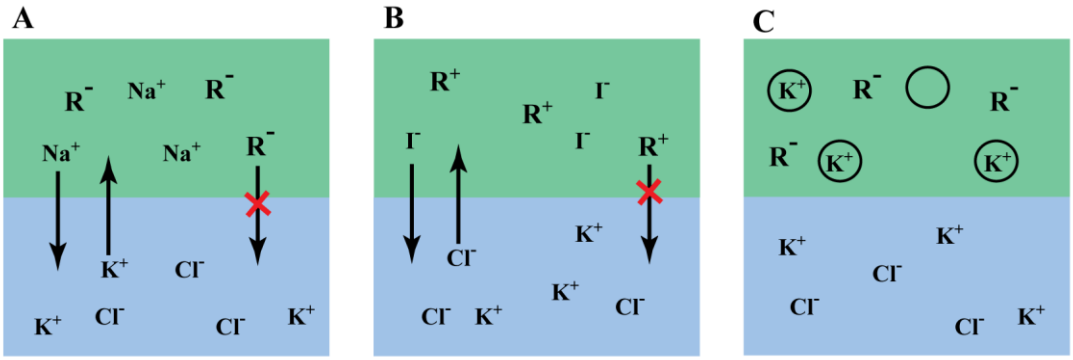

Figure 8. ISE membrane with the anionic site NaR shown in (A), and in (B) membrane with cationic site RI. (C) ISE membrane with ionophores that bind K^+ ions: the concentration of K^+ in the membrane is controlled by the concentration of the anionic site.

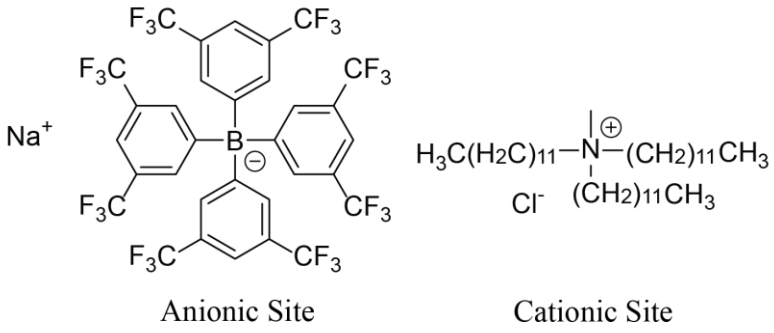

Figure 9. Structures of representative ionic sites used in ISEs.

Ionophores determine the selectivity of the ISE by reducing the free energy of transfer of the target ion from the sample solution into the membrane. The ionophore must be soluble in the polymer membrane, and should strongly but reversibly complex the ion of interest. The concentration of primary ion in the ISE membrane is controlled by the ionic site; see Figure 8C. An ISE exhibits selectivity because ionophores have lower free energies of complexation with their primary ions than interfering ions. In the absence of ionophore, the ISE selectivity is determined by the free energy of transfer of ions from the aqueous phase into the ISE membrane, e.g., an ISE membrane including an anionic

site shows a higher selectivity for Cs^+ than K^+; see Figure 10A. Incorporating a K^+ ionophore in the membrane results in a lower free energy of transfer for K^+ than Cs^+, thus, the resulting ISE shows a higher selectivity for K^+ than for Cs^+; see Figure 10B. The strong binding of the ionophore to the target ion improves the detection limit of the ISE; however, it affects the working range of the electrode since it can result in interference due to co-extraction of the target ion and counter-ion into the membrane, leading to co-ion interference.[45] This is referred to as Donnan failure.[43]

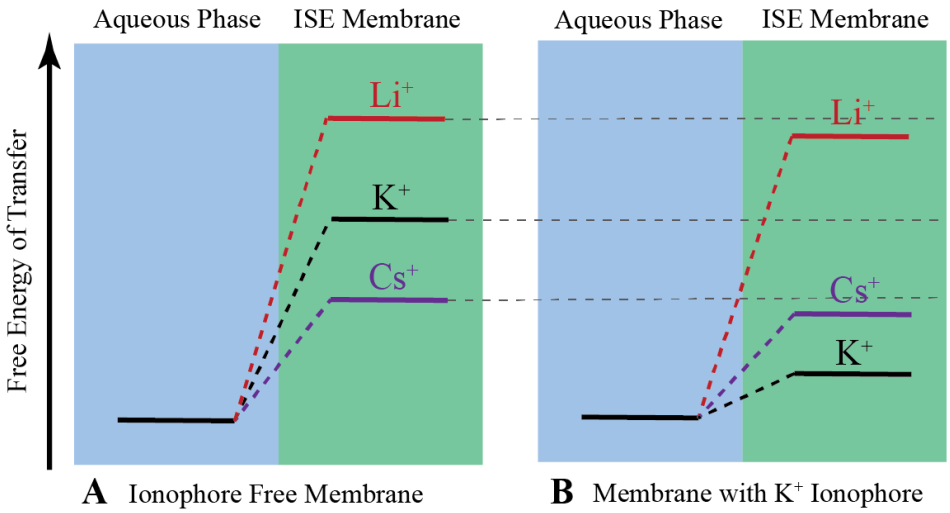

Figure 10. Free energy of transfer for an ionophore-free ISE and an ISE with an ionophore that selectively binds to K^+.

1.4.4 Quantifying ISE Selectivity

The most important characteristic of an ISE is its selectivity towards the ion of interest. Selectivity is defined as the preference for the primary ion I over an interfering ion J. This is controlled by two parameters, the free energy of transfer, and the binding strength of the ionophore. The free energy of transfer is the difference of the dehydration and solvation energies of the ion moving from the aqueous phase of the sample to the membrane phase. The ion with the lowest free energy of transfer is most preferred and,

therefore, is the ion for which the highest selectivity is observed. For an ISE with no ionophore the selectivity follows the Hofmeister series of free energy of transfer. For a cation-exchange electrode it is as follows: $Cs^+ > Rb^+ > K^+ > Na^+ > Li^+$.[43,45] The selectivity for a target ion can be enhanced with the introduction of an ionophore that preferentially binds to the ion and lowers the free energy of transfer.

The selectivity of the membrane can be quantified using the selectivity coefficient, as defined by the semi-empirical Nikolskii-Eisenman equation, in which the activity term in the Nernst equation is replaced by the selectivity-weighted activities of the two ions.[59] When an ISE is exposed to a sample containing a primary ion I (with charge z_I) and interfering ion J (with charge of z_J), this equation can be written as:

$$E = E^0 + \frac{RT}{z_I F} \ln(a_I(IJ) + K_{I,J}^{pot}\, a_J(IJ)^{z_I/z_J}) \qquad (19)$$

where a_I (IJ) and a_J (IJ) are the activities of ions I and J, respectively. However, this equation fails in the event that ions I and J have different charges. The selectivity coefficient, $K_{I,J}^{pot}$, can be derived as:

$$K_{I,J}^{pot} = \exp(\frac{(E_J^0 - E_I^0)\, Z_I F}{RT}) \qquad (20)$$

where E_J° and E_I° are the standard potentials for ions J and I, respectively. There are two methods used to determine the selectivity coefficient of a sensor, the separate solution method (SSM) and the fixed interference method (FIM).

In the separate solution method, the calibration curves for ions I and J are determined independently by using solutions only containing one of the ions. Since E_J and E_I are equal to E_J° and E_I° in solutions that are 1 M in the activity of the respective ion, the calibration curves can be extrapolated to 1 M, and the values of E_J° and E_I° can be

determined; see Figure 11A. By substituting E_J° and E_I° in equation (11), the selectivity coefficient, $K_{I,J}^{pot}$, can be calculated.[42,43]

In the fixed interference method, the calibration curve for the primary ion I is determined in the presence of a background of interfering ion J with a fixed concentration; see Figure 11B. At high concentrations of primary ion I, the electrode should exhibit a Nernstian response to ion I. At lower concentrations of ion I, the slope decreases, and eventually the potential stays constant due to the response of the electrode to the fixed background of interfering ion J. The resulting calibration curve can be used to determine the selectivity coefficient using the equation:

$$K_{I,J}^{pot} = {a_I(DL)}\Big/{a_J(BG)^{z_I/z_J}} \qquad (21)$$

where a_I (DL) is the activity of the primary ion at the lower detection limit, which can be calculated by extrapolating the Nernstian response region to the potential for the background interference; a_J (BG) is the activity of the interfering ion in the background. Theoretically, the values obtained for the selectivity coefficients from the separate solution method (SSM) and the fixed interference method (FIM) should be identical.[60]

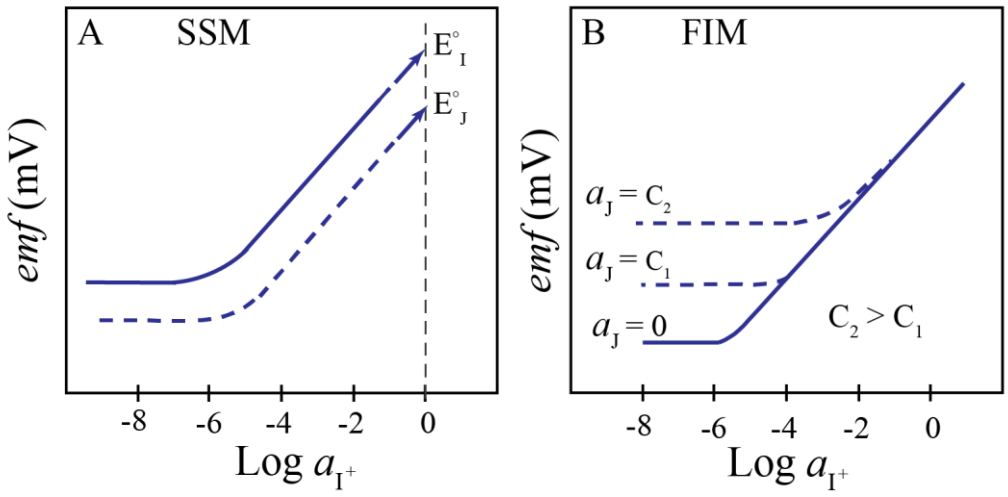

Figure 11. Measurement of ISE selectivity. (A) Potentiometric response curves to the primary and interfering ions as measured with the separate solution method (SSM). (B) Potentiometric responses to a primary ion (I^+) in a background with a constant concentration of an interfering ion (J^+).

1.4.5 Resistance of ISE Membrane

Ideally, ISEs function under zero-current conditions; however, this assumption is only valid if potential measurements are carried out with an ideal voltmeter with an infinite input resistance. In real-life potentiometric measurements, small currents (the magnitude of which depends on the input resistance of potentiometer) can pass through the circuit, which will cause errors in potential measurements. This error can be estimated by mentally replacing the real voltmeter with an ideal voltmeter and a resistor with an equivalent resistance of the real voltmeter, and the ISE with a voltage source and a resistor with the equivalent resistance of the ISE; see Figure 12. By applying Kirchhoff's second law, which dictates that the sum of the electrical potential differences (voltage) around any closed circuit is zero, equation 13 is obtained.

$$R_{ISE} \cdot i + V - V_{ISE} = 0 \qquad (22)$$

$$V = i \,.\, R_V \qquad (23)$$

Substitution of equation 22 into 23 results in equation 24:

$$V = (\, V_{ISE} \,.\, R_V \,) \,/\, (R_V + R_{ISE}\,) \qquad (24)$$

According to equation 24, only for the ideal case of R_{ISE}=0 V, the V is equal to V_{ISE}. Since in most cases the resistance of the ISE membrane is substantially larger than that of the Ag/AgCl wire, the inner-filling solution, Ag/AgCl reference electrode, and also the salt bridge, the resistance of the ISE can be approximated by the resistance of the ISE membrane. Using a voltmeter with internal resistance of 1.00 TΩ, a membrane resistance of 10.00 GΩ will result in a 1% error in the measured potential.

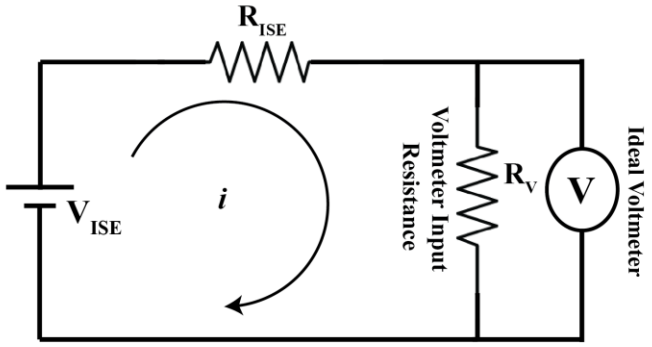

Figure 12. The equivalent circuit for a potential measurement with an ISE using a real voltmeter.

Increasing the concentration of ionic species in the membrane will increase the conductivity of the ISE membrane. The polarity of the membrane matrix also affects the membrane resistivity. Polar membrane plasticizers decrease the resistivity of the membrane but may reduce its selectivity.[61] The electrical resistance may also be lowered by adding a salt of two lipophilic ions. Such a salt has no ion-exchanging properties, will further decrease membrane resistances and can be applied in excess relative to the

ionophore.[42,61] Increasing the surface area of the membrane and decreasing the membrane thickness will also result in a smaller membrane resistance.

1.4.6 Ion-Selective Microelectrodes

With the motivation of decreasing the sample volume needed for potentiometric measurements, the experimental design of ISEs was modified to develop ion-selective micro-electrodes (μ-ISEs). μ-ISEs were successfully applied to measurements in small volumes such as in impaled biological cells, in the eluent coming from a chromatographic column or electrophoresis capillary, and in close proximity to the surface of various materials.[42,62,63] The earliest type of ionophore-based potentiometric microelectrodes were prepared in the mid-1970s from micrometer-sized glass pipettes, filled at the end with the ionophore-doped hydrophobic phase.[42,64,65] These microelectrodes continue to have a variety of applications in biochemical and medical research; for instance, they have been used to study intracellular ion concentrations, the release and uptake of ions into cells, and they were recently used as the scanning probe in scanning electrochemical microscopy (SECM).[42,66]

A key feature in the design of μ-ISEs is the resistance of the ISE membrane. Low membrane resistance for ISEs is essential to overcome problems related to shielding and to response times limited by electronic instrumentation.[62,65] Since in μ-ISEs the membrane is located at the tip of the micropipette, which results in increased thickness and decreased surface area of the membrane, higher membrane resistances are obtained in μ-ISEs compared to conventional ISEs with the same membrane composition. Some neutral ionophores have proved valuable in macroelectrode systems but are not appropriate as membrane components in microelectrodes because of the extremely high membrane resistances. In order to make miniaturization of such ISEs possible, the resistivity of the membrane should be significantly decreased to keep the total resistance of the microelectrode low enough to allow potential measurements, even at the increased

thickness and decreased surface area which are unavoidable in the micropipette design of microelectrodes.[61,67]

1.4.7 Biofouling of ISEs

Due to the fast, non-destructive, and label-free detection mechanism of ISEs, these sensors are appealing tools for detection in complex environments such as clinical, environmental, and food samples. However, such conditions can increase the drift of the ISE signal, cause loss of ISE selectivity, and decrease sensor lifetime.[68] The gradual malfunctioning of ISEs as a result of their exposure to biological media it referred to as biofouling of ISEs.[42] Biofouling of ISE membranes upon exposure to complex samples such as biological, food or environmental samples is still the biggest challenge in the development of ISEs for real-life samples, i.e., for the food industry, environmental monitoring, and long-term implantation of these sensors into the human body.[42,69,70] Three phenomena contribute to biofouling of ISEs, i.e., loss of membrane components, adsorption of biological species to the sensor surface, and partitioning of sample components into the sensing membrane.

1.4.7.1 Leaching of Membrane Components.

Membrane components with low-molecular weights, i.e., plasticizers, ionic sites, and ionophores, can gradually leach from ISE membranes into the tested solutions. Compounds with higher hydrophobicity leach into the test solution to a lesser extent. Test solutions that contain hydrophobic compounds increase leaching of components of ISE membrane. For example, ionophores leach into whole blood much more quickly than into aqueous samples. This is the result of hydrophobic interactions between the leached compounds and components of whole blood. Leaching can be reduced by use of ionophores with higher hydrophobicity or the covalent attachment of ionophores to the polymer fraction of the sensing membrane.[71-73]

1.4.7.2 Adsorption of Biological Species onto the Surface of ISE Membranes

Due to similar hydrophobicities, biological molecules and cells can adsorb onto the ISE sensing membrane. Because ISEs function under zero-current conditions, as long as the blockage of the ISE membrane is partial, the measuring potential of ISEs should not be affected. However, when a large fraction of the ISE membrane is covered by a thin layer of adsorbents, response times of ISEs (the time required for the ISE to reach the equilibrium potential upon changing sample composition) are affected. Thicker layers of adsorbed materials may affect the local concentration of the analyte at the sensor surface and cause errors in the determination of bulk concentration of the analyte.[42] Nitric oxide releasing polymers have been developed to overcome this issue and avoid adhesion of cells to the ISE sensing membranes.[74,75]

1.4.7.3 Partitioning of Sample Components into ISE Membranes

Electrically neutral hydrophobic components of the sample solutions can partition into ISE membranes and affect the performance of ISEs. For example, the presence of several lipids and lipophilic proteins were shown to lower the selectivity of ISEs.[42,74,76] Such compounds can act as non-specific receptors and thereby change the overall selectivity of the membrane.[76] Several methods have been successfully applied to reduce leaching of ISM membrane components; yet, the partitioning of lipophlilic components into the ISE membranes has not been fully addressed. To address this issue, fluorous compounds have recently been applied as sensing membranes of ISEs.[77]

1.4.8 Fluorous-phase ISEs

Fluorous compounds are organic molecules with a high content of fluorine atoms within their structure and have much lower hydrophobicity compared to biological molecules. Perfluorinated compounds exhibit extremely low polarities and polarizabilities.[78,79] The symmetric shape of these molecules and the strong electronegativity of the fluorine atoms result in small permanent dipole moments and in the extremely low polarizability of the

C-F bond, respectively.[78] These compounds have such low polarizablity and polarity that they are not only immiscible with water but also with many lipophilic compounds such as hydrocarbons. The term “fluorous” is often used to differentiate these compounds from other organic compounds.[77]

Perfluorinated matrixes have been applied to prepare sensing membrane of ISEs to develop sensors that are more resistive towards biofouling in real-life samples. Fluorous liquids such as perfluoroperhydrophenanthrene and perfluoropolyethers (see Figure 13) were used as membrane matrixes for ISE sensing membranes; polytetrafluoroethylene (PTFE) filter disks were used to provide mechanical stability for the ISE membrane.[80] Although ISEs with fluorous sensing membranes offer several advantages of increased working ranges, selectivities, lifetimes and decreasing the effects of biofouling, most ionophores and ionic site salts that have been described in the literature are poorly soluble in fluorous phases, which limits the application of fluorous ISEs. Long perfluorinated alkyl chains were incorporated in the structures of ionophores and ionic sites to develop fluorophilic compounds with sufficient solubility in the fluorous sensing membrane; see Figure 13 for examples.

The interfering lipids and proteins are unable to dissolve in the extremely low polarity fluorous phases, which results in decreased effects of biofouling. Also the selectivity of these ISEs is significantly enhanced by use of low polarity fluorous membrane matrixes. Ionic species that do not form ionophore complexes are poorly solvated in fluorous media and strong binding between the ionophore and the target ion is favored in these weakly coordinating matrixes.[81] ISEs based on a fluorophilic cation exchanger were shown to exhibit a selectivity range that is 8 orders of magnitude wider than that of conventional non-fluorous membranes.[77,82] ISEs with a fluorophilic Ag^+ ionophore showed selectivities much larger (by two orders of magnitude) than any Ag^+ ISEs with a non-fluorous membrane.[51] Moreover, weak solvation of counter ions inhibits the coextraction of target ions along with their counter ions into ISE membranes (Donnan failure), thereby

providing a wider working range for these ISEs.[42,83] To date, fluorous membrane ISEs have been used to detect CO_3^{2-}, Ag^+, perfluorinated acids, and H^+.[84-87]

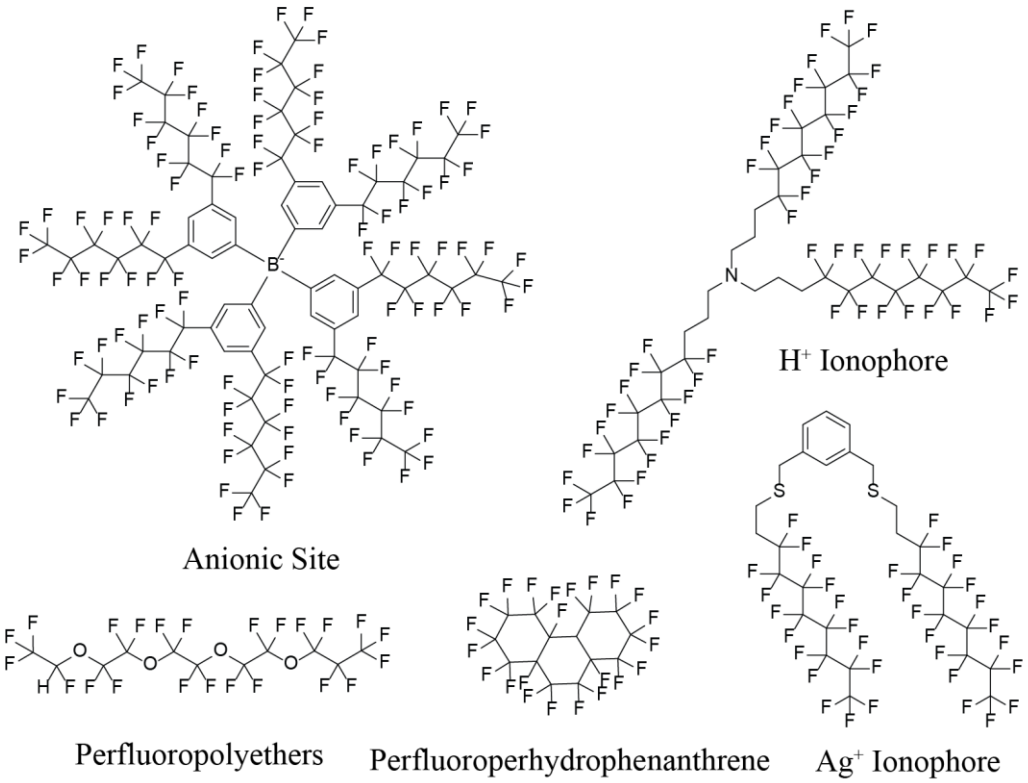

Figure 13. Structures of fluorous solvents and fluorophilic ionophores and ionic sites used for the development of fluorous-phase ISEs.

2 CHAPTER TWO

Unbiased Quantification of the Electrochemical Stability Limits of Electrolytes and Ionic Liquids

In part from:

Mousavi, M. P. S.; Dittmer, A. J.; Wilson, B.; Hu, J.; Stein, A.; Buhlmann, P., Unbiased Quantification of the Electrochemical Stability Limits of Electrolytes and Ionic Liquids. *J. Electrochem. Soc.* **2015,** *162* (12), A2250-A2258.

This work was a joint effort by this author and Adam J. Dittmer (who carried out the COMSOL simulations) and Benjamin Wilson and Jinbo Hu (who synthesized and characterized the porous carbon films).

The electrochemical window is the potential range in which an electrolyte/solvent system does not get reduced or oxidized. Usually, voltammograms are measured, and the potentials at which specific current densities are reached are identified as the electrochemical limits. We measured electrochemical limits of several electrolytes—including ionic liquids—and show that this approach has disadvantages that can be overcome by an alternate approach of defining electrochemical limits. The choice of the cut-off current density, $J_{\text{cut-off}}$, is arbitrary and strongly affects the determined electrochemical windows, which are strongly influenced by electrolyte mass transport. Moreover, the $J_{\text{cut-off}}$ method does not provide an accurate estimate of the electrochemical window at electrodes with high surface areas, where the capacitive currents are large. We propose a method that requires no definition of $J_{\text{cut-off}}$. This method minimizes electrolyte mass transport effects, gives realistic electrochemical stability limits at high surface area electrodes, and is less affected by experimental parameters such as the scan rate. The method is based on linear fits of the current–voltage curve at potentials below and above the onset of electrolyte decomposition. The potential at which the two linear fits intersect is defined as the electrolyte electrochemical limit.

2.1 Introduction

Electrolytes and solvents are essential for the proper function of variety of electrochemical devices, such as batteries and supercapacitors. The voltage polarization in these devices can cause electrochemical degradation of the electrolyte and solvent, resulting in device malfunction. This can be avoided by constraining the working range of the device to the electrochemical window limited by the electrolyte and solvent, i.e., the potential range in which they are chemically stable and do not get reduced or oxidized.[6,17] Due to their localized charges, the inherently ionic electrolytes often have a lower electrochemical stability than neutral solvent molecules, and therefore frequently limit the device working range.[17] There has been extensive research on modifying the structure of electrolytes to improve their electrochemical stability, and thus expanding their working range.[24-27,88]

The determination of the electrochemical window of the electrolytes is not well defined. Generally a current–voltage polarization curve is measured, starting at a voltage at which the electrolyte is electrochemically stable, followed by increasing or decreasing the potential to observe the anodic or cathodic decompositions, respectively. The potential at which a specific current density, J, is reached is defined as the cathodic or anodic limit of the electrolyte. This approach has several disadvantages, as noted by several researchers.[24-26] Firstly, since the choice of the cut-off current density is arbitrary, different standards have been applied in the literature. Cut-off current densities, $J_{\text{cut-off}}$, in the range of 0.01 to 5.0 mA/cm^2 were reported,[25,27-40] resulting in electrochemical windows for individual electrolytes that differ by as much as 0.9 V.[24] Therefore, the comparison of data from studies that used different $J_{\text{cut-off}}$ values is not readily possibly, making it difficult to gain a collective understanding of the effect of the electrolyte structure on its electrochemical stability. Electrochemical windows determined by the conventional $J_{\text{cut-off}}$ method are strongly affected by mass transport of the electrolyte. Consequently, changing the electrolyte concentration affects the determined

electrochemical windows.[17] Other experimental parameters, such as the type of the working electrode and the scan rate, also affect the determined electrochemical window, although to a lesser extent.[17,24]

Another disadvantage of the $J_{\text{cut-off}}$ method is its limited applicability to real-life devices. For this method, it is assumed that the current arises exclusively from electrolyte decomposition, ignoring non-faradaic (capacitive) current.[89] This approximation is generally quite good for non-porous electrodes with smaller surface areas such as non-porous glassy carbon, gold, or platinum, where the magnitude of the capacitive current is small. However, many real-life electrochemical devices contain porous carbon electrodes with high surface areas (500–2500 m^2/g),[90,91] resulting in non-faradaic currents as large as 5.0 mA/cm^2.[89,92] In such cases, the non-faradaic current is not negligible when compared to the faradaic current produced by electrolyte decomposition and, therefore, use of the $J_{\text{cut-off}}$ method gives unrealistic electrochemical limits. Clearly, more reliable methods for the quantification of the electrochemical stability of electrolytes are needed.

Recently, some of us made a preliminary report of a method for assessing the electrochemical stability of electrolytes that is based on linear fits of the current–voltage curve at potentials below and above the onset of cathodic or anodic decompositions.[17] We defined the intercept of the approximately linear portions of the current–voltage curve as the cathodic or anodic limit of the electrolyte. Since no cut-off current density is used in this approach, it eliminates discrepancies that result from the choice of an arbitrary value of $J_{\text{cut-off}}$. We applied this method previously to determine the cathodic stability of tetraalkylammonium perchlorates in propylene carbonate and suggested that this approach decreases mass transport effects on the cathodic limit of tetrabutylammonium perchlorate.[17] In this contribution, we provide a more refined set of instructions on how the linear fit method should be applied, show its applicability for the determination of both cathodic and anodic limits of a variety of electrolytes (including ionic liquids), and quantitatively confirm that this method substantially decreases effects of mass transport

on experimentally determined electrochemical limits. The effects of the experimental parameters on the electrochemical stability limits determined with the conventional $J_{\text{cut-off}}$ method and the proposed linear fit method are studied, and the advantages and limitations of each technique are quantitatively discussed. Moreover, we show that the linear fit method can be used in practical devices with high surface area electrodes, such as electric double-layer capacitors, demonstrating the advantages of this approach over the conventional $J_{\text{cut-off}}$ method. Numerical simulations of linear sweep voltammograms of electrolytes, taking into account not only the redox reaction and diffusion but also *iR* drop and migration, confirm the experimentally observed advantages of the linear fit method.

2.2 Experimental

2.2.1 Chemicals

All reagents were used as received without further purification unless otherwise noted. Anhydrous acetonitrile, anhydrous propylene carbonate, tetrabutylammonium perchlorate (NBu_4ClO_4), tetrabutylammonium iodide, phenol (>99%), formaldehyde (aqueous solution, 37 wt %), tetrahydrofuran, polytetrafluoroethylene (PTFE, 60 wt % in water), tetraethylorthosilicate (TEOS, 99%), L-lysine (98%), hydrochloric acid (37 wt %), and sodium hydroxide were obtained from Sigma-Aldrich (St. Louis, MO). The ionic liquids, 1-ethyl-3-methylimidazolium bis(trifluoromethylsulfonyl)imide (EMI TFSI), butyltrimethylammonium bis(trifluoromethylsulfonyl)imide ($BuNMe_3$ TFSI), and tributylmethylammonium bis(trifluoromethylsulfonyl)imide ($MeNBu_3$ TFSI), were purchased from IoLiTec (Tuscaloosa, AL). Black Pearl 200 carbon was obtained from Cabot Corporation (Boston, MA). Tetrahydrofuran (HPLC grade, >99.9%) and hydrofluoric acid (48–52 wt%) were purchased from Fisher Scientific (Waltham, MA).

2.2.2 Carbon Film Preparation

Colloid-Imprinted Mesoporous **(**CIM) carbon with mesopores of about 24 nm diameter was synthesized according to a previously reported method.[93,94] Three-dimensionally

ordered mesoporous (3Dom) carbon was prepared through infiltration of a phenol–formaldehyde resol into an ordered silica template made from sedimented silica spheres, as described previously.[91] A final pore size of 37 nm was determined through nitrogen sorption, and an ordered structure was observed through transmission electron microscopy and small-angle X-ray scattering. CIM and 3DOm carbon films were prepared by finely grinding the carbon powder with an agate mortar and pestle, followed by addition of an aqueous suspension of PTFE (19:1:20 carbon:PTFE:water by mass) and grinding until a homogenous paste was formed. The paste was rolled out with a mechanical press to a thickness of approximately 250 μm and dried at 110 °C for 24 h under vacuum. The carbon films were then cut into 3.0 mm-diameter circles for use in electrodes. For the preparation of the carbon electrodes, carbon films were immersed in EMI TFSI ionic liquid, followed by application of a vacuum for 1 h to ensure infiltration of the ionic liquid into the carbon pores. Electrodes were fabricated using an experimental procedure published earlier.[94] Briefly, each carbon film was mounted on a gold disk electrode (CH Instruments, Austin, TX), and a layer of porous polyethylene film (CelGard 3501, Charlotte, NC) was placed on top of the carbon film to increase the mechanical stability of the electrode. To avoid delamination of the carbon film from the underlying gold, the electrodes were mounted into cylindrical bodies custom-made from Dupont Delrin acetal resin. A screw cap at the opposite end of the electrode pressed the carbon film onto the electrode.

2.2.3 Electrochemical Measurements

Voltammetry experiments were carried out with a CHI600C Potentiostat (CH Instruments, Austin, TX). A three-electrode set up with a 3.0 mm-diameter glassy carbon (GC) disk working electrode (BAS, West Lafayette, IN), a 0.25 mm Pt wire coil (99.998%, Alfa Aesar, Ward Hill, MA) auxiliary electrode, and a Ag^+/Ag reference electrode was used (reference solution: 10 mM $AgNO_3$ and 100 mM NBu_4ClO_4 in acetonitrile). The working electrode was polished on Microcloth polishing pads using 5.0

μm Micropolish II deagglomerated alumina, both from Buehler (Lake Bluff, IL). After polishing, the electrode was rinsed thoroughly, first with deionized water and then with ethanol, followed by drying under a stream of Ar. The reference electrode was prepared as described previously.[10] Briefly, a glass tube equipped with a Vycor glass plug was filled with acetonitrile solution of 10.0 mM $AgNO_3$ and 100 mM NBu_4ClO_4, and an Ag wire was inserted into the tube. The reference electrode was kept in a solution of identical composition for at least 1 week prior to measurements. All potentials reported herein are with respect to 10 mM Ag^+/Ag. The anhydrous solvents used in this work were stored and transferred under argon. Prior to measurements, all solutions were purged with argon for 15 min while stirring vigorously to remove dissolved oxygen. Linear fits were performed in Microsoft Excel 2010, and statistical analysis was based on a two-tailed T-test at the significance level of 0.95.

2.2.4 Simulations

All voltammetry simulations were performed using COMSOL Multiphysics version 5.1 software (COMSOL, Burlington, MA). Calculations were performed by utilizing both secondary current distribution physics with transport of diluted species and tertiary current distribution in two-dimensional space. The electrode was assumed to be 0.1 mm in length, with a 0.6 mm distance between the working and reference electrodes. Simulations assume a generic one-electron transfer reaction in a two-electrode system with an ideal reference electrode. Diffusion coefficients used were 0.5×10^{-9} m^2/s for the oxidized and reduced species and 1.0×10^{-9} m^2/s for the counter ion. The exchange current density was 100 A/m^2 and the scan rate was 1 V/s for all simulations unless noted otherwise.

2.3 Results and Discussion

2.3.1 Linear fit and cut-off current density methods

Figure 1 illustrates how the two methods of $J_{\text{cut-off}}$ and linear fit can be applied to a real sample. Figures 1A and 1B show the current–voltage polarization curve of tetrabutylammonium iodide, NBu_4I, near the cathodic limit. According to the $J_{\text{cut-off}}$ method, the potential at which a specific value of $J_{\text{cut-off}}$ is reached is defined as the electrolyte electrochemical limit. In Figure 1A, the $J_{\text{cut-off}}$ values of 0.5 and 1.0 mA/cm^2 are highlighted as horizontal dashed lines, and the vertical lines show the potentials at which these $J_{\text{cut-off}}$ values are reached.

Using the linear fit method as alternate approach to determine the electrochemical limit, two separate linear fits of the current–voltage relationship are applied before and after the onset of electrochemical reduction of the electrolyte[17] (Figure 1B, dashed lines). The electrochemical limit is obtained by the intersection of the two linear fits (Figure 1B, vertical dotted line). The linearity of the current density vs. potential curve before and after the onset of electrochemical decomposition can be confirmed by monitoring the slope of the current density–voltage curve, dJ/dE, as shown in Figure 1C. As the potential is swept from -1 to -3 V vs. Ag^+/Ag, i.e., before reaching the onset of reduction, dJ/dE is very close to zero, and there are only minimal changes in the magnitude of the slope. As the onset of the electrolyte reduction is reached at approximately -3.2 V, the current density starts to increase, and the curvature of the J vs. E curve changes (i.e., the slope of J vs. E curve increases). A rapid increase in dJ/dE is observed between -3.2 and -3.5 V, a region in which mass transport of the electrolyte is controlled by diffusion and migration. The further decrease in the applied potential results in electrolyte migration becoming the dominant mass transport mode. As a result, the slope of the J vs. E curve is approximately constant (dJ/dE reaches a value of approximately 30 mA/Vcm^2 between -4 to -5 V), which makes this the appropriate potential range for the second linear fit.

Figure1C and the inset of Figure 1D also show that the d*J*/d*E* vs. *E* plot can provide a useful visualization of the onset of the electrochemical reduction or oxidation.

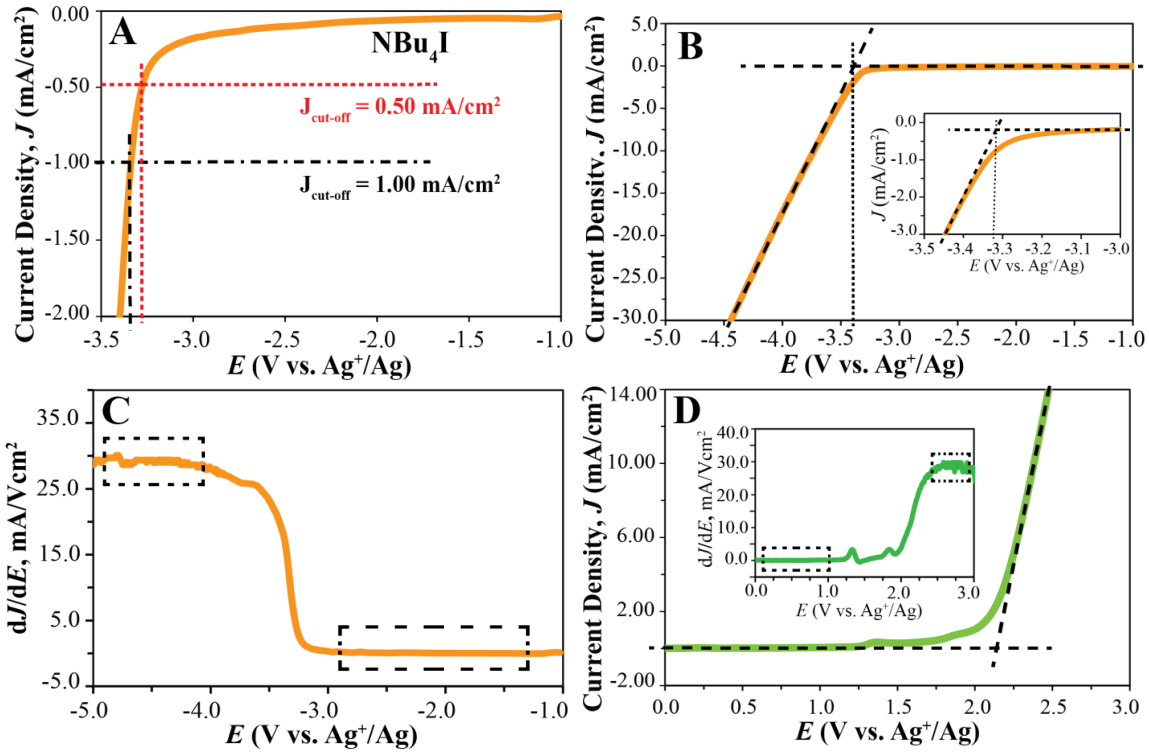

Figure 1. Comparison of the $J_{\text{cut-off}}$ and linear fit methods: (A) and (B) Linear sweep voltammogram of NBu_4I (300 mM) in propylene carbonate. (A) illustrates use of $J_{\text{cut-off}}$ values of 0.5 and 1.0 mA/cm^2. (B) Dashed lines are linear fits before and after the onset of NBu_4I reduction; the vertical dotted line highlights the potential at which the two fits intersect. (C) d*J*/d*E* for the data of panel (B). (D) Linear sweep voltammogram of EMI TFSI (300 mM) in propylene carbonate; linear fits before and after the onset of oxidation shown as dashed lines; inset shows corresponding d*J*/d*E*. Dashed boxes in panels C and D highlight the regions in which the linear fits were performed. (A) to (D): Scan rate, 100 mV/s; Pt coil auxiliary electrode, GC working electrode, and Ag^+/Ag reference electrode.

Our first report of the linear fit method did not provide specific instructions on how to perform the linear fits.[17] Specifically, it did not comment on the potential range in which the linear fits are preferentially applied, and it did not discuss the correlation coefficients of the linear fits that should be expected. The current density vs. voltage curves for NBu_4I shown in Figures 1A and 1B illustrate these aspects. The linear fit of the background current in the range from -2.0 to -3.0 V (five replicates, average coefficient of determination of the linear fit, R^2, of 0.954) intersects with the linear fit in the range from -3.3 to -3.5 V (average R^2 of 0.965) at -3.349 ± 0.072 V, which we define as the cathodic limit of NBu_4^+ in PC.

Altering the range where the linear fit of the (mostly capacitive) background current was applied did not have significant effects on the determined electrochemical limits. Changing the range of the second linear fit to -3.5 to -3.7 V (average R^2 of 0.998) or -3.6 to -3.8 (average R^2 of 1.000) yields electrochemical limits of -3.365 ± 0.045 and -3.376 ± 0.055 V, respectively. Clearly, the electrochemical limit is affected to a small extent by the potential range of the fit. This can be explained by the dependence of the electrochemical limit on the slope of the *J* vs. *E* curve, (i.e., d*J*/d*E*) after the onset of reduction (see Figure 1C). While there are steep changes in d*J*/d*E* right after the onset of reduction (see Figure 1C), the further the linear fit range is from the onset of the reduction, the smaller are the changes in d*J*/d*E* and, therefore, the higher are the correlation coefficients of the linear fits. The range from -4 to -5 V has the least variation in d*J*/d*E*, and thus is suggested for the linear fit. It gives an electrochemical limit of -3.423 ± 0.010 V. Note that the standard deviation of the latter value is much smaller than the corresponding value of 72 mV for the fit in the -3.3 to -3.5 V range. Altering the potential range of the linear fit to -3.5 to -5.0 V (which is still far beyond the onset of the reduction and only shows minimal changes in d*J*/d*E*) did not significantly affect the electrochemical limit of NBu_4^+. In summary, if not carefully chosen, the potential ranges at which the linear fits are applied can affect the determined electrochemical limits by less than 100 mV. To minimize this effect, we recommend choosing potential ranges in

which there are minimal changes in dJ/dE, as, e.g, those highlighted in Figure 1C by dashed boxes. Generally, we obtained linear fits with R^2 values larger than 0.990 for all the systems studied in this work.

The linear fit method can also be used to determine the anodic limits of electrolytes, as shown in Figure 1D. The linear sweep voltammogram of 1-ethyl-3-methylimidazolium bis(trifluoromethylsulfonyl)imide, EMI TFSI, is shown in Figure 1D. The dashed lines show the fits used for the determination of the anodic limit. The linear fit method results in an anodic limit of 2.150 ± 0.004 V (vs. Ag^+/Ag) for EMI TFSI, whereas the conventional cut-off current density method results in 1.755 ± 0.042 V and 1.969 ± 0.033 V when $J_{cut\text{-}off}$ values of 0.5 and 1.0 mA/cm^2 are used, respectively.

2.3.2 Effect of Effect of $J_{cut\text{-}off}$ on the Electrolyte Electrochemical Window

Values of $J_{cut\text{-}off}$ ranging from 0.01 to 5.0 mA/cm^2 have been used in the literature (e.g., 0.01,[27] 0.05,[25,28] 0.1,[29,30] 0.2,[31] 0.3,[32] 0.5,[33] 1.0,[34-40] 1.5,[32] 2.0,[95] 2.5,[32] 3.0,[32] and 5.0[39] mA/cm^2), although 1.0 mA/cm^2 is the most frequently used value. Clearly, the selection of the cut-off current density significantly influences the electrochemical limit. While this conclusion is not new, prior reports with the same conclusion were based on single current–potential polarization measurements and did not include a quantification of the error associated with the determination of the electrochemical limit[26,28,32,39] or were based on the comparison of electrochemical limits of the same electrolyte but from multiple studies with different $J_{cut\text{-}off}$ criteria.[24,25] However, the effect of $J_{cut\text{-}off}$ cannot be readily distinguished from the effects of different experimental conditions, such as different concentrations and scan rates.

To quantify the effect of $J_{cut\text{-}off}$ on the electrochemical limits systematically, five replicates of the current–voltage curve were measured in this work for a variety of electrolytes and ionic liquids. They were chosen because they are all commonly used in electro-analytical devices[90,91,96-98] and electrochemical capacitors[25,27,88,99] due to their

wide electrochemical windows. The electrochemical limits were determined based on $J_{cut\text{-}off}$ values of 0.5, 1.0, and 5.0 mA/cm^2 and are listed in Table 1. The use of 0.01 and 0.2 mA/cm^2 $J_{cut\text{-}off}$ values was attempted, but these values were too close to the background current density to give meaningful results. For the electrolyte solutions, propylene carbonate, PC, was used as solvent due to its wide electrochemical window.[17,25,88] Due to solvent-electrolyte interactions, the choice of solvent can slightly affect the electrochemical stability of electrolytes, and therefore, the solvent in which the cathodic or anodic limits were measured must be reported; in this study, unless noted otherwise, all the electrochemical limits were measured in PC.

TABLE 1. Cathodic limits (V vs. Ag^+/Ag) from cut-off current density and linear fit methods.

	Cut-off current density method			Linear fit method
	$J_{cut\text{-}off}$ = 0.5 mA/cm^2	$J_{cut\text{-}off}$ = 1.0 mA/cm^2	$J_{cut\text{-}off}$ = 5.0 mA/cm^2	
NBu_4I (75 mM)*	-3.293 ± 0.004	-3.383 ± 0.006	-3.789 ± 0.022	-3.414 ± 0.005
NBu_4I (150 mM)*	-3.287 ± 0.004	-3.357 ± 0.004	-3.633 ± 0.004	-3.433 ± 0.002
NBu_4I (300 mM)*	-3.297 ± 0.032	-3.360 ± 0.028	-3.541 ± 0.017	-3.423 ± 0.010
NBu_4I (600 mM)*	-3.393 ± 0.013	-3.459 ± 0.010	-3.597 ± 0.013	-3.473 ± 0.015
$MeNBu_3$ TFSI (300 mM)*	-3.183 ± 0.056	-3.297 ± 0.024	-3.565 ± 0.027	-3.415 ± 0.005
$MeNBu_3$ TFSI (ionic liquid)	-3.639 ± 0.049	-3.939 ± 0.048	-5.930 ± 0.126	-3.494 ± 0.048
$BuNMe_3$ TFSI (ionic liquid)	-3.033 ± 0.033	-3.311 ± 0.014	-3.783 ± 0.033	-3.368 ± 0.019
EMI TFSI (300 mM)*	-2.513 ± 0.008	-2.559 ± 0.005	-2.725 ± 0.046	-2.550 ± 0.019
EMI TFSI (ionic liquid)	-2.381 ± 0.054	-2.469 ± 0.005	-2.599 ± 0.023	-2.555 ± 0.015

*Solvent: propylene carbonate.
Scan rate, 100 mV/s; auxiliary electrode, Pt coil; working electrode, GC; reference electrode, Ag^+/Ag.

Table 1 confirms that $J_{cut\text{-}off}$ has a large effect on the electrochemical stability limits. For example, a change of $J_{cut\text{-}off}$ from 0.5 to 1.0 mA/cm^2 significantly decreased the cathodic limit of NBu_4I at all concentrations from 75 to 600 mM, giving 40 to 90 mV changes in

the cathodic limit. Further increases of $J_{cut\text{-}off}$ to 5.0 mA/cm^2 resulted in 250 to 400 mV changes in the cathodic limit. Similarly, increases in $J_{cut\text{-}off}$ also affected the cathodic limit of $MeNBu_3$ TFSI and EMI TFSI (both in propylene carbonate) by as much as 380 mV. The effect of $J_{cut\text{-}off}$ on the electrochemical stability of the ionic liquids in absence of a solvent was even higher. Changing $J_{cut\text{-}off}$ from 0.5 mA/cm^2 to 1.0 mA/cm^2 resulted in a 300 mV decrease in the cathodic limits of $MeNBu_3$ TFSI, $BuNMe_3$ TFSI, and EMI TFSI. The potential at which $J_{cut\text{-}off}$ reached 5.0 mA/cm^2 for the ionic liquid $MeNBu_3$ TFSI was as high as -5.930 V, which is 2.3 V more negative than the analogous value at 0.5 mA/cm^2. These data highlight the key advantage of the proposed linear fit method, which is the independence from a cut-off value.

2.3.3 Effect of Electrolyte Mass Transport

The electrochemical limits determined by the cut-off current density method are strongly influenced by electrolyte mass transport. In this section, we demonstrate that the linear fit method corrects for such effects. The total transport or flux of any chemical species to an electrode is described by the Nernst–Planck equation, which combines the individual contributions from diffusion (resulting from concentration gradients), migration (due to electric fields), and convection (caused by hydrodynamic velocity). For mass transport in one dimension only, the flux, J, of a species is given by[1]

$$J(x,t) = -\left[D\,\frac{\partial C(x,t)}{\partial x}\right] - \left[\frac{zF}{RT}DC(x,t)\right]\left(\frac{\partial \phi(x,t)}{\partial x}\right) + C(x,t)V(x,t)$$

where D and C are the diffusion coefficient and the concentration of the species in consideration, ϕ is the electrostatic potential, and V is the hydrodynamic velocity. Typically, voltammograms of redox-active molecules are measured in unstirred solutions and in the presence of high concentrations of supporting electrolyte; this minimizes convection and the migration of the redox-active molecule, making diffusion the main mode of mass transport.[1] The shape of the diffusion-controlled cyclic voltammogram

(CV) for a fully reversible single-electron transfer reaction and diffusion along one coordinate is shown in Figure 2A (labeled with "Model without distortion from resistance and migration"). Very different voltammetric responses are observed in the case of electrolyte reduction or oxidation (see Figure 1 for examples). Even though electro-decomposition of electrolytes has been experimentally studied for several decades, surprisingly, there has been no theoretical work to date that specifically discusses linear sweep voltammograms that exhibit electrolyte oxidation or reduction. Here, we used COMSOL Multiphysics to perform numerical simulations to illustrate the parameters that affect such voltammograms and the electrolyte electrochemical limits determined therefrom.

A first correction that has to be applied to linear sweep voltammograms dominated by electrolyte decomposition is the inclusion of resistive distortion. Since there are no ionic species that can carry current other than the redox-active electrolyte itself, solution resistance, *R*, decreases the potential applied to the solution–electrode interface by a term directly proportional to the current, *i*. This decreases the slope of the *J* vs. *E* curve, resulting in resistive distortion of the voltammetric response.[17,100] The typical effect of resistive distortion on the numerically simulated voltammetric response is shown in Figure 2A, again illustrated for the simplest example of a fully reversible single-electron transfer. Increasing the solution resistivity decreases the height of the peak current, increases the peak separation, and widens the sections of the voltammogram in which the current increases approximately linearly with the applied voltage. Yet, resistive distortion does not fully explain the observed voltammetric response shown in Figure 1.

As a second correction, migration as a mode of mass transport needs to be considered. Unlike in most conventional voltammetry experiments, when electrolyte electro-decomposition occurs the concentration of the reacting species is high compared to the total ion concentration, and diffusion is no longer the sole mode of mass transport. The simulated voltammetric response that takes into account both migration and diffusion

agrees well with the experimental observations. Figures 2 illustrates how parameters such as standard redox potentials, concentrations, and diffusion coefficients affect the voltammetric response. For a kinetically facile electro-decomposition reaction, the onset of reduction occurs close to the standard redox potential (see Figure 2B). Figure 2C demonstrates that the electrolyte concentration does not influence the onset of reduction but affects the slope of the linear portion of the voltammogram, where higher concentrations result in steeper slopes. This is consistent with the experimentally observed effect of electrolyte concentration, as evident from Figure 3A, which shows that for 75, 150, and 300 mM NBu_4I solutions, the slope of *J* vs. *E* increased with increasing NBu_4I concentration. Importantly, the slope of the *J* vs. *E* curve obtained from the simulation (see inset in Figure 2C) exhibits for all electrolyte concentrations a plateau starting a few hundred mV beyond the standard redox potential, which matches well with experimental observations shown in Figure 1C and Figure 3. The effect of the diffusion coefficients on the simulated voltammograms (see Figure 2D) are completely analogous to those of the electrolyte concentration; larger diffusion coefficients result in faster mass transport and a steeper slope for the linear portion of the voltammogram, but cause no change in the onset of the redox reaction. The parallel effects of diffusion coefficients and concentrations can be readily explained by the direct proportionality of both the diffusion and the migration terms of the total flux on both the diffusion coefficient and the concentration.

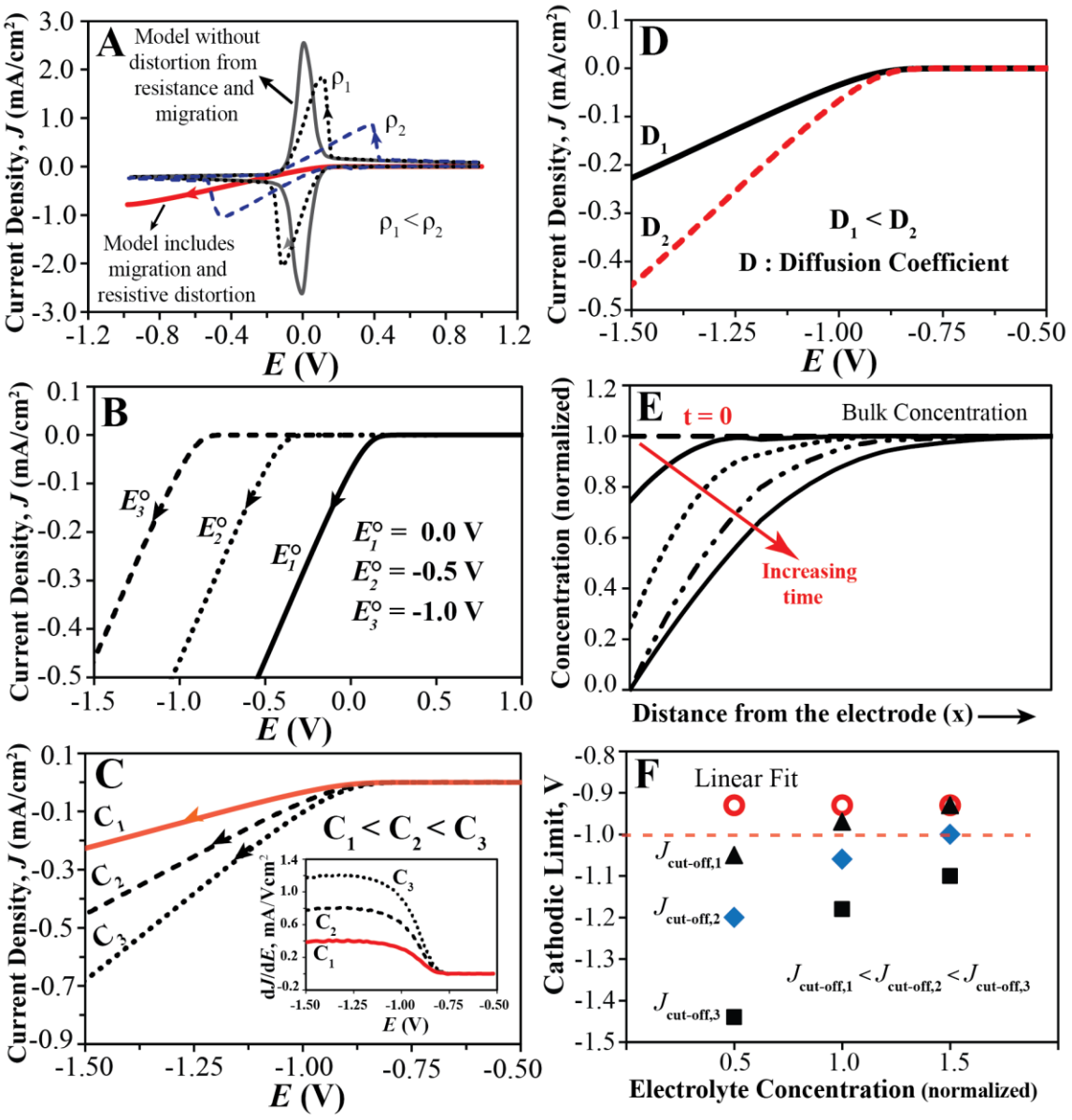

Figure 2. COMSOL simulations: (A) Ideal diffusion-controlled CV shown as solid line, labeled "Model without distortion from resistance and migration". Dashed CVs are affected by resistive distortion; specific resistivities, ρ_1 and ρ_2, 6.2 and 62.0 $\Omega \cdot m^{-1}$, covering the typical experimental range of this study. The red solid line shows the CV taking into account also migration. (B) to (D) Linear sweep voltammograms simulated with both diffusion and migration as mass transport modes; (B) for different E^o, (C) E^o =

-1.0 V, C equal to 0.5, 1.0, and 1.5 (normalized); (D) E^o = -1.0 V, diffusion coefficients of the oxidized and reduced species, D_2 = 4 × 10^{-9} m^2/s and D_1 = 2.0 × 10^{-9} m^2/s, respectively. (E) Concentration of the oxidized species vs. distance from the electrode at different time points, taking migration into account. (F) E^o = -1.0 V; cathodic limits obtained from the linear fit and $J_{cut\text{-}off}$ methods, shown as a function of electrolyte concentration for $J_{cut\text{-}off}$ of 0.05, 0.1, and 0.2 mA/cm^2.

A key difference between the simulations that take migration into account and those that do not are the wider linear ranges of the slopes of the *J* vs. *E* curve, as can be seen in Figure 2A. As illustrated in the electrolyte concentration profiles of Figure 2E (which closely resemble the well-known concentration profiles for linear diffusion systems in which migration does not play a significant role), electrolyte depletion at the electrode surface proceeds quickly and increases over time. Because of the concentration dependence of the flux, this lowers the rate of the redox reaction, and it also increases the *iR* drop.

To further compare the linear fit and $J_{cut\text{-}off}$ method, electrochemical stability limits were also determined from the simulated voltammograms. As shown by Figure 2F, the electrochemical limits obtained with the linear fit method were not affected by the electrolyte diffusion coefficient or concentration, while quite the opposite was true for electrochemical limits determined with the $J_{cut\text{-}off}$ method, see Figure 2F. In conclusion, numerical simulations confirm that the linear fit method is not biased by electrolyte mass transport, demonstrating the advantages of this method over the $J_{cut\text{-}off}$ method.

The effect of electrolyte mass transport was further studied experimentally. When some of us previously introduced the linear fit method in an attempt to minimize the concentration dependence of the electrochemical limit, we gave examples of cathodic limits for NBu_4ClO_4 decomposition. However, those early examples did not include a statistical analysis of the error associated with this new method.[17] Here, we quantitatively

show the effect of electrolyte mass transport on the electrochemical limits obtained from both the $J_{cut\text{-}off}$ and the linear fit method.

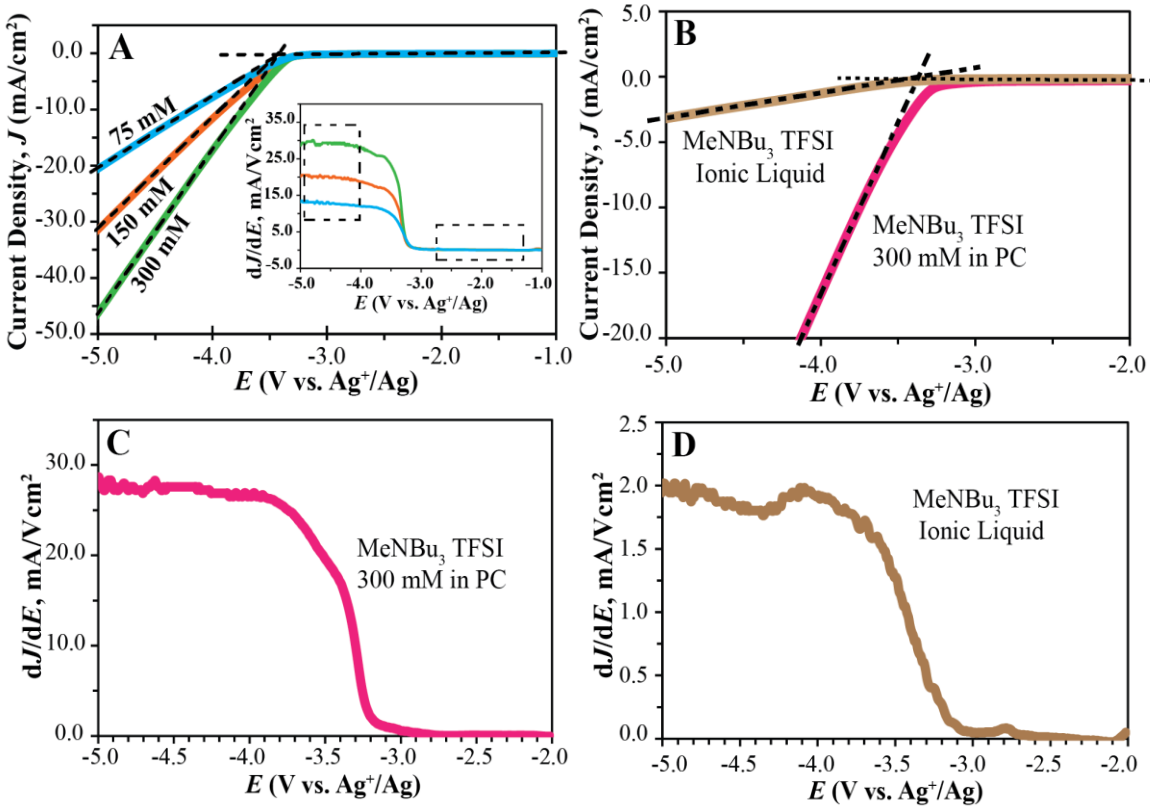

Figure 3. Effect of electrolyte mass transport on electrochemical stability limits. (A) Linear sweep voltammogram of 75, 150, and 300 mM solutions of NBu_4I in propylene carbonate (PC). Dashed lines show linear fits before and after onset of NBu_4I reduction. Inset: Corresponding dJ/dE curves. (B) Linear sweep voltammogram of $MeNBu_3$ TFSI as pure ionic liquid and as 300 mM solution in propylene carbonate; corresponding dJ/dE curves are shown in Panels (C) and (D), respectively. Scan rate, 100 mV/s; Pt coil auxiliary electrode, GC working electrode, and Ag^+/Ag reference electrode.

Cathodic limits of 75 to 600 mM NBu_4I are presented in Table 1. At both $J_{cut\text{-}off}$ values of 0.5 and 1.0 mA/cm^2, the cathodic limits for 75, 150, and 300 mM NBu_4I solutions do not

differ significantly from one another, but for the 600 mM solution a lower cathodic limit is determined. At the higher $J_{\text{cut-off}}$ of 5.0 mA/cm^2, higher resistive distortions are observed, and thus the cathodic limits at different concentrations of 75, 150, 300, and 600 mM—which are characterized by different solution resistances—are significantly different from each other.

Using the linear fit method, the fits were applied in the -4 to -5 V region, where the current density exceeds 5 mA/cm^2. Notwithstanding, the cathodic limits of the 75 to 300 mM NBu_4I solutions as determined with this method are not statistically different from one another. While the limit for the 600 mM NBu_4I solution is significantly lower than the ones for 75 to 300 mM NBu_4I, the difference is only on the order of 40 to 60 mV.

The cathodic limits of $MeNBu_3$ TFSI were measured both for the pure ionic liquid and a 300 mM solution in propylene carbonate (see Figure 3B). At the $J_{\text{cut-off}}$ values of 0.5 and 1.0 mA/cm^2, the cathodic limits for the ionic liquid form are approximately 500 and 700 mV lower, respectively, than for the 300 mM $MeNBu_3$ TFSI solution (see Table 1). Figures 3C and 3D show that the onset of the reduction occurs at approximately -3.2 V for both the ionic liquid and the solution. There are no noticeable differences in the electrochemical behavior of $MeNBu_3$ TFSI in the two cases other than the fact that the J vs. E curve is much steeper in case of the 300 mM $MeNBu_3$ TFSI (see Figures 3B to 3D; note different scales for dJ/dE in Figures 3C and 3D). Due to different conductivities, mass transport characteristics in the pure ionic liquid and solution are drastically different. The cathodic limit of the ionic liquid as determined with the cut-off current density method is 500 mV lower than the one determined for the solution. In contrast, the linear fit method minimizes the mass transport and resistive distortion effects, and gives similar values of -3.494 ± 0.048 and -3.415 ± 0.005 V for the pure ionic liquid and the solution form, respectively.

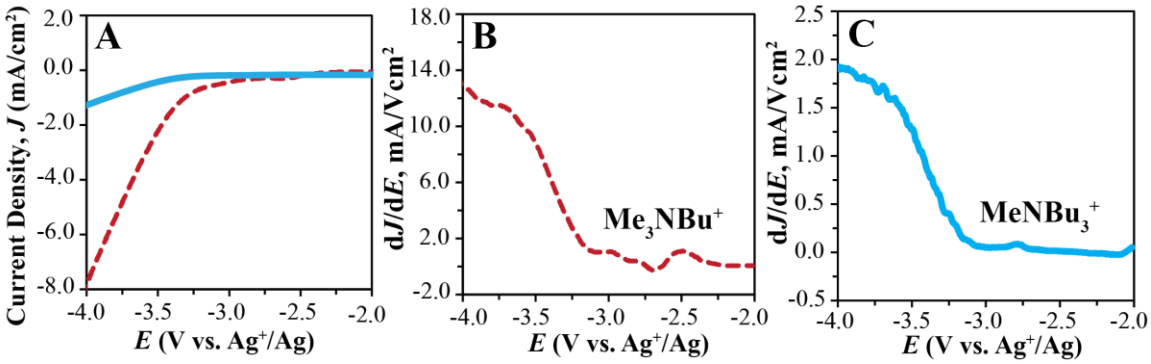

Figure 4. Effect of resistive distortion on electrochemical limits of ionic liquids. (A) Linear sweep voltammogram of $MeNBu_3$ TFSI (solid line) and $BuNMe_3$ TFSI (dashed line); corresponding d*J*/d*E* curves are shown in Panels (B) and (C), respectively. Scan rate, 100 mV/s; Pt coil auxiliary electrode, GC working electrode, and Ag^+/Ag reference electrode.

Similar observations were made when comparing the cathodic limits of the ionic liquids $MeNBu_3$ TFSI and $BuNMe_3$ TFSI. The $J_{cut\text{-}off}$ method gives for both $J_{cut\text{-}off}$ values of 0.5 and 1.0 mA/cm^2 a difference of 600 mV in the cathodic limits for the two ionic liquids (see Table 1 and Figure 4). While Figures 4B and 4C show similar onsets of the reduction, they show very different plateau values of d*J*/d*E* for the two ionic liquids (note the different *y*-axis scales), clearly indicating that a 600 mV difference between the cathodic limits of ionic liquids gives an unrealistic representation of the onset of ionic liquid reduction. The specific resistivity of $BuNMe_3$ TFSI is approximately one order of magnitude lower than that of $MeNBu_3$ TFSI (2.88×10^{-2} vs. 2.06×10^{-1} $\Omega^{-1}m^{-1}$),[97,101] resulting in a much larger d*J*/d*E* value for the latter and, consequently, the cathodic limit as given by the $J_{cut\text{-}off}$ method. The linear fit method corrects for the effect of the *iR* distortion and mass transport and gives more representative cathodic limits of -3.494 ± 0.048 for $MeNBu_3$ TFSI and -3.368 ± 0.019 V (vs. Ag^+/Ag) for $BuNMe_3$ TFSI. Similarly, compared to the $J_{cut\text{-}off}$ method, the linear fit method predicts closer cathodic limits for

EMI TFSI as a pure ionic liquid and as 300 mM solution in propylene carbonate (see Table 1).

2.3.4 Effect of the Scan Rate

It is well known that the scan rate can affect current–voltage curves and, consequently, change the electrolyte electrochemical limits determined with the $J_{\text{cut-off}}$ method,[24,26] but in the past this effect was not quantitatively studied. In this work, the cathodic limit of NBu_4I was measured at scan rates of 1, 10, 100, and 1000 mV/s (see Table 2). The scan rate had only a minor effect on the slope of the *J* vs. *E* curve and the onset of electrolyte reduction (see Figure 5B) but, as expected, a higher capacitive background current is observed at higher scan rates (see Figure 5A).

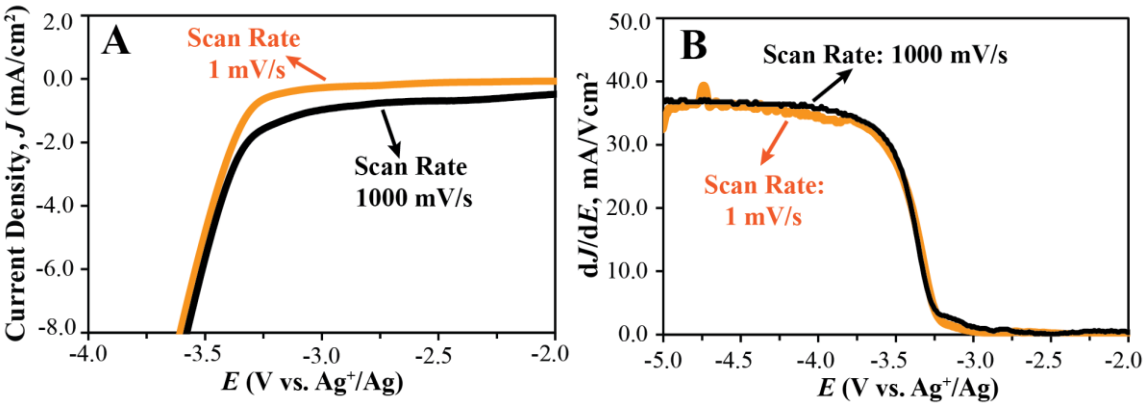

Figure 5. Effect of scan rate on the electrochemical window. (A) Linear sweep voltammogram of 300 mM NBu_4I in propylene carbonate at scan rates of 1 mV/s (orange) and 1000 mV/s (black); corresponding d*J*/d*E* shown in (B). Scan rate, 100 mV/s; Pt coil auxiliary electrode, GC working electrode, and Ag^+/Ag reference electrode.

Because the $J_{\text{cut-off}}$ method does not correct for the background current, the electrochemical limits determined with this method are affected by the scan rate more than the electrochemical limits obtained with the linear fit method. For example, at a

$J_{cut\text{-}off}$ of 0.5 mA/cm^2, cathodic limits of -2.240 ± 0.193 and -3.295 ± 0.070 V are determined for the scan rates of 1000 mV/s and 1 mV/s, respectively. The difference of more than 1.0 V in the cathodic stability of NBu_4I at these two scan rates is clearly an unrealistic representation of the electrochemical stability of the electrolyte. This effect is decreased at very high $J_{cut\text{-}off}$ values (e.g., 5.0 mA/cm^2), where the Faraday current is much larger than the background current and cathodic limits are less dependent on scan rate. The linear fit method gives similar cathodic limits of -3.513 ± 0.049 V and -3.422 ± 0.016 V at the two scan rates of 1 mV/s and 1000 mV/s respectively. In conclusion, the proposed linear fit method is less affected by the scan rate and provides a more realistic evaluation of the electrochemical stability of electrolytes.

Table 2. Effect of scan rate on cathodic limit (V vs. Ag^+/Ag) of NBu_4I.

	Scan rate			
	1 mV/s	10 mV/s	100 mV/s	1000 mV/s
$J_{cut\text{-}off}$ = 0.5 mA/cm^2	-3.295 ± 0.070	-3.273 ± 0.010	-3.145 ± 0.054	-2.240 ± 0.193
$J_{cut\text{-}off}$ = 1.0 mA/cm^2	-3.385 ± 0.042	-3.341 ± 0.008	-3.303 ± 0.019	-3.015 ± 0.082
$J_{cut\text{-}off}$ = 5.0 mA/cm^2	-3.611 ± 0.063	-3.539 ± 0.012	-3.509 ± 0.015	-3.480 ± 0.023
Linear fit method	-3.513 ± 0.049	-3.480 ± 0.018	-3.407 ± 0.010	-3.422 ± 0.016

300 mM NBu_4I in propylene carbonate; auxiliary electrode, Pt coil; working electrode, GC; reference electrode, Ag^+/Ag.

2.3.5 Electrochemical Limits at High Surface Area Carbon Electrodes

Porous high-surface-area carbon materials commonly used in electrochemical capacitors include commercially available activated carbons,[90] carbide-derived carbons with small, disordered mesopores,[102] nanofibers,[103] and porous templated carbons with large, open mesopores.[91] To obtain a representative selection, three high-surface-area carbon materials were used for this work, that is, Black Pearl 2000 (a commercially available microporous carbon), three-dimensionally ordered mesoporous (3DOm) carbon,[91] and colloid-imprinted mesoporous (CIM) carbon with a disordered pore structure.[94]

TABLE 3. Cathodic limit of EMI TFSI (V vs. Ag^+/Ag) at high surface area carbon electrodes.

	Glassy Carbon	Black Pearl	3DOm Carbon	CIM Carbon
$J_{cut\text{-}off}$ = 0.5 mA/cm^2	-2.425 ± 0.085	-0.102 ± 0.128	-0.185 ± 0.093	-0.315 ± 0.050
$J_{cut\text{-}off}$ = 1.0 mA/cm^2	-2.500 ± 0.066	-0.490 ± 0.128	-0.552 ± 0.131	-1.012 ± 0.233
$J_{cut\text{-}off}$ = 5.0 mA/cm^2	-2.552 ± 0.045	-2.298 ± 0.089	-2.595 ± 0.131	-2.365 ± 0.380
Linear fit method	-2.510 ± 0.033	-2.262 ± 0.148	-2.378 ± 0.067	-2.330 ± 0.158

Scan rate, 1 mV/s; auxiliary electrode, Pt coil; working electrode, GC; reference electrode, Ag^+/Ag.

The total current observed at any electrode is the sum of the faradaic (oxidative or reductive) current, and non-faradaic (i.e., capacitive) current.[1] During a linear potential sweep of the potential, E, with the scan rate v (where $E = vt$) within the potential window of the electrolyte (where there is no significant electrolyte decomposition), the capacitive current is given by vC_d $(1 - \exp[-t/(R_sC_d)])$, where C_d is the electrode capacitance and R_s the voltage independent solution resistance.[1] As the scan starts, the non-faradaic current rises from zero to reach a steady value of vC_d. Since the electrode capacitance is proportional to the surface area of the electrode, high surface areas result in large capacitive currents. This is clearly shown in Figure 6A, which shows the capacitive current at a non-porous glassy carbon electrode to be much smaller than in the case of the highly porous Black Pearl 2000 carbon. Note that the two electrodes have the same cross-sectional ("geometric") surface area. While the current density at the glassy carbon electrode (defined as current per geometric surface area) is less than 0.05 mA/cm^2, current densities as high as 1.0 mA/cm^2 are observed for the Black Pearl 2000 carbon electrode.

The electrochemical limit of the ionic liquid EMI TFSI (commonly used in electrochemical devices with high-surface-area carbon electrodes[90,91]) at electrodes consisting of non-porous glassy carbon or of a high-porosity carbon (Black Pearl carbon, 3DOm carbon, or CIM carbon) are shown in Table 3 for several $J_{cut\text{-}off}$ values. While the

onset of reduction occurs at approximately -2.5 V (see Figure 6B), the most commonly used $J_{\text{cut-off}}$ value of 1.0 mA/cm^2 predicts for all highly porous carbons unreasonably small cathodic limits in the range of -0.5 to -1.0 V. This is readily explained by the large capacitive current at these high-surface area electrodes.[25,92,104] This problem was also observed by Jow and co-workers, who recommended an alternative method for assessing the electrochemical electrolyte stability at electrodes with high surface areas.[89,92] They proposed an approach according to which the limit of electrochemical electrolyte stability is defined by the voltage at which the faradaic current associated with electrolyte decomposition reaches one ninth of the capacitive current (i.e., 10% of the total current, also referred to as $1/R_{\text{cut-off}}$; see Figure 3 in ref. 21). Even though this method takes into account the non-faradaic current, introducing an arbitrary cut-off value for $R_{\text{cut-off}}$ opens the door for disagreements on what that value should be. Indeed, Moosbauer et al. already suggested to change the $R_{\text{cut-off}}$ from 0.1 to 0.02 or lower,[105] and Weingarth suggested cut-off values of 0.05 for d^2R/dV^{*2} instead.[104] To the contrary, the linear fit method provides electrochemical stability limits without the need to define any cut-off value, as shown in Table 3.

Note that current densities at porous electrodes are calculated here based on the geometric surface area (i.e., the area obtained by projection of the electrode shape on a plane). Due to the micropores and mesopores in the electrode material, the real surface area that is accessible to the electrolyte is much larger than the geometric surface area. Therefore, it is difficult to assess the real current density at these electrodes accurately. The linear fit method does not require converting currents to current densities as the surface area of the electrode appears as a constant in the linear fit equations and will be omitted during the intersection of the two. Therefore, there is no need to know the real surface area of highly porous electrodes, which adds to the convenience of this method.

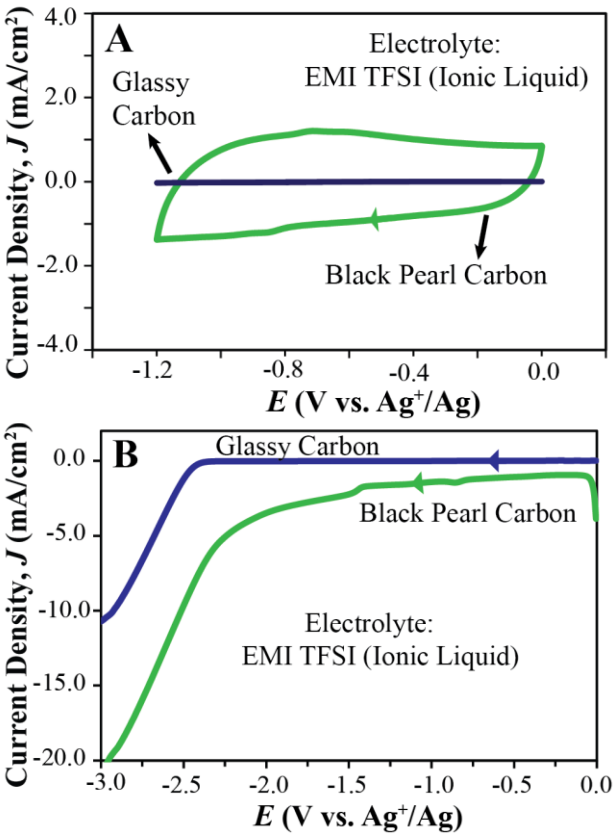

Figure 6. Electrochemical limits at high-surface-area carbon electrodes. CV (A) and linear sweep voltammogram (B) of EMI TFSI at a GC (blue) and a Black Pearl carbon electrode (green). For the CV, the second cycle is shown to avoid first cycle effects. Scan rate, 1 mV/s; Pt coil auxiliary electrode, GC working electrode, and Ag^+/Ag reference electrode.

2.4 Conclusions

In this contribution, we illustrated that the determination of electrolyte electrochemical limits with the cut-off current density method has three main disadvantages that can be overcome by the proposed linear fit method. Firstly, the arbitrariness associated with the selection of a cut-off current density results in variabilities of the electrochemical limit of 1.0 V and more, often not providing meaningful electrochemical stability limits. This

problem cannot be resolved by recommending one specific cut-off current density for all conceivable systems because this value inherently depends on the electrolyte concentration and diffusion coefficients, as also confirmed by numerical simulations taking into account diffusion and migration as mass transport modes. Choosing a cut-off current density can be avoided by using the linear fit method. The second disadvantage of the $J_{\text{cut-off}}$ method is related to the electrolyte mass transport effects on the current–voltage curve, altering the electrochemical limits determined with the cut-off current density method by as much as 600 mV. The linear fit method minimizes such effects. Finally, the $J_{\text{cut-off}}$ method does not provide a reliable assessment of the electrochemical windows at electrodes with high surface areas, where large capacitive currents are observed, whereas electrochemical windows determined with the linear fit method are minimally affected by capacitive currents.

2.5 Acknowledgments

This project was partially supported by a Graham N. Gleysteen Excellence Fellowship and a University of Minnesota Doctoral Dissertation Fellowship to M. P. S. M., and Grant RL-0012-12 from the Initiative for Renewable Energy and the Environment of the University of Minnesota. J. H. appreciates the Krogh family for support with a Lester C. and Joan M. Krogh Fellowship in Chemistry.

3 CHAPTER THREE

Electrochemical Stability of Quaternary Ammonium Cations: An Experimental and Computational Study

In part from:

Mousavi, M. P. S.; Kashefolgheta, S.; Stein, A.; Buhlmann, P., Electrochemical stability of quaternary ammonium cations: An experimental and computational study. *J. Elec. Soc.* **2016,** *163*, H74-H80.

This work was a joint effort by this author and Sadra Kashefolgheta who carried out the computational calculations.

Quaternary ammonium ions, NR_4^+, are among the most electrochemically stable classes of organic cations. Because of their wide electrochemical windows, they are frequently used in batteries and electrochemical capacitors. Improving the electrochemical stability and expanding the electrochemical windows of quaternary ammoniums is highly desired. In this work, we investigated the electrochemical stability of quaternary ammonium ions and showed that the chain length, type (primary vs. secondary), size, and steric hindrance of the saturated alkyl substituents have only a very small effect (less than 150 mV) on their electrochemical stability towards reduction. To provide a molecular understanding of substituent effects on electrochemical stability, quantum calculations were performed employing density functional theory, and it was shown that the structure of saturated aliphatic alkyl substituents has only minimal effects on the electronic environment around the positive nitrogen center and the LUMO energy level of quaternary ammonium cations. Moreover, a linear correlation between the cathodic limit and the LUMO energy levels of the NR_4^+, *N*-butylpyridinium, and 1-ethyl-3-methylimidazolium ions was found, suggesting that electrochemical stabilities of new cations may be computationally predicted on the basis of LUMO energies of these systems.

3.1 Introduction

With the increasing global demand for energy, improving existing energy storage technologies is as critical as developing more efficient methods for energy production. For one important class of energy storage technologies, namely electrical energy storage, the energy density of a device is usually limited by the voltage window in which the device can function. Therefore, expanding the working voltage range of such devices is highly desired. The electrochemical decomposition of electrolytes, which are commonly used in energy storage devices such as electrochemical capacitors, often limits the useful voltage window[17] because these device can function properly only within the electrochemical window of their electrolyte. Modifying the structure of electrolytes and

improving their electrochemical stabilities has been the focus of numerous studies to date.[24-29,34-38,40,88,106]

The electrochemical window of an electrolyte is the voltage range in which the electrolyte is chemically stable and does not get reduced or oxidized as a result of the applied potential.[6] The upper end of the electrochemical window is usually limited by the oxidation of the anion, and the lower end of the electrochemical window is determined by the reduction of the cation.[17] One of the most electrochemically stable classes of organic cations comprises the quaternary ammonium ions, NR_4^+. These are highly inert towards reduction, offer wide electrochemical windows, and are, therefore, frequently used in batteries and capacitors.[25,27,88,99] Much research has been devoted to improving the electrochemical stability of quaternary ammonium ions.[24,28,29,34,35,37,38,40]

Reduction of quaternary ammonium ions occurs via radical intermediates and involves the loss of an alkyl substituent.[24,34,95,107-109] Therefore, the nature of the alkyl substituents strongly affects the electrochemical stability of these cations.[28] Quaternary ammonium ions with aromatic substituents such as benzyl groups have lower electrochemical stabilities than saturated quaternary ammonium ions.[34] This effect is likely due to the higher stability of benzyl radicals as compared to alkyl radicals, making the former a better leaving group, and thus making quaternary ammonium ions with benzyl substituents more sensitive to reduction.[34] Incorporation of oxygen atoms in the alkyl substituents of quaternary ammonium ions also diminishes their electrochemical stability towards reduction, likely due to the electrostatic effects of the oxygen atoms.[29,35,37,38,40] Changing the structure of the saturated alkyl substituent (increasing the alkyl chain length, size, etc.) can also affect the electrochemical stability of quaternary ammonium ions. Unfortunately, there are discrepancies in the literature on this topic.

Several reports have indicated that increasing the chain length or size of alkyl substituents in quaternary ammonium ions improves the electrochemical stability of these

ions.[25,28,34,35,37,110,111] The increased stability was attributed to the higher blocking and shielding effect and increased electron donating characteristics of larger alkyl groups.[28,34,110] In contrast, no substantial improvement in the cathodic stability of quaternary ammonium ions was observed in another study upon increasing the length of the alkyl substituent.[26] Yet another study reported a decreased electrochemical stability of quaternary ammonium ions towards reduction with increasing chain length of the alkyl substituent.[95] There are also discrepancies in what has been reported on the effect of ion size on the electrochemical properties of quaternary ammonium cation. Increasing the cation size was concluded in one study to increase electrochemical stability,[35] whereas another one found no such result.[26] The effect of the alkyl substituent is not only a function of size, but the nature of the alkyl group is also important, as structurally isomeric alkyl groups are expected to have different effects on the electrochemical stability of quaternary ammonium ions. For example, changing the quaternary ammonium substituent from butyl to *iso*-butyl was reported to improve electrochemical stability.[25,28] However, changing from a primary to a secondary alkyl substituent was reported to drastically reduce electrochemical stability in one study (*n*-Bu to *s*-Bu)[28] and to improve electrochemical stability in another (*n*-Pr to *i*-Pr)[25]. Clearly, there is a need to clarify the aforementioned discrepancies.

In this work, we provide a comprehensive investigation of the effect of a series of alkyl substituents on the electrochemical stability of quaternary ammonium cations. The effect of alkyl chain length, size, and type (i.e., primary vs. secondary alkyl groups) is studied. Our findings are compared to published reports, and the discrepancies in the literature are discussed and explained. In addition to the experimental characterization of the electrochemical stabilities of quaternary ammonium cations, the lowest unoccupied molecular orbital (LUMO) energy levels of quaternary ammonium cations were calculated using the time-dependent density functional theory,[112-114] TD-DFT, method, providing a molecular understanding of the electrochemical behavior of these cations.

3.2 Experimental

3.2.1 Electrochemical Measurements

Linear sweep voltammetry experiments were carried out with a CHI600C potentiostat (CH Instruments, Austin, TX). A three-electrode set up with a 3.0 mm-diameter glassy carbon (GC) disk working electrode (BAS, West Lafayette, IN), a 0.25 mm Pt wire coil (99.998%, Alfa Aesar, Ward Hill, MA) auxiliary electrode, and a Ag^+/Ag reference electrode (reference solution: 10 mM $AgNO_3$ and 100 mM NBu_4ClO_4 in acetonitrile) was used for all measurements (scan rate: 100 mV/s). The reference electrode was prepared in house according to a previously described procedure.[10,115] The distance between the working and reference electrode was kept small (≈0.5 cm) to minimize the *IR* drop while not physically obstructing the working electrode. The working electrode was polished on Microcloth polishing pads using 5.0 μm Micropolish II deagglomerated alumina, both from Buehler (Lake Bluff, IL). After polishing, the electrode was rinsed thoroughly with deionized water and then with ethanol, followed by drying under a stream of Ar. The anhydrous solvents used in this work were stored and transferred under argon. Prior to measurements, all solutions were purged with argon for 15 min while stirring vigorously to remove dissolved oxygen. The magnitude of the capacitive current was less than 0.02 mA/cm^2. All quaternary ammonium salt solutions were 300 mM in concentration, except for the NEt_4I solution, which was 100 mM due to the limited solubility of this salt. Different concentration of NEt_4I is not a concern because we are reporting cathodic stabilities measured by the linear fit method which corrects for the effect of electrolyte concentration on the electrochemical stability limits. Synthesis of quaternary ammoniums and material venders are provided in the supporting information.

A 1255B frequency response analyzer and a SI 1287 electrochemical interface from Solartron (Farnborough, Hampshire, UK) with a conductivity cell from Cole-Parmer (Vernon Hills, IL, USA) were used to determine the specific resistivity of propylene carbonate solutions of the quaternary ammonium iodides. A 500 μS/cm conductivity

standard solution was used to determine the cell constant. Resistances were obtained by fitting of impedance spectra with ZPlot software (Scribner Associates, Southern Pines, NC, USA) in the 10^4 to 10^5 Hz range. A specific resistivity of 7.1 ± 0.4 Ω m was obtained for the propylene carbonate solution of 300 mM tetrabutylammonium iodide (the specific resistivity of the remaining quaternary ammoniums used in this study is expected to close to specific resistivity of NBu_4I, as it was shown that the chain length of substituents (ethyl to hexyl) and the symmetry of quaternary ammonium salts changes the specific conductivity by less than 10%).[116-118] The *IR* drop across the working and reference electrodes at current densities of 1 to 5 mA/cm^2 is less than 1 mV in this study. ($I\,R = J.\,A\,(\rho\,L/A) = J\,\rho\,L$ = 5 mA cm^{-2} × 0.071 Ω cm × 0.5 cm $<$ 1 mV, where A, L, ρ, and R are the surface area of working electrode, distance between the reference and working electrode, specific resistivity of the solution, and solution resistance, respectively.)

3.2.2 Computational Methods

To calculate the LUMO and HOMO energies of the quaternary ammonium cations, density functional theory (DFT) was used as the quantum mechanical method.[119] All structures were optimized to reach the lowest ground state energy. The structures of cations were optimized using the DFT method with the B3LYP density functional[120-123] and the triple-zeta basis set 6-311++(d,p). To take into the account solvation effects, DFT was combined with the polarizable continuum model IEF-PCM[124-128] for propylene carbonate (see Supporting Information for details). This is an implicit solvation model in which the solvent has no molecular structure, and solvent effects are approximated by creating a solvent cavity around the solute molecules using macroscopic parameters for, e.g., the solvent dielectric constant and the solvent radius. As a part of the optimization process, the energies of all occupied and unoccupied molecular orbitals are calculated. DFT HOMO energies (Kohn-Sham HOMO eigenvalues) were reported to have a linear correlation with experimental ionization potentials. However, LUMO energies (KS LUMO eigenvalues) from DFT show poor correlation with the experimental LUMO

energies.[119,129,130] (An experimental LUMO energy is defined as the difference between the experimental ionization potential and the experimental first excitation energy.)[119]

A better estimate of LUMO energies can be obtained by calculation of the first excitation energy using the time-dependent density functional theory (TD-DFT), followed by addition of the resulting value to the calculated energy for the HOMO (see Supporting Information for details). The TD-DFT is an extension of the DFT method for the treatment of time-dependent phenomena such as excitation energies, and assumes the electron density to be a function of time in addition to space.[112] The excitation energies (HOMO-LUMO energy gaps) obtained with TD-DFT were reported to have a good linear correlation with respect to the experimental values, and, therefore, the LUMO energies that are obtained this way are expected to be more reliable than the directly calculated Kohn-Sham LUMO eigenvalues.[119] All calculations were performed with the Gaussian03 package.[131]

3.3 Results and Discussion

Reduction of quaternary ammonium cations occurs by quantum tunneling of an electron from an occupied state at the Fermi energy level of the electrode to the LUMO of the cation.[1,111] The rate of electron transfer is maximized when the electrode Fermi level reaches the cation LUMO energy level.[1] The structure of the alkyl groups can affect the LUMO energy level of the quaternary ammonium, consequently affecting its electrochemical stability. Electron donating alkyl groups can decrease the positive charge density of the nitrogen atom in the quaternary ammonium ion and improve its stability towards reduction. The rate of electron transfer is also affected by the donor–acceptor distance, decaying exponentially as the donor–acceptor distance increases.[111] As any cations, at negative potentials quaternary ammonium ions adsorb electrostatically on the electrode surface, and the electron transfer occurs over a short-range distance.[111] Bulkier or more sterically hindered alkyl groups may increase the tunneling distance, reduce the

rate of electron tunneling to the LUMO, and consequently increase the stability of the quaternary ammonium towards reduction.[111] To study such effects, we investigated the series of quaternary ammoniums displayed in Scheme 1. Parameters such as alkyl chain length (RNR'_3^+, where R is Me, Et, Pr, or Bu and R' is Pr or Bu), the size of the quaternary ammonium cation (NR_4^+, where R is Me, Et, Pr, Bu, Pent, or Hex) and the nature of the alkyl substituent (as in $MeN(i\text{-}Bu)_3^+$, $Et_2N(i\text{-}Pr)_2^+$, or $MeEtN(i\text{-}Pr)_2^+$) were varied to understand the different structural effects on the electrochemical stability of these cations and address the discrepancies in the literature that were highlighted in the introduction.

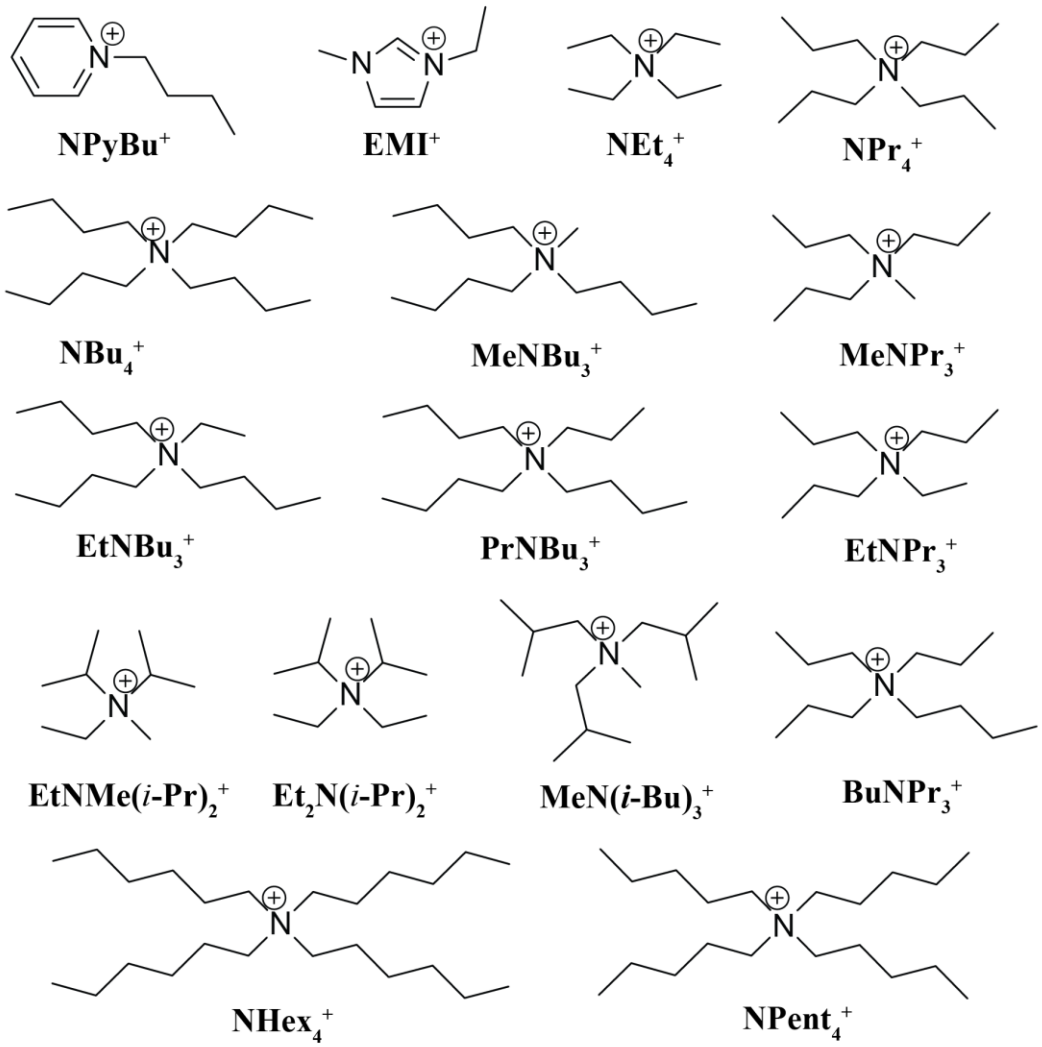

Scheme 1. Structures and abbreviations of organic cations investigated in this study.

3.3.1 Assessment of the electrochemical stability of electrolytes: origin of discrepancies

Many of the discrepancies in the reported effects of substituents on the electrochemical stability of quaternary ammonium cations are likely caused by two reasons: lack of robustness in the method used for quantifying the electrolyte electrochemical stability, and lack of properly addressing the reproducibility of the results. In the past, the

determination of the electrochemical stability limit of electrolytes has not been well defined. Usually, a current–voltage polarization curve has been measured, and the voltage at which a specific current density, J, is reached, has been defined as the cathodic or anodic electrochemical limit of the electrolyte (see Figure 1A).[6] The choice of the cut-off current density, $J_{\text{cut-off}}$, is quite arbitrary, and a number of $J_{\text{cut-off}}$ values (0.01 to 5.0 mA/cm^2) have been used in the literature.[24-41] Unfortunately, the choice of $J_{\text{cut-off}}$ can influence the electrochemical limit of electrolytes by as much as 0.9 V.[24,41] Figure 1 shows the linear sweep voltammogram of NEt_4I; the voltages at which $J_{\text{cut-off}}$ values of 0.5 and 1.0 mA/cm^2 are reached are shown in Panel A. Clearly, the choice of the $J_{\text{cut-off}}$ value affects the electrochemical limit determined for NEt_4I. In addition to the value of $J_{\text{cut-off}}$, parameters such as electrolyte concentration and conductivity can bias the determined electrochemical limit by as much as 500 mV.[17,41] Other experimental parameters, such as the type of the working electrode and the scan rate, have been found to affect the determined electrochemical limits to a lesser extent.[17,24,41] In case of measurements performed with working electrodes with very high surface areas, such as porous carbon electrodes, the capacitive current may bias the determination of electrochemical limits by the cut-off current density method by as much as 2.0 V.[41] Therefore, electrolyte stability limits as reported by different authors do not solely represent the thermodynamic properties of the electrolyte but are affected by different experimental procedures and assessment criteria.

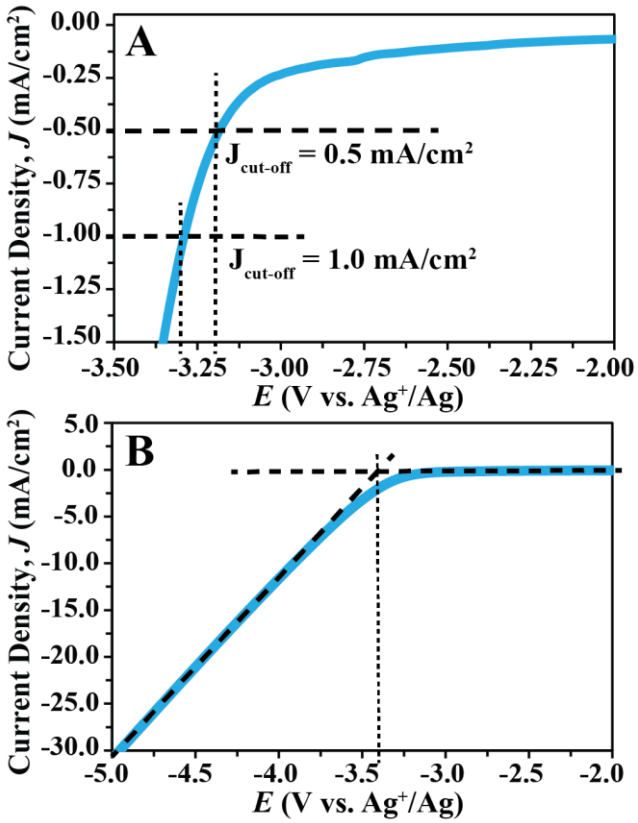

Figure 1. Determination of the electrochemical stability limit of electrolytes. (A) and (B) show the linear sweep voltammograms of NEt_4I (100 mM) in propylene carbonate. Panel (A) illustrates the use of $J_{cut\text{-}off}$ values of 0.5 and 1.0 mA/cm^2. The dashed lines in panel (B) are linear fits before and after the onset of NBu_4I reduction; the vertical dotted line highlights the potential at which the two fits intersect. Scan rate, 100 mV/s; Pt coil auxiliary electrode, GC working electrode, and Ag^+/Ag reference electrode.

In our work, to assess the electrochemical stability of quaternary ammonium ions more comprehensively, we determined the electrochemical limit of these cations at $J_{cut\text{-}off}$ of 0.1, 0.5, 1.0, and 5.0 mA/cm^2. The resulting values are presented in Table 1, which shows that changes in $J_{cut\text{-}off}$ can shift electrochemical stability limits by as much as 1.8 V. Moreover, the order of the electrochemical stability of the quaternary ammoniums changes when altering the $J_{cut\text{-}off}$ criterion. For instance, at $J_{cut\text{-}off}$ of 0.1 and 5.0 mA/cm^2,

NEt_4^+ is predicted to have a higher stability towards reduction than $NHex_4^+$; however, at 0.5 and 1.0 mA/cm^2 the order is reversed, and $NHex_4^+$ has a higher electrochemical limit (see entries 3 and 7 in Table 1). Similarly, changing the $J_{cut\text{-}off}$ criterion influences the order of the electrochemical stabilities of $MeNPr_3^+$ and $BuNPr_3^+$ as well as $MeN(i\text{-}Bu)_3^+$ and $EtNMe(i\text{-}Pr)_2^+$ (see entries 11, 13, 14, and 15 in Table 1). Even though not discussed by the authors of the original literature, this phenomenon can also be observed in the electrochemical stability limits of room temperature ionic liquids, where a different order of electrochemical stability for imidazolium-based ionic liquids is obtained at $J_{cut\text{-}off}$ of 1.0 and 5.0 mA/cm^2.[39] This confirms that small differences in the observed electrochemical stability limits should not be attributed hastily to the molecular properties such as electron donating or shielding effect of the alkyl groups, and the effect of experimental conditions and the $J_{cut\text{-}off}$ choice must be considered carefully.

Surprisingly, all the conclusions drawn in the literature regarding the electrochemical stability of quaternary ammoniums were based on single measurements, and data reproducibility was not investigated. The latter explains some of the contradictory reports on the electrochemical stability of quaternary ammoniums. In several cases, small differences in electrochemical stability limits were attributed to intrinsic properties of the electrolyte, and often it is not clear whether the observed differences are statistically significant or not. For instance, stability limits of -1.89 and -1.95 V vs. Ag/AgCl for Et_3NMeCl and Bu_3NMeCl were reported, respectively, and it was concluded that increasing the alkyl substituent chain length improves the electrochemical stability of quaternary ammoniums.[34] Other examples include interpreting 50 mV,[28] 90 mV,[37] 140 mV,[34] and 160 mV[28] differences in the electrochemical limit of quaternary ammonium ions, without assuring statistical significance. In our analysis, we performed five replicates of the current-voltage polarization curves for each quaternary ammonium. As shown in Table 1, standard deviations as high 80 mV at $J_{cut\text{-}off}$ of 0.5 to 5.0 mA/cm^2, and as high as 500 mV at $J_{cut\text{-}off}$ of 0.1 mA/cm^2 were observed. Of course, the standard deviations reported here are specific to our measurements, and the data reproducibility,

which is affected by many parameters that are not easy to control. In this study, we attempted to minimize the effect of these parameters by using high purity quaternary ammonium salts, carefully polishing and cleaning the working electrode, and by decreasing the *IR* drop between the working and reference electrodes to less than 1.0 mV. The latter was achieved by using high concentrations of quaternary ammonium salts to obtain low solution resistivity, and by minimizing the distance between the working and reference electrodes (see the Experimental Section for details).

To improve the ability to compare different electrochemical limits, we recently developed a new method (referred to as the linear fit method) for assessing the electrochemical stability of electrolytes.[17,41] Using this method, two linear fits are applied to the current–voltage polarization curve of the electrolyte at potentials below and above the onset of cathodic or anodic decomposition (see Figure 1B). The intercept of the two approximately linear portions of the current–voltage relationship below and above the electrochemical limit is defined as the cathodic or anodic limit of the electrolyte.[17,41] We recently showed that the linear fit method does not rely on any $J_{\text{cut-off}}$ value and minimizes effects of the scan rate, electrolyte concentration, diffusion coefficients, capacitive current, and *IR* drop between the working and reference electrodes.[41] Thereby, it provides electrochemical limits that are more representative of the inherent properties of the electrolyte and are less affected by experimental parameters.[41] Electrochemical stability limits obtained from the linear fit method are also presented in Table 1.

TABLE 1. Cathodic limits (V vs. Ag^+/Ag) from the cut-off current density and linear fit methods.

		$J_{cut\text{-}off}$ = 0.1 mA/cm^2	$J_{cut\text{-}off}$ = 0.5 mA/cm^2	$J_{cut\text{-}off}$ = 1.0 mA/cm^2	$J_{cut\text{-}off}$ = 5.0 mA/cm^2	Linear fit method
1	**NPvBu TFSI**	-1.523 ± 0.004	-1.571 ± 0.005	-1.603 ± 0.004	-1.735 ± 0.009	-1.584 ± 0.004
2	**EMI TFSI**	-1.905 ± 0.423	-2.513 ± 0.008	-2.559 ± 0.005	-2.725 ± 0.046	-2.550 ± 0.019
3	**NEt_4I***	-2.447 ± 0.067	-3.183 ± 0.012	-3.293 ± 0.012	-3.619 ± 0.008	-3.403 ± 0.005
4	**NPr_4I**	-2.507 ± 0.594	-3.261 ± 0.005	-3.341 ± 0.005	-3.623 ± 0.008	-3.396 ± 0.004
5	**NBu_4I**	-2.463 ± 0.076	-3.297 ± 0.032	-3.359 ± 0.028	-3.541 ± 0.017	-3.423 ± 0.010
6	**$NPent_4I$**	-1.995 ± 0.126	-3.201 ± 0.005	-3.287 ± 0.004	-3.501 ± 0.008	-3.394 ± 0.007
7	**$NHex_4I$**	-1.741 ± 0.342	-3.257 ± 0.007	-3.337 ± 0.008	-3.603 ± 0.012	-3.449 ± 0.008
8	**$MeNBu_3I$**	-1.371 ± 0.268	-3.123 ± 0.046	-3.275 ± 0.041	-3.509 ± 0.038	-3.390 ± 0.040
9	**$EtNBu_3I$**	-1.548 ± 0.302	-3.208 ± 0.011	-3.303 ± 0.019	-3.558 ± 0.080	-3.384 ± 0.009
10	**$PrNBu_3I$**	-1.929 ± 0.049	-3.061 ± 0.038	-3.377 ± 0.039	-3.671 ± 0.172	-3.453 ± 0.018
11	**$MeNPr_3I$**	-2.329 ± 0.083	-3.121 ± 0.083	-3.259 ± 0.005	-3.491 ± 0.012	-3.361 ± 0.016
12	**$EtNPr_3I$**	-2.387 ± 0.033	-3.187 ± 0.004	-3.273 ± 0.004	-3.487 ± 0.005	-3.386 ± 0.006
13	**$BuNPr_3I$**	-1.917 ± 0.019	-3.241 ± 0.005	-3.315 ± 0.003	-3.541 ± 0.005	-3.464 ± 0.002
14	**$MeN(i\text{-}Bu)_3I$**	-2.417 ± 0.099	-3.169 ± 0.016	-3.265 ± 0.014	-3.523 ± 0.035	-3.383 ± 0.008
15	**$EtNMe(i\text{-}Pr)_2I$***	-2.631 ± 0.018	-3.133 ± 0.004	-3.251 ± 0.005	-3.623 ± 0.004	-3.400 ± 0.002
16	**$Et_2N(i\text{-}Pr)_2I$***	-2.647 ± 0.019	-3.051 ± 0.004	-3.163 ± 0.004	-3.605 ± 0.006	-3.400 ± 0.001

3.3.2 Effect of alkyl substituents on the electrochemical stability of quaternary ammonium ions

Electrochemical stability measurements were carried out using propylene carbonate solutions of quaternary ammonium electrolytes because propylene carbonate has an electrochemical window wider than quaternary ammonium ions.[17,25,88] The $J_{cut\text{-}off}$ of 0.1 mA/cm^2 did not provide a realistic assessment of electrochemical stabilities. A stability limit of -2.507 ± 0.594 V vs. Ag^+/Ag was determined for NPr_4I when using this $J_{cut\text{-}off}$ value, while clearly the onset of electrochemical reduction is not reached at this potential (see Figure 2). On the other hand, the $J_{cut\text{-}off}$ of 5.0 mA/cm^2 overestimates electrochemical stability (-3.623 ± 0.008 V vs. Ag^+/Ag) and predicts stability limits that are well past the onset of reduction. Therefore, we consider hereon stability limits obtained from $J_{cut\text{-}off}$ values of 0.5 and 1.0 mA/cm^2 and also the linear fit method.

3.3.2.1 Effect of alkyl chain length/quaternary ammonium size

In this work, we do not distinguish between the effects of the length of straight alkyl chains and the size of the corresponding quaternary ammonium ions because the two effects are clearly directly related to one another. Overall, we found no correlation between the alkyl chain length and the electrochemical stability of the quaternary ammonium ions. The linear sweep voltammograms of NEt_4^+, NPr_4^+, NBu_4^+, $NPent_4^+$, and $NHex_4^+$ are shown in Figure 2. Visually, there seems to be no difference in the onset of reduction of the aforementioned cations. At $J_{cut\text{-}off}$ of 0.5 and 1.0 mA/cm^2, there is no significant difference in the cathodic stability of NEt_4^+ and $NPent_4^+$. Similarly, the cathodic limits of NPr_4^+, NBu_4^+, and $NHex_4^+$ are not significantly different, yet these ions are significantly more stable than NEt_4^+ and $NPent_4^+$ by approximately 60 mV (see entries 3 to 7 in Table 1). The linear fit method predicts no significant change in the cathodic stability of NR_4^+ by increasing the alkyl chain length from ethyl to propyl, butyl,

and pentyl. However, going from NEt_4^+ to $NHex_4^+$ results in a statistically significant improvement in the cathodic limit by 40 mV.

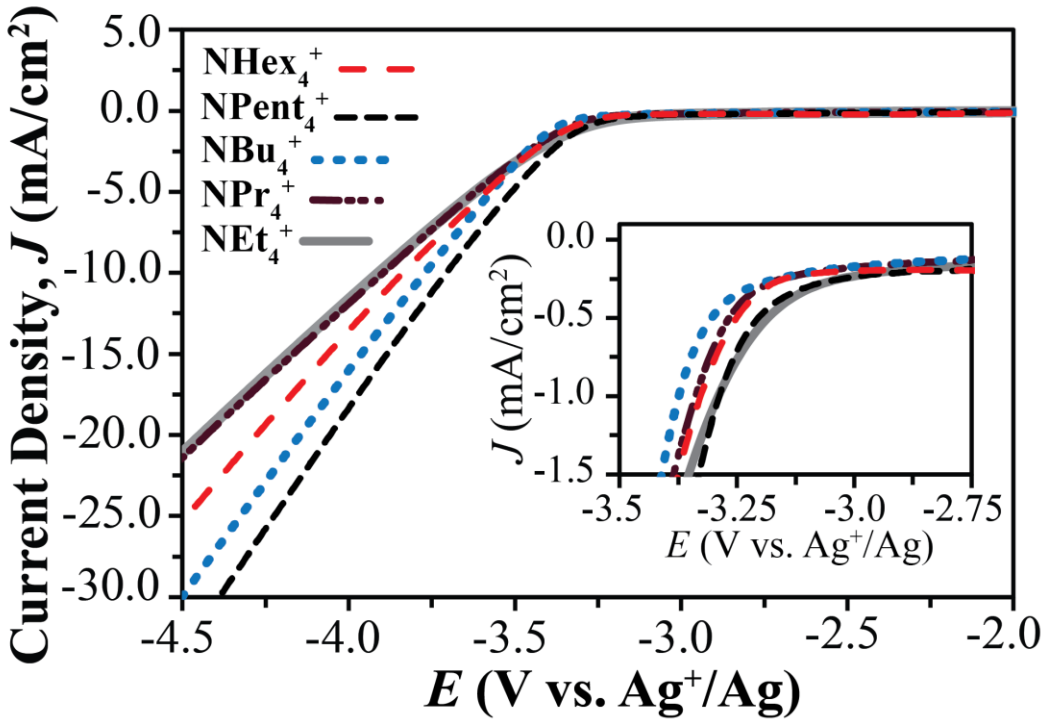

Figure 2. Linear sweep voltammogram of 100 mM NEt_4I, and 300 mM NPr_4I, NBu_4I, $NPent_4I$, and $NHex_4I$ in propylene carbonate. Scan rate, 100 mV/s; Pt coil auxiliary electrode, GC working electrode, and Ag^+/Ag reference electrode. The inset zooms in the region where the onset of reduction occurs.

In the $RNPr_3^+$ series (entries 4, and 11 to 13 in Table 1), increasing the length of R from methyl to ethyl did not affect the electrochemical stability significantly. Further increasing the R to propyl and butyl did cause a statistically significant improvement in the cathodic stability at all three assessment criteria of $J_{cut\text{-}off}$ of 0.5 and 1.0 mA/cm^2, and the linear fit method. However, the magnitudes of the change in the stability limits were small and less than 120 mV. Also, the electrochemical stabilities of $PrNPr_3^+$ and $BuNPr_3^+$ were not significantly different from one another.

For $RNBu_3^+$ (entries 5, and 8 to 10 in Table 1), increasing R from methyl to ethyl caused a significant improvement (80 mV) in the stability limit at the assessment criterion of $J_{cut-off}$ of 0.5 mA/cm^2; however, $J_{cut-off}$ of 1.0 mA/cm^2 and the linear fit method did not predict a significant change in the cathodic stability. Changing R from methyl to propyl or butyl has no significant effect on the stability limit determined with the linear fit method and with the $J_{cut-off}$ of 0.5 mA/cm^2, but at $J_{cut-off}$ of 1.0 mA/cm^2 it results in a statistically significant improvement of 100 mV in the stability limit. Finally, replacing methyl with butyl results in no significant effect on the stability limit determined with the linear fit method, and 174 and 90 mV improvements in the cathodic stability at $J_{cut-off}$ of 0.5 and 1.0 mA/cm^2, respectively.

Clearly, increasing the alkyl chain length does not improve the cathodic limit consistently, the effects are relatively small (less than 150 mV), and different effects were observed for the different criteria of $J_{cut-off}$ of 0.5 and 1.0 mA/cm^2 and when using the linear fit method. This suggests that many of the observed changes in the cathodic stability are more an artifact of the cathodic limit quantification rather than an increased electrochemical stability in the molecular level. Figure 3 shows the relationship between the cathodic stability and the number of carbon atoms (representative of size) in the quaternary ammonium ions both for the linear fit and the $J_{cut-off}$ assessment methods. The overall range of observed cathodic limits was less than 150 mV. It is noticeable that the range of cathodic stabilities is narrower when these limits are determined with the linear fit method (Figure 3C), which is consistent with a lesser effect of electrolyte mass transport on this method. Using the linear fit method and the 0.5 mA/cm^2 data, no significant correlation between cathodic stabilities and the number of carbon atoms could be confirmed, even at the relaxed α of 0.1 (see the Supporting Information for results of the ANOVA test). A correlation between the cathodic stabilities measured as determined for a $J_{cut-off}$ value of 1.0 mA/cm^2 and the number of carbon atoms can be confirmed at significant level of 90%, but not at significance level of 95%. This can be explained easily as an artifact of the $J_{cut-off}$ method since the cathodic limits measured with the J_{cut-}

$_{off}$ method are biased by the rate of cation transport to the electrode, which is affected by the cation's size and mass. A smaller diffusion coefficient along with an unchanged electrochemical stability results in no change in the onset of reduction, but a decrease in the slope of the current density vs. voltage relationship after the onset of reduction of the cation.[41] Because larger cations diffuse more slowly, the slopes of their current density vs. voltage relationships after their onsets of reduction are smaller. Consequently cathodic stabilities as assessed by the $J_{cut\text{-}off}$ method are misjudged to be larger. This bias becomes larger the higher the $J_{cut\text{-}off}$ value is chosen.

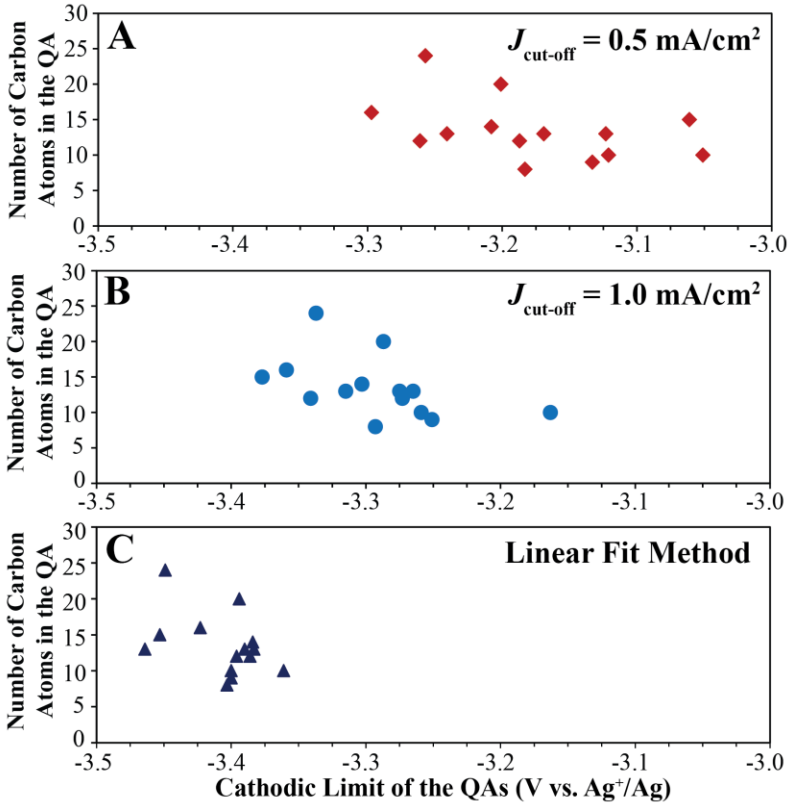

Figure 3. Dependence of cathodic limit of quaternary ammoniums (QA) on the number of carbon atoms in their substituents. No correlation between the electrochemical stability (obtained by the $J_{cut\text{-}off}$ of 0.5, and 1.0 mA/cm^2, and the linear fit method) and number of carbon atoms was observed.

3.3.2.2 Effect of alkyl type

Similar linear sweep voltammograms were observed for $MeNBu_3^+$ I^- and $MeN(i\text{-}Bu)_3^+$ I^- **(**see Figure 4). No significant difference was noticed in the cathodic limits of the two cations at $J_{cut\text{-}off}$ of 0.5 and 1.0 mA/cm^2 and also the linear fit method (see Table 1, which includes standard deviations). Our findings contradict those of Xu et al. who reported -0.11 and -0.50 V vs. Li^+/Li (which corresponds to -3.64 and -4.03 V vs. Ag^+/Ag)[132] for the cathodic limits of $MeNBu_3^+$ PF_6^- and $MeN(i\text{-}Bu)_3^+$ PF_6^-, respectively (0.05 mA/cm^2 as $J_{cut\text{-}off}$, working electrode: GC), and concluded that *iso*-butyl increases the cathodic stability.[25] A similar conclusion was drawn elsewhere upon observing a 50 mV improvement in the cathodic limit of *N*-alkyl-*N*-methyl-pyrrolidinium by changing the alkyl group from butyl to isobutyl.[28] Both reports did not provide evidence that the observed differences in the cathodic limits were statistically significant.

Changing the alkyl group from *n*-Bu to *s*-Bu was previously reported to result in a more than 2.0 V decrease (no error range reported) in the cathodic limit (0.1 mA/cm^2 as $J_{cut\text{-}off}$) of *N*-alkyl-*N*-methyl-pyrrolidinium.[28] Also, substituting the primary propyl groups in Pr_3NMe^+ PF6$^-$ by secondary isopropyl groups was reported to improve the cathodic limit (0.05 mA/cm^2 as $J_{cut\text{-}off}$) by 200 mV (no error range reported).[25] In contrast, we found that changing from primary to secondary alkyl groups has minimal effects on the cathodic stability of quaternary ammonium ions, as shown for $EtNPr_3I$, $Et_2N(i\text{-}Pr)_2I$, and $EtNMe(i\text{-}Pr)_2I$ in Table 1 (entries 12, 15, and 16). Replacing Pr with *i*-Pr resulted in a statistically significant decrease (less than 100 mV) in the magnitude of the cathodic limits at $J_{cut\text{-}off}$ of 0.5 and 1.0 mA/cm^2; however, it significantly improved the cathodic limits as determined with the linear fit method by 25 mV. This confirms that the small differences in the cathodic limits are most likely an artifact of experimental parameters rather than an intrinsic property of the cations with primary or secondary alkyl substituents.

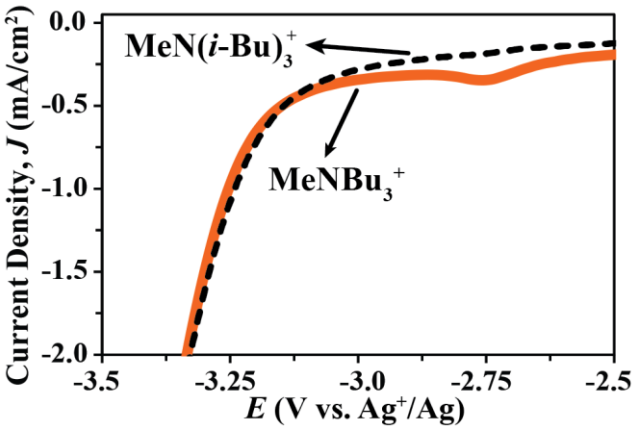

Figure 4. Effect of alkyl type. Linear sweep voltammograms of 300 mM $MeNBu_3I$ and $MeN(i\text{-}Bu)_3I$. Solvent, propylene carbonate; scan rate, 100 mV/s; Pt coil auxiliary electrode, GC working electrode, and Ag^+/Ag reference electrode.

3.3.3 Computational studies on the electrochemical stability of quaternary ammoniums

Computational calculations can help to provide a molecular understanding of the effect of electrolyte structure on electrochemical stabilities. The reduction and oxidation potentials are determined by the LUMO and HOMO, respectively.[1,133-135] For example, for a one-electron transfer (e is the electron charge, $\boldsymbol{\varepsilon}$ represents the energies of the HOMO or LUMO, and A and B are constants that are determined by the choice of the reference electrode, solvent, model details, etc.):[133-135]

$$(1) \qquad V_{Cathodic\ Limit} = A\frac{|\varepsilon_{LUMO}|}{e} + B$$

$$(2) \qquad V_{Anodic\ Limit} = A'\frac{|\varepsilon_{HOMO}|}{e} + B'$$

Based on Equations 1 and 2, a few models were suggested for the prediction of electrochemical windows of electrolytes (based on ab initio calculations, molecular

dynamics, and density functional theory).[133,134,136,137] Equations 1 and 2 imply that the LUMO and HOMO energy levels of molecules have a linear correlation with the corresponding standard reduction and oxidation potentials, respectively.

The LUMO energies of the cations shown in Scheme 1 were calculated using TD-DFT method and are listed in Table 2. A very poor linear correlation was found between the LUMO energy levels and the cathodic limits of quaternary ammoniums (compounds 3 to 16) (coefficient of determination, R^2, of 0.001; see Figure S1). This is not surprising because the cathodic limits of the quaternary ammoniums are all scattered over a small 100 mV window, with differences only in some cases beyond the experimental error. Another parameter to consider is that the measured cathodic limits are very close to but not identical to the thermodynamic standard reduction potentials shown in Equation 1.[41] Hence a linear correlation between the LUMO energy levels and the cathodic limits in such a small potential range is not expected.

When linear regression is performed over a wider potential range, i.e., including EMI^+ and $NPyBu^+$, which have much lower cathodic limits compared to the quaternary ammoniums (entries 1 and 2 in Table 1), a good linear correlation between the LUMO energy levels (obtained from TD-DFT) and the cathodic limits is obtained (see Figure 5). The range in the computationally predicted LUMO energy levels of the quaternary ammonium ions with different alkyl groups was approximately 0.2 eV. Using the linear approximation equation for the whole data set shown in Figure 5, the 0.2 eV range in the LUMO energy levels corresponds to a 150 mV range in the cathodic limits. This suggests that changing the chain length and type of branching of the saturated alkyl groups of quaternary ammonium ions results only in a minimal effect on the electronic environment of the positive nitrogen, as reflected in the LUMO energy levels.

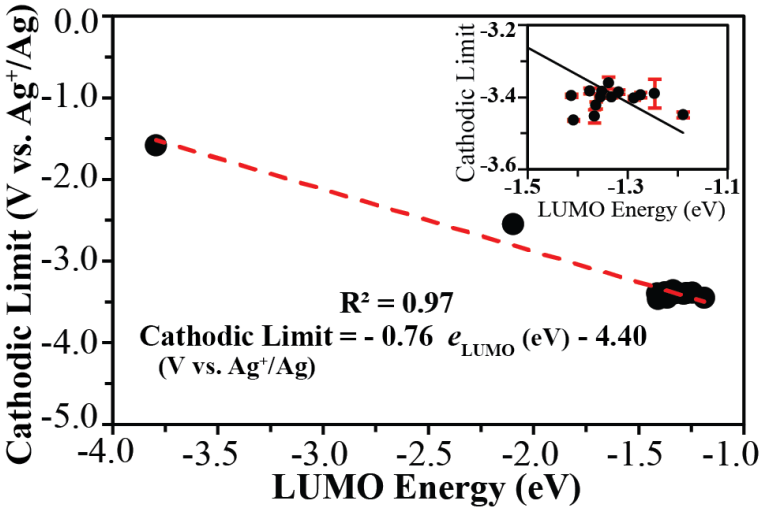

Figure 5. Correlation between the cathodic limits and LUMO energy levels. The cathodic limits obtained from the linear fit method are plotted vs. the LUMO energy levels obtained from the TD-DFT method. The dashed line shows the linear regression. The linear fit gives the cathodic limit (V vs. Ag^+/Ag) as $(0.76 \pm 0.037) \times e_{LUMO}$ (eV) – (4.40 ± 0.06). The inset shows a zoomed-in view of the quaternary ammonium ions only. Cathodic limits obtained for $J_{cut\text{-}off}$ of 0.5 and 1.0 mA/cm^2 had a similar linear correlation with the LUMO energy levels.

The empirically observed linear relationship between the LUMO energy levels and the cathodic limits can be used to predict the effect of other structural variations on the electrochemical stability of quaternary ammoniums. For example, our model predicts that incorporation of oxygen and aromatic groups in the alkyl substituents of quaternary ammonium ions may substantially decrease the electrochemical stability of $(CH_3CH_2OCH_2)_2NBu_2^+$ and $(PhCH_2)_2NBu_2^+$, with calculated LUMO energy levels of -2.79 and -2.40 eV, as compared to -1.36 V for NBu_4^+. This prediction agrees well with numerous experimental observations.[29,34,35,37,38,40]

Because of the minimal effect of the alkyl chain length on cathodic limits and the limited precision with which the cathodic limit can be quantified, the effect of the chain length on

the tunneling probability of electrons (from the Fermi level of the electrode to the LUMO) could not be investigated experimentally. A computational study of the structure of these ions could provide us with an estimate of the chain length contribution to the tunneling rate. Although longer chains are expected to introduce more hindrance to the system, in order to evaluate the donor-acceptor distances, the dynamics of these chains in the vicinity of electrodes would have to be considered as well. This could be done using molecular dynamics simulations that are beyond the scope of this study.

Table 2. The LUMO energy levels (eV) of the cations shown in Scheme 1.

Entry Number	Cation Structure	LUMO Energy
1	$NPyBu^+$	-3.794
2	EMI^+	-2.096
3	NEt_4^+	-1.287
4	NPr_4^+	-1.412
5	NBu_4^+	-1.363
6	$NPent_4^+$	-1.274
7	$NHex_4^+$	-1.189
8	$MeNBu_3^+$	-1.246
9	$EtNBu_3^+$	-1.351
10	$PrNBu_3^+$	-1.366
11	$MeNPr_3^+$	-1.338
12	$EtNPr_3^+$	-1.318
13	$BuNPr_3^+$	-1.408
14	$MeN(i\text{-}Bu)_3^+$	-1.375
15	$EtNMe(i\text{-}Pr)_2^+$	-1.354
16	$Et_2N(i\text{-}Pr)_2^+$	-1.332

3.4 Conclusions

The cathodic limits of quaternary ammonium cations with various alkyl substituents were measured using the conventional cut-off current density method at the cut-off current values of 0.1, 0.5, 1.0, and 5.0 mA/cm^2. Cathodic limits were also obtained by a recently proposed method that is less biased by electrolyte mass transport and provides more

reliable electrochemical stability limits. The new method is based on applying linear fits to the current–voltage polarization curve of the electrolyte at potentials below and above the onset of cathodic or anodic decompositions. It was shown that the chain length, type of branching, size, and steric hindrance of the saturated alkyl substituents have only a minimal effect on the electrochemical stability of quaternary ammonium cations. The LUMOs of cations were computed using time-dependent density functional theory with the IEFPCM model. This showed that the cathodic limits have a linear correlation with the LUMO energy level of the cation. Moreover, we showed that the structure of saturated aliphatic alkyl substituents has minimal effects on the electronic environment around the positive nitrogen center and the LUMO energy level of the quaternary ammonium cations, which correlates linearly with the experimental electrochemical limit. We suggest that the effect of chain length on the tunneling rate in propylene carbonate solutions, if any, does not affect the cathodic limit significantly and falls in the range of experimental errors, and therefore cannot be inferred from the experimental results.

3.5 Acknowledgments

This project was partially supported by Grant RL-0012-12 from the Initiative for Renewable Energy and the Environment of the University of Minnesota and a Graham N. Gleysteen Excellence Fellowship and a UMN Doctoral Dissertation Fellowship to M. P. S. M. We acknowledge Dr. Ana Vila Verde for informative discussions on molecular dynamics of our systems, and Dr. Aniko Nemes (Eötvös Loránd University) for her advice on the synthesis of the quaternary ammonium cations. S. K. acknowledges the scholarship from the International Max Planck Research School on Multiscale Bio-Systems.

3.6 Supporting Information

3.6.1 Computational Details

Optimized structures of ions were obtained with B3LYP/6-311++G(d,p) level of theory using the IEFPCM solvent model. Since solvent parameters for propylene carbonate are not available in Gaussian03 software, we used the static dielectric constant, EPS of 62.93,[138] the dynamic dielectric constant, EpsInf, of 2.02,[138] and the solvent radius, Rsolv, of 2.70 Å.[139] The molecular number density and molar volume of propylene carbonate are 0.007 $Å^{-3}$ and 85 $cm^3\ mol^{-1}$, respectively.[140] The united atom topological model UAHF[141] was used to build up the molecular cavities.

The LUMO energy values were estimated as the sum of the first excitation energy, obtained from the TD-DFT calculations, and the HOMO energy level, eq. S1.

$$\varepsilon_{LUMO} = \varepsilon_{HOMO} + \varepsilon_{Excitation\ energy} \qquad \text{(S1)}$$

In the time-dependent density functional theory (TD-DFT), a time-dependent perturbation (oscillating electric field) is applied to the ground state density and one-electron excitation energies are approximated as the linear response to the time dependent perturbation.[142]

3.6.2 Materials

All reagents were used as received without further purification unless otherwise noted. Anhydrous acetonitrile, anhydrous propylene carbonate, tetrabutylammonium iodide, tetrapropylammonium iodide, tetraethylammonium iodide, tetrapentylammonium iodide, tetrahexylammonium iodide, tributylamine, triisobutylamine, diisopropylethylamine, and tetrahexylammonium iodide were obtained from Sigma-Aldrich (St. Louis, MO). 1-Ethyl-3-methylimidazolium bis(trifluoromethylsulfonyl)imide (EMI TFSI) and *N*-butylpyridinium bis(trifluoromethylsulfonyl)imide (NPyBu TFSI) were purchased from

IoLiTec (Tuscaloosa, AL). Quaternary ammonium iodides were synthesized by reacting 1.0 equivalent of tributylamine, triisobutylamine, tripropylamine or diisopropylethyl amine with 1.5 equivalents of the appropriate alkyl iodide. The acetonitrile solution of the reactants was refluxed for 48 h at 80 ºC. The solid residue was filtered off and washed with diethyl ether and analysed by ^{1}H NMR spectroscopy (300 MHz, $CDCl_3$).

3.6.3 Correlation between the cathodic limits and LUMO energy levels

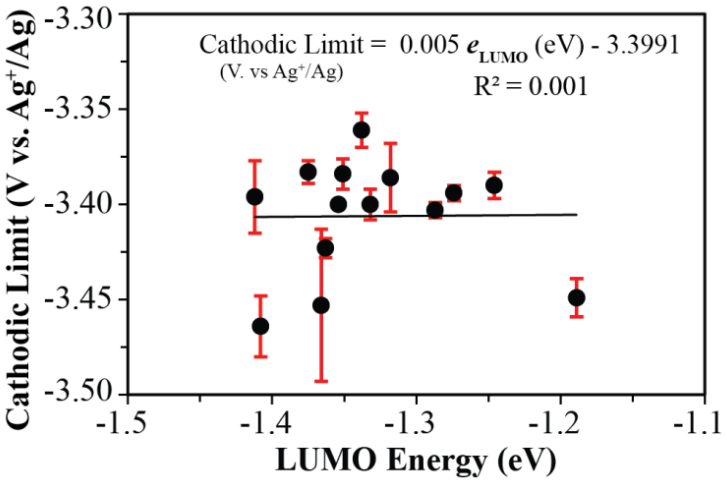

Figure S1. Correlation between the cathodic limits and LUMO energy levels of the quaternary ammonium ions only. The cathodic limits obtained from the linear fit method are plotted vs. the LUMO energy levels obtained from the TD-DFT method. The solid line shows the linear regression.

3.6.4 Statistical analysis of linear correlation

The results of the one-way ANOVA test for confirmation of linear correlation between the cathodic stability values and number of carbon atoms are as follows:

Linear fit method:

ANOVA

	df	*SS*	*MS*	*F*	*Significance F*
Regression	1	45.81	45.81	2.81	0.12
Residual	12	195.69	16.31		
Total	13	241.50			

0.5 mA/cm^2

ANOVA

	df	*SS*	*MS*	*F*	*Significance F*
Regression	1	0.01	0.01	2.79	0.12
Residual	12	0.06	0.00		
Total	13	0.07			

1.0 mA/cm^2

ANOVA

	df	*SS*	*MS*	*F*	*Significance F*
Regression	1	0.01	0.01	3.63	0.08
Residual	12	0.03	0.00		
Total	13	0.04			

4 CHAPTER FOUR

Ionic Liquids as Electrolytes for Electrochemical Double-Layer Capacitors: Structures that Optimize Specific Energy

Adapted from:

[†]Mousavi, M. P. S.; [†]Wilson, B.; Kashefolgheta, S.; Anderson, E.; Bühlmann, P.; He. S. and Stein, Ionic Liquids as Electrolytes for Electrochemical Double-Layer Capacitors: Structures that Optimize Specific Energy, accepted for publication in *ACS. App. Mater. Inter*. **2015.** ([†]equal contribution)

This work was a joint effort by this author and Benjamin Wilson (who carried out the synthesis of porous carbon films and double-layer capacitance measurements), Sadra Kashefolgheta (who carried out the calculation of ionic radia), Evan Anderson (who assisted with conductivity measurements), and Siyao He (who carried out the TEM imaging).

Key parameters that influence the specific energy of electrochemical double-layer capacitors (EDLCs) are the double-layer capacitance and the operating potential of the cell. The operating potential of the cell is generally limited by the electrochemical window of the electrolyte solution, that is, the range of applied voltages within which the electrolyte or solvent is not reduced or oxidized. Ionic liquids are of interest as electrolytes for EDLCs because they offer relatively wide potential windows. Here, we provide a systematic study of the influence of the physical properties of ionic liquid electrolytes on the electrochemical stability and electrochemical performance (double-layer capacitance, specific energy) of EDLCs that employ a mesoporous carbon model electrode with uniform, highly interconnected mesopores (3DOm carbon). Several ionic liquids with structurally diverse anions (tetrafluoroborate, trifluoromethanesulfonate, trifluoromethanesulfonimide) and cations (imidazolium, ammonium, pyridinium, piperidinium, and pyrrolidinium) were investigated. We show that the cation size has a significant effect on the electrolyte viscosity and conductivity, as well as the capacitance of EDLCs. Imidazolium- and pyridinium-based ionic liquids provide the highest cell capacitance, and ammonium-based ionic liquids offer potential windows much larger than imidazolium and pyridinium ionic liquids. Increasing the chain length of the alkyl substituents in 1-alkyl-3-methylimidazolium trifluoromethanesulfonimide does not widen the potential window of the ionic liquid. We identified the ionic liquids that maximize the specific energies of EDLCs through the combined effects of their potential windows and the double-layer capacitance. The highest specific energies are obtained with ionic liquid electrolytes that possess moderate electrochemical stability, small ionic volumes, low viscosity, and hence high conductivity, the best performing ionic liquid tested being 1-ethyl-3-methylimidazolium bis(trifluoromethylsulfonyl)imide.

4.1 Introduction

Electrochemical double-layer capacitors (EDLCs), or supercapacitors, are rechargeable energy storage devices with many applications in the transportation, consumer electronics, and communication sectors.[143-146] EDLCs are comprised of two high surface area electrodes separated by an electrolyte solution. Charge separation is achieved upon charging of the device, and the energy is stored by the double layer at the interface between the electrode and the electrolyte. Because the energy is stored by a reversible physical phenomenon at an interface rather than a chemical reaction within a bulk material, EDLCs have rapid charging and discharging rates, high specific power, and long lifespans of thousands to millions of cycles.[145] Due to these characteristics, there has been growing interest in EDLCs, and much research has been devoted to improving the performance and specific energy of these devices.[14,15,98,145,147]

The specific energy of an EDLC is proportional to the capacitance of the cell multiplied by the square of the operating potential; therefore, maximizing both the cell capacitance and the potential window of the device is crucial for engineering high-energy-density EDLCs.[15] The cell capacitance has been significantly improved by maximizing the accessible surface area of the electrodes through application of highly porous materials, primarily porous carbon, as the electrode materials. For example, a double-layer specific capacitance as high as 282 F/g has been achieved in nanocrystalline graphite.[90,147-149] Such a value is exceeded only when pseudocapacitive mechanisms are also active. The maximum accessible potential window of such devices is usually limited by electro-decomposition of the electrolyte or solvent, and these devices should not be charged beyond a voltage that can cause degradation of these components. Since electrolytes bear localized charges, they often have lower electrochemical stability than neutral solvent molecules. Therefore, the choice of electrolyte determines the potential window of EDLCs.[17]

Four primary classes of electrolyte solutions have been used in EDLCs: aqueous,[18] organic,[19] polymeric,[20] and ionic liquid (IL) electrolytes.[21] Among these, ILs have the largest potential windows, exceeding 5 V,[22] compared to aqueous and polymer electrolyte solutions, which typically are limited to 1 V, and organic electrolyte solutions (typically based on acetonitrile or cyclic carbonates such as propylene carbonate) that are limited to 3.5 V due to decomposition of the solvent.[18,19] Additionally, ILs typically have a high decomposition temperature, allowing for a wider range of applications where high temperatures (exceeding 100 °C) are expected.[23,24] Despite these advantages, there has not been a comprehensive and systematic study about the effect of IL structure on the performance of IL-based EDLCs, and the few reports found in the literature investigated only a small selection of ILs or studied ILs diluted in solvents, which affect the electrochemical properties of the ILs.[34,150-152]

The structure of an IL affects the double layer capacitance, *C*, and also the accessible potential window, *V*, of an EDLC, which both determine the specific energy of the device (proportional to CV^2).[15] A change in the structure of an IL that can increase the EDLC double-layer capacitance does not necessarily improve the electrochemical stability of the IL, and, therefore, it is critical to investigate the combined effects of double layer capacitance and electrochemical stability on the specific energy of a device. Unfortunately, most studies focused on either the double layer capacitance or the electrochemical stability.[20,21,98,151] For example, Sato et al. showed that at room temperature, an EDLC with *N*,*N*-diethyl-*N*-methyl-*N*-(2-methoxyethyl)ammonium tetrafluoroborate as the electrolyte has a wider potential window but lower discharge capacity than an EDLC with 1-ethyl-3-methylimidazolium tetrafluoroborate as the electrolyte.[98] Incrementing the chain length of alkyl substitutes was reported to enhance the electrochemical stability of *N*-alkyl-*N*-methylimidazolium bis(trifluoromethylsulfonyl)imide ionic liquids[153] and to enlarge the potential window of *N*-alkyl-*N*-methylpyrrolidinium bis(trifluoromethylsulfonyl)imide.[28] However, the same structural change (increasing the alkyl chain length) was reported to shrink the potential

window of *N*-alkyl-*N*-methylpyrrolidinium bis(trifluoromethylsulfonyl)imide.[152] Sedev et al. showed that the double layer capacitance (at 100 °C) of 1-alkyl-3-ethylimidazolium chloride at glassy carbon electrodes decreases when the alkyl chain length is increased.[154] Similarly, 1-ethyl-3-methylimidazolium tetrafluoroborate was shown to yield a larger double layer capacitance than 1-butyl-3-methylimidazolium tetrafluoroborate at room temperature[90] and tetraalkylammonium tetrafluoroborate (alkyl: ethyl, propyl, butyl, and hexyl) was shown to give a size-dependent double layer capacitance.[95] In contrast to all these studies that suggest an effect of the cation structure, Yuyama and co-workers showed that the double layer capacitance of a quaternary ammonium salt with a methoxyalkyl group on the nitrogen atom depends more on the nature of the anion rather than on the cation structure.[150] Clearly, comparisons made between only a few ionic liquids do not allow for the determination of meaningful trends.

Moreover, the double layer capacitance of a given IL is strongly affected by the choice of electrode material.[102,155-157] In addition, the criterion used for quantification of electrochemical stability strongly influences the reported IL potential window.[17,24,41] Because of the diverse range of electrode materials and potential window quantification criteria, a direct comparison between many reports in the literature is not feasible. For meaningful comparisons, it is necessary to study the effect of the IL structure on the specific energy of EDLCs made of the same electrode materials and characterized with the same potential window quantification method. In this work, the electrochemical stabilities of several room-temperature ionic liquids with common types of core structures of the cation and anion and various alkyl substituents in the cation were investigated. Using three-dimensionally ordered mesoporous (3DOm) carbon electrodes as a model system because of the uniformity and high degree of interconnectedness of their mesopores,[91] we studied the effect of the IL structure on the double layer capacitance of EDCLs, allowing us to determine IL characteristics that yield EDLCs with optimum energy densities.

4.2 Experimental

All materials were used without further purification. Material vendors, and experimental procedures for conductivity and viscosity measurements are mentioned in the Supporting Information. The electrode material used for the fabrication of the EDLCs, i.e., three-dimensionally ordered mesoporous (3DOm) carbon, was prepared following a published procedure (see the Supporting Information for the description of the synthesis).[158]

4.2.1 Electrochemical Measurements

Linear sweep voltammograms were measured with a CHI600C Potentiostat (CH Instruments, Austin, TX), a three-electrode cell with a 3.0 mm-diameter glassy carbon (GC) disk working electrode (BAS, West Lafayette, IN), a 0.25 mm Pt wire coil (99.998%, Alfa Aesar, Ward Hill, MA) auxiliary electrode, and a Ag^+/Ag reference electrode, at a scan rate of 100 mV/s. The reference electrode was prepared as reported previously.[10] Briefly, a glass tube equipped with a Vycor glass plug was filled with an acetonitrile solution containing 10.0 mM $AgNO_3$ and 100 mM NBu_4ClO_4, and an Ag wire was inserted into the tube. All the potentials reported in this work are with respect to 10 mM Ag^+/Ag. For the observation of the cathodic and anodic decomposition currents, the potential was scanned from 0 to -5 V and from 0 to +4 V (vs. Ag^+/Ag), respectively. The working electrode was polished on Microcloth polishing pads using 5.0 μm Micropolish II deagglomerated alumina (both from Buehler; Lake Bluff, IL) and rinsed thoroughly, first with deionized water and then with ethanol, followed by drying under a stream of argon. Prior to measurements, all ionic liquids were purged with argon for 15 min while stirring vigorously to remove dissolved oxygen. All measurements were performed in pure ionic liquids, and solvents were not used for diluting the ILs. Statistical analyses were based on a two-tailed *t*-test at the significance level of 0.95.

4.2.2 Calculation of Ion Volumes

The structures of the ions were optimized with the B3LYP[121,122,131,159,160] density functional at the 6-311++G(d,p) level. Frequency calculations were performed at the same level of theory to ensure that all ions were in a minimum energy conformation. All calculations were made using the Gaussian 03 package.[131] Van der Waals volumes were obtained as superpositions of van der Waals spheres of atoms with Multiwfn software using the Monte Carlo method.[161]

4.2.3 Cell Preparation and Galvanostatic Tests

Electrodes were prepared by grinding the 3DOm carbon powder with a binder (19:1:10 carbon:PTFE:water) until a homogenous paste was formed, as previously described.[91] The paste was rolled into self-supporting films using a mechanical roller, cut into 8 mm diameter circles, and dried overnight at 110 °C under vacuum to obtain final dried masses of 1.8–2.0 mg per electrode and thicknesses of approximately 150 μm. Electrochemical cells were assembled by wetting two electrodes of similar mass with the desired ionic liquid electrolyte and held under vacuum for 1 h, followed by the removal of excess electrolyte. The wetted electrodes were layered between steel current collectors in a two-electrode configuration, separated by a porous polypropylene membrane within a cell body that was previously described.[91] All cell assembly was performed in a dry room maintained below 100 ppm H_2O to minimize contamination.

Galvanostatic tests were performed on an Arbin BT2000 electrochemical station. To measure the capacitance, various rates were used, followed by 1000 cycles to determine cell stability. All cells were cycled between 0 and 2.0 V vs. the open circuit potential to maintain a constant potential window for all electrolytes well within the decomposition limits for any of the selected ionic liquids. The specific capacity of the 3DOm carbon was calculated using eq. 1, assuming that the contribution from each electrode is identical in the symmetric cell,

$$C_{material} = \frac{4I \cdot \delta t}{m \cdot \delta V} \quad (1)$$

where I is the discharge current, δt is the discharge time, m is the total mass of carbon in the cell, and δV is the cell discharge voltage.

4.3 Results and Discussion

The structures of the cations and anions of the ILs investigated in this work are shown in Figure 1. This selection covers the main categories of cations (pyridinium, imidazolium, pyrrolidinium, piperidinium, and ammonium) and anions (bistrifluoromethanesulfonylimide, tetrafluoroborate, and trifluoromethanesulfonate) that are used in room-temperature ionic liquids. The alkyl substituents of these cations can be readily modified to alter the electrochemical properties of the ions.[24,25,28] Therefore, in addition to the core cation structures, we also studied ILs with different alkyl substituents. Only saturated hydrocarbon groups were considered as alkyl substituents in this work because non-saturated or oxygenated alkyl groups were shown in prior work to lower the electrochemical stability of the cations without improving their contribution to the double-layer capacitance.[29,34,35,37,38,40] In this section, we will first discuss the electrochemical behavior and stability of these ILs and then follow with an analysis of the double-layer capacitance and specific energy of EDLCs incorporating these ILs.

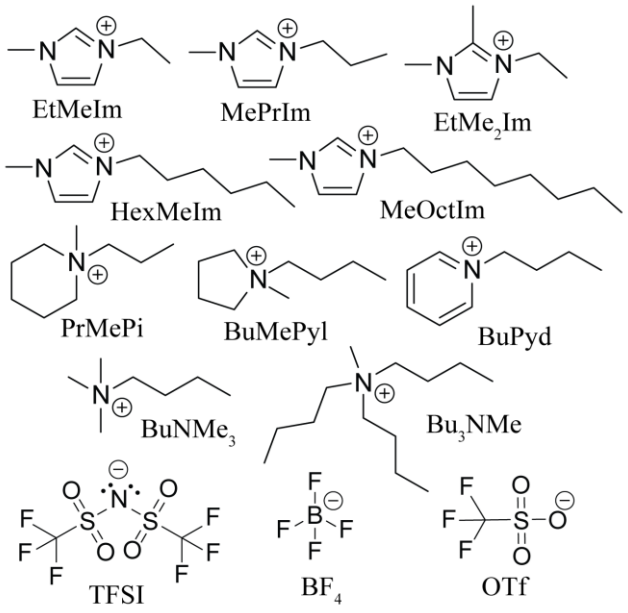

Figure 1. Structures and abbreviations of the cations and anions investigated in this study.

4.3.1 Electrochemical Stability of ILs

In order to reduce complications introduced by very large capacitive currents,[41] electrochemical stability measurements were performed with glassy carbon working electrodes and not the 3DOm carbon electrodes used in the fabrication and characterization of the EDLCs. The selection of electrode material can slightly affect the determined potential window of ILs, but the trends in the electrochemical stability of different ILs using different carbon-based electrodes are very similar.[17,41] Glassy carbon is a non-porous electrode material with a small surface area, commonly used in electrochemical stability measurements. Its use minimizes the capacitive currents during the voltage sweep.[41] Electrochemical stability limits determined at the surface of glassy carbon and various porous carbon electrodes were shown to be similar.[41] Therefore, the potential windows determined with this type of electrode provide useful insight into the inherent electrochemical stability of ILs and the accessible potential window for EDLCs comprising IL-infused mesoporous carbon electrodes.

4.3.1.1 Methods for Quantifying the IL Potential Window

The electrochemical stability of electrolyte solutions and ionic liquids can be quantified by measuring a current–voltage polarization curve, starting at potentials in which small current densities are observed, with no significant electrochemical reactions, followed by increasing or decreasing the potential to obtain large current densities caused by oxidation or reduction of the electrolyte, solvent, or ionic liquid.[6] The voltage at which a specific current density, *J*, is reached, is commonly defined as the cathodic or anodic electrochemical limit.[6] The biggest disadvantage of this approach is that the selection of the cut-off current density, $J_{cut\text{-}off}$, is arbitrary, and widely varying $J_{cut\text{-}off}$ values from 0.1 to 5.0 mA/cm^2 have been used in the literature.[24-41] As an example, the cathodic decomposition of the ionic liquid EtMeIm TFSI is shown in Figure 2A, and the potentials at which $J_{cut\text{-}off}$ values of 0.5 or 1.0 mA/cm^2 are reached are labeled with dashed lines. Evidently, the selection of the value of $J_{cut\text{-}off}$ affects the cathodic limit for EtMeIm TFSI as determined with this method. In many cases, the value of the electrochemical limit of a given electrolyte may vary as a result of the chosen $J_{cut\text{-}off}$ by as much as 0.9 V.[24,41] Therefore, IL potential windows from different studies with different $J_{cut\text{-}off}$ values cannot be compared directly to each other. This limitation motivated us to conduct an analysis of potential windows of a large list of ILs using the same assessment criteria. Here, we report cathodic and anodic stability limits for 0.5 and 1.0 mA/cm^2, which are the most common $J_{cut\text{-}off}$ values used in the literature (see Table 1). Stability limits at the less common $J_{cut\text{-}off}$ values of 0.1 and 5 mA/cm^2 are provided in the Supporting Information (see Table S1).

Figure 2B shows that the cathodic decomposition of EtMeIm TFSI is characterized by a current-voltage curve that is linear before and after the onset of reduction (see the inset for changes in the slope of the current-voltage curve). We recently reported on the same type of linear relationship observed as the result of electro-decomposition of various electrolyte solutions and showed that the potential at which the onset of reduction or oxidation occurs is determined by the inherent electrochemical stability of the

electrolyte.[17,41] The slope of the current-voltage curve after the onset of oxidation or reduction is affected by diffusion coefficients and the concentration of the electrolyte.[41] We showed that using the $J_{\text{cut-off}}$ criterion, different potential windows are obtained for a given electrolyte at different concentrations. Therefore, the electrochemical stability limits obtained with the $J_{\text{cut-off}}$ method are not representative of the inherent electrochemical stability of the electrolyte and are biased by electrolyte mass transport as well as the selection of the value for $J_{\text{cut-off}}$.[17,41] We recommended instead that linear fits be performed of the current–voltage curve before and after the onset of reduction or oxidation, and that the electrochemical stability limit be defined by the potential at which the two linear fits intersect, as illustrated in Figure 2B.[17,41] This linear fit method was shown to provide electrochemical stability limits that are less biased by experimental conditions such as the scan rate, electrolyte concentration, and diffusion rate and are more representative of the thermodynamic properties of the electrolyte.[17,41] Hence, in this work, we used the linear fit method as the primary assessment criterion for quantifying electrochemical stabilities of ILs. However, we also provide stability limits determined with the conventional $J_{\text{cut-off}}$ method to facilitate the comparison of our results to prior reports. The cathodic and anodic stabilities of ILs are summarized in Table 1 and Figure 3.

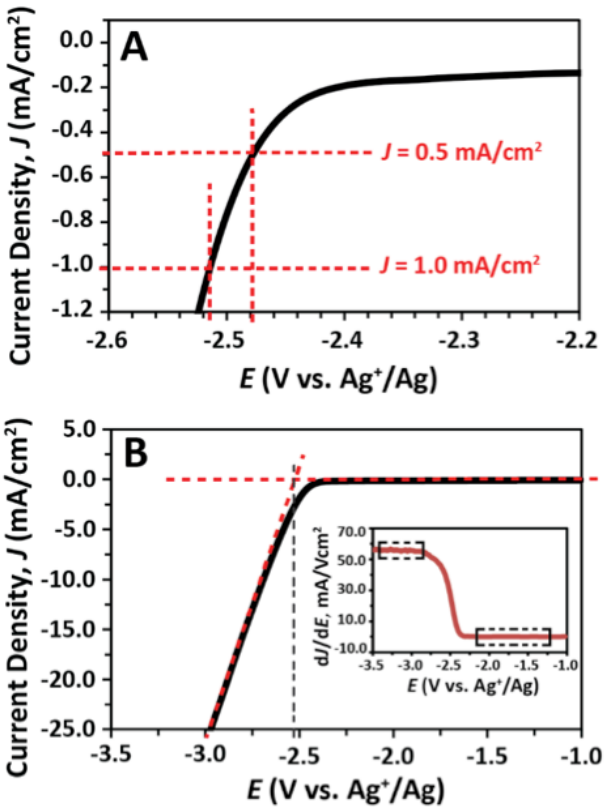

Figure 2. Determination of the electrochemical stability limits of ILs. (A) and (B) show the linear sweep voltammograms of EtMeIm TFSI. In (A), $J_{\text{cut-off}}$ values of 0.5 and 1.0 mA/cm^2 are shown. The dashed lines in panel (B) are linear fits before and after the onset of the reduction of EtMeIm TFSI; the vertical line highlights the potential at which the two fits intersect.

Table 1. Electrochemical Stability of Room Temperature ILs (V vs. Ag^+/Ag)

	cathodic stability			anodic stability		
	0.5 mA/cm^2	1.0 mA/cm^2	linear fit	0.5 mA/cm^2	1.0 mA/cm^2	linear fit
EtMeIm BF_4	-2.121 ± 0.192	-2.413 ± 0.042	-2.601 ± 0.012	1.115 ± 0.161	1.787 ± 0.130	1.994 ± 0.005
EtMeIm OTf	-2.273 ± 0.012	-2.487 ± 0.012	-2.598 ± 0.009	1.073 ± 0.283	1.517 ± 0.169	1.940 ± 0.013
EtMeIm TFSI	-2.381 ± 0.054	-2.469 ± 0.015	-2.555 ± 0.015	1.755 ± 0.042	1.969 ± 0.033	2.150 ± 0.004
MePrIm TFSI	-2.401 ± 0.073	-2.481 ± 0.008	-2.529 ± 0.009	2.045 ± 0.030	2.151 ± 0.005	2.191 ± 0.007
HexMeIm TFSI	-2.511 ± 0.010	-2.579 ± 0.008	-2.561 ± 0.011	2.097 ± 0.032	2.225 ± 0.011	2.171 ± 0.013
MeOctIm TFSI	-2.535 ± 0.006	-2.631 ± 0.008	-2.546 ± 0.004	2.119 ± 0.016	2.291 ± 0.010	2.143 ± 0.002
$EtMe_2Im$ TFSI	-2.691 ± 0.005	-2.745 ± 0.006	-2.736 ± 0.007	1.963 ± 0.008	2.027 ± 0.008	1.990 ± 0.002
Bu_3NMe TFSI	-3.639 ± 0.049	-3.939 ± 0.048	-3.494 ± 0.048	2.747 ± 0.064	4.073 ± 0.613	2.580 ± 0.033
$BuNMe_3$ TFSI	-3.033 ± 0.033	-3.313 ± 0.013	-3.368 ± 0.019	2.267 ± 0.127	2.573 ± 0.023	1.982 ± 0.088
BuMePyl TFSI	-3.179 ± 0.031	-3.309 ± 0.014	-3.358 ± 0.019	2.225 ± 0.083	2.497 ± 0.033	2.356 ± 0.030
PrMePi TFSI	-3.259 ± 0.021	-3.395 ± 0.009	-3.344 ± 0.012	2.361 ± 0.114	2.617 ± 0.013	2.340 ± 0.029
BuPyd TFSI	-1.379 ± 0.103	-1.473 ± 0.012	-1.441 ± 0.040	2.239 ± 0.134	2.543 ± 0.023	2.425 ± 0.015

Glassy carbon as working electrode, scan rate 100 mV/s.

4.3.1.2 Effect of Anion Type on Potential Window

The potential windows of ILs comprised of the same cation, EtMeIm, but three different anions, i.e., OTf, BF_4, and TFSI, are shown in Figure 3. The following trend for anodic stability can be observed:

EtMeIm OTf < EtMeIm BF_4 < EtMeIm TFSI

Figure 4 shows current–voltage curves exhibiting anodic decomposition of these ILs, confirming the onsets of oxidation consistent with the trend mentioned above. While the anodic limit of EtMeIm TFSI is approximately 200 mV larger than that of EtMeIm OTf (see Table 1 for values), the anion type seems to have only slight effects on the cathodic stability of these ILs. The cathodic limits of EtMeIm OTf and EtMeIm BF_4 do not differ statistically from one another at the 95% confidence interval, and are approximately 40 mV lower (more negative) than for EtMeIm TFSI.

4.3.1.3 Effect of the Cation Type on Potential Window

In Figure 3, the potential windows of ILs comprising pyridinium, saturated quaternary ammonium, and imidazolium cations are highlighted in purple, blue, and orange, respectively. Clearly, the type of cation has a major effect on the ILs' cathodic stabilities and potential windows. Saturated cations with quaternary ammonium substituents generally provide the highest cathodic stabilities, whereas ILs with aromatic cations are less stable towards reduction. The cathodic stability of the cations is determined by the energy level of their LUMO orbitals,[95,133,162] and aromatic cations generally have lower LUMO energy levels, which makes them more susceptible to reduction. A recent study showed the order of the LUMO energy levels of these cations to be in the order of butylpyridinium < ethylmethylimidazolium < tributylmethylammonium,[163] which agrees well with their experimentally observed cathodic stabilities.

Figure 3 shows that type of the cation also affects the anodic limit. ILs with different cations and with TFSI as their anion show anodic limits in a range of +1.990 to +2.580 V (vs. Ag^+/Ag), with ILs based on quaternary ammonium and pyridinium ions having higher anodic stabilities. Consistent with our observations, Tatsumi et al. reported that among several electrolytes with $C_2F_5BF_3^-$ as the anion, electrolytes comprising quaternary ammonium cations had higher stabilites towards oxidation than those with the EtMeIm cation.[38] They suggested that in ammonium electrolytes, the reduction limit is determined by the cation, and the oxidation limit is controlled by the anion. In contrast, in imidazolium salts, both the reduction and oxidation limit are determined by the cation since reduction of EtMeIm occurs before the $C_2F_5BF_3^-$ anion.[35,38,164] This finding was supported by calculations of the density of states of ILs, which showed that in MePrPyl BF_4, the HOMO of the anion has a higher energy than the HOMO of the cation, while in BuMeIm BF_4, the HOMO of the cation has a higher energy than the HOMO of the anion (oxidation occurs at the HOMO with the higher energy level).[133] While this report gave examples of cations limiting the oxidation of ILs, it does not always have to be the cation that is oxidized. For example, calculations by the same authors suggested that two ILs with the same anion (i.e., BuMeIm TFSI and MePrPyl TFSI) have different anodic stabilities, even though their HOMOs are dominated by anion states.[133] An explanation for significant cation effects on the anodic limit of an IL may be that different degrees of ion stabilization resulted from differences in the extent and type of ion pairing in these ILs.[165-167]

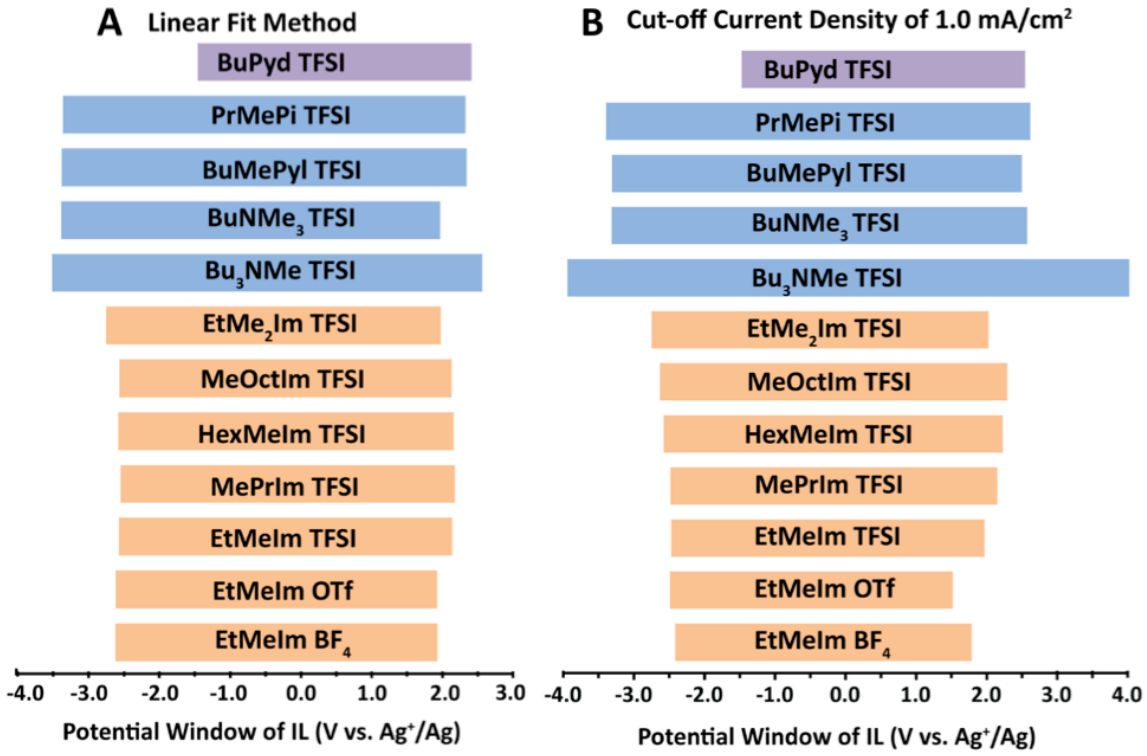

Figure 3. The solid bars represent the potential window in which the ILs are stable. The lower and higher ends of each bar indicate the cathodic and anodic limits of the IL, respectively. Both limits were measured with the linear fit method for panel A, and with the $J_{\text{cut-off}}$ value of 1.0 mA/cm^2 for panel B. Error bars are not shown because their values were too small to be readily visually recognizable.

4.3.1.4 Effect of Alkyl Substituents on Potential Windows of Imidazolium-Based ILs

Because there have been numerous reports that increasing the chain length of aliphatic substituents in organic cations improves their stability towards reduction,[28,37,39,152,153] we studied a series of *N*-alkyl-*N*-methyl imidazolium TFSI ILs, increasing the chain length of the alkyl group from ethyl to octyl. In addition to the length of the alkyl chains, we also investigated the effect of the number of alkyl substituents on the imidazolium ring.

Interestingly, increasing the alkyl chain length in *N*-alkyl-*N*-methyl imidazolium TFSIs resulted in a systematic increase in the width of the potential windows as determined by the cut-off current density of 1.0 mA/cm^2 (see Figure 2B), and no significant change in the potential windows as determined with the linear fit method (see Figure 2A).

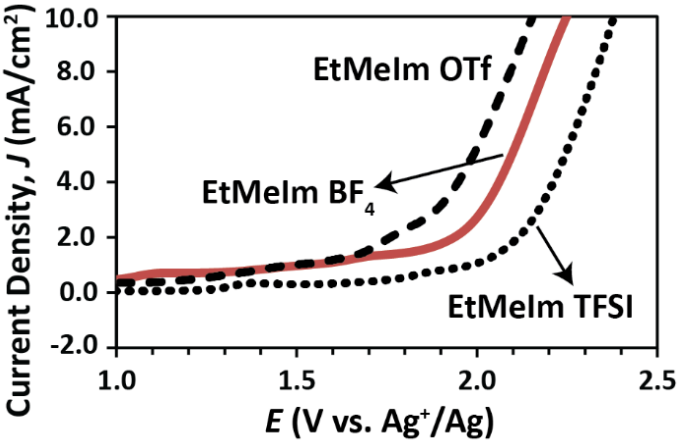

Figure 4. Linear sweep voltammograms of EtMeIm OTf, EtMeIm BF_4, and EtMeIm TFSI.

Figure 5A shows similar onsets of reduction, yet decreasing slopes in the current density vs. voltage plot for EtMeIm, MePrIm, HexMeIm, and MeOctIm TFSI (the changes in the slope of *J* vs. *E* are better visualized in Figure 5B). The same behavior is observed for anodic decompositions of these ILs (see Figure 5C). The onsets of cathodic and anodic decomposition are determined by thermodynamic properties of the electrolyte,[41] suggesting that EtMeIm, MePrIm, HexMeIm, and MeOctIm have similar electrochemical stability. The slopes of the current–voltage curves after the onset of reduction or oxidation are determined by mass transport of ions in the solution, i.e., they depend on the ion diffusion coefficients and concentration (smaller *J* vs. *E* slopes are observed for smaller diffusion coefficients and lower concentrations).[41] To confirm different ion transport rates in EtMeIm, MePrIm, HexMeIm, and MeOctIm TFSI, we measured the conductivity and viscosity values of these ILs (shown in Table 2). Increasing the size of

the cation causes a significant increase in the viscosity of the IL and also a decrease in the IL conductivity, which is consistent with a lower ion transport rate and a lower *J* vs. *E* slope, agreeing well with observed slopes as shown in Figure 5. While EtMeIm, MePrIm, HexMeIm, and MeOctIm TFSI have similar electrochemical stabilities, the cut-off current density method is biased by ion transport rates and misleads by suggesting larger potential windows for ILs with larger viscosities and lower conductivities.

Attachment of an additional alkyl substituents in the C2 position of the imidazolium ring results in a significant improvement in the cathodic stability of the ILs. Figure 5 shows an improvement of approximately 200 mV in the onset of reduction of $EtMe_2Im$ TFSI as compared to EtMeIm TFSI. This is an important finding, suggesting that modifying the substituents on the aromatic ring can have a more substantial effect on the electrochemical stability of the aromatic organic cations than altering the length of the aliphatic alkyl group attached directly to the ring nitrogen. Since the effect of electron withdrawing substituents on the stability of aromatic rings are well known, this finding appears to be consistent with a thermodynamic explanation of the reduction limit, as opposed to the effect of chain length effects, which would be rather suggestive of kinetic limitations. Given that the degradation of 1,3-dialkylimidazolium cations was reported to be influenced by the acidic proton in the C2 position,[24,168] replacing this proton with an alkyl group seems consistent with an improvement in the stability of the imidazolium cation. Indeed, 1,2,3-trialkylimidazolium cations were reported to have higher deprotonation energies than 1,3-dialkylimidazolium cations.[24,169] While the cathodic stability of $EtMe_2Im$ TFSI was improved in comparison to EtMeIm TFSI, the anodic stability of this IL was lower, resulting in similar potential windows for the two ILs.

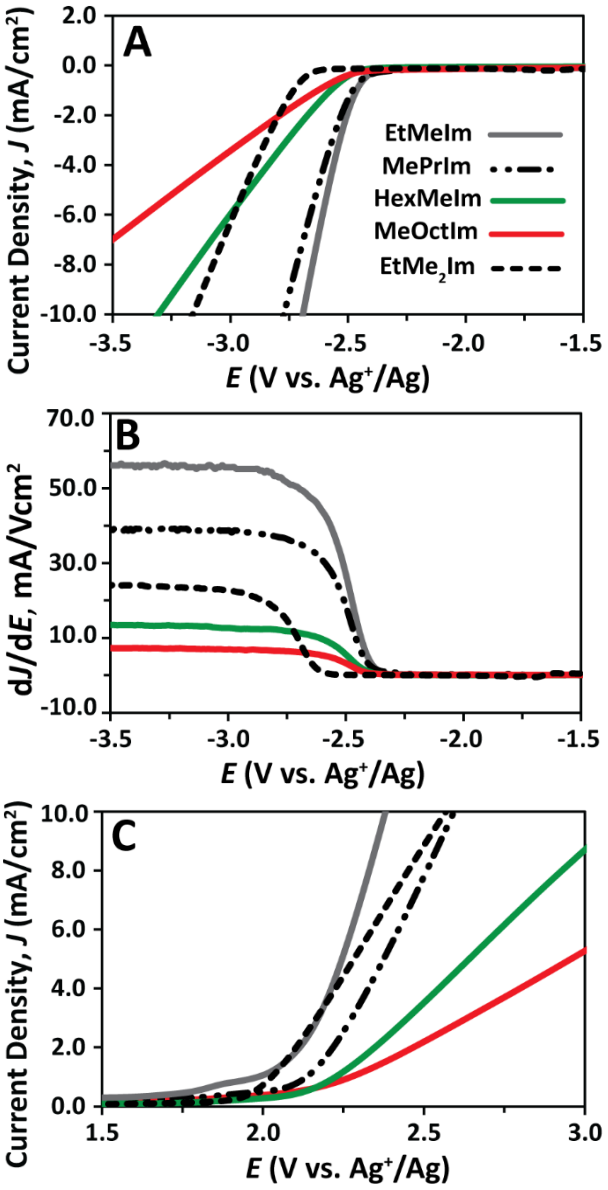

Figure 5. Effect of alkyl substituents on electrochemical stability of imidazolium based ILs. Linear sweep voltammograms of EtMeIm TFSI, MePrIm TFSI, HexMeIm TFSI, MeOctIm TFSI, and $EtMe_2Im$ TFSI are shown in Panels A (cathodic decomposition) and C (anodic decomposition). The d*J*/d*E* curves corresponding to panel A are shown in panel B.

4.3.1.5 Quaternary Ammonium-Based ILs

Figure 6 compares the cathodic stability of ILs with saturated quaternary ammonium ions. Bu_3NMe TFSI shows higher stability towards reduction (≈150 mV, as determined with the linear fit method) than $BuNMe_3$ TFSI. However, this single observation should not lead to the conclusion that larger alkyl substituents generally improve electrochemical stability of cations. Indeed, in the previous section, it was shown that larger alkyl substituents did not have a significant effect on the electrochemical stability of dialkylimidazolium-based ILs. It is noticeable that the slope of the current–voltage curve after the onset of reduction for Bu_3NMe TFSI is much lower than that for $BuNMe_3$ TFSI. This is not surprising, given that the conductivity of Bu_3NMe TFSI is significantly lower than that of $BuNMe_3$ TFSI (see Table 2), resulting in a much lower mass transport rate. The anodic stability of Bu_3NMe TFSI is also much higher (≈500 mV, as determined with the linear fit method) than that of $BuNMe_3$ TFSI. It should be noted that because of the high viscosity and low conductivity of Bu_3NMe TFSI, the cut-off current density method suggests an unrealistically high electrochemical stability and overly wide potential window (≈8 V) for this IL. There have been multiple reports that increasing the size of quaternary ammonium cations improves their electrochemical stability towards reduction.[28,37,152] While this stipulation is correct for the pair of Bu_3NMe TFSI and $BuNMe_3$ TFSI, increasing the cation size does not always result in an improvement of cathodic stability. For example, BuMePyl and PrMePi have larger sizes than $BuNMe_3$ (see Table 2 for ion sizes), yet, there is no significant difference between the cathodic stabilities of BuMePyl TFSI, PrMePi TFSI, and $BuNMe_3$ TFSI (see Figure 5 to compare the onsets of reduction for these ILs).

Several studies suggested that quaternary ammonium ions with cyclic structures (e.g., pyrrolidinium and piperidinium) have better cathodic stabilities than their non-cyclic counter parts.[24,170,171] This conclusion was drawn from the comparison of a limited set of cyclic and non-cyclic quaternary ammonium ions using the cut-off current density method for quantification of the electrochemical stability (values that are biased, e.g., by

electrolyte mass transport and concentration). Our results show that the two cyclic ammonium cations BuMePyl and PrMePi have lower cathodic stabilities than the non-cyclic Bu_3NMe, questioning the validity of the hypothesis that cyclic structures generally result in increased electrochemical stability. Any attempts to establish a general effect of cyclic structures of quaternary ammonium ions on electrochemical stabilities should consider the effects of electrolyte mass transport on the inherent electrochemical stability of the cation.

In summary, the following trends were observed for potential windows of the ILs studied in this work: Bu_3NMe TFSI > BuMePyl TFSI ~ PrMePi TFSI > $BuNMe_3$ TFSI > EtMeIm TFSI ~ MePrIm TFSI ~ HexMeIm TFSI ~ MeOctIm TFSI ~ $EtMe_2Im$ TFSI > EtMeIm BF_4 > EtMeIm OTf > BuPyd TFSI.

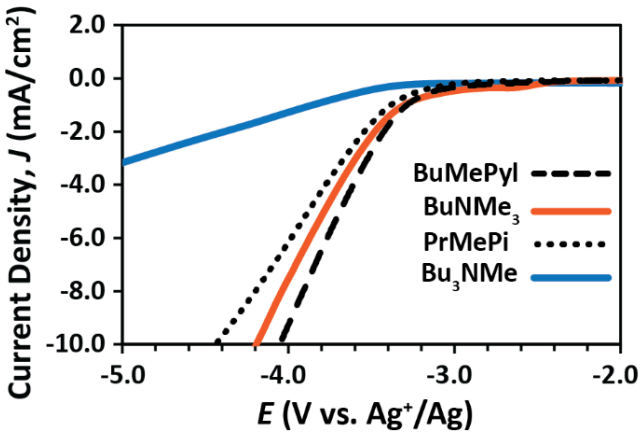

Figure 6. Linear sweep voltammograms of BuMePyl TFSI, $BuNMe_3$ TFSI, PrMePi TFSI, and Bu_3NMe TFSI.

4.3.2 Electrochemical Capacitance

4.3.2.1 3DOm Carbon Electrodes

For practical EDLCs, a critical parameter is the capacitance achieved with an IL electrolyte. To test the capacitance achieved with the various ILs, we utilized three-dimensionally ordered mesoporous (3DOm) carbon-based electrodes. 3DOm carbon was chosen as a model electrode material because it has a well-defined pore structure with highly-interconnected pores and large pore windows, allowing for complete infiltration with the tested ILs (except for EtMeIm BF_4) and ready access to the large surface area delivered by the mesopores. High specific capacitance was demonstrated using this system with both organic and ionic liquid electrolytes.[91,172] For this study, a large single batch of 3DOm carbon was prepared using as the template silica spheres of 38.4 ± 1.2 nm that were sedimented to form a close-packed array (Figure S2A). The final carbon product shows the characteristic 3DOm structure with well-defined pores and open windows (Figure S2B). Gas sorption analysis of the 3DOm carbon shows a type IV isotherm with a type H1 hysteresis, consistent with previously reported 3DOm carbon samples (Figure S3A). A total surface area of 1074 m^2/g was determined using a QSDFT model designed for mesoporous carbon samples.[173] The pore size distribution shows two major peaks, one at approximately 37 nm and one at 29 nm, corresponding to the pore diameter and pore windows, respectively. Small-angle X-ray scattering shows two well-defined peaks and a shoulder that can be indexed to a face-centered cubic structure with a d_{111} spacing of 30.5 nm (Figure S3B).

4.3.2.2 Method for Quantifying the Specific Capacitance

The specific capacitance achievable with the various ionic liquids was measured in a symmetric, two-electrode cell employing the 3DOm carbon electrodes. The cells were charged and discharged at increasing current densities from 0.1 A/g to 20 A/g, followed by 1000 cycles at 1.0 A/g to determine the rate capabilities as well as capacitance

retention (Figure 7). For most specific capacitance comparisons, the average value of the final 1000 cycles was used.

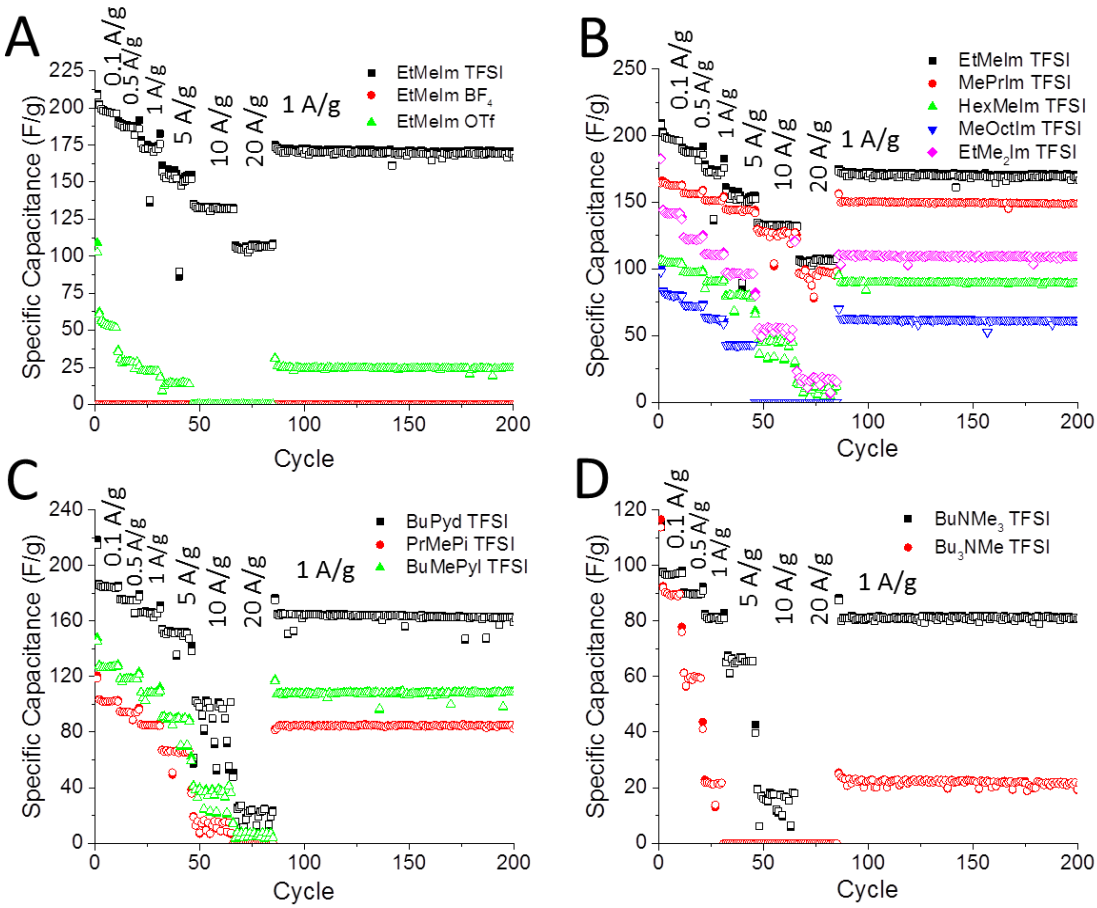

Figure 7. Specific capacitance values at various rates for 3DOm carbon electrodes using the IL electrolytes listed in the legends. Comparisons of (A) anion effects, (B) alkyl chain length effects, (C) cations with cyclic cores, and (D) cation volume effects.

Table 2. Physical Properties of the Ionic Liquid Electrolytes Studied in this Work

	cation volume (nm^3)	anion volume (nm^3)	viscosity (mPa·s)	conductivity (S/m)	potential window (V)	specific capacitance (F/g @1 A/g)	specific energy ($0.5\ CV^2$, J/g)
EtMeIm BF_4	0.118	0.049	27.9	1.44	4.595 ± 0.016	0	0
EtMeIm OTf	0.118	0.082	24.9	0.88	4.538 ± 0.016	24	246
EtMeIm TFSI	0.118	0.151	24.1	0.96	4.705 ± 0.015	160	1771
MePrIm TFSI	0.134	0.151	32.6	0.53	4.720 ± 0.011	148	1649
HexMeIm TFSI	0.185	0.151	57.5	0.22	4.732 ± 0.017	89	995
MeOctIm TFSI	0.219	0.151	79.5	0.13	4.689 ± 0.004	60	654
$EtMe_2Im$ TFSI	0.134	0.151	74.1	0.26	4.726 ± 0.007	101	1128
Bu_3NMe TFSI	0.245	0.151	481	0.03	6.074 ± 0.058	21	384
$BuNMe_3$ TFSI	0.144	0.151	80.0	0.22	5.350 ± 0.090	81	1158
BuMePyl TFSI	0.167	0.151	53.0	0.30	5.714 ± 0.035	108	1763
PrMePi TFSI	0.183	0.151	110	0.17	5.684 ± 0.032	85	1373
BuPyd TFSI	0.149	0.151	52.6	0.33	3.866 ± 0.043	156	1166

4.3.2.3 Effect of Anion Type on Specific Capacitance

For the three anions tested (using the ILs EtMeIm TFSI, EtMeIm OTf, and EtMeBF_4), there was little correlation between the anion type, specific capacitance, and any of the other variables tested. This is likely a result of different wetting behaviors of the three ionic liquids. EtMeIm TFSI, the IL with the highest specific capacitance, wets the electrode quickly with no observable beading on the surface. EtMeIm BF_4, on the other hand, forms a bead on the surface of the electrode that did not appear to wet the surface at all and, therefore, did not penetrate the mesopores. EtMeIm OTf spread out on the surface of the electrode, but more slowly than EtMeIm TFSI, indicating less favorable wetting behavior for that anion. The wetting behavior is a function of the type of carbon used for the electrode. In the present case, the carbon precursor, a phenol–formaldehyde-based resol, introduces oxygen functional groups, such as ketones, phenols, and carboxylic acids into the porous electrode and increases the polarity of the surface.[174] Similarly, oxygen groups are present in activated carbons, making these more hydrophilic. When used with more hydrophobic carbon electrodes, the less polar BF_4 and OTf-based ionic liquids may be able to provide higher specific capacitance values because they would wet the nonpolar electrode surface better and increase the interfacial contact area between the electrolyte and the electrode surface. Our observations show the importance of system-specific determination of electrolytes, especially with regards to the wetting behavior of the ionic liquid into the porous electrode. Because the ionic liquid with TFSI as the anion was most suitable for the model carbon system in this study, ionic liquids containing this anion were employed to determine the effects of different cations on electrochemical properties.

4.3.2.4 Effect of Cation Type on Specific Capacitance

To evaluate the effects of the cation type, ILs with different structures of the cation core but similar cationic volumes were compared. Specifically, BuPyd TFSI, $BuNMe_3$ TFSI, and MePrIm TFSI were compared because all have cationic volumes between 0.13 and 0.15 nm^3. In this set, the pyridinium-based IL electrolyte yields the highest specific capacitance at low to moderate current densities. The imidazolium-based cations provide slightly lower specific capacitance values and the ammonium-based cations the lowest values. The high performance of the BuPyd TFSI electrolyte, however, is reduced at higher current densities, for which the specific capacitance drops to 21 F/g at 20 A/g while MePrIm TFSI maintains 102 F/g at the same rate. This is likely due to the higher viscosity and lower conductivity of BuPyd, limiting the capacitance at the higher rates. The larger size appears to restrain charge carrier transport within the electrode pores, probably both due to the lower conductivity experienced in larger pores and due to wall interactions within the smaller pores. As a result, the formation of the electronic double layer requires a longer period of time, limiting the capacitance at higher rates.

4.3.2.5 Effect of Alkyl Substituents on Specific Capacitance of Imidazolium-Based ILs

To compare the effect of alkyl substituents on the specific capacitance of imidazolium-based cations, the chain length of the alkyl group in alkylmethylimidazolium cations was varied from two to eight carbon atoms (Figure 1). In this series, the specific capacitance decreases monotonically with increasing carbon chain length. Besides being related to increasing viscosity and decreasing conductivity of the IL, the decrease in specific capacitance can be explained by the smaller number of ions that can be accommodated in the double layer when the ion volume is increased. However, when comparing two electrolytes with different numbers of alkyl substituents but identical cation volume, i.e., $EtMe_2Im$ TFSI and MePrIm TFSI, the much higher specific capacitance for MePrIm TFSI is mainly explained by its lower viscosity, which results in higher conductivity.

These effects are most pronounced at the higher current densities (Figure 6B) so that the specific capacitance of $EtMe_2Im$ TFSI drops much more significantly as the current density is increased.

4.3.2.6 Effect of Alkyl Substituents on the Specific Capacitance of Quaternary Ammonium-Based ILs

To measure the effect of the alkyl substituents on quaternary ammonium-based ILs with TFSI as anion, both cyclic (PrMePi and BuMePyl) and noncyclic ($BuNMe_3$ and Bu_3NMe) cations were examined. At moderate current densities, the cyclic ammonium-based cations yield higher specific capacitances, even though they have larger ionic volumes and, in the case of PrMePi TFSI, lower conductivity than $BuNMe_3$ TFSI. This would indicate that the projection of these cyclic cations onto the electrode surface gives a smaller area, allowing a higher concentration of ions in the double layer. Within the set of cyclic and noncyclic cations, the trend of larger ions giving lower specific capacitance is maintained. Additionally, Bu_3NMe TFSI, which has the lowest conductivity of any of the ILs tested with the TFSI anion, shows the greatest drop in capacitance with increasing current density. It is unable to cycle at even 5 A/g even though it has a similar capacitance at low current densities as $BuNMe_3$ TFSI.

In summary, the ionic volume of the cations has the greatest effect on the maximum specific capacitance of the IL in a porous electrode, provided the electrolyte is able to fully wet the electrode pores. As the current density increases, the conductivity of the electrolytes limits the performance of the cell because of reduced mass transport within the pores during cycling. Therefore, based on specific capacitance, EtMeIm TFSI has the best overall performance as an IL electrolyte, which can be explained by its small ionic volume, low viscosity, and hence relatively high conductivity.

4.3.3 Specific Energy

As discussed above, the structures of cations and anions making up an IL affect the electrochemical stability and potential window of the IL, as well as the double layer capacitance of EDLCs in which the IL is used as an electrolyte. The specific energy of EDLCs is determined by both the specific capacitance and potential window of the IL electrolytes ($0.5\ CV^2$). We showed that while ILs based on a quaternary ammonium cation offer wider potential windows than imidazolium based ILs, and yield much lower specific capacitance values in EDLCs. It is therefore important to balance both of these properties to identify the ILs that offer optimized energy densities. The maximum achievable energy densities were calculated from the potential window of the IL (determined with the linear fit method) and the specific capacitance (cycled at 1 A/g and from 0 to 2 V vs. open circuit potential) and are presented in Table 2. The following trend can be observed for the energy densities: EtMeIm TFSI ~ BuMePyl TFSI > MePrIm TFSI > PrMePi TFSI > BuPyd TFSI ~ $BuNMe_3$ TFSI > HexMeIm TFSI > MeOctIm TFSI > Bu_3NMe TFSI > EtMeIm OTf. It is interesting to note that Bu_3NMe TFSI, which offers an exceptionally wide potential window, yields one of the lowest energy densities and is a poor choice for EDLCs. In contrast, even though EtMeIm TFSI does not have the largest potential window, the combination of an intermediate potential window and high capacitance makes it an excellent electrolyte choice for EDLCs. We realize that changing between different carbon materials as the electrode may slightly affect the magnitudes of both the potential window and the specific capacitance, yet, the observed trends should still apply if the electrolyte wets the electrode surface sufficiently. Therefore, these findings can provide insight into choosing the best IL to achieve high energy densities in a desired application.

4.4 Conclusions

This work has provided a systematic comparison of twelve ionic liquids as potential electrolytes for EDLC cells, relating structural features to trends in electrochemical

properties. We showed that ILs based on quaternary ammonium cations and TFSI anion offer the widest potential windows. The ionic liquid Bu_3NMe TFSI offers an exceptionally wide potential window of 6 V. Increasing the length of the alkyl chain in 1,3-dialkyl-imidazolium TFSI ILs does not improve their stability towards reduction, yet, adding an alkyl group to the C2 position in the aromatic ring results in a significant improvement of cathodic stability. The highest capacitance was measured for EDLCs employing EtMeIm TFSI as an electrolyte, with an average specific capacitance of 162 mAh/g at 1 A/g during the final 1000 cycles. The specific capacitance and conductivity are both related to cation size and viscosity. The highest specific energy was achieved using EtMeIm TFSI and BuMePyl TFSI as electrolytes. On the basis of these results, high performance ionic liquid electrolytes benefit from small sizes and low viscosity while maintaining the right polarity of the IL ions to sufficiently wet the electrode used in an EDLC.

4.5 Acknowledgments

The authors would like to thank Professor William Smyrl for his invaluable discussions and contributions. This project was partially supported by a Graham N. Gleysteen Excellence Fellowship and a University of Minnesota Doctoral Dissertation Fellowship to M. P. S. M., and Grant RL-0012-12 from the Initiative for Renewable Energy and the Environment of the University of Minnesota. Portions of this work were carried out in the University of Minnesota Characterization Facility, which receives partial support from the NSF though the MRSEC, ERC, MRI, and NNIN programs.

4.6 Supporting Information

Experimental details (materials, conductivity and viscosity measurements, preparation of 3DOm carbon), characterization of 3DOm carbon, electrochemical stability aft various cut-off current densities.

4.6.1 Experimental

4.6.1.1 Materials

The ionic liquids butyltrimethylammonium (Me_3BuN) bistrifluorosulfonylimide (TFSI), tributylmethylammonium (Bu_3MeN) TFSI, 1-ethyl-3-methylimidazolium (EtMeIm or EMI) TFSI, 3-methyl-1-propylimidazolium (PrMeIm) TFSI, 1-hexyl-3-methylimidazolium (HexMeIm) TFSI, 3-methyl-1-octylimidazolium (OcMeIm) TFSI, 1-ethyl-2,3-dimethylimidazolium ($EtMe_2Im$) TFSI, *N*-methyl-*N*-propylpiperidinium (PrMePi) TFSI, *N*-butyl-*N*-methylpyrrolidinium (BuMePyl) TFSI, *N*-butylpyridinium (BuPyd) TFSI, EMI triflate, and EMI BF_4 all with a purity of 99% and a water content below 100 ppm were purchased from IoLiTec, phenol (>99%), formaldehyde (aqueous solution, 37 wt%), tetrahydrofuran, polytetrafluoroethylene (PTFE, 60 wt% in water), tetraethylorthosilicate (TEOS, 99%), L-lysine (98%), hydrochloric acid (37 wt%), potassium hydroxide, and sodium hydroxide were purchased from Sigma Aldrich, tetrahydrofuran (HPLC grade, >99.9%) and hydrofluoric acid (48–52 wt%) from Fisher Scientific. All chemicals were used without further purification. Water was deionized (DI) on site to a final resistivity of >18.0 MΩ·cm, using a Barnstead Sybron purification system.

4.6.1.2 Conductivity Measurements

Conductivity was measured using a custom-made conductivity cell, made of two temperature-controlled stainless steel plates and a Teflon spacer to hold the sample. The cell temperature was allowed to equilibrate at 25 °C for 15 min prior to measurements. Impedance measurements were carried out using a two-electrode cell with a Solartron 1255B frequency response analyzer and a SI 1287 electrochemical interface from Solartron (Farnborough, Hampshire, U.K.). The frequency range for these measurements was from 1 MHz to 1 Hz with a constant AC amplitude of 100 mV. Conductivities were calculated from resistances obtained by fitting of impedance spectra with ZView software (Scribner Associates, Southern Pines, NC) in the 500 to 1 kHz range. The cell constant

was measured using a 500 μS/cm^2 KCl conductivity standard. Each measurement was repeated five times.

4.6.1.3 Viscosity Measurements

Viscosity was measured on a TA Instruments AR G2 rheometer using parallel steel plates separated by 300 μm. The shear rate was increased logarithmically from 1 to 100 rad/s, then decreased at the same rate with 5 s equilibration and 5 s integration per point. The viscosity was determined by averaging data points during the decrease in shear rate; see Figure S1.

4.6.1.4 Preparation of Three-Dimensionally Ordered Mesoporous (3DOm) Carbon

Silica spheres were synthesized as previously described.[175] Briefly, a solution of L-lysine (70 mg) in water (70 g) was prepared in a 100 mL perfluoroalkoxy alkane round-bottom flask using a ¾ inch egg-shaped magnetic stir bar. While rapidly stirring, TEOS (5.4 g) was added dropwise and left to stir under ambient conditions for 1 h. This suspension was then heated in an oil bath at 90 °C while stirring at 500 rpm for 48 h under a condenser. TEOS (10.8 g) was again added dropwise in five equal portions, each 1 h apart, and the suspension was left for an additional 48 h. This was repeated once more for a total of 28 g of TEOS over the synthesis. The suspension was dried in a Petri dish at 70 °C overnight, then calcined at 550 °C for 6 h in air to remove residual organic components and form the colloidal crystal template. The final average silica sphere diameter was 38.4 ± 1.2 nm, determined by measuring over 300 separate spheres.

A phenol-formaldehyde (PF) resol was prepared according to an established method.[176] Briefly, phenol (61 g) was melted at 50 °C in a 500 mL glass round-bottom flask, followed by the addition of a 20 wt% aqueous NaOH solution (13.6 g). An aqueous formaldehyde solution (37 wt%, 200 mL) was added dropwise while stirring. The solution was heated to 70 °C and left for 1 h while stirring at 300 rpm with a Teflon-coated magnetic stir bar to increase the extent of polymerization. The product was

neutralized to pH ~7 using an aqueous HCl solution (0.6 M, ~30 mL). Water was removed through rotary evaporation at 40 °C, and the polymer was re-dispersed in THF to achieve a concentration of 50 wt%. After the NaCl precipitate was allowed to settle overnight, the solution was isolated by decanting. The resulting stock solution was stored in a refrigerator until use.

The 3DOm carbon was prepared following a literature procedure.[158] Briefly, the PF resol solution was vacuum infiltrated into the silica template (1:1 w:w) for 1 h at 40 °C, followed by cross-linking the resol at 120 °C for 24 h in a covered glass dish. The PF/silica composite was pyrolyzed under flowing nitrogen at 900 °C (1 °C/min ramp rate to 600 °C, then 5 °C/min to 900 °C). The silica template was removed through hydrothermal treatment in 6 M KOH for 48 h at 180 °C. The carbon product was isolated through vacuum filtration and washed repeatedly, then allowed to soak in DI water for 30 minutes, followed by additional washing until the pH of the effluent was ~7.

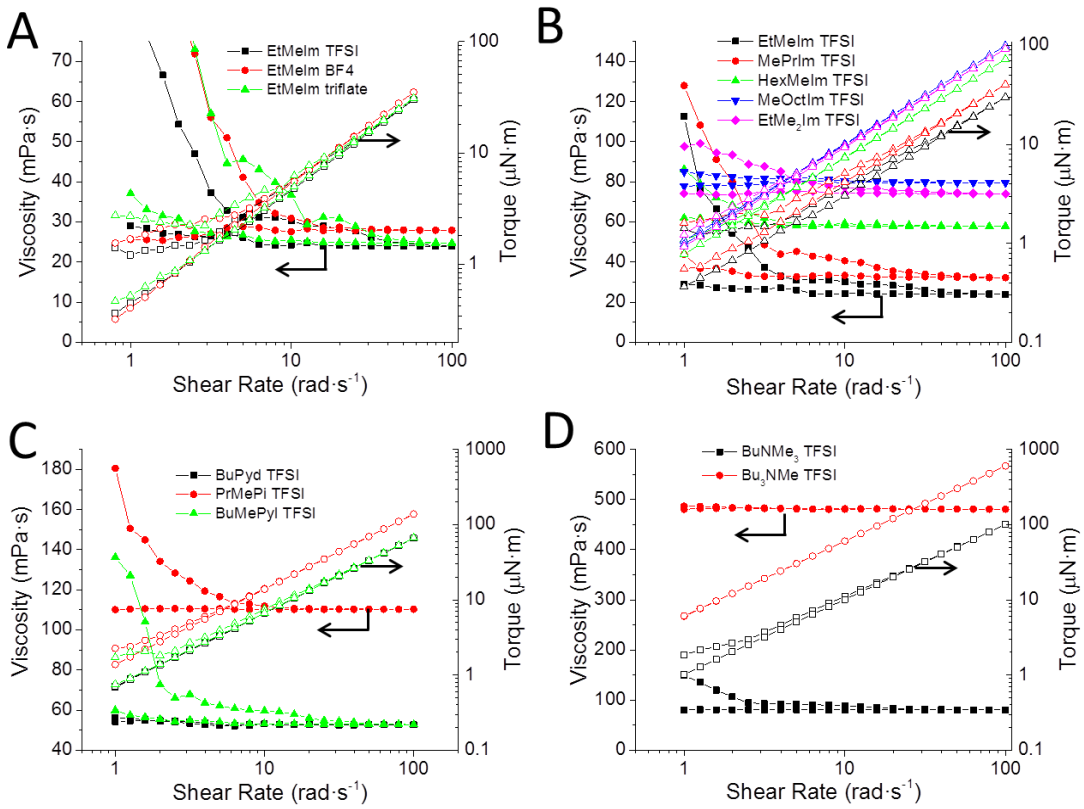

Figure S1. Viscosity and torque of ionic liquids sorted by (A) varied anions, (B) imidazolium-based cations, (C) nitrogen-containing cyclic cations, and (D) ammonium-based cations. The initial decrease in the measured viscosity with increasing shear rate is followed by level measurements as the shear rate was decreased again. This behavior is associated with shear ordering. The average of the data obtained during the shear rate decrease was used as the final reported number for viscosity.

4.6.1.5 3DOm Carbon Characterization

Transmission electron microscopy (TEM) images were obtained on an FEI Technai T12 microscope operated at 120 kV with a LaB_6 filament. Samples were prepared by suspending them in ethanol and bath sonicating for 15 min. Cu grids coated in Formvar

were dipped into the resulting suspension and dried. The TEM images of the templating spheres and the 3DOm C product are shown in Figure S2.

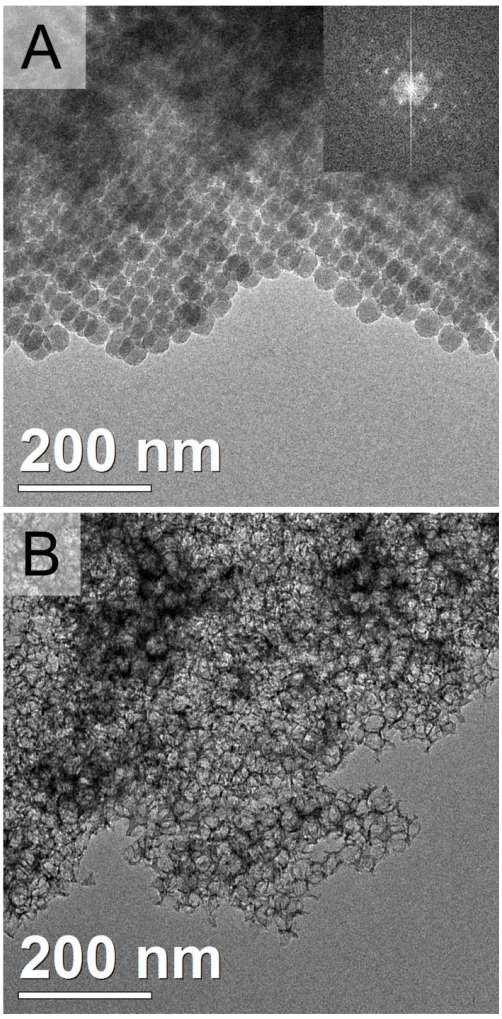

Figure S2. TEM images of (A) the silica colloidal crystal used as a template (FFT inset) and (B) the resulting 3DOm carbon used as an electrode material showing the open, interconnected pore structure.

Nitrogen sorption was performed using a Quantachrome Autosorb iQ instrument. 3DOm carbon samples were outgassed for 12 h at 200 °C prior to analysis. The total surface area and other pore characteristics were calculated using the quenched-solid-density-functional-theory (QSDFT) adsorption model optimized by Quantachrome for

mesoporous carbon materials with spherical pores. The 3DOm carbon material gives a type IV isotherm with a type H1 hysteresis (Figure S3A), typical for 3DOm and other mesoporous structures, indicating a well-formed bulk pore structure. A total surface area of 1074 m^2/g was measured. The pore size distribution plot showed two primary peaks (Figure S3A, inset), one at 37 nm and one at 29 nm. These values correspond to the observed sizes of the pores and the windows seen in the TEM images.

Small-angle X-ray scattering (SAXS) was used to determine the extent of pore ordering. The measurements were carried out on a Rigaku RU-200BVH 2D SAXS instrument operating with a pathlength of 183 cm using a 12 kW, rotating Cu anode and a Siemens Hi-Star multiwire area detector. In the SAXS pattern (Figure S3B), two clear peaks can be observed, at q = 0.21 and 0.36 nm^{-1}, along with a shoulder at q = 0.25, which index well to the expected face-centered cubic array of pores. Further, the d_{111} value is 30.5 nm, which would match an ideal pore array with diameters of 37.4 nm, consistent with the observed peak in the gas sorption pore size distribution.

4.6.2 Electrochemical Stability at $J_{cut\text{-}off}$ of 0.1 and 5.0 mA/cm^2

Electrochemical stability limits of ILs at the less common $J_{cut\text{-}off}$ values of 0.1 and 5 mA/cm^2 are provided in Table S1. The $J_{cut\text{-}off}$ value of 0.1 mA/cm^2 yielded unreasonably small potential windows for ILs and was not large enough to allow distinction of the redox peaks from the background current. This is evident from high standard deviations and poor data reproducibility at this $J_{cut\text{-}off}$ value.

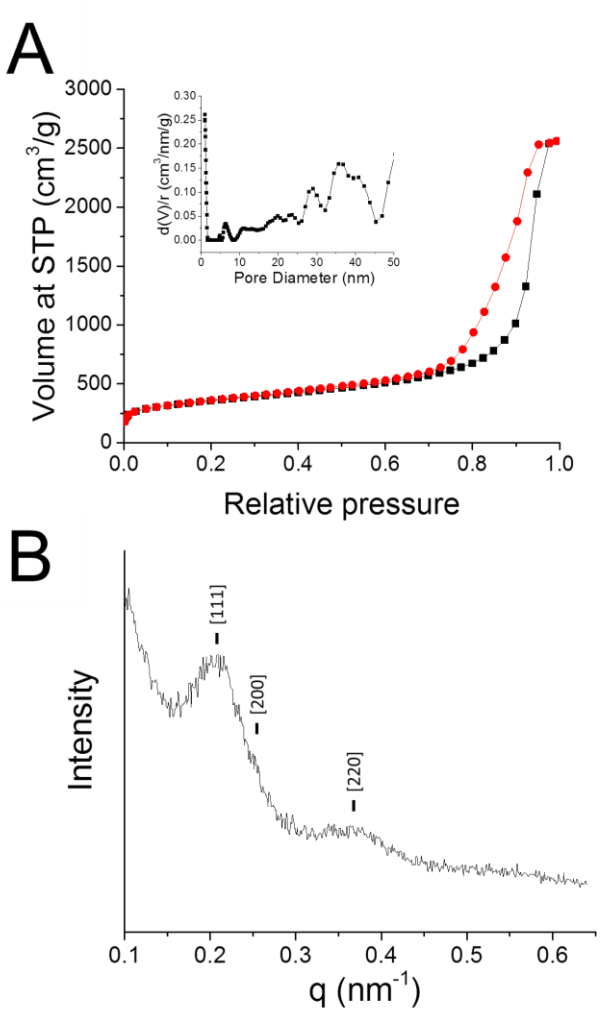

Figure S3. (A) Nitrogen sorption isotherm of the 3DOm carbon showing the characteristic type IV isotherms with type H1 hysteresis for mesoporous carbon and in the inset the QSDFT-modeled pore size distribution. (B) SAXS pattern for the 3DOm carbon.

Table S1. Electrochemical Stability of Room Temperature ILs (V vs. Ag^+/Ag)

	cathodic stability		anodic stability		potential window	
	0.1 mA/cm^2	5.0 mA/cm^2	0.1 mA/cm^2	5.0 mA/cm^2	0.1 mA/cm^2	5.0 mA/cm^2
EtMeIm BF_4	-1.663 ± 0.180	-2.599 ± 0.023	0.425 ± 0.011	2.100 ± 0.015	2.088 ± 0.180	4.699 ± 0.028
EtMeIm OTf	-1.547 ± 0.021	-2.665 ± 0.013	0.213 ± 0.551	1.903 ± 0.199	1.760 ± 0.551	4.568 ± 0.199
EtMeIm TFSI	-1.422 ± 0.190	-2.599 ± 0.015	1.225 ± 0.040	2.251 ± 0.017	2.647 ± 0.194	4.850 ± 0.023
MePrIm TFSI	-1.973 ± 0.148	-2.631 ± 0.005	1.393 ± 0.037	2.359 ± 0.010	3.366 ± 0.153	4.990 ± 0.011
HexMeIm TFSI	-2.068 ± 0.562	-2.917 ± 0.012	1.489 ± 0.192	2.649 ± 0.016	3.557 ± 0.594	5.566 ± 0.020
MeOctIm TFSI	-1.749 ± 0.270	-3.179 ± 0.029	1.493 ± 0.048	3.009 ± 0.037	3.242 ± 0.274	6.188 ± 0.047
$EtMe_2$Im TFSI	-2.513 ± 0.102	-2.975 ± 0.030	1.569 ± 0.070	2.291 ± 0.021	4.082 ± 0.124	5.266 ± 0.037
Bu_3NMe TFSI	-1.863 ± 0.048	-3.939 ± 0.126	1.589 ± 0.071	> 4.0*	3.452 ± 0.086	> 7.9*
$BuNMe_3$ TFSI	-2.335 ± 0.029	-3.783 ± 0.033	1.505 ± 0.096	3.241 ± 0.049	3.840 ± 0.100	7.024 ± 0.059
BuMePyl TFSI	-2.303 ± 0.612	-3.657 ± 0.026	1.527 ± 0.052	3.321 ± 0.122	3.830 ± 0.614	6.978 ± 0.125
PrMePi TFSI	-2.841 ± 0.609	-3.871 ± 0.026	1.571 ± 0.096	3.951 ± 0.128	4.412 ± 0.619	7.822 ± 0.131
BuPyd TFSI	-1.197 ± 0.156	-1.657 ± 0.044	1.499 ± 0.105	3.148 ± 0.060	2.696 ± 0.188	4.805 ± 0.074

* Current density not reached within the scanned potential window (0 to 4 V)

5 CHAPTER FIVE

Characterization of Silver Ion Dissolution from Silver Nanoparticles using Fluorous-phase Ion-selective Electrodes

Adapted from:

[†]Maurer-Jones, M. A.; [†]Mousavi, M. P. S.; Chen, L. D.; Buhlmann, P.; Haynes, C. L., Characterization of Silver Ion Dissolution from Silver Nanoparticles using Fluorous-phase Ion-selective Electrodes and Assessment of Resultant Toxicity to Shewanella oneidensis, *Chem. Sci.* **2013**, *4*, 2564. ([†]equal contribution)

This work was a joint effort by this author and Melissa Maurer-Jones (who carried out the nanoparticle synthesis and characterization and toxicity assesments), and Li Chen (who measured release of silver ions from silver nanoparticles in deionized water).

Silver nanoparticle (Ag NP) dissolution, or ionization from Ag(0) to Ag^+, is an important determinant of the nanoparticles' toxicity as silver ions are considered to be a major contributor to Ag NP cytotoxicity. In this work, we characterize ion dissolution from Ag NPs using a selective and dynamic technique, Ag^+-selective electrodes (ISEs) with ionophore-doped fluorous sensing membranes. We examined dissolution of various concentrations of Ag NPs (0.3, 3, and 15 μg/mL) in water and bacterial growth medium in real-time. A decrease in the concentration of free Ag^+ was observed as a result of complexation with components of the growth medium. Overall, a greater percentage of the nanoparticles dissolve in growth medium than water (28% vs 13%). Individual chemical components of the growth medium were examined for their complexation capability, and it was determined that ammonia–silver complexes are the predominant species of dissolved Ag^+, with 8.9% occurring as $AgNH_3^+$, 87.8% occurring as $Ag(NH_3)_2^+$, and only 3.3% occurring as free Ag^+. After characterizing Ag NP dissolution in growth medium, the viability and growth of *Shewanella oneidensis*, a ubiquitous beneficial bacterium, were monitored upon exposure to the known in situ levels of Ag^+ and Ag NPs. Ag^+ and Ag NPs both caused a dose-dependent decrease in bacterial viability and growth rate, though the growth and viability changes upon Ag NP exposure did not correlate with the ISE-measured Ag^+. Using ISEs to monitor Ag NP dissolution in the presence of *S. oneidensis* revealed that the presence of the organisms influences the nanoparticle dissolution profile, a result not previously reported that has significant implications for understanding nanotoxicity. This work lays the foundation for the use of fluorous-phase ISEs as an in situ nanoparticle characterization tool, addressing a critical technology gap in the field of nanoparticle toxicology.

5.1 Introduction

Dynamic characterization of nanoparticles is important within toxicity studies to understand how nanoparticle characteristics affect toxicity. Currently, there are a range of analytical tools employed to characterize nanoparticles at specific times in the toxicity assessment; yet, it is clear from the literature that nanoparticle characteristics readily change in complex environments (e.g., body or environment) due to their high surface reactivity, and these characteristics evolve over time.[177,178] Unfortunately, limited analytical tools exist for in situ nanoparticle characterization, impeding the fundamental understanding necessary to advance the field of nanotoxicology. One nanoparticle characteristic that is particularly important in nanotoxicology is dissolution of nanoparticles into toxic ions.

Silver nanoparticles (Ag NPs) are considered to be the most widely used nanoparticles in consumer products, with inclusion in various wound dressings, toys, and clothing.[179] Primarily used as an antimicrobial agent, global production was 280 tons in 2011 and is expected to increase to 1200 tons by 2015,[180], augmenting silver release into the environment further. The antimicrobial nature of Ag NPs is imparted primarily through the dissolution and ionization of Ag NPs (i.e., Ag(0)) to Ag^+,[181] which can be internalized by the bacterial capsule and bind proteins, enzymes and DNA, disrupting normal cell function and/or causing cell death.[182,183] Ag^+ can also cause pits on the bacterial cell wall that can lead to increased cell permeability and death.[184] Therefore, it is critical to understand the extent and kinetics of dissolution to Ag^+ to understand Ag NP toxicity.

Due to the role of ion release in nanotoxicity, many studies have characterized Ag NP dissolution. Atomic spectrometry/spectroscopy is commonly used for characterization, where the supernatants of nanoparticle suspensions are analyzed using mass (inductively coupled plasma mass spectrometry, ICP-MS), atomic emission, or atomic absorption of the atom of interest.[185-188] These techniques are highly selective and sensitive, with

picomolar detection limits. Another common method is to monitor the localized surface plasmon resonance of Ag NPs, where a decrease or shift in extinction correlates with dissolving nanoparticles, though this technique requires high concentrations of Ag NPs that are largely environmentally unrealistic.[189] Both of these techniques, however, only provide a snapshot of the ion content, failing to provide real-time, in situ assessment of the Ag^+ concentration. Another disadvantage to these techniques is that they are limited in their ability to differentiate between free and complexed Ag^+. It is well known that Ag^+ forms stable complexes with Lewis bases such as chloride, amines, and thiols, which are present in body fluids and cell culture media.[190] Complexation results in lowered activities of free Ag^+ and can alter the bioavailability and toxicity of Ag^+. For example, increased reaction of Ag^+ and Ag NPs with inorganic and organic sulfur compounds can decrease bioavailability and toxicity in a variety of organisms.[178,191,192] therefore, understanding the Ag species formed by Ag NP dissolution is also important.

Ion-selective electrodes (ISEs) provide inexpensive, continuous, sensitive, and selective measurements of Ag^+, which make them an appealing tool for studying the kinetics of Ag NP dissolution. Additionally, ISEs have the ability to quantitatively differentiate between free and complexed Ag^+, permitting a more accurate assessment of species contributing to Ag NP toxicity. There has been some literature precedent for use of commercially available solid state Ag_2S ISEs to study nanoparticle dissolution,[190,192] including an investigation of Ag^+ release in a cell culture in which five discrete measurements were recorded over a period of 24 h.[190] While the latter study confirmed complexation of Ag^+, biofouling[69,70,193] due to protein adsorption to Ag_2S severely limits long term measurements in typical biological samples.

Herein, we use fluorous-phase ionophore-doped ISEs for the continuous monitoring of dissolution of citrate-capped Ag NPs in water and bacterial growth media. Fluorous phases have extraordinarily low polarity and polarizability, and, as a result, many alkanes are not miscible with perfluoroalkanes, and many lipids have poor solubility in fluorous

phases.[79,194,195] These characteristics limit the nonspecific extraction of hydrophobic and electrically neutral species into fluorous phases,[53] and make ISEs based on fluorous sensing membranes less susceptible to biofouling.[193] In addition to lowering the susceptibility to biofouling, Ag^+ ionophore-doped ISEs offer exceptional Ag^+ selectivity,[196] which arises from the non-coordinating and poorly solvating properties of their fluorous sensing phases. The Ag^+ ionophore-doped fluorous-phase ISEs are a uniquely appropriate tool for continuous monitoring of Ag NP dissolution into water and complex bacterial growth media.

Using fluorous-phase ISEs, we measured the concentration of Ag^+ and correlated the results with the toxicity to the bacterium *Shewanella oneidensis* MR-1. *S. oneidensis* is a minimally pathogenic bacterium found in a wide range of geographical and ecological conditions and is notable for its role in geochemical nutrient cycling.[197] More specifically, it is a metal reducer and therefore, the likelihood of interaction between *S. oneidensis* and metal nanoparticles is high, making *S. oneidensis* a relevant model species to investigate Ag NP toxicity. Additionally, it has recently been suggested in other nanotoxicity studies that *S. oneidensis* makes a good environmental bacteria model.[198,199] By combining dissolution measurement with toxicity assessment, this study lays the foundation for the development of an in situ nanoparticle characterization and toxicity assessment tool that can be used for understanding both ecological, as demonstrated herein, and biological consequences of nanoparticle exposure.

5.2 Results and Discussion

5.2.1 Nanoparticle Characterization

Citrate-capped Ag NPs, synthesized in house according to Hackley and co-workers,[200] were chosen for the study of dissolution because citrate is one of the most widely used Ag NP capping agents. Careful characterization of the nanoparticles is important for understanding dissolution and toxicity results, and herein, Ag NPs were characterized with transmission electron microscopy (TEM), dynamic light scattering (DLS), ζ-

potential, and UV-visible spectroscopy. A summary of nanoparticle characteristics can be found in Table 1.

Table 1. Summary of Ag NP characteristics. Solution phase measurements performed in ferric citrate growth medium.

Characteristic	Value
Size (as determined by TEM)	11 ± 3 nm
Hydrodynamic diameter (DLS)	112 ± 6 nm
ζ-potential	-29 ± 3 mV
LSPR (λ_{max})	389 ± 1 nm

Fresh nanoparticles were synthesized for each experiment to ensure that the nanoparticles were similar for each ISE and toxicity assessment. To confirm consistency from synthesis to synthesis, triplicate syntheses were performed and size was characterized with TEM (Figure 1A). As can be seen in Figure 1B, the distribution of sizes is consistent between preparations, with an average diameter of 11 ± 3 nm, and this consistency was verified based on the nanoparticle-localized surface plasmon resonance (LSPR), as measured with UV-visible spectroscopy (Table 1). Further characterization of the nanoparticle stability over time was assessed using DLS in both water and ferric citrate bacterial growth medium, the medium used for the *S. oneidensis* toxicity studies. In both water and ferric citrate medium, there is an initial increase in the aggregate size over the first 6 h, with a plateau of aggregate size at longer times. However, ferric citrate medium causes larger Ag NP agglomerates to form, which agrees with the correlation of increased ionic strength—as in the growth medium—with greater agglomeration/aggregation of the Ag NPs, as established in the literature.[201]

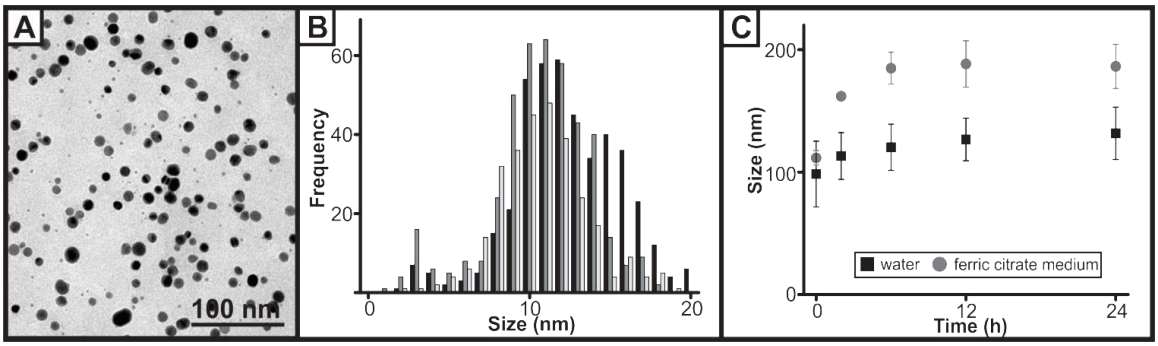

Figure 1. Nanoparticle characterization. (A) TEM images of Ag NPs (B) Histogram of Ag NP sizes, as measured with ImageJ (NIH, Washington DC) from TEM images collected from 3 separate syntheses (n=296, 422, and 433) (C) hydrodynamic diameter of 3 µg/mL Ag NP in deionized water and ferric citrate growth medium.

5.2.2 Characterization of Dissolution with Fluorous-phase ISEs in Water

Ag^+ dissolution kinetics were first monitored in deionized water. After calibration and equilibration, Ag NPs were added to water, and the resulting suspensions were monitored over 24 h. A typical electrode response observed in these experiments is shown in Figure 2A (for dissolution of 3.0 µg/mL Ag NPs). The measured potential was converted to concentration of free Ag^+ (Figure 2C) using a calibration curve (Figure 2B). The concentrations of Ag NPs and Ag^+ are reported here with different units (µg/mL or M, respectively) so as to use the most commonly utilized description of concentration in the literature for each speices.

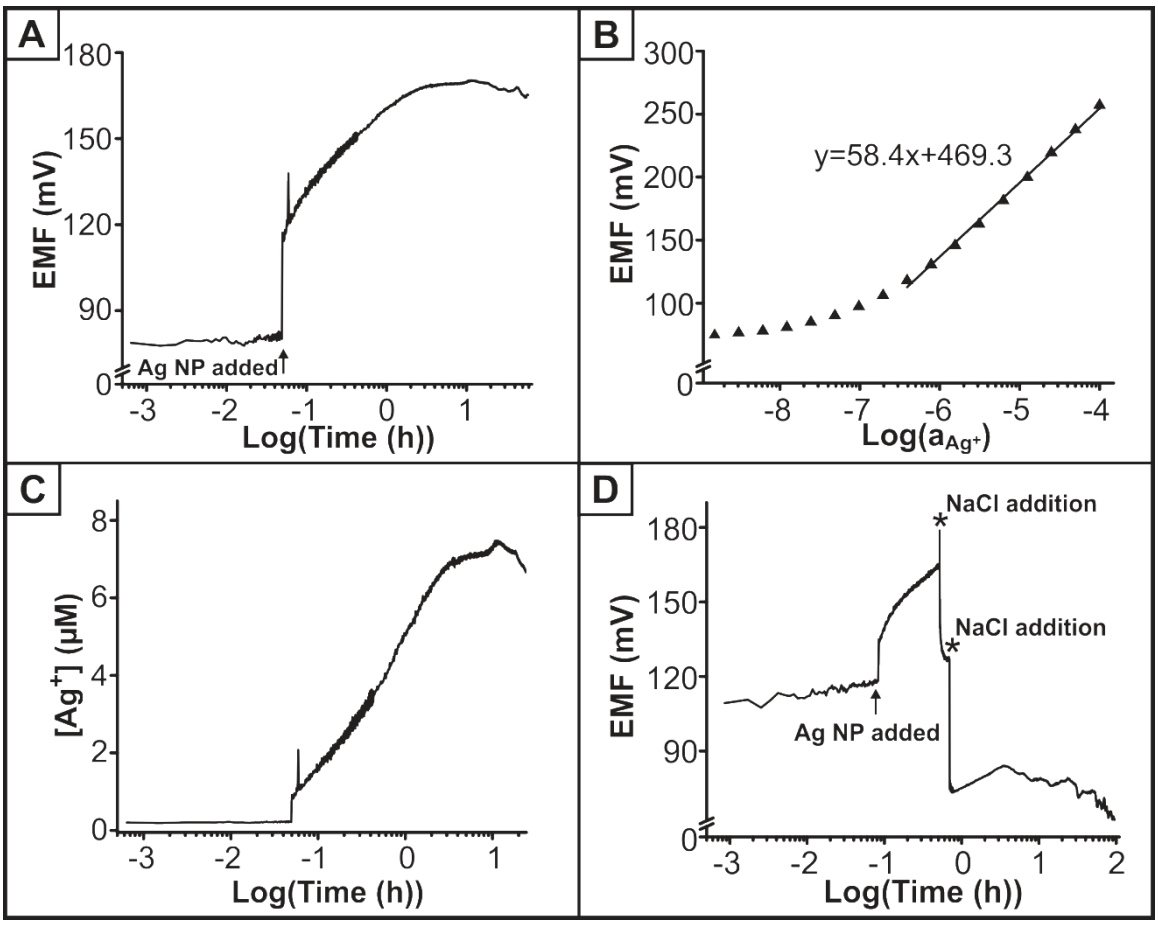

Figure 2. Characterization of Ag NP dissolution in deionized water with fluorous-phase ISEs. (A) Typical response of an electrode to Ag^+ upon addition of 3 μg/mL Ag NP (arrow) (B) a representative calibration curve. (C) Concentration of Ag^+ over time as converted from the calibration curve in B. (D) Response of electrode after addition of 3 μg/mL Ag NP (arrow) followed by two additions of 1 M NaCl (asterisks), where a drop in the EMF is the result of Cl^- binding to free Ag^+.

To corroborate that the initial quick change in EMF observed upon addition of the Ag NPs into the water (Figure 2A) was due to an increase in the Ag^+ concentration and to confirm that the electrode response time was fast enough to capture this immediate burst, dissolution was also monitored for 30 min from 3 μg/mL Ag NPs in water, after which aliquots of 1.0 M NaCl were added (Figure 2D). After each addition of NaCl, the

potential dropped instantaneously, indicating that there is a decrease in free Ag^+ as the result of Cl^- binding to Ag^+ and AgCl precipitation. Since the ISE is responding quickly to the changes in concentration of free Ag^+, it can be concluded that the fluorous-phase ISEs have a very fast response time and that the initial burst upon addition of Ag NPs is the result of free Ag^+ due to Ag NP dissolution. Additionally, the reaction of Cl^- with Ag^+ emphasizes the importance of choosing an appropriate bacterial growth medium. Many growth media are chloride rich, which affects the free Ag^+ concentration. In this study, the chloride content of the ferric citrate bacterial growth medium was consequently minimized to avoid influencing the dissolution of the Ag NPs.

Nanoparticle dissolution in deionized water was quantified for 3 different Ag NP concentrations: 0.3, 3, and 15 μg/mL (Figure 3). The concentrations of Ag NPs released into the environment through wastewater effluent as predicted by exposure models ranges between 0.01-18 μg/mL;[202,203] therefore, these concentrations represent a relevant range of released engineered nanoparticles into the environment. For all nanoparticle concentrations, a similar behavior was observed, as seen in Figure 2, where an initial burst of Ag^+ is observed, followed by a steady increase in free Ag^+ with an eventual plateau in concentration over time. It appears that the plateau concentration is achieved faster for lower concentrations. This burst behavior and concentration response have been observed previously in other dissolution studies.[186,204] At 0 h, i.e., immediately after addition of the washed Ag NPs to deionized water, the suspensions with 3 and 15 μg/mL NPs have a similar concentration of free Ag^+, while the 0.3 μg/mL solution exhibits a lower concentration. This may be an indication of an equilibrium concentration of free Ag^+ present in the suspensions containing high nanoparticle concentrations.

In parallel experiments, nanoparticle dissolution was monitored with ICP-MS by analyzing the supernatant for Ag at discrete time points throughout the 24 h dissolution experiment (Figure 3, symbols). In comparing the ICP-MS results to the ISE responses shown in Figure 3, the ICP-MS results demonstrate a similar kinetic pattern in dissolution

(i.e., initial burst followed by a later plateau); yet, there are some significant differences ($p<0.05$, students pair-wise t-test) between the ISE and ICP results. Because these experiments were run in parallel and samples were not taken of the same solution, these discrepancies are likely the result of varied oxygenation of the samples, which influences the rate of dissolution (with higher oxygen content increasing nanoparticle dissolution).[204]

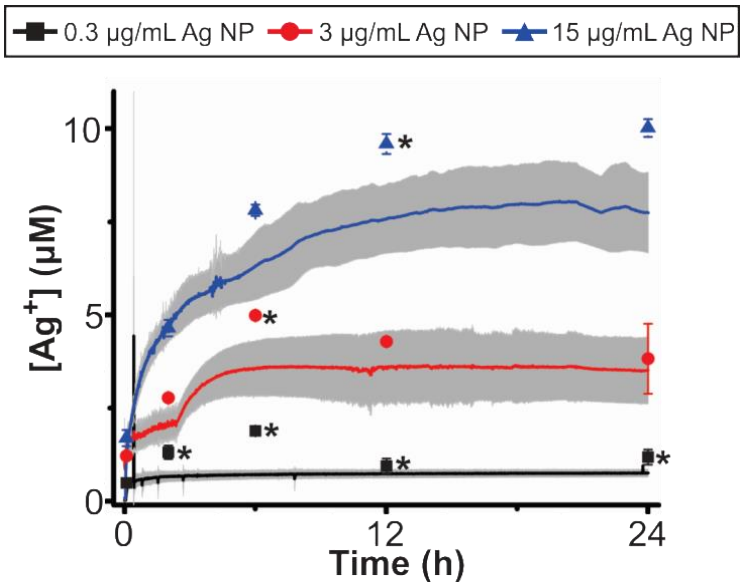

Figure 3. Concentration of Ag^+ dissolved from Ag NPs added to deionized water at different concentrations, as measured over time with Ag^+ ionophore-doped fluorous-phase ISEs (continuous lines with standard deviation shown as shaded gray) and ICP-MS (symbols). Black = 0.3 µg/mL Ag NP added initially, red = 3 µg/mL Ag NP added initially, and blue = 15 µg/mL Ag NP added initially. *$p<0.05$ between ISE and ICP-MS measurements at each particular time point.

To confirm that oxygen caused the difference between the ICP-MS and ISE results of Figure 3 and to validate the fluorous-phase ISE measurements, nanoparticle dissolution was monitored in deionized water with modulated oxygen levels. Oxygen content was modified by alternately bubbling of O_2 and N_2 through the solution to intentionally alter

the dissolution kinetics, measuring with the ISE and collecting ICP-MS samples from the same solution (Figure 4). The ISE results are represented as squares at discrete time points before which gas bubbling was stopped briefly to avoid the gas bubbles from interfering with the potentiometric measurement. These results reveal that there are no statistical differences between the ICP-MS and ISE results; this supports the interpretation that the discrepancies between the ICP-MS and ISE data shown in Figure 3 are the results of varied dissolved oxygen levels, and ISE measurements provide a level of sensitivity and selectivity similar to ICP-MS, which has been often considered to be the "gold standard" for the field. From the ISE data of these and the previous results, we calculate a percent dissolution of the nanoparticles from 16–30%, 5–13%, and 1–6% for the 0.3, 3, and 15 µg/mL Ag NP solutions, respectively. These ranges represent the extent of dissolution at various time points within the 24 h of the experiments.

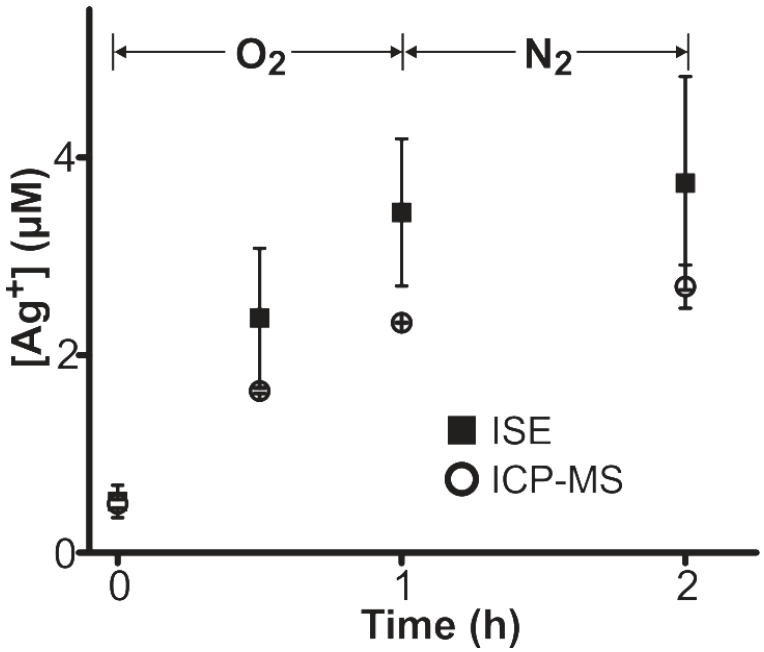

Figure 4. ISE and ICP-MS measurements of 3 µg/mL Ag NP dissolution under varied oxygen exposure. Prior to measurement, N_2 was bubbled through the water followed by 1 h O_2 and then N_2 again.

5.2.3 Detection of Ag Complexes in Ferric Citrate Medium

While the characterization of Ag NP dissolution in water provides important information regarding the response of fluorous-phase ISEs to nanoparticle dissolution, water is an unrealistic medium for performing bacterial toxicity studies. Because Ag^+ can form complexes with inorganic and organic ligands, complexation of Ag^+ with the components of bacterial growth media has to be considered. In these studies, a ferric citrate medium, modified to a lower chloride concentration, was chosen as it is a standard growth medium for *Shewanellae*.[205] To measure the response of the ISEs to Ag^+ in ferric citrate medium, aliquots of 10.0 mM $AgCH_3CO_2$ were added to 100 mL of ferric citrate medium while monitoring the EMF. As Figure 5A shows, the EMF values in the growth medium were significantly lower than in water. Since ISEs only respond to free Ag^+, the lower EMF values indicate that the growth medium contains species that bind to Ag^+. The comparison of the total Ag^+ concentration and the free Ag^+ concentration in the growth medium, as determined by the ISE measurements, shows that throughout the whole range of added Ag^+ concentrations, approximately 95% of the Ag^+ is in a complexed form (Figure 5B).

To determine which Ag^+ complexes are formed in ferric citrate medium, the effect of the individual components of the ferric citrate medium on the EMF was investigated at the pH of the growth medium and their concentrations therein. Specifically, H_3BO_3, MoO_4, $CuSO_4$, $AlK(SO_4)_2$, $FeSO_4$, $CoCl_2$, $CaCl_2$, $MnSO_4$, NaOAc and KOAc were added step by step to a solution containing 1 µM AgOAc while continuously monitoring the EMF. None of these components of the growth medium caused a significant change in the EMF, confirming that none of the medium components significantly affects the free Ag^+ concentration (for details, see Table S1 in the supplementary information). However, Ag^+ forms complexes with NH_3, which is present in the growth medium because of its $(NH_4)_2SO_4$ content (19 mM).

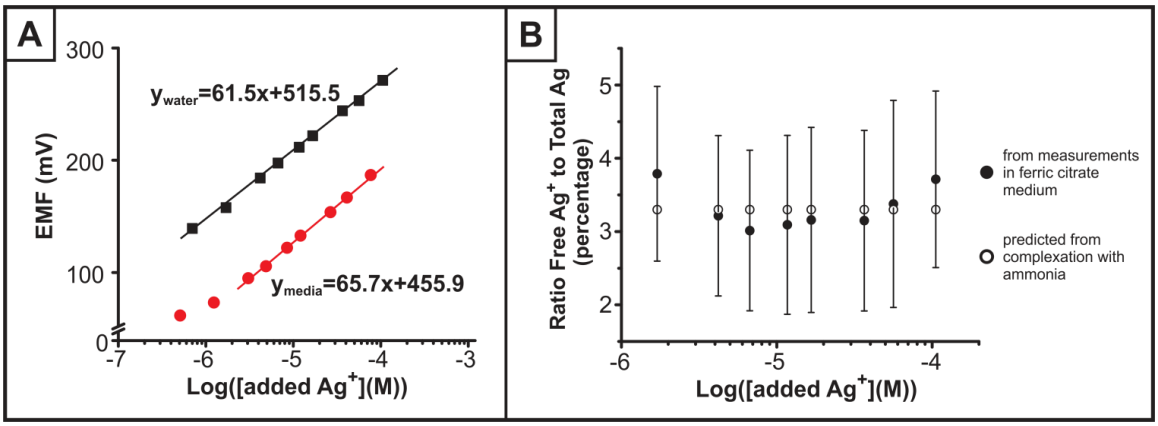

Figure 5. ISE response in ferric citrate growth medium. (A) Comparison of response curves in water (black) and in growth medium (red). (B) Measured and predicted percentages of Ag^+ complexation with ammonia.

The fractions of Ag^+ in its free and complexed forms can be predicted from known complexation equilibria. For this purpose, the concentration of NH_3 in solution was determined by the measurement of the pH (pH=7.9, independent of the Ag^+ concentration) and calculation of the NH_3 species concentration from the pK_a of NH_4^+. Using the thus determined NH_3 concentration and the stability constants of $Ag(NH_3)^+$ and $Ag(NH_3)_2^+$, the concentrations of uncomplexed Ag^+ at various total concentrations of added Ag^+ were calculated (see Figure 5B). Details of these calculations are provided in the supplementary information. The results show that complexation with NH_3 lowers the activity of Ag^+ to 3.3% of the total silver ion concentration in the growth medium. Of the total Ag^+, 87.8% is in the form of $Ag(NH_3)_2^+$ and 8.9% in the form of $Ag(NH_3)^+$. Figure 5B shows that the free Ag^+ activities calculated this way agree within error with the free Ag^+ activities determined potentiometrically in ferric citrate medium.

The utility of the Ag^+-selective ISE is also illustrated by its ability to assess the effect of citrate on Ag NP dissolution. While citrate is known to bind Ag^+, the dissociation of ferric citrate is the only possible source of citrate in ferric citrate buffer, and the high stability of the ferric citrate alone suggests very low concentrations of free citrate and

Fe^{3+}. However, at neutral pH, the free Fe^{3+} activity predicted from ferric citrate dissociation exceeds the solubility of ferric oxides, which have the potential to favor ferric citrate dissociation. The situation is further complicated by the fact that equilibration of solid ferric oxides with their solutions is kinetically very slow, making it difficult to predict on the basis of thermodynamic equilibria alone whether citrate binding to Ag^+ in ferric citrate buffer is a concern. Fortunately, the ISEs make it possible to clarify this matter conclusively. The Ag^+-selective ISEs do not show a significant difference between free Ag^+ in ferric citrate medium and free Ag^+ in ferric citrate medium with an additional 10 mM sodium citrate, confirming that citrate in ferric citrate medium does not affect the free Ag^+ activity in this medium. (See supplementary information Figure S1).

To our knowledge, this is the first example of quantification of free and complexed silver species in a real-time measurement of Ag NP dissolution, an approach that has the potential to contribute greatly to the understanding of Ag NP toxicity.

5.2.4 Characterization of Ag NP Dissolution in Ferric Citrate Medium

To assess the dissolution of Ag NPs, ferric citrate medium containing 3 µg/mL Ag NPs was prepared. The experimental set up was the same as that described for the complexation studies described above, and the dissolution of Ag NPs in the medium was monitored with ISEs over 24 h, followed by recalibration of the ISEs to ensure proper response. While the ISEs responded to changes in the Ag^+ concentration as the result of Ag NP dissolution, complexation of the released Ag^+ with NH_3 kept the free Ag^+ activity low. To obtain a better measure of the extent of Ag NP dissolution, the measured potentials were converted to total concentration of dissolved silver, using the response curves discussed above (i.e, Figure 5). Figure 6 details the dissolution of 3 µg/mL Ag NPs in media as compared to water. The calculated percentages of dissolution in ferric citrate medium ranged from 7–28%, depending on the time (0–24 h) in the medium as

opposed to 5–13% in water. Another difference between the dissolution characteristics in medium and water is that in the medium the plateau region is reached more slowly. This is likely the result of a Le Chatelier effect, i.e., the decrease in free Ag^+ due to complexation with ammonia causes a faster dissolution of the nanoparticles. However, a greater percentage of dissolution takes longer to reach equilibrium, accounting for the greater time to reach the plateau. To determine if the dissolution was impacted by the presence of *S. oneidensis*, we repeated the dissolution measurement in the presence of $\approx 10^8$ bacterial cells. Interestingly, the dissolution profile changes, and the amount of dissolved Ag^+ as calculated from the ISE measurement was diminished in the presence of the bacteria, both in the early stages of dissolution as well as after 24 h. To our knowledge, such changes in nanoparticle dissolution as the result of cells or organisms being present have not been reported previously and have major implications for understanding Ag NP-induced toxicity. This result highlights the importance of in situ nanoparticle characterization.

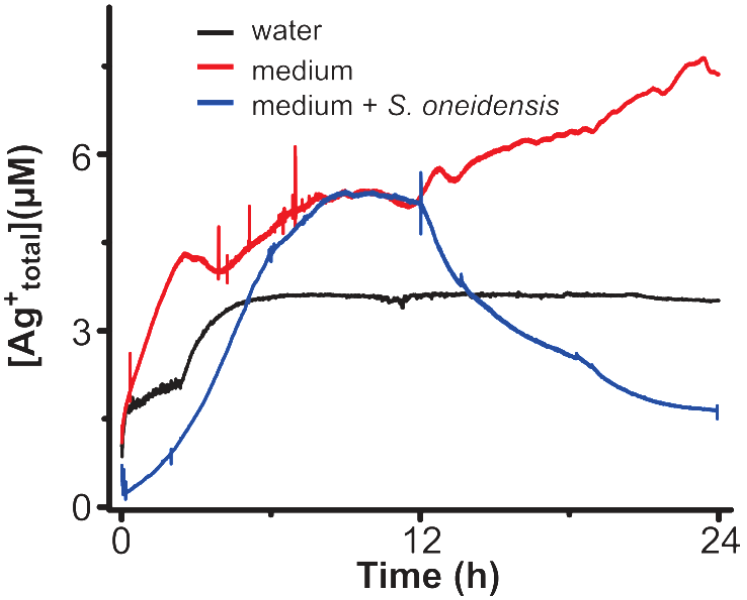

Figure 6. Comparison of 3 μg/mL Ag NP dissolution in water, ferric citrate medium, and ferric citrate medium with $\approx 10^8$ *S. oneidensis* cells added.

ICP-MS measurements in ferric citrate medium consistently revealed dissolved Ag concentrations lower than those measured by ISE (data not shown). However, this difference is attributable to sample preparation methods used for ICP-MS analysis. Indeed, adding 5 µM $AgCH_3CO_2$ into ferric citrate medium and performing the same sample preparation as for the Ag NP experiments resulted in ICP-MS results much less than 5 µM (Figure S2). ISE measurements avoid this source of error, adding to the advantages this technique offers for in situ nanoparticle characterization.

5.2.5 Assessment of Ag NP and Ag Ion Toxicity to *S. oneidensis*

To determine the effects of Ag NPs and Ag^+ on *S. oneidensis* morphology and the localization of the nanoparticles with respect to individual bacteria, TEM analysis after exposure to control, 3 µg/mL Ag NPs, and 3 µM Ag^+ was performed (Figure 7). No notable changes in bacteria morphology were observed. Examination of unstained samples revealed that Ag NPs were not internalized by the bacteria but seem to localize near the bacterial membrane (Figure 7B), which is in agreement with previous work with naturally sampled bacteria,[206] *E. coli, and B. subtilis.*[207] While the control cells have some electron dense material close to the surface (Figure 7A), this is likely the result of some precipitated iron species from the medium; the electron dense areas in the Ag NP-exposed bacteria are larger and in higher abundance. In fact, the size distribution of nanoparticles in proximity to the bacteria is similar to the as-synthesized nanoparticles (Figure S3). Interestingly, in qualitative observations, it was found that Ag^+-exposed bacteria (Figure 7C) also have more abundant electron dense regions near the *S. oneidensis* outer cell membranes, which is potentially the result of the bacterial function of metal reduction, where Ag^+ is reduced to Ag^0. In fact, previous work has demonstrated that *S. oneidensis* can biosynthesize Ag NPs when presented with Ag^+,[208] indicating the potential for these bacteria to be used as an environmental remediation tool.

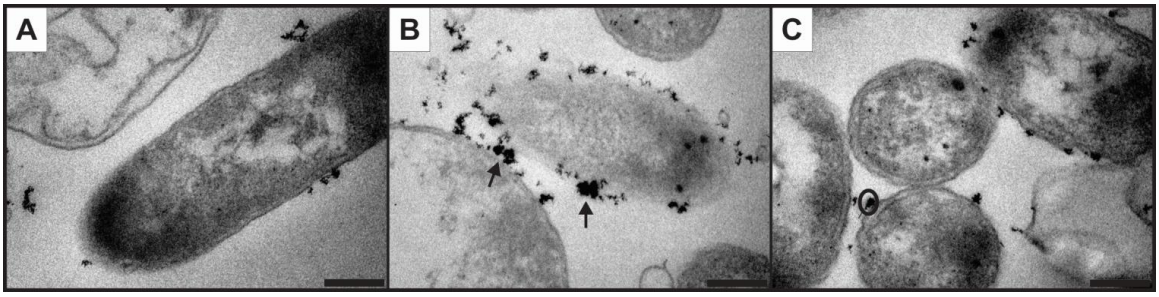

Figure 7. TEM of unstained *S. oneidensis* exposed to (A) control, (B) 3 μg/mL Ag NPs, and (C) 3 μM Ag^+. Scale bar = 1 μm, arrows in B indicate Ag NPs, and circle in C indicates possible biosynthesized Ag NPs upon exposure to Ag^+.

Characterization of Ag NP dissolution in growth medium alone (Figure 5 red line) was used to determine relevant concentrations of total dissolved Ag and nanoparticles to be compared to in toxicity assessments. A LIVE/DEAD BacLight assay was performed to determine the viability of *S. oneidensis* after varied time (0–24 h) and concentration of exposure to Ag^+ (1-10 μM) or Ag NPs (0.3-15 μg/mL). As seen in Figure 8, a significant decrease in the viability is observed after 6 h exposure to 4 μM Ag^+ and 15 μg/mL Ag NPs. Interestingly, at 24 h, lower concentrations of Ag^+ tend to cause an increase in viability up until 3 μM Ag^+, but viability drastically drops below the control at 4 μM Ag^+. A similar increase in viability is observed upon 24 h exposure to 0.3 μg/mL Ag NP, followed by a significant decrease in viability of *S. oneidensis* exposed to 3 and 15 μg/mL Ag NP. The stimulation of *S. oneidensis* viability at lower concentrations of Ag^+ and Ag NPs may be the result of *S. oneidensis'* ability to respire a variety of metals, including Ag;[197] increased respiration stimulates growth which is measured as increased viability in this assay. It appears, however, that there is a sharp threshold whereupon the presence of Ag causes a decrease in viability because by 4 μM Ag^+ or 3 μg/mL Ag NP, a reduction in viability is observed. *E. coli* has a similar viability decrease upon Ag NP and Ag^+ exposure in similar concentrations ranges,[181,207,209] though other species, including *B. subtilis*, show some silver resistance.[207] Comparison of *S. oneidensis* bacterial viability at 3 μg/mL versus the equivalent total dissolved Ag^+ measured in ISE experiments reveals a

clear discrepancy in induced toxicity, with higher toxicity observed in the Ag^+ exposures (Figure 8C). These discrepancies are likely the result of the change in dissolution profile observed in the presence of *S. oneidensis*, where less Ag^+ than expected is available.

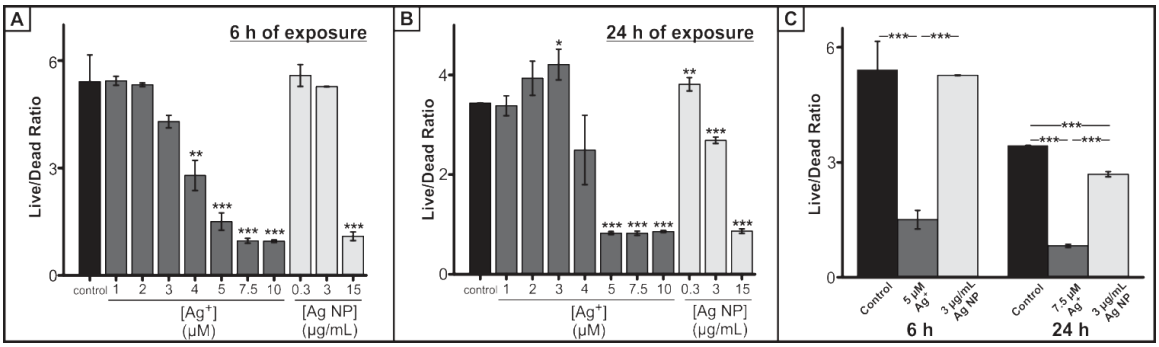

Figure 8. Assessment of viability of *S. oneidensis* after (A) 6 h and (B) 24 h exposure to Ag^+ and Ag NP. (C) Comparison of *S. oneidensis* viability response to Ag NP and ISE-measured total dissolved Ag^+ at each particular time point. Samples were measured in triplicate and *p<0.05, **p<0.01, and ***p<0.001.

Another measurement of toxicity is the growth of the bacteria in the presence of Ag^+ and Ag NPs, where growth is monitored by measurement of optical density (Figure S4). As in the viability assessment, 4 μM Ag^+ and higher concentrations of Ag^+ cause no growth, and, in fact, a decrease in optical density is observed by 3 h, indicating cell death. Lower Ag^+ and all Ag NP concentrations, however, do not arrest growth, though there is a decrease in the rate of growth (Table S2). Again, relating the toxicity induced by 3 μg/mL Ag NP to the measured concentration of dissolved Ag^+, there is a difference in the bacterial response, likely due to the overestimation of the amount of Ag^+ released from Ag NP without the organism present.

To demonstrate the capability of ISEs to be used as an in situ tool, a live/dead viability assessment was performed on the bacteria used in the characterization of Ag NP dissolution in Figure 6 (blue line) at 0, 2, 6, 12, and 24 h (0 and 2 h data not shown). Figure 9 shows no change in *S. oneidensis* viability as compared to the control, except at

12 h. The dissolution profile shows that after 6 h the total Ag^+ concentration reaches 4 µM, which coincides with the threshold value where toxicity is observed (Figure 8 and S3). However, an immediate decrease in viability is not observed, apparently because the time of exposure to that 4 µM concentration is too short. The total Ag^+ concentration continues to rise to 5 µM at 12 h before dropping down to 1.6 µM at 24 h. The Ag^+ concentration-dependent toxicity observed in Figure 8 supports the toxicity results observed in this in situ experiment. After 6 h, exposure to concentrations of Ag^+ >4 µM causes decreases in viability but does not cause toxicity at < 3 µM. The toxicity response correlating to the concentration of Ag^+ supports the idea that Ag^+ is a major cause of Ag NP toxicity, and the release of the toxic ion is mitigated in the presence of the bacteria. Additionally, since the toxicity effects mirror the Ag NP dissolution and the Ag^+ concentration varies over a period of 24 h, this result strongly supports the importance of toxicity assessments with in situ nanoparticle characterization.

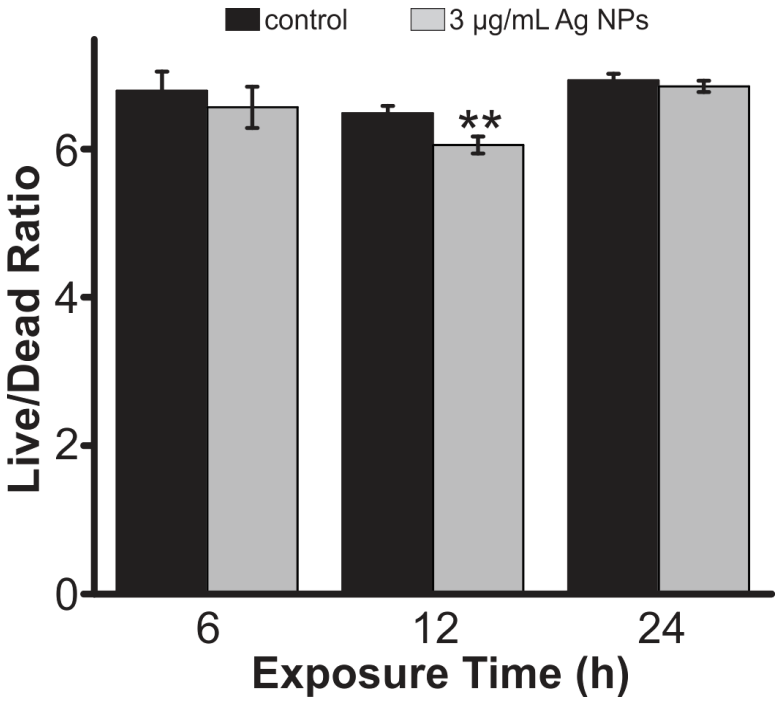

Figure 9. LIVE/DEAD BacLight viability assessment of *S. oneidensis* exposed to 3 µg/mL Ag NPs in which dissolution was monitored using ISEs. **p<0.01

5.3 Conclusions

This works details the use of fluorous-phase ISEs for the characterization of Ag NP dissolution, including the rate and extent of nanoparticle dissolution along with the characterization of the species of dissolved Ag that are formed upon nanoparticle dissolution. One important conclusion from this study is that even in a simplified, defined bacterial culture medium, the majority of silver dissolved from Ag NPs will be in a complexed form, thus affecting the bioavailability and toxicity of silver ions. In nearly all realistic ecological compartments (e.g., rivers and oceans), dissolved Ag^+ complexes will be the predominant species entering the environment due to Ag NP release, and having the ability to determine percentages of each dissolved Ag^+ species is a crucial advance toward determining the impact of nanoparticles on the environment. In addition to characterizing Ag NP dissolution in relevant media, this work also highlights the importance of understanding dissolution in the presence of organisms, which is often not considered in previous assessments.

Considering the toxicity of Ag^+ and Ag NPs to *S. oneidensis*, a critical constituent of the food web, it was demonstrated that total Ag^+ and Ag NPs at low concentrations cause an increase in *S. oneidensis* viability but cause significant cell death above threshold concentrations; all concentrations of Ag^+ and Ag NP considered herein slow the bacterial growth rate. However, the toxicity of Ag NPs compared to ex situ, ISE-measured Ag^+ concentrations from said Ag NPs yielded major differences in the toxic response, supporting the result that the concentration of toxic Ag^+ is decreased in the presence of *S. oneidensis*. In situ toxicity assessments in this work demonstrated a strong correlation between Ag^+ concentration and toxicity to *S. oneidensis*. These results illuminate the importance of moving toward in situ nanoparticle characterization so as to better describe the nanotoxicity. Ultimately, better characterization of nanoparticles will lead to a clearer mechanistic view of the nano-bio interaction, which could ultimately lead to design rules for sustainable use of nanotechnology.

5.4 Acknowledgements

We gratefully acknowledge the Jeff Gralnick lab at the University of Minnesota for the generous gift of *S. oneidensis* MR-1 and their help answering our questions. We acknowledge Rick Knurr of the Earth Sciences Department at the University of Minnesota for his work on the ICP-MS data collection and John A. Gladysz from Texas A&M University for the help in the initial development of the Ag^+ ISEs. This research was financially supported by a grant from the National Science Foundation (CHE-1152931), the Center for Analysis of Biomolecular Signalling at the University of Minnesota, and a University of Minnesota Doctoral Dissertation Fellowship awarded to M.A.M.-J. Parts of this work were carried out in the Characterization Facility, University of Minnesota, which receives partial support from NSF through the MRSEC program.

5.5 Supporting Information

5.5.1 Experimental Methods

5.5.1.1 Nanoparticle Synthesis and Characterization

Citrate-capped Ag NPs were synthesized freshly for every experiment following a procedure detailed by Hackley and coworkers.[200] Prior to synthesis, glassware was cleaned with aqua regia (3:1 HCl:HNO_3) and rinsed three times with deionized purified water (18MΩ·cm specific resistance, EMD Millipore, Burlington, MA, USA). For the synthesis, 50 mL deionized water was brought to a boil and then 365 μL of 34 mM trisodium citrate dihydrate (Sigma Aldrich, St. Louis, MO, USA) and 211 μL $AgNO_3$ (Sigma Aldrich) were added, followed by drop-wise addition of freshly prepared 250 μL $NaBH_4$ (Sigma Aldrich). Upon addition of $NaBH_4$, the solution immediately turned yellow, and the mixture was allowed to boil for 15 min before removing the nanoparticles from heat and allowing them to come to room temperature. Nanoparticles were purified with regenerated cellulose (MWCO 50,000) centrifugal filter units (EMD Millipore) where 15 mL of the nanoparticle suspension were centrifuged at 1500 g for 4 min and then resuspended in deionized water, with the centrifuge/resuspension steps repeated in

triplicate. The concentration of nanoparticles in the final, purified nanoparticle solution was determined with UV-visible spectroscopy (USB2000, Ocean Optics, Dunedin, FL, USA) using the extinction coefficient 8.7×10^8 M^{-1} cm^{-1}, as determined experimentally via correlation of absorbance values to concentrations of nanoparticles measured with ICP-MS (ICP-MS method below). Nanoparticle concentrations were converted to μg/mL by calculating the number of atoms per nanoparticle and converting atoms to mass using the atomic weight of Ag. The number of atoms per nanoparticle (U) were determined based on Equation 1 from Marquis et al.[210]

$$U \approx \frac{2}{3}\left(\frac{D}{a}\right)^3 \quad (1)$$

where *D* is the nanoparticle diameter (11 nm) and *a* is the edge length of the unit cell (4.0857 Å for Ag).

Nanoparticles were characterized by transmission electron microscopy (TEM – JEOL 1200EX III, JEOL, Tokyo, Japan), UV-visible spectroscopy (USB2000, Ocean Optics), dynamic light scattering (DLS – 90Plus, Brookhaven Instruments), and ζ-potential measurement (ZetaPALS, Brookhaven Instruments). The stability of the nanoparticles was monitored over 24 h with both DLS and ζ-potential in both deionized water and bacterial ferric citrate medium (described below).

5.5.1.2 Fluorous-phase Ion-selective Electrode Fabrication

Ionophore-doped fluorous-phase ion-selective electrodes (ISEs) were prepared as reported previously.[51] To prepare the sensing phase, 0.5 mM ionic sites (sodium tetrakis[3,5-bis(perfluorohexyl)phenyl]borate) and 1.5 mM ionophore (1,3-bis(perfluorooctyl-ethylthiomethyl)benzene) were added to perfluoroperhydrophenanthrene (Alfa Aesar, Ward Hill, MA, USA), and the resulting mixture was stirred for at least 24 h to ensure complete dissolution. Fluoropore™ filters (porous poly(tetrafluoroethylene), 47 mm diameter, 0.45 μm pore size, 50 μm thick, 85%

porosity, EMD Millipore, Bedford, MA, USA) were sandwiched between two note cards, and cut with a 13 mm diameter hole punch, giving porous filter disks to mechanically support the sensing phase. Fluorous sensing phase was then applied with a micropipet to a stack of 2 porous filter disks. Full penetration of the fluorous phase into the porous supports was confirmed by a translucent appearance of the thus prepared sensing membranes.

The filter disks impregnated with fluorous sensing phase were then mounted into custom-machined electrode bodies made of poly(chlorotrifluoroethylene), as described previously.[51] In brief, a screw cap with a hole (8.3 mm diameter) in the center was screwed onto the electrode body, mechanically securing the sensing membrane in between the electrode body and the cap but leaving the center of the membrane exposed. The electrode bodies were then filled with 1 µM $AgCH_3CO_2$ (Sigma Aldrich, USA) for studies in bacterial growth medium or with 1 µM $AgNO_3$ for studies in water, and a AgCl/Ag inner reference electrode was inserted into this inner solution. Prior to measurements with bacterial growth medium, all electrodes were conditioned first for 24 h in 100 mL 0.1 mM $AgCH_3CO_2$ solution ($AgNO_3$ for studies in water) and then for another 24 h in 100 mL 1.0 µM $AgCH_3CO_2$ ($AgNO_3$ for studies in water). The same salt of silver was used for the inner filling and conditioning solutions.

5.5.1.3 Fluorous-phase ISE Measurements

Potentials were monitored with an EMF 16 potentiometer (Lawson Labs, Malvern, PA, USA) controlled with EMF Suite 1.02 software (Lawson Labs) at room temperature (25 °C) in stirred solutions. The external reference electrode consisted of a double-junction AgCl/Ag electrode with a 1.0 M LiOAc bridge electrolyte and a 3.0 M KCl reference electrolyte. All measurements were performed with 3 replicate electrodes. For studies in water, calibration curves were obtained by successive dilution of a 10 mM $AgNO_3$ solution with water. For studies in bacterial growth medium, calibration curves were

obtained by addition of various volumes of 10 mM $AgCH_3CO_2$ to 100 mL water or culture medium. To monitor the dissolution of nanoparticles over 24 h, 3 electrodes were prepared, calibrated, and placed in 100 mL of the solution of interest. Purified Ag NPs as described above were added to give varying Ag NPs concentrations (0.3–15 µg/mL), and the EMF was monitored for 24 hours, after which the electrodes were again calibrated to ensure stability of response and sensitivity to Ag^+. Ag NP dissolution was monitored in water and ferric citrate bacterial growth medium.

5.5.1.4 Bacterial Growth Media

Ferric citrate media for bacterial culture was prepared with a much lower chloride content than previously reported in the literature[205] to prevent AgCl precipitation. It consisted of 56 mM ferric citrate (Sigma Aldrich), 30 mM sodium lactate (from 60% solution, Spectrum Chemical, Redondo Beach, CA, USA), 30 mM $NaHCO_3$ (Sigma Aldrich), 5 mM NaH_2PO_4 (Sigma Aldrich, St. Louis, MO, USA), 19 mM $(NH_4)_2SO_4$ (Fisher Chemical, Fairlawn, NJ, USA), 1 mM KCH_3CO_2 (Mallinckrodt, Phillipsburg, NJ, USA), and hundredfold diluted mineral stock solution (see details below). To make the growth medium, ferric citrate was dissolved in deionized water by mild heating, and then the pH was adjusted to 6.7 with NaOH (Mallinckrodt). Addition of the other components yielded a final pH of ≈7.7. The mineral stock solution consisted of 17.3 mM $NaCH_3CO_2$ (EMD, Gibbstown, NJ, USA), 8.7 mM $MnSO_4 \cdot H_2O$ (Mallinckrodt), 0.9 mM $CaCl_2$ (Fisher Chemical), 0.4 mM $CoCl_2 \cdot 6H_2O$ (Mallinckrodt), 0.4 mM $FeSO_4 \cdot 7H_2O$ (Fisher Chemical), 0.15 mM H_3BO_3 (Mallinckrodt), 25 µM $AlK(SO_4)_2 \cdot 12H_2O$ (Mallinckrodt), 46 µM $CuSO_4 \cdot 5H_2O$ (Spectrum Chemical, Redondo Beach, CA, USA), and 41 µM $Na_2MoO_4 \cdot 2H_2O$ (Sigma Aldrich).

5.5.1.5 ICP-MS Studies

Ag NP dissolution in deionized water and ferric citrate growth medium was monitored at discrete time points in parallel experiments using ICP-MS (XSeries 2, Thermo Scientific,

Beverly, MA, USA). In these experiments, aliquots were collected at 0, 2, 6, 12, and 24 h, and supernatants were separated from the nanoparticles by centrifugation at 4000 g for 10 min using centrifugal filter units. Supernatants were analyzed for m/z 107 for Ag quantitation, with an indium internal standard monitored at m/z 115. The concentrations of Ag NPs and Ag^+ ion are reported here with different units (μg/mL or M, respectively) so as to align with common literature practice.

5.5.1.6 Bacterial Culture

Shewanella oneidensis MR-1 were generously gifted by the Gralnick lab at the University of Minnesota. To prepare bacteria for toxicity assessments, cells stored at -80 °C were streaked onto an agar plate, allowing colonies to grow for 18–24 h, upon which colonies were transferred to Luria-Bertani (LB) growth medium (1 colony per 5 mL medium). Cells were cultured to stationary phase overnight (over 15 h) on a shaking incubator (200 rpm at 30 °C), pelleted by centrifugation at 750 g for 10 min, and resuspended in the ferric citrate growth medium. This suspension of cells was used going forward for toxicity assessments, and is herein referred to as "bacteria suspension," the cell density of which was consistently 10^9 cells/mL. When bacteria were not being used or measured, the suspension was placed on the shaking incubator.

5.5.1.7 Bacterial Toxicity Assays

Bacterial nanoparticle uptake/association, and/or *S. oneidensis* morphology changes as the result of exposure to Ag^+ and Ag NPs were assessed by TEM. The bacterial suspensions were diluted to 10^8 cells/mL, and cells were exposed to control, 3 μM Ag^+, 3 μg/mL Ag NPs conditions for 24 h, after which, bacteria samples were prepared as previously described for mammalian cells.[211] Briefly, cells were pelleted by centrifugation at 500 g for 10 min and washed with 0.1 M sodium cacodylate buffer. Bacteria were fixed with 2.5% glutaraldehyde (Sigma Aldrich) in 0.1 M sodium cacodylate buffer for 1 h, followed by a post-fixation for 1 h in 1% osmium tetroxide

(Sigma Aldrich). Samples were dehydrated in a series of ethanol washes with increasing percentages of ethanol, followed by propylene oxide and finally Epon Polybed 812 resin (Miller-Stephenson, Columbus, OH, USA). Resin was exchanged 5 times over 36 h to allow proper intercalation and cured for 24 h at 45 °C, followed by 60 °C for 24 h. A diamond knife was used to cut 60 nm sections with an ultramicrotome, and sections were collected on a Formvar-coated copper grid and imaged at 60 kV on a JEOL 1200 EXII TEM (JEOL, Tokyo, Japan).

LIVE/DEAD® BacLight™ (Life Technologies, Grand Island, NY, USA) was used to assess viability of *S. oneidensis* after exposure to varying concentrations of $AgCH_3CO_2$ (referred to as Ag^+) and Ag NPs for up to 24 h. Cells from the bacteria suspension were diluted to a density of 10^8 cells/mL with ferric citrate medium and exposed to varying concentrations of Ag^+ (1-10 μM) or Ag NPs (0.3-15 μg/mL), with each condition cultured in triplicate and periodic assessment of viability taken over the 24 h exposure. To perform the viability assay, the staining solution was prepared as specified by the manufacturer (kit L7012) and was comprised of 2 fluorescent dyes, where live cells were stained with membrane-permeable SYTO-9 and dead cells were stained with red fluorescent propidium iodide. Periodically, 0.5 mL aliquots of the samples were centrifuged at 500 g for 10 min, and pelleted cells were resuspended in HEPES (4-(2-hydroxyethyl)-1-piperazineethanesulfonic acid) buffer solution with mineral additives to avoid scattering by iron oxide precipitates formed in the ferric citrate medium. HEPES buffer with mineral additives consisted of 100 mM HEPES, 7.8 mM $NaCH_3CO_2$, 1.3 mM K_2HPO_4, 1.7 mM KH_2PO_4, 1.7 mM $(NH_4)_2SO_4$,1 mM $MgSO_4$, 9.5 μM $ZnCl_2$, 1.9 μM $NiCl_2$, 0.5 μM $Na_2MoO_4{\cdot}2H_2O$, 0.4 μM Na_2WO_4, 0.2 μM $AlK(SO_4)_2{\cdot}12H_2O$, 1.8 μM $FeSO_4{\cdot}7H_2O$, 13.5 μM $MnSO_4{\cdot}H_2O$, 0.2 μM $CuSO_4{\cdot}5H_2O$, and 3.25 μM $CoSO_4{\cdot}7H_2O$ adjusted to pH 7.2 with NaOH.[212] Equal aliquots of the staining solution and resuspended bacteria (100 μL:100 μL) were mixed, placed in a 96-well plate, and incubated for 15 min in the dark. Fluorescence intensity was measured on a Synergy 2 (Biotek, Winooski, VT, USA) multi-well plate-reader ($\lambda_{excitation}$ = 485 nm; $\lambda_{emission\ SYTO\text{-}9}$ = 528 nm and

$\lambda_{emission\ propidium\ iodide}$ = 630 nm). Measurements were performed after 0, 2, 6, 12, and 24 h exposure, and results were analyzed by comparing the ratio of live cells (green fluorescence) to dead cells (red fluorescence) for the control and silver exposure conditions.

The phases of bacterial growth (lag, exponential, and stationary phases) were monitored for *S. oneidensis* after exposure to varying concentrations of Ag^+ and Ag NPs. The bacterial suspension was diluted to 10^7 cells/mL in ferric citrate medium with exposure to 1–10 μM Ag^+, 0.3–15 μg/mL Ag NPs, or water for the control, with each condition in triplicate. Growth was monitored over 48 h with periodic measurements of the optical density (OD) at λ=600 nm with a Spectronic 20D spectrophotometer (Milton Roy Company, Ivyland, PA, USA). Manual inspection of each curve to determine the exponential phase of growth was performed, and the growth rate, in generations/h, was calculated using Equation 2, which is based on the classic model of binary fission.

$$growth\ rate = \frac{\log OD_2 - \log OD_1}{0.301 * \Delta t_{2-1}} \quad (2)$$

5.5.2 Calculations and Results

5.5.2.1 Complexation of Ammonia with Ag^+

Ammonium, one of the components of the ferric citrate bacterial growth medium, dissociates to ammonia and becomes available to form stable complexes with Ag^+ (formation constants of $K_{f,1}=10^{3.24}$ and $K_{f,2}=10^{3.81}$).[213] The pH of the bacterial growth medium was measured and found to be 7.9, independent of the concentration of Ag^+. Using the dissociation equation and mass balance for ammonium (Equations 3 and 4), the concentration of ammonia in solution can be calculated, as described in the following.

$$\frac{a_{NH_3}\, a_{H^+}}{a_{NH_4^+}} = K_a \quad (3)$$

$$[NH_3] + [NH_4^+] = C_{\text{total, } NH_4^+} \quad (4)$$

Activity coefficients were calculated using the Debye-Hückel extended theory (Equations 5 and 6), where I is the ionic strength of the solution, z is the charge of ions, α is the ion size parameter (0.76 Å for NH_4^+) and, at 25 °C, A and B are 0.509 and 0.328 $Å^{-1}$, respectively.[214]

$$\log \gamma_{\pm} = -\frac{A\,(z_+\ z_-)\sqrt{I}}{1 + B\alpha\sqrt{I}} \quad (5)$$

$$\log \gamma_{\pm} = -\frac{A\,(z_+\ z_-)\sqrt{I}}{1 + B\alpha\sqrt{I}} \quad (6)$$

Using the acid dissociation constant of $10^{-9.244}$,[215] a total concentration of 38 mM for ammonium, and $10^{-7.9}$ M for a_{H^+}, the concentration of ammonia in the bacterial growth medium with an ionic strength of 0.123 was calculated to be 1.5×10^{-3} M. By using the formation equations for the silver ammonia complexes (Equations 7 and 8) and the mass balance for all dissolved species containing silver, the percentages of all Ag^+ species can been calculated (see below). As an approximation, the activity coefficients of the complexed silver ions were assumed to be identical to those of the free Ag^+.

$$\frac{a_{AgNH_3^+}}{a_{Ag^+}\, a_{NH_3}} \cong \frac{[AgNH_3^+]}{[Ag^+][NH_3]} = K_{f,1} \quad (7)$$

$$\frac{a_{Ag(NH_3)_2^+}}{a_{AgNH_3^+}\, a_{NH_3}} \cong \frac{[Ag(NH_3)_2^+]}{[AgNH_3^+][NH_3]} = K_{f,2} \qquad (8)$$

$$C_{total,Ag} = [Ag^+] + [AgNH_3^+] + [Ag(NH_3)_2^+] \qquad (9)$$

Combining Equations 7, 8, and 9 gives Equation 10.

$$C_{total,Ag} = [Ag^+] + [Ag^+][NH_3]\, K_{f,1} + [Ag^+]\,[NH_3]^2\, K_{f,1}K_{f,2}$$

$$= [Ag^+]\left(1 + [NH_3]\, K_{f,1} + [NH_3]^2\, K_{f,1}K_{f,2}\right) \qquad (10)$$

Equation 10 can be readily reformed to give the ratio of free silver ions and the total silver concentration. Using the known values of $K_{f,1}$ and $K_{f,2}$ and the activity of ammonia, this ratio is calculated as 0.033:

$$\frac{[Ag^+]}{C_{total,Ag}} = \frac{1}{\left(1 + [NH_3]\, K_{f,1} + [NH_3]^2\, K_{f,1}K_{f,2}\right)} = 0.033$$

The ratios of the silver complexes and the total silver concentrations can be obtained analogously:

$$\frac{[AgNH_3^+]}{C_{total,Ag}} = \frac{[NH_3]\, K_{f,1}}{(1 + [NH_3]\, K_{f,1} + [NH_3]^2\, K_{f,1}K_{f,2})} = 0.089$$

$$\frac{[Ag(NH_3)_2^+]}{C_{total,Ag}} = \frac{[NH_3]^2\, K_{f,1}K_{f,2}}{\left(1 + [NH_3]\, K_{f,1} + [NH_3]^2\, K_{f,1}K_{f,2}\right)} = 0.878$$

Thus, it can be concluded that 3.3% of total ionic silver species are in the form of free Ag^+, 8.9% are in the form of $AgNH_3^+$, and 87.8% are in the form of $Ag(NH_3)_2^+$.

5.5.2.2 Effect of Ferric Citrate Components on the EMF Response

To investigate the effect of the individual components of the ferric citrate medium on the response of the Ag^+ ISEs, solutions containing 1μM $AgCH_3CO_2$, and individual medium components ($MnSO_4 \cdot H_2O$, $CaCl_2$, $CoCl_2 \cdot 6H_2O$, $FeSO_4 \cdot 7H_2O$, H_3BO_3, $AlK(SO_4)_2 \cdot 12H_2O$, $CuSO_4 \cdot 5H_2O$, $Na_2MoO_4 \cdot 2H_2O$, KCH_3CO_2, and sodium lactate) were prepared, and the pH of the solutions was adjusted as for the ferric citrate medium by addition of sodium hydroxide or acetic acid. The electrodes were placed in 100 mL of 1.0 μM $AgCH_3CO_2$, followed by step-by-step addition of known volumes of solutions of the ferric citrate medium components to make the final concentrations very similar to those in the complete ferric citrate medium. None of the species caused a significant change in the EMF, indicating that they do not interfere with the response and do not have any specific interaction with Ag^+. The average EMF changes for 3 replicate electrodes are shown in Table S1.

Table S1. Effect of broth components on EMF measurements. The electrodes were placed in 100 mL 1.0 μM $AgCH_3CO_2$ solution, followed by step-by-step addition of known volumes of solutions of the ferric citrate medium components to give final concentrations very similar to those in the ferric citrate medium.

	Concentration (μM)	**Average change in EMF (mV)**
$AgCH_3CO_2$	1.0	–
After addition of:		
H_3BO_3	1.5	0.7 ± 2.5
Na_2MoO_4	0.41	0.7 ± 2.1
CuSO4	0.46	-1.2 ± 1.9
$AlK(SO_4)_2$	0.25	-1.1 ± 1.1
$FeSO_4$	4.0	3.7 ± 3.1
$CoCl_2$	4.0	0.8 ± 4.4
$CaCl_2$	9.0	-3.3 ± 4.0
$MnSO_4$	87.0	0.4 ± 0.3
$NaCH_3CO_2$	173.0	1.5 ± 3.5
KOAc	1.0	3.3 ± 3.0

In a similar experiment, less than 3 mV change in the EMF was observed after addition of 30 mM sodium lactate to ferric citrate medium containing 1 μM $AgCH_3CO_2$, indicating that in the ferric citrate medium there is no significant complexation between Ag^+ and lactate anion.

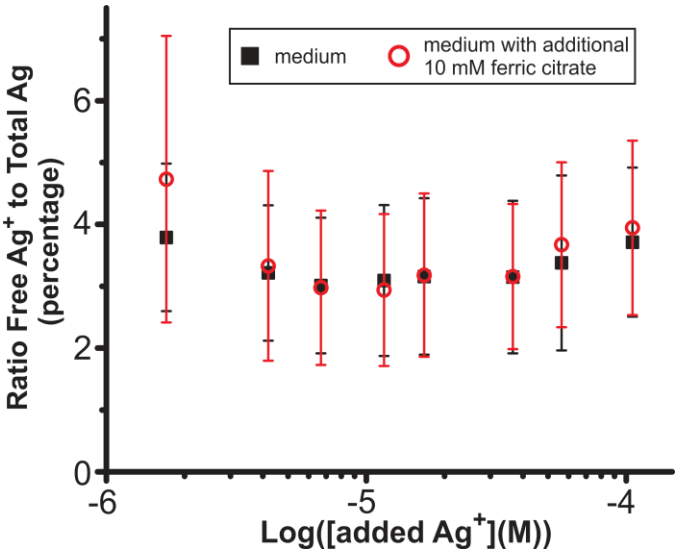

Figure S1. The Ag^+-selective ISEs do not show a significant difference between free Ag^+ in ferric citrate medium and free Ag^+ in ferric citrate medium with an additional 10 mM sodium citrate, confirming that citrate in ferric citrate medium citrate does not affect the free Ag^+ activity in this medium.

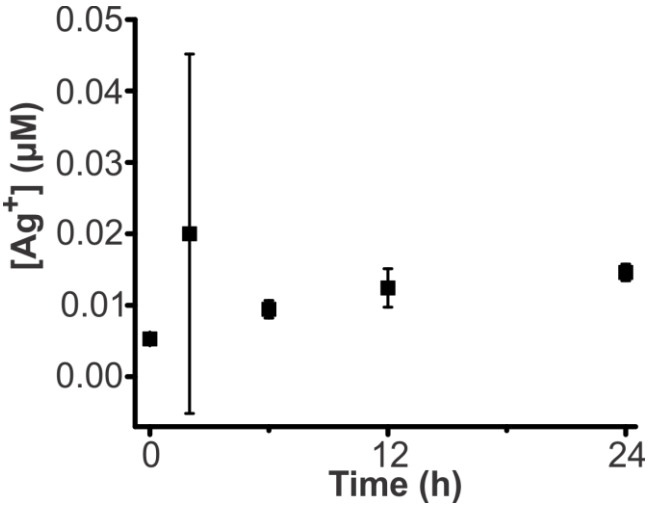

Figure S2. ICP-MS measurement over time of ferric citrate media spiked with 5 µM $AgCH_3CO_2$ reveals that the ICP-MS sample preparation method causes a significant decrease in the Ag^+. The decrease may be due to adsorption of Ag^+ onto the iron precipitate that commonly forms in the ferric citrate medium, which is filtered off in the

ICP-MS sample preparation. This artifact further supports the need for in situ nanoparticle characterization such as the ISE employed herein.

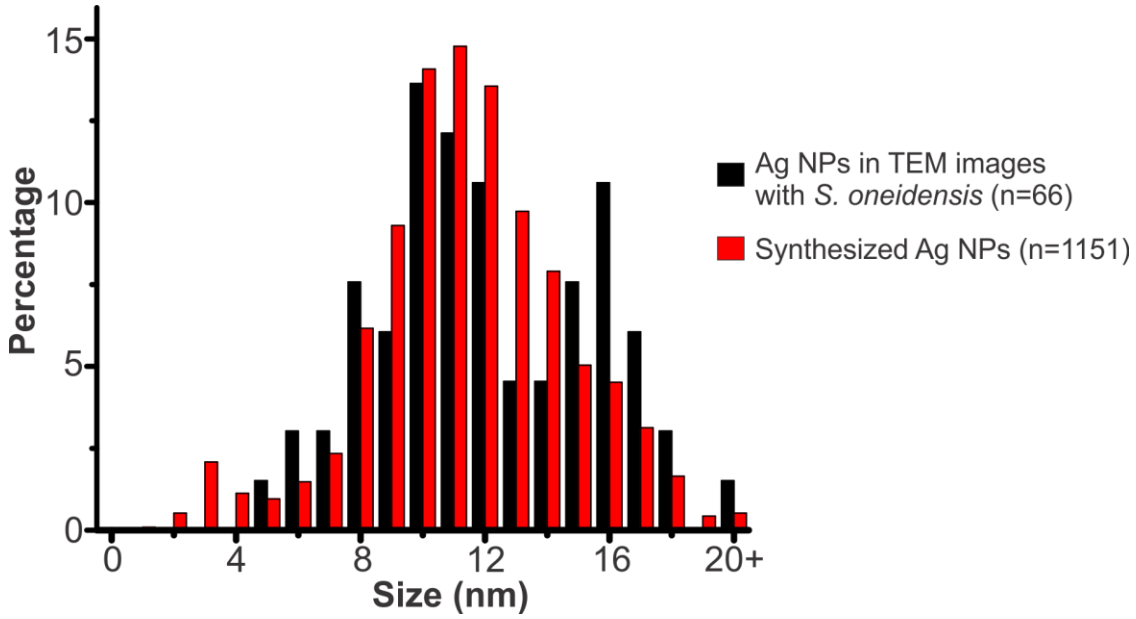

Figure S3. Histogram analysis of nanoparticle diameter found in proximity to bacteria (as seen in Figure 7B) as compared to the synthesized nanoparticle size distribution (as compiled from Figure 1B). The similarity of these distributions suggests that the nanoparticles near the bacteria are, in fact, the synthesized Ag nanoparitcles.

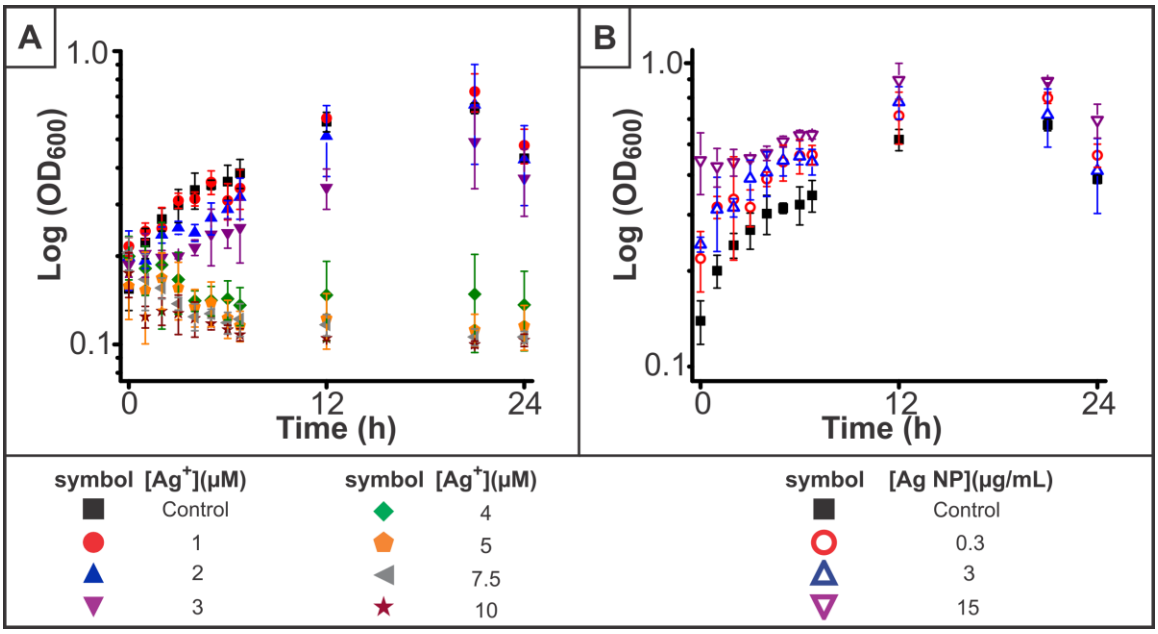

Figure S4. Growth curves for *S. oneidensis* in the presence of (A) Ag^+ or (B) Ag NPs.

Table S3. Growth rate of *S. oneidensis* exposed to Ag^+ or Ag NPs, as determined from the exponential growth phase in Figure S3, using Equation 2.

Concentration Ag NP (μg/mL)	**Growth rate (generations/h)**	**Concentrations Ag^+ (μM)**	**Growth rate (generations/h)**
Control	0.16	1	0.12
0.3	0.09	2	0.12
3	0.09	3	0.09
15	0.09	4, 5, 7.5, and 10	no growth

6 CHAPTER SIX

Dynamic Silver Speciation as Studied with Fluorous-phase Ion-selective Electrodes: Effect of Natural Organic Matter on the Toxicity and Speciation of Silver

Adapted from:

Mousavi, M. P. S.; Gunsolus, I. L.; Pérez De Jesús, C. E.; Lancaster, M.; Hussein, K.; Haynes, C. L.; Bühlmann, P., Dynamic silver speciation as studied with fluorous-phase ion-selective electrodes: Effect of natural organic matter on the toxicity and speciation of silver, *Sci. Total Environ.* **2015**, *537*, 453.

This work was a joint effort by this author and Ian Gunsolus who carried out the synthesis and characterization of silver nanoparticle and toxicity assesments. Carlos Pérez De Jesús, Mitchel Lancaster (undergraduate students mentored by this author), and Kadir Hussein (undergraduate student mentored by Ian Gunsolus) assisted with solution preparation and fabrication and calibration of electrodes.

The widespread application of silver in consumer products and the resulting contamination of natural environments with silver raise questions about the toxicity of Ag^+ in the ecosystem. Natural organic matter, NOM, which is abundant in water supplies, soil, and sediments, can form stable complexes with Ag^+, altering its bioavailability and toxicity. Herein, the extent and kinetics of Ag^+ binding to NOM, matrix effects on Ag^+ binding to NOM, and the effect of NOM on Ag^+ toxicity to *Shewanella oneidensis* MR-1 (assessed by the BacLight Viability assay) were quantitatively studied with fluorous-phase Ag^+ ion-selective electrodes (ISEs). Our findings show fast kinetics of Ag^+ and NOM binding, weak Ag^+ binding for Suwannee River humic acid, fulvic acid, and aquatic NOM, and stronger Ag^+ binding for Pony Lake fulvic acid and Pahokee Peat humic acid. We quantified the effects of matrix components and pH on Ag^+ binding to NOM, showing that the extent of binding greatly depends on the environmental conditions. The effect of NOM on the toxicity of Ag^+ does not correlate with the extent of Ag^+ binding to NOM, and other forms of silver, such as Ag^+ reduced by NOM, are critical for understanding the effect of NOM on Ag^+ toxicity. This work also shows that fluorous-phase Ag^+ ISEs are effective tools for studying Ag^+ binding to NOM because they can be used in a time-resolved manner to monitor the activity of Ag^+ in situ with high selectivity and without the need for extensive sample preparation.

6.1 Introduction

Silver has been estimated to be released into the environment at more than 2500 tons annually.[216] Since ionic silver, Ag^+, is known to be highly toxic to bacteria, the sustainable use of silver-containing products, such as silver nanoparticles, requires a thorough understanding of the environmental toxicity of Ag^+ ions. Silver toxicity cannot be correlated to just the total silver present. Instead, the individual silver species must be considered for a correct assessment of toxicity. One of the main mechanisms of silver speciation is Ag^+ coordination with ligands that occur naturally in the environment. For example, Ag^+ is known to form stable complexes with Lewis bases such as amines, halides, and thiolates. Thiosulfate, sulfide, and chloride binding to Ag^+ have been shown to reduce the toxicity of Ag^+.[217-220] Consequently, the formation of silver complexes depends heavily on the environmental conditions [216]. For a meaningful assessment of Ag^+ toxicity, the coordinating ligands present in any particular environment must be identified, and their effect on the Ag^+ toxicity must be characterized.

One of the most common coordinating substances in natural soil and aquatic environments is natural organic matter (NOM; also commonly referred to as dissolved organic matter, DOM). There have been several reports of heavy metal ion binding to NOM, such as for Cu^{2+}, Pb^{2+}, Cd^{2+}, and Zn^{2+}.[221-225] This binding results in the formation of new chemical species with altered toxicity and transport properties, which affects the bioavailability of these metals.[222,226,227] NOM is found in environmental systems, such as surface waters, ground waters, soils, and sediments, in concentrations ranging from 1 up to more than 100 mg/L.[228-233] NOM results from the decomposition of plant and animal residues and is inherently a mixture of compounds without a well-defined molecular structure.[234] NOM consists largely of humic substances (humic acids, HA, and fulvic acids, FA) but also includes non-humic substances, such as fatty acids, sterols, natural sugars, amino acids, urea, and porphyrins.[232] Humic substances have molecular weights in the range from 300 to 300,000 and have a predominantly aromatic structure. Because

they have many oxygen- and nitrogen-containing functional groups, such as carboxylic, phenolic, and amino groups, they exhibit an acidic and hydrophilic character and have high metal coordinating abilities.[232,233,235] Due to their abundance in the hydrosphere, biosphere, and lithosphere, and their ability to form stable complexes with metals from both natural and anthropogenic sources, humic substances are commonly used as models for studying metal and NOM speciation.[222,230,232,234,236] In this study, we utilized humic substances as models for studying the effect of NOM on Ag^+ speciation and toxicity.

Analytical methods that have been used in NOM/Ag^+ speciation studies have been based on ion exchange equilibrium,[237,238] equilibrium dialysis,[232,238,239] atomic absorption and emission spectroscopy, mass spectrometry,[228,231,240] ion-selective potentiometry,[224,231,241,242] and the assessment of Ag^+ and Ag^+-NOM complex toxicity towards organisms.[230,237] Several reports suggest that NOM samples from various sources decrease the toxicity of Ag^+ to various organisms.[220,226,243-248] This effect is usually attributed to Ag^+ binding to NOM, which lowers the free Ag^+ activity and, thereby, mitigates the ability of silver to act at the sites of toxic action in organisms.[219,226] On the contrary, some NOM samples were reported to have no significant effect on the toxicity of Ag^+ to multiple organisms, and in these cases Ag^+ binding to NOM was concluded to be insignificant.[230,237] Surprisingly, there has been no report to date that quantitatively investigates the correlation between the extent of Ag^+ binding to NOM and Ag^+ toxicity. Clearly, to investigate this correlation, it is advantageous to use techniques that directly probe Ag^+ speciation without the added complexity introduced by the choice of organism, cell culture medium, and the type of toxicity assay as it is necessary in an indirect toxicology assessment.

A challenge in direct Ag^+ speciation studies is distinguishing different silver species, i.e., Ag NPs, free Ag^+, and Ag^+-NOM complexes. Except for ion-selective potentiometry, all the techniques mentioned above lack this ability. To account for this lack of selectivity, specific silver species are usually isolated by several sample preparation steps, e.g., by

using molecular cut-off filters[240] or centrifugation.[240] Unfortunately, this sample preparation can introduce further complexity and potential errors in measurements and the interpretation of results. Such complications include silver adsorption to sample containers and interference from positively charged complexes (in the case of the ion exchange equilibrium method). Moreover, these methods cannot be used for in situ or kinetic studies due to the long analysis time resulting from the need for sample preparation (e.g., analysis times are approximately 2 h for ion exchange equilibrium methods[238] and 3 days for equilibrium dialysis[238]). Even though binding of Ag^+ to NOM has been studied for more than a decade, and several hypotheses about its kinetics have been proposed, the kinetics of this reaction have not been investigated directly, possibly due to the lack of appropriate methodology.[225,241,245]

Potentiometry with ion-selective electrodes, ISEs, offers selective and sensitive in situ Ag^+ detection, requires no substantial sample preparation, is non-destructive, has fast response times, detects only non-complexed ions, and can be used for speciation and kinetics studies.[42] There have been few literature precedents for use of commercially available solid-state ISEs to study Ag^+ speciation,[85,224,231,241,249] possibly due to the common issue of solid state ISE biofouling in biological samples (biological molecules such as proteins adsorb strongly through sulfur groups to silver halide and sulfide electrodes).[43,250-252] ISEs with polymeric sensing membranes suffer less from adsorption but extraction of lipophilic biological interferents into their sensing membranes is still causing biofouling of these ISEs.[69,70] In this work, we used ionophore-doped ISEs with fluorous sensing membranes that are less susceptible to biofouling effects. Fluorous phases prepared from perfluorocarbon derivatives have low polarity and polarizability, are both hydrophobic and lipophobic (i.e., alkanes are not miscible with perfluoroalkanes), limit extraction of lipophilic interferents into the sensing membrane, and thus are less susceptible to biofouling than other polymeric membrane ISEs.[80] Moreover, fluorous-phase Ag^+ ISEs offer exceptional Ag^+ selectivity due to the non-coordinating and poorly solvating properties of the fluorous phase. They also exhibit a

fast response times (less than 1 s), making them a unique tool for environmental Ag^+ speciation studies.[51,77,85] We used these sensors to study open questions regarding the interaction of Ag^+ and NOM, specifically the kinetics of Ag^+ and NOM binding and the correlation between the extent of Ag^+ binding to NOM and the resulting Ag^+ toxicity. While the current study focuses on Ag^+ binding to NOM, the effect of NOM on the toxicity of silver nanoparticles is also crucial for a thorough risk assessment of silver-containing products and was addressed in parallel work.[242]

6.2 Experimental

NOM samples: Suwannee River humic acid II, SRHA (Cat. No. 2S101H), Suwannee River fulvic acid II, SRFA (Cat. No. 2S101F), Pony Lake fulvic acid, PLFA (Cat. No. 1R109F), Pahokee Peat humic acid standard, PPHA (Cat. No. 1S103H), and Suwanee River Aquatic NOM, SRNOM (Cat. No. 2R101N) were purchased from International Humic Substances Society, IHSS (St. Paul, MN). The fabrication and calibration of fluorous-phase Ag^+ ISEs was reported previously[85] and is discussed in the Supporting Information along with a description of the data analysis methods. Buffer preparation and toxicity assessments are also explained in detail the Supporting Information. All the solutions were prepared with deionized water (18 MΩ cm specific resistance, EMD Millipore, Burlington, MA). For preparation of the pH = 6.0 buffer, 0.100 M $NaCH_3CO_2$ and 0.006 M CH_3CO_2H were mixed at room temperature, followed by adjustment of the pH by addition of aliquots of NaOH or CH_3CO_2H. The components of the pH = 7.5 buffer were 0.028 M K_2HPO_4 and 0.015 M KH_2PO_4. The pH of the solution was adjusted to 7.5 by addition of aliquots of KOH. The pH = 9.0 buffer contained 0.087 M $NaHCO_3$ and 0.044 M Na_2CO_3, and the pH was adjusted by addition of aliquots of NaOH. The HEPES buffer with pH = 7.5 was prepared by dissolving 0.20 M HEPES, 4-(2-hydroxyethyl)piperazine-1-ethanesulfonic acid, in deionized water, and the pH of the solution was adjusted to 7.5 by addition of aliquots of KOH. The MOPS buffer with pH = 7.5 was prepared by dissolving 0.30 M MOPS, *N*-morpholino-3-propanesulfonic acid, in

deionized water, and the pH of the solution was adjusted to 7.5 by addition of aliquots of KOH.

The components of the phosphate (pH=7.5), carbonate (pH=9.0), and acetate (pH=6.0) pH buffers were chosen to interact minimally with Ag^+ and thus minimize the interference with respect to Ag^+ binding to NOM. The latter was assessed by measurements of the potentiometric response to Ag^+ by fluorous-phase Ag^+ ISEs in deionized water and in pH buffers. The response for deionized water and all the pH buffer solutions were very similar, which confirmed that Ag^+ did not bind significantly to the pH buffer components (less than 15 mV and 2 mV change in the intercept and slope of the calibration equation, respectively). In the case of Ag^+ binding to the pH buffer components, the calibration equation would have shifted to lower emf values because of the lowering of the concentration of free Ag^+ ions as a result of complexation [85], which must be prevented to avoid errors and an unrealistic evaluation of Ag^+ binding to NOM. Silver toxicity to the test organism, *Shewanella oneidensis* MR-1*, assessed by* evaluating bacterial membrane integrity after exposure to Ag^+ using the LIVE/DEAD BacLight Viability Kit (Product L-7012, Life Technologies).

6.3 Results and discussion

6.3.1 Ion-Selective Electrodes

The electrical potential of an ISE is measured with respect to a reference electrode and is referred to as emf (see Figure 1). At a constant temperature, the emf increases linearly with the logarithm of the Ag^+ activity. For example, at 20 ºC, a 10-fold increase in the activity of Ag^+ results in a 58.2 mV increase in the emf.[42,253,254] The fluorous-phase Ag^+ ISEs were calibrated by addition of aliquots of concentrated $AgCH_3COO$ (aq), followed by measurements of the emf. As predicted by theory, a linear relationship between the emf and Log c (Ag^+) was observed for solutions with a fixed ionic strength, where activity coefficients are assumed to be constant (see Figure 1). The experimentally obtained emf data can be easily converted to Ag^+ concentrations using the calibration

equations. The inherent response time of an ionophore-based ISE for the target ion is determined by ionic redistribution across the nanometer-sized charge separation layer at the interface of the sample and the ISE sensing membrane. In a typical experiment, the response time of the ISE measurement is, therefore, determined by how quickly an old sample can be replaced by a new one and not by a property of the electrode itself. In this work, all solutions were stirred, resulting in response times of less than one second (see Figure 1). The detection limit of the fluorous-phase Ag^+ ISEs used in this work was 0.05 µM. This is not an inherent limitation of these ISEs and with proper optimization, detection limits as low as 4.0×10^{-11} M have with been achieved with fluorous sensing membranes.[51] It should be noted that ISEs selectively detect un-complexed ("free") Ag^+. This allowed us, in previous work, to utilize fluorous-phase Ag^+ ISEs to quantify the Ag^+ speciation in bacterial growth media and show that, in cell culture media that are rich in coordinating ligands, less than 5% of the silver is in the free Ag^+ form.[85] We also showed that these sensors can be used for dynamic monitoring of Ag^+ release from silver nanoparticles in the presence of interfering capping agents such as trisodium citrate.[85,242] That work suggested that these sensors would very likely also be useful analytical tools for probing Ag^+ binding to NOM.

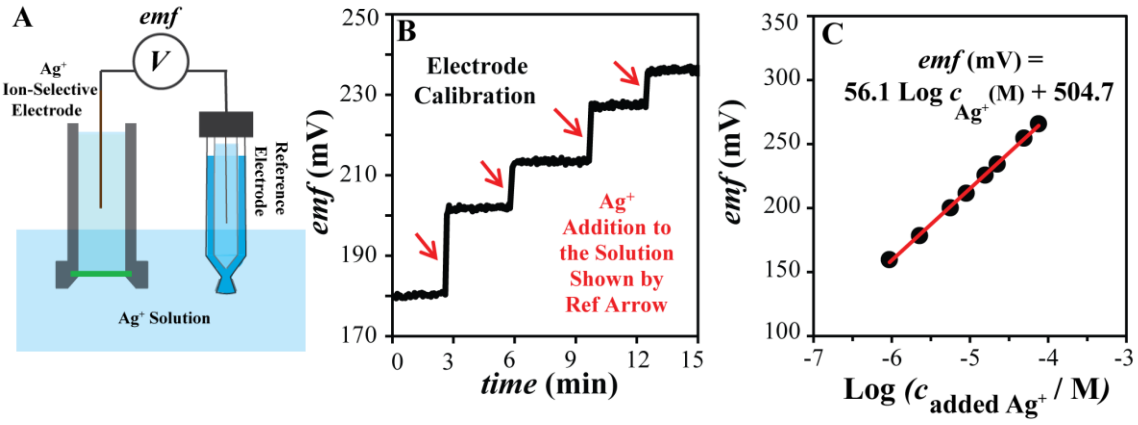

Figure 1. Representative calibration curve of a fluorous-phase Ag^+ ISE. **(A)** Experimental Setup. (B) Red arrows indicate additions of $AgCH_3COO$ aliquots to the measuring solution. The emf of the fluorous-phase Ag^+ ISE increases after each rise in Ag^+ concentration. For better visualization, only a snapshot of the addition experiment is shown. **(C)** The linear relationship between the emf and Log c_{Ag+} can be used as the calibration equation for converting emf values to Ag^+ concentrations.

6.3.2 Interference of the Sample Matrix on Ag^+ Binding to NOM

NOM has both acidic and basic functional groups and, upon introduction into a solution, can affect the pH, which will influence the strength of Ag^+ binding to NOM. For a meaningful evaluation of the extent of Ag^+ binding to NOM it is, therefore, important to choose pH-buffered test solutions that are representative for environmental samples. There have been several reports of silver speciation in silver nanoparticle solutions as well as of Ag^+ binding to NOM that described the use of pH buffer components such as *N*-morpholino-3-propanesulfonic acid (MOPS) or 4-(2-hydroxyethyl)piperazine-1-ethanesulfonic acid (HEPES).[237-239,255-259] HEPES and MOPS were recommended because they were reported not to bind several heavy metal ions such as copper, cadmium, and zinc.[238,260-262] Because HEPES and MOPS contain amino groups (see structure formulas in Scheme S1 in the SI), and because Ag^+ is well known to form stable complexes with

amines, we suspected that HEPES and MOPS form complexes with Ag^+, considerably complicating any speciation studies. The complexation of HEPES and MOPS with Ag^+ was confirmed by monitoring the emf of fluorous-phase Ag^+ ISE. Immediately after addition of HEPES and MOPS to a 5.0 μM Ag^+ solution, the emf decreased, indicating a decrease in the concentration of free Ag^+ as a result of Ag^+ binding to the buffer species (see Figure 2A). To quantify the extent of HEPES and MOPS complexation with Ag^+, HEPES, MOPS, and phosphate buffers (the latter has a low tendency to coordinate with Ag^+) with pH=7.5 and an ionic strength of 0.1 M were prepared, and potentiometric responses to Ag^+ in these pH buffers as well as in deionized water were measured (see Figure S1). Because of Ag^+ binding to the pH buffer components, the calibration curves shifted to lower emf values when the emf was plotted versus the total silver concentration in the calibration solutions (see Figure 2B).[85] Use of the calibration curve obtained in deionized water for comparison (Figure S1) shows that only 10% of the Ag^+ in the MOPS buffer and less than 1% of the Ag^+ in the HEPES buffer is in its free (uncomplexed) form. In contrast, almost 99% of the Ag^+ in the phosphate buffer is in the free and non-complexed form (see Figure 2C). This is of great importance because HEPES and MOPS have been used as pH buffer components in a number of Ag^+ speciation and mechanistic studies without consideration of their high tendency for coordination with Ag^+.[237,238,256,259]

Figure 2D illustrates the extent of HEPES interference in Ag^+ binding to NOM, where Pony Lake fulvic acid (PLFA) was added to 5.0 μM Ag^+ in either HEPES buffer (which competes with NOM in binding to Ag^+) or phosphate buffer (which does not interfere with binding). Both buffers had the same pH (7.5). Upon addition of PLFA to 5.0 μM Ag^+ in the phosphate buffer, the emf is significantly decreased by more than 20 mV (which corresponds to a 50% decrease in the free Ag^+ concentration due to Ag^+ binding to NOM), but a similar addition of PLFA to 5.0 μM Ag^+ dissolved in HEPES buffer resulted in no detectable emf change (two-tailed t test, $p < 0.05$). This can be explained

by considering that 99% of the silver is bound to the HEPES buffer, making it impossible for the PLFA to compete with HEPES to form Ag^+-NOM complexes in a significant amount.

Coordinating ligands such as HEPES and MOPS are not present in authentic environmental samples. To prevent errors in the evaluation of Ag^+ binding to NOM, such buffers should be avoided. Herein, we will utilize a potassium phosphate buffer with an ionic strength of 0.1 M to minimize buffer artifacts. Use of a fixed ionic strength ensures that the activity coefficients are approximately constant and that the interaction of Ag^+ and the NOM is not simply electrostatically driven but is the result of specific metal ligation to functional groups of the NOM.[224] Note that the phosphate buffer is representative of real-life conditions since most high concentration components of real-life samples (i.e., specifically, Na^+, K^+, HCO_3^-, SO_4^{2-}, NO_3^-, F^-, Mg^{2+}, and Ca^{2+}) will not directly interfere with Ag^+ speciation.[85,263] However, chloride, which occurs in natural water supplies in high concentrations, will compete with NOM to bind to Ag^+ and will affect the extent of Ag^+ binding to NOM binding. Therefore, we excluded Cl^- from our test matrix, facilitating the investigation of the extent of Ag^+ binding to NOM and its correlation to protective effects of NOM against Ag^+ toxicity.

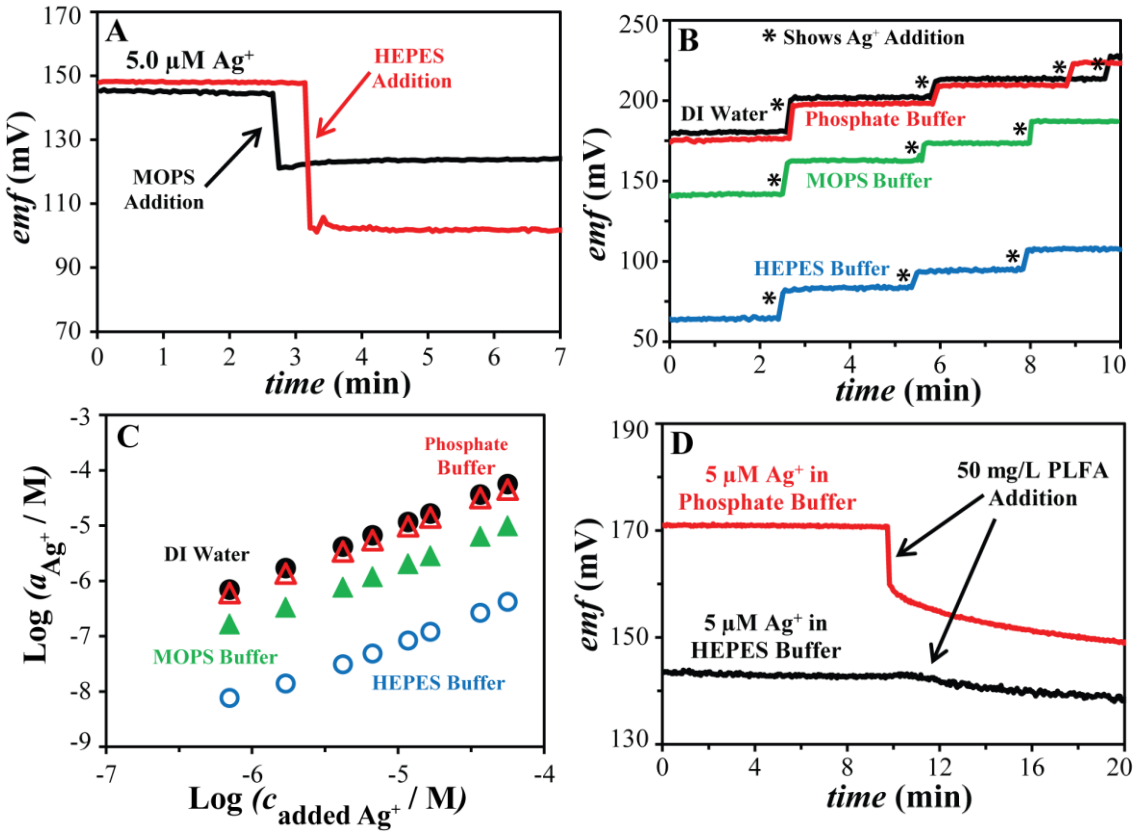

Figure 2. Interference of buffer components on Ag^+ binding to NOM at pH 7.5, as studied by fluorous-phase Ag^+ ISEs. (A) Concentrated HEPES (shown in red) and MOPS (shown in black) were added to 5.0 µM Ag^+ solutions to reach a final concentration of the buffer of 0.05 M. (B and C) Aliquots of $AgNO_3$ were added (shown by asterisks) to deionized water (black), phosphate buffer (pH = 7.5, red), MOPS buffer (pH = 7.5, green), and HEPES buffer (pH = 7.5, blue), while monitoring the emf. The quickness of the emf response is illustrated by the emf time trace shown in Panel A. Panel C shows the concentration of free Ag^+ in the buffer solutions as a function of the total silver concentration in solution, as determined from the calibration curve in buffer free solution. Panel D illustrates the interference of HEPES when studying Ag^+ binding to NOM.

6.3.3 Binding of Ag^+ to NOM

The concentration of NOM in natural environments ranges from 0.1 to 100 mg/L, with a mean value of 45 mg/L.[232,233,264-266] Thus, to cover the most environmentally relevant NOM concentration range, we looked at 50 mg/L NOM in this study. We considered five different NOM isolates: Suwannee River humic acid II (SRHA), Suwannee River fulvic acid II (SRFA), Pony Lake fulvic acid (PLFA), Pahokee Peat humic acid standard, PPHA, and Suwanee River Aquatic NOM (SRNOM). To quantify Ag^+ binding to NOM, fluorous-phase Ag^+ ISEs were placed in a solution of 5.0 μM $AgCH_3COO$ with a pH buffered to 7.5 and a fixed ionic strength. Aliquots of concentrated solutions of NOM were added to this solution, and the emf of the ISE was monitored continuously. The Ag^+ concentration of 5 μM was chosen to mimic the concentration of Ag^+ released from 1-5 mg/L Ag NPs (12-nm-diameter).[85] Results are depicted in Figure 3A. When Ag^+ binds to NOM, the concentration of free Ag^+ is reduced. Consequently, a decrease in the emf is observed. Stronger binding of Ag^+ to NOM results in a larger decrease in the concentration of free Ag^+ ions and, therefore, a greater decrease in the emf values. Addition of SRFA, SRNOM, SRHA, PPHA, and PLFA resulted in 8.5 ± 0.2%, 11.1 ± 2.1%, 15.4 ± 2.0%, 40.4 ± 1.8%, and 57.7 ± 0.2% decreases in the free Ag^+ concentration, respectively (all changes were statistically significant, as assessed by the two-tailed *t* test, $p < 0.05$). It follows that the ability of different NOM types to bind Ag^+ falls in the sequence:

$$PLFA > PPHA > SRHA > SRNOM > SRFA$$

Based on our findings, we conclude that fulvic acid does not bind Ag^+ more or less strongly than humic acid, but it is noticeable that NOM types that are rich in nitrogen show higher binding of Ag^+. Specifically, the nitrogen contents of PLFA and PPHA of 6.5% and 3.7%, respectively, are much higher than for SRHA, SRFA, and SRNOM, which contain 0.7%, 1.2%, and 1.1% nitrogen, respectively.[235] Most of the nitrogen in these NOM samples was shown to be in the form of amides, aminoquinones, amino

sugars, and heterocyclic nitrogen structures, which can all bind Ag^+.[267] Moreover, NOM also contains sulfur-containing functionalities in the form of exocyclic and heterocyclic sulfur and sulfoxide, sulfone, sulfonate, and sulfate groups.[268] It has been shown that the majority of sulfur in SRHA, SRFA, and PLFA is in low oxidation states as exocyclic and heterocyclic sulfur,[268] which binds strongly with Ag^+. Therefore, the high Ag^+ binding ability of PLFA is also the result of its sulfur content (3.0%), which is much higher than in the case of SRFA and SRHA (0.5%).

Our observations are consistent with findings of Sikora and Stevenson, who concluded that amine and thiol functional groups are mainly responsible for Ag^+ complexation while oxygen-containing functional groups have only minor effects on Ag^+ binding to NOM.[224,232,269] This conclusion is also consistent with representative stability constants for oxygen, nitrogen, and sulfur containing functional groups. For example, the stability constants K_{11}, for the 1:1 Ag^+ complexes[224] are 4.4 with the oxygen ligand acetate, 2.1 x 10^3 for ammonia, 2.5 x 10^2 for NEt_3, 1.2 x 10^2 for pyridine, and 6.6 x 10^8 for the sulfur ligand thiosulfate.[270,271] Further research with techniques such as X-ray photoelectron spectroscopy (XPS) or X-ray absorption near edge structure (XANES) spectroscopy could be used to study the identity of the functional groups involved in the binding process.[268,272]

Observing a relatively low Ag^+ binding extent for Suwannee River humic and fulvic acids can explain the discrepancies among published reports on the extent of Ag^+ binding to Suwannee River NOM isolates.[226,237,238,240,244,248] Differences in the experimental conditions used in those studies, such as different pH values, affect the extent of binding and cause contradicting conclusions. To understand the extent of the pH effect, we quantified Ag^+ binding to SRFA and SRHA at pH = 6.0, 7.5, and 9.0 (see Figure S5). Interestingly, at pH = 6.0, no significant change in the free [Ag^+] can be detected upon SRFA and SRHA addition to Ag^+ solutions (two-tailed *t* test, $p < 0.05$), which confirms that Ag^+ does not bind to SRFA or SRHA at acidic pH. Increasing the pH to 7.5 and 9.0

results in 9 ± 2% and 40 ± 1% Ag^+ binding to SRFA, and 16 ± 1% and 55 ± 1% binding to SRHA, respectively (Figure S5). (Increases in extent of Ag^+-NOM binding are significant as assessed by the two-tailed *t* test, $p < 0.05$.) Clearly, the pH at which binding occurs plays a critical role in the extent of Ag^+ and NOM binding when the NOM binds Ag^+ weakly.

Figure 3 also illustrates the kinetics of Ag^+ binding to NOM. Even though binding of Ag^+ to NOM has been studied for more than a decade, and several hypotheses about its kinetics have been proposed, the kinetics of this reaction has not been investigated directly, possibly due to the lack of proper methodology.[225,241,245] The fast response time of fluorous-phase Ag^+ ISEs (< 1.0 s) allows real-time detection of Ag^+ and makes it possible to directly observe the kinetics of Ag^+ binding to NOM. On one hand, after additions of SRHA, SRFA, SRNOM, or PPHA to a Ag^+ solution, the emf decreased in less than 1 s, indicating a fast decrease in the free Ag^+ concentration as the result of fast Ag^+ binding to NOM. No further changes were observed over the following 24 hours, showing that equilibrium was reached very quickly.

On the other hand, after addition of PLFA to 5.0 μM $AgCH_3COO$, the emf did not stabilize after the initial very quick decrease, but continued to drift even after 24 h, albeit at a decreasing rate (see Figure S2). Stepwise addition of PLFA and alteration of the pH of the solution did not eliminate this drift (see Figure S3). To confirm that this behavior was indeed caused by Ag^+ binding to PLFA and not by an artifact of the ISE measurement, the fluorous-phase Ag^+ ISEs were recalibrated after exposure to PLFA, confirming that the fluorous-phase Ag^+ ISEs were still fully functional and that the calibration curve was valid throughout the experiment. Moreover, when fluorous-phase Ag^+ ISEs were inserted into a solution of Ag^+ and PLFA that had been preequilibrated for 24 h, the measured emf did not show any drift, confirming that the observed emf drifts after PLFA addition to the Ag^+ solution were indeed caused by a chemical transformation

in the solution (see Figure S4) and not by some unexplained effect of PFLA on the response of the ISE.

An explanation for the slow decrease in the free silver ion activity after the addition of PLFA to 5.0 μM $AgCH_3COO$ is given by the reduction of Ag^+ to Ag by PLFA as the reducing agent. Indeed, the formation of Ag NPs as the result of Ag^+ reduction by NOM in environmentally relevant conditions at ambient laboratory temperature and lighting was shown by Akaighe and co-workers.[273] Under their experimental conditions, Ag^+ reduction by NOM took, depending on the NOM source and concentration, up to several days before the formation of Ag NPs was visually noticed.[273] Slow Ag^+ reduction by NOM under environmentally relevant conditions was also reported by F. Maurer and co-workers.[241] In this study, formation of Ag NPs through reduction of Ag^+ by PLFA was also confirmed using transmission electron microscopy and dark-field microscopy with hyperspectral imaging (see Figures S7 and S8).

Reduction of Ag^+ by NOM also appears to be consistent with findings by Glover et al., who observed that longer incubation of Ag^+ and NOM before addition to *Daphnia Magna* (a freshwater flea) resulted in lower Ag^+ toxicity.[245] Glover et al. explained the time-dependent toxicity of Ag^+ in the presence of NOM by the hypothesis of slow kinetics of Ag^+ binding to NOM. However, these authors provided no evidence to exclude alternative explanations, such as the reduction of Ag^+ by NOM. Based on the findings from our study and evidence from other studies employing a variety of experimental techniques, we believe that binding of Ag^+ and NOM is fast and that the reduction of Ag^+ by certain types of NOM in environmentally relevant conditions has slow kinetics and contributes to gradual changes in $[Ag^+]$ in NOM-containing media.

An alternative explanation for the slow changes in the free Ag^+ activity could be gradual changes in the macromolecular structure of NOM and, concomitantly, changes in the NOM's ability to bind Ag^+. The conformation of humic substances depends on

physicochemical parameters such as pH, ionic strength, and the composition of the samples,[274] which were all kept constant throughout our experiments with a phosphate pH buffer. Whereas conformational changes of NOM induced by iron complexation have been reported recently,[274,275] evidence that those conformational changes have a major effect on the activity of free iron does not exist. The slow conformational changes induced by the presence of iron may be preceded by comparatively fast binding of iron to NOM. In the case of Ag^+, no reports of such conformational changes of NOM have been made to date.

6.3.4 Effect of NOM on Ag^+ Toxicity

NOM has been reported to reduce Ag^+ toxicity to large and micro-organisms by binding to Ag^+ and reducing the concentration of free Ag^+.[220,246-248,276] After quantifying the extent of Ag^+ binding to different NOM isolates, we were able to assess the validity of the commonly held belief that NOM reduces Ag^+ toxicity to organisms by binding to Ag^+. We employed a bacterial model (*Shewanella oneidensis* MR-1) to study the effect of NOM on silver toxicity. *Shewanella oneidensis* MR-1 is a facultative anaerobe and also a metal reducing bacterium. This respiratory diversity allows it to survive in a variety of locations, e.g., in freshwater, saltwater, and sediments, making it a relevant model to assess the environmental impact of silver-containing products that may leach silver into a variety of natural environments.[197] We assessed changes in membrane integrity of *Shewanella oneidensis* MR-1 (using the LIVE/DEAD BacLight Viability Kit, see Supporting Information) after exposure to Ag^+ with and without NOM, using similar experimental conditions as those used for studying the extent of Ag^+ binding to NOM (pH 7.5, potassium phosphate buffer, 5.0 μM Ag^+, and 51 mg/L NOM). It should be noted that, under nutrient-poor conditions like those employed in these experiments, NOM can serve as a source of nutrition for bacteria and thereby increase their viability. We observed siginficantly higher cell viability (two-tailed *t* test, $p < 0.05$), presented as the ratio of cells identified to be live vs. dead, in the presence of 51 mg/L PLFA, SRFA,

SRHA, PPHA, and SRNOM (with no silver present) than in the absence of NOM (see Figure 3C). Exposing the bacteria to 5.0 μM Ag^+ reduced the live to dead cell ratio from 3.2 (0.0 μM Ag^+ control) to less than 1.0 (see Figure 3C), confirming that Ag^+ is toxic to the bacteria at this concentration. Addition of 51 mg/L NOM induced no significant changes in the toxicity of 5.0 μM Ag^+ to the bacteria in the case of SRFA, SRHA, and SRNOM (shown in purple in Figure 3C). Our finding is consistent with precedent studies that observed no significant effect of SRHA on the toxicity of Ag^+ to *Pseudomonas fluorescen,*[230] *Chlamydomonas reinhardtii,*[237] and *Pseudokirchneriella subcapitata.*[237] As discussed in the previous section, SRNOM, SRFA, and SRHA have a low affinity for Ag^+, and less than 20% of the Ag^+ is bound to NOM present in a concentration of 51 mg/L. Given that these NOM types only decrease the free [Ag^+] slightly (see Figure 3A), we attribute their insignificant effects on the Ag^+ toxicity to *Shewanella oneidensis* MR-1 to their low affinity for Ag^+. Even PPHA with its slightly higher Ag^+ binding affinity (upon binding to Ag^+ reduces its concentration by 50%) did not improve viability of *Shewanella oneidensis* MR-1. This confirms that due to overall weak Ag^+-NOM binding, the NOM-induced changes in Ag^+ concentration do not nessecarily result in significant effects on the Ag^+ toxicity to the *Shewanella oneidensis MR-1*.

Even though PPHA and PLFA showed similar affinities for Ag^+, i.e., 50% binding for PPHA and 60% binding for PLFA, only the addition of PLFA improved the viability of cells exposed to 5.0 μM Ag^+ (the live to dead ratio increased from less than 1.0 to 2.0, two-tailed *t* test, $p < 0.05$), while PPHA had no significant protective effect against Ag^+ toxicity. The latter can be explained based on the gradual decrease in [Ag^+] in presence of PLFA. Immediately following NOM addition to Ag^+, the [Ag^+] was observed to be similar for both PLFA and PPHA (2–3 μM Ag^+). However, during the time that the bacteria were incubated with the Ag^+- and NOM-containing solution, [Ag^+] gradually decreased to less than 1.0 μM, likely due to Ag^+ reduction by PLFA, as explained in the previous section, whereas [Ag^+] remained approximately constant in PPHA-containing solutions. Even though PLFA and PPHA showed similar initial extents of Ag^+ binding,

PLFA reduced the total effective exposure of the cells to Ag^+, resulting in higher cell viability. (Note that 1.0 μM Ag^+ cannot be confirmed to be toxic to the bacteria, while 2.5 μM Ag^+ reduces the viability of *Shewanella oneidensis* MR-1, as shown in Figure S8). Given that PPHA, SRFA, SRHA, and SRNOM all have different binding abilities but exhibit similar effects on Ag^+ toxicity to *Shewanella oneidensis* MR-1, our results demonstrate that the effect of NOM on bacterial cell viability does not necessarily correlate with the extent of Ag^+ binding to NOM, but strongly depends on free Ag^+ concentration. To confirm this, after addition of PLFA or PPHA to 5.0 μM Ag^+, which significantly reduced the free Ag^+ concentration due to binding to NOM, we adjusted the free Ag^+ concentration to 5.0 μM by adding aliquots of $AgNO_3$ to the solution while monitoring the emf using fluorous-phase ISEs (see Figure 3B). $AgNO_3$ was added until the ISE indicated that the concentration of free Ag^+ had again reached 5.0 μM, as was the case before NOM addition. As shown in Figure 3C, a similar toxicity was found for solutions that contained 5.0 μM free Ag^+ and no added NOM as for solutions that contained 5.0 μM free Ag^+ and 51.0 mg/L PPHA or PLFA, despite the fact that the latter solutions contained 3.5 and 5.3 μM complexed silver, respectively.

These findings are important since the protective ability of NOM against Ag^+ toxicity is usually attributed to direct binding of Ag^+ to NOM whereas other forms of speciation, such as NOM-induced Ag^+ reduction and nanoparticle formation, are often ignored. This study provides evidence that the protective ability of NOM against Ag^+ toxicity results both from Ag^+ binding to NOM and NOM-induced Ag^+ reduction, and also shows that lack of NOM effect on Ag^+ toxicity does not exclude the possibility of Ag^+ binding to NOM.

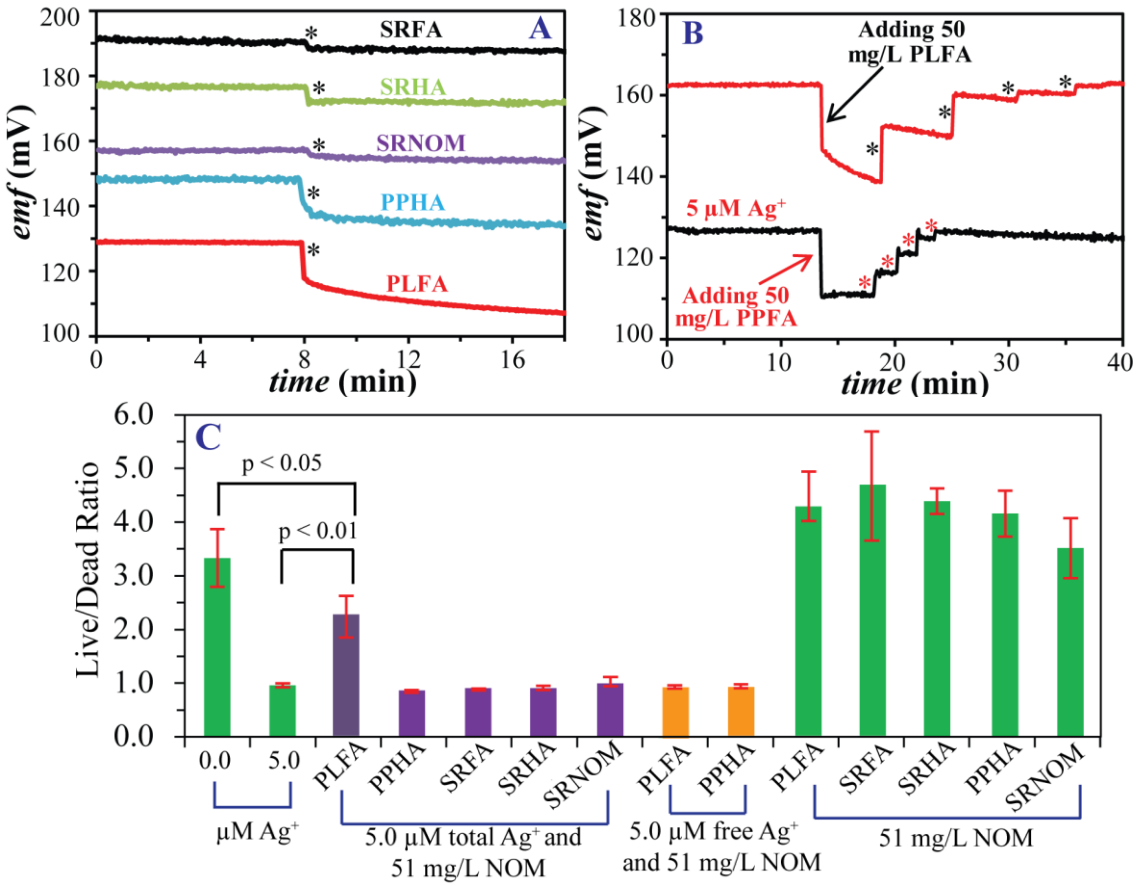

Figure 3. Ag^+ and NOM binding and its effect on Ag^+ toxicity: (A) Shown are the emf values measured with fluorous-phase Ag^+ ISEs in 5.0 µM $AgNO_3$ followed by 51.0 mg/L addition of (indicated by asterisks) of SRFA (black), SRHA (green), SRNOM (purple), PPHA (blue), or PLFA (red). For better visualization, the emf traces are shifted vertically relative to one another. (B) Aliquots of $AgNO_3$ were added (indicated by asterisks) to the Ag^+ and NOM solution to readjust [Ag^+] to 5.0 µM. (C) Viability of *S. oneidensis* after 30 minute exposure to Ag^+ and NOM solutions with specified identities and concentrations. Error bars represent the standard deviation of three biological replicates. Statistical significance was determined using the paired t-test.

6.4 Conclusions

This work has demonstrated that fluorous-phase Ag^+ ISEs are effective tools for the dynamic investigation of Ag^+ binding to NOM as they can be used to monitor the in situ activity of Ag^+ in a time-resolved manner with high selectivity and without the need for substantial sample preparation. The extent of Ag^+ binding to NOM was quantified using these sensors, showing the following trend for Ag^+ binding capacities of different NOM types:

Pony Lake fulvic acid > Pahokee Peat humic acid standard > Suwannee Humic fulvic acid II > Suwanee River Aquatic NOM, SRNOM > Suwannee River fulvic acid II, SRFA

We showed fast kinetics for Ag^+ binding to NOM and slow kinetics for the reduction of Ag^+ by certain types of NOM in environmentally relevant conditions. This is the first report on the kinetics of Ag^+ binding to NOM with time resolution of less than a second. Moreover, we showed that pH affects the extent of Ag^+ binding to NOM binding, where higher pH results in stronger binding. Studies of Ag^+ speciation should ensure that buffer components are selected to avoid unwanted complexation with Ag^+. We showed that buffer compounds such as HEPES and MOPS should be excluded from Ag^+ speciation studies since they form stable complexes with Ag^+ and interfere with NOM binding to Ag^+. Lastly, we showed that the ability of NOM to protect against Ag^+ toxicity does not directly correlate with the extent of Ag^+ binding to NOM. Other aspects of silver speciation, such as NOM-induced Ag^+ reduction and nanoparticle formation, also affect the observed toxicity.

6.5 Acknowledgements

This work was supported by a Graham N. Gleysteen Excellence Fellowship and a UMN Doctoral Dissertation Fellowship for M. P. S. Mousavi, a National Science Foundation MRSEC REU award for C. E. Pérez De Jesús, a University of Minnesota Biotechnology Institute Training Grant and Minneapolis Torske Klubben Graduate Fellowship to I. L.

Gunsolus, a University of Minnesota Heisig/Gleysteen fellowship to K. Hussein, and National Science Foundation (CHE-1152931) funding to C.L. Haynes.

6.6 Supporting Information

6.6.1 Experimental Methods

6.6.1.1 Measurements with Ion-selective Electrodes with Fluorous Sensing Membranes

Ag^+ ion-selective electrodes (ISEs) with fluorous sensing membranes were prepared as reported previously.[51] For preparation of the sensing phase, 0.5 mM ionic sites (sodium tetrakis[3,5-bis(perfluorohexyl)phenyl]borate) and 1.5 mM ionophore (1,3-bis(perfluorooctyl-ethylthiomethyl)benzene)[77] were added to perfluoroperhydrophenanthrene (Alfa Aesar, Ward Hill, MA), and the resulting mixture was stirred for at least 24 h to ensure that all the membrane components had completely dissolved. Fluoropore filters (porous poly(tetrafluoroethylene), 47 mm diameter, 0.45 μm pore size, 50 μm thick, 85% porosity, EMD Millipore, Bedford, MA) were sandwiched between two small pieces of printing paper, and cut with a 13 mm diameter hole punch, giving porous filter disks to mechanically support the sensing phase. Approximately 25 μL of fluorous sensing phase was then applied with a micropipet to a stack of 2 porous filter disks. Full penetration of the fluorous phase sensing membrane into the porous supports was confirmed by a translucent appearance of the filter disks.

The filter disks that contained the fluorous sensing phase were then mounted into custom-machined electrode bodies made of poly(chlorotrifluoroethylene), as described previously.[77] In brief, a screw cap with a hole (8.3 mm diameter) in the center was screwed onto the electrode body, mechanically securing the sensing membrane in between the electrode body and the cap but leaving the center of the membrane exposed. The electrode bodies were then filled with 1 μM $AgCH_3CO_2$ (Sigma Aldrich), and an AgCl/Ag inner reference electrode was inserted into this inner solution. Prior to measurements, all electrodes were soaked first for 24 h in 100 mL 0.1 mM $AgCH_3CO_2$

solution and then for another 24 h in 100 mL 1.0 μM $AgCH_3CO_2$. The same silver salt was used for the inner filling and conditioning solutions.

Potentials were monitored with an EMF 16 potentiometer (Lawson Labs, Malvern, PA) controlled with EMF Suite 1.02 software (Lawson Labs) at room temperature in stirred solutions. The external reference electrode consisted of a double-junction AgCl/Ag electrode with a 1.0 M LiOAc bridge electrolyte and a 3.0 M KCl reference electrolyte. All measurements were performed with at least 3 replicate electrodes. The detection limit was determined by emf measurements of the prepared electrodes in solutions resulting from successive dilutions of 100 μM $AgCH_3CO_2$ (Fig. S1). Calibration curves were obtained by successive additions of aliquots of a 10 mM $AgCH_3CO_2$ solution to deionized water or the pH buffers.

6.6.1.2 Solution Preparation and Binding Measurements

All the solutions were prepared with deionized water (18 MΩ cm specific resistance, EMD Millipore, Burlington, MA). For preparation of the pH = 6.0 buffer, 0.100 M $NaCH_3CO_2$ and 0.006 M CH_3CO_2H were mixed at room temperature, followed by adjustment of the pH by addition of aliquots of NaOH or CH_3CO_2H. The components of the pH = 7.5 buffer were 0.028 M K_2HPO_4 and 0.015 M KH_2PO_4. The pH of the solution was adjusted to 7.5 by addition of aliquots of KOH. The pH = 9.0 buffer contained 0.087 M $NaHCO_3$ and 0.044 M Na_2CO_3, and the pH was adjusted by addition of aliquots of NaOH. The HEPES buffer with pH = 7.5 was prepared by dissolving 0.20 M HEPES, 4-(2-hydroxyethyl)piperazine-1-ethanesulfonic acid, in deionized water, and the pH of the solution was adjusted to 7.5 by addition of aliquots of KOH. The MOPS buffer with pH = 7.5 was prepared by dissolving 0.30 M MOPS, *N*-morpholino-3-propanesulfonic acid, in deionized water, and the pH of the solution was adjusted to 7.5 by addition of aliquots of KOH. (Structures of HEPES and MOPS are provided in Scheme S1.)

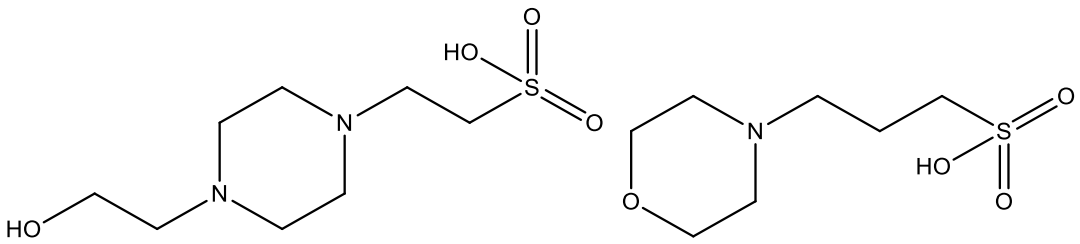

Scheme S1. The structure of HEPES (on the left) and MOPS (on the right)

The components of the phosphate (pH=7.5), carbonate (pH=9.0), and acetate (pH=6.0) pH buffers were chosen to interact minimally with Ag^+ and thus minimize the interference with respect to Ag^+ binding to NOM. The latter was assessed by measurements of the potentiometric response to Ag^+ by fluorous-phase Ag^+ ISEs in deionized water and in pH buffers. The response for deionized water and all the pH buffer solutions were very similar, which confirmed that Ag^+ did not bind significantly to the pH buffer components (less than 15 mV and 2 mV change in the intercept and slope of the calibration equation, respectively). In the case of Ag^+ binding to the pH buffer components, the calibration equation would have shifted to lower emf values because of the lowering of the concentration of free Ag^+ ions as a result of complexation,[85] which must be prevented to avoid errors and an unrealistic evaluation of Ag^+ binding to NOM. Binding of buffer components to Ag^+ occurs in the case of the commonly used HEPES and MOPS buffers, as shown in Figure S2. The calibration equations in Figure S2B are shifted to lower emf values because of Ag^+ complexation with HEPES and MOPS. Using the calibration curve obtained in water, the emf values measured with the HEPES and MOPS buffers were converted to Ag^+ concentrations. This showed that in the MOPS and HEPES buffers 90% and 99% of the added Ag^+ is in the complexed form, respectively (Figure S2C).

Concentrated solutions of Suwannee River humic acid II (SRHA), Suwannee River fulvic acid II (SRFA), and Suwannee River Aquatic NOM were prepared by dissolving 30.0 mg of each in 3.0 ml of deionized water, followed by stirring for at least two hours.

Concentrated solutions of Pony Lake fulvic acid (PLFA) and Pahokee Peat humic acid (PPHA) were prepared in an identical manner and were sonicated for two minutes immediately prior to use (to suspend undissolved material).

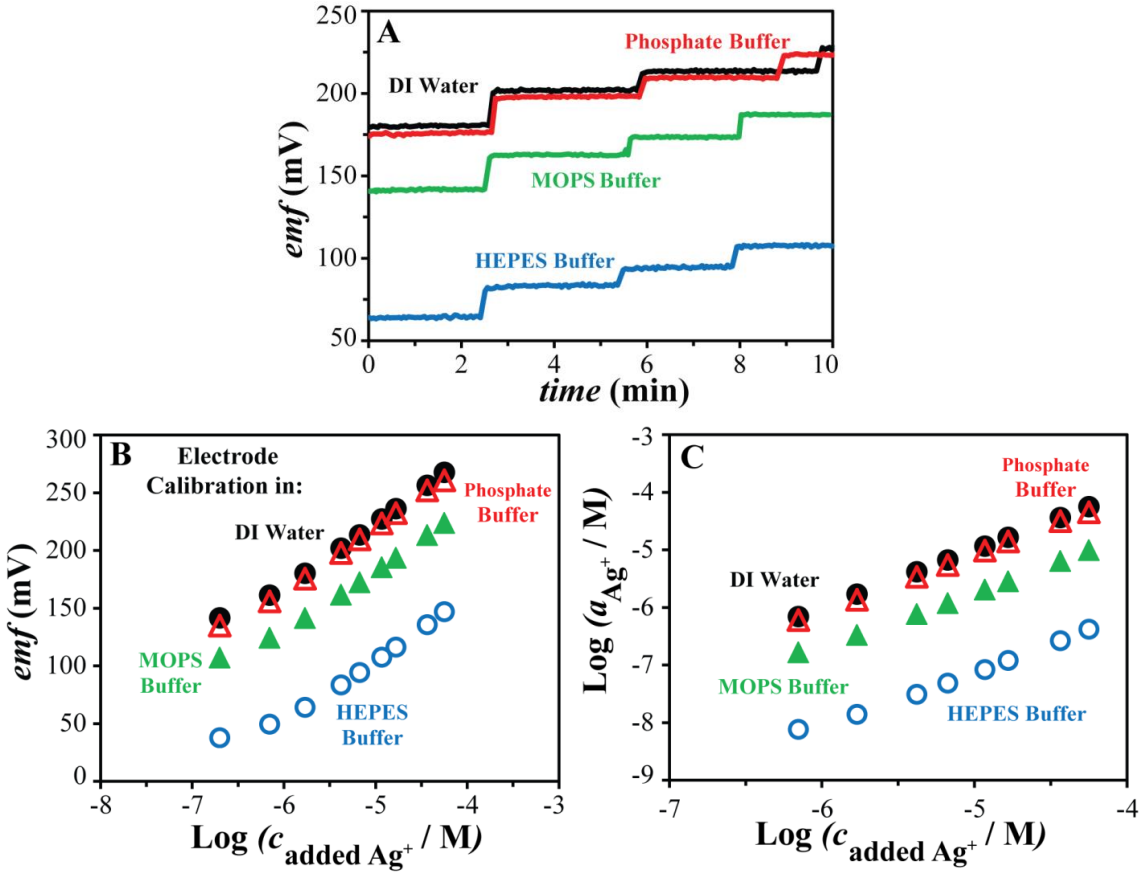

Figure S1. Ag^+ complexation with buffer components studied by fluorous-phase Ag^+ ISEs. Aliquots of $AgNO_3$ were added to deionized water (shown in black), phosphate buffer with pH = 7.5 (shown in red), MOPS buffer with pH = 7.5 (shown in green), or HEPES buffer with pH = 7.5 (shown in blue), while monitoring the emf. A snapshot of the calibration experiments, i.e., emf values over time, is shown in panel A. $AgNO_3$ is added to the solution after approximately 2, 6, and 8 min. Panel B shows the response curve in each pH buffer, and panel C shows the corresponding amounts of free Ag^+ after each $AgNO_3$ addition.

For NOM titration experiments, Ag^+ ISEs were placed in a pH-buffered solution of 1.0 µM $AgCH_3COO$ (pH = 6.0, 7.5, or 9.0), and aliquots of 10.0 g/L NOM were added to this solution while monitoring the emf of the Ag^+ ISEs continuously. In the NOM addition experiments, Ag^+ ISEs were placed in a solution of 5.0 µM $AgCH_3COO$ buffered to pH 7.5, and aliquots of 10.0 g/L NOM were added to this solution to achieve the final concentration of 51 mg/L for the NOM.

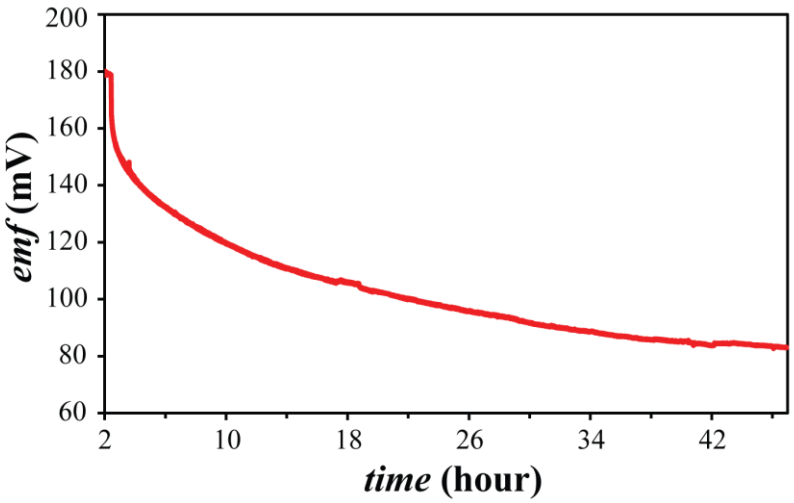

Figure S2. Emf response of a fluorous-phase Ag^+ ISE in a solution containing 5.0 µM Ag^+ and 51 mg/L PLFA over 48 h. The concentration of free Ag^+ decreases by one order of magnitude over 48 h.

6.6.2 Effect of NOM on Toxicity of Ag^+ and Ag NPs

There are several reports that NOM extracted from different sources mitigates the toxicity of Ag NPs to various organisms. The decrease in toxicity is usually attributed to complexation of Ag^+ with NOM. Complexation of Ag^+ with NOM reduces the concentration and bioavailability of the toxic free metal and reduces its ability to interact with the site of toxic action in the organism, resulting in reduced overall toxicity.[226,219]

Examples include reduced toxicity of Ag^+ and Ag NPs to *Pseudomonas fluorescens* in the presence of NOM (Pahokee peat humic acid purchased from the International Humic Substances Society, IHSS),[243] decreased toxicity of Ag NPs to *Daphnia* and *Daphnia magna* with increased concentration of NOM (Suwannee River humic acid II purchased from IHSS and humic acid purchased from Aldrich, St. Louis, MO),[226,244] and mitigated toxicity of Ag NPs to *Daphnia magna* in a dose-dependent manner in the presence of NOM (humic acid purchased from Aldrich).[245] Moreover, protective effects of NOM (humic acid from Aldrich) against toxicity of Ag^+ to *Oncorhynchus mykiss,*[220,246] Japanese medaka embryos,[247] and *Pimephales Promelas*[248] have been reported. On the contrary, in similar toxicity studies, NOM (Suwannee River humic acid II purchased from IHSS) had no significant effect on the toxicity of Ag^+ to *Pseudomonas fluorescens,*[230] *Chlamydomonas reinhardtii,*[237] and *Pseudokirchneriella subcapitata.*[237] Clearly, these discrepancies in the literature make it difficult to assess toxicity trends and point to the need for time-resolved measurements of Ag species in controlled environments.

6.6.3 Kinetics of Ag^+ and NOM binding

For Ag^+ speciation studies, the ability to detect Ag^+ in real time with high time resolution gives ion-selective potentiometry a distinct advantage over conventional techniques. The response time of fluorous-phase Ag^+ ISEs is very fast (< 1.0 s), which allows the investigation of the kinetics of Ag^+ binding to NOM. In this work, fluorous-phase Ag^+ ISEs were immersed in a solution of 1 μM $AgCH_3COO$ buffered to pH = 6.0, 7.5, or 9.0 (ionic strength, 0.1 M), and aliquots of concentrated NOM were added to these solutions while the response of the ISEs was monitored continuously. After additions of SRHA and SRFA, a decrease in the emf was observed in less than 1 s, which is indicative of fast complexation of Ag^+ and NOM and a concomitant decrease in the free silver concentration, $[Ag^+]$. No further changes were observed thereafter, showing that equilibrium was reached very quickly (see Figures 3A and 3B). While Figure S4 shows

representative results for pH = 9.0 only, similar results were obtained for pH = 6.0 and 7.5.

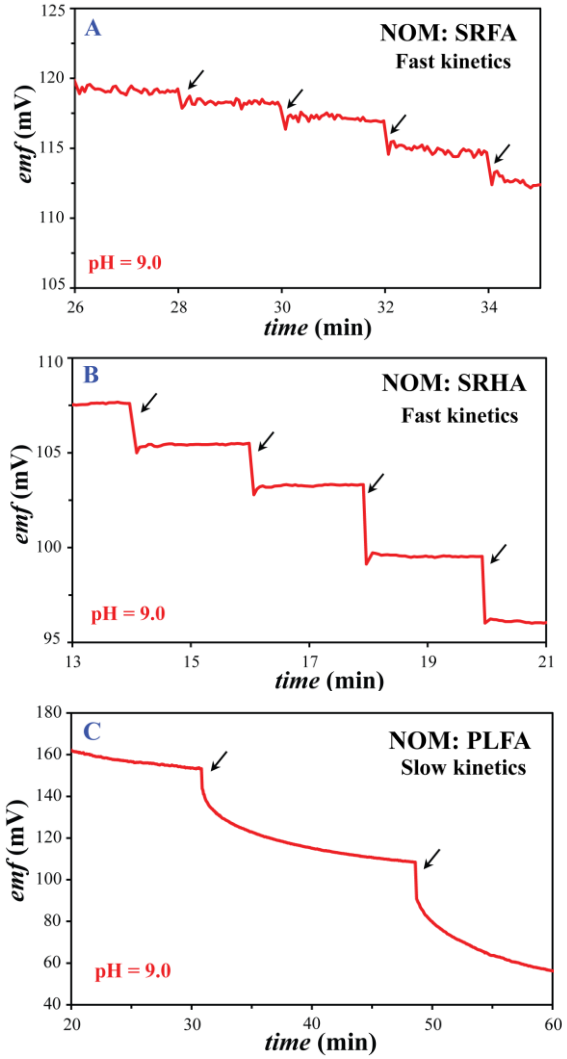

Figure S3. Kinetics of Ag^+ binding to NOM at pH 9: Addition of NOM to 1.0 µM $AgCH_3COO$. Fast binding kinetics is observed for SRFA (4A) and SRHA (4B), whereas Ag^+ binding to PLFA is slow (4C). Similar results were obtained for pH 6.0 and 7.5.

In contrast, after addition of PLFA to 1.0 µM $AgCH_3COO$, the initial decrease in the emf was not followed by a constant emf value, but rather the emf continued to decrease

slowly. At low concentrations of PLFA (less than 11.0 mg/L), each addition caused the emf to drift to lower values over 10 to 20 min before the emf became stable (see Figure S4C). At higher PLFA concentrations (11.0 to 51.0 mg/L), up to 10 h were required for the emf to exhibit a drift smaller than 0.1 mV/min. To confirm that the observed emf drift was indeed caused by Ag^+ binding to PLFA and was not caused by an experimental artifact, two experiments were performed. First, after the PLFA was added to the pH (6.0, 7.5, or 9.0) buffer solution and a stable emf was reached, the fluorous-phase Ag^+ ISEs were recalibrated. Similar calibration curves were obtained before and after the PLFA addition experiment, confirming that the fluorous-phase Ag^+ ISEs were not affected by biofouling and were still fully functional after exposure to PLFA. Moreover, the fluorous-phase Ag^+ ISEs were immersed in a preequilibriated solution of 1.0 µM $AgCH_3COO$ and 51 mg/L PLFA. The result of this latter experiment is shown in Figure S5. The emf values measured in the preequilibriated solutions prepared with 1 µM $AgCH_3COO$ and 51 mg/L PLFA solution were stable and were much lower than for a 1.0 µM $AgCH_3COO$ solution. This confirms that the observed drifts in the emf after addition of PLFA to the 1.0 µM $AgCH_3COO$ are indicative of a chemical transformation in the solution.

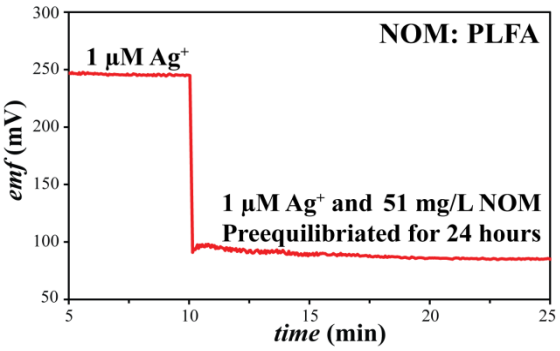

Figure S4. Emf response of a fluorous-phase Ag^+ ISE, first in 1.0 µM $AgCH_3COO$ solution, and then in a preequilibriated solution of 1.0 µM $AgCH_3COO$ and 51 mg/L PLFA.

6.6.4 Effect of pH on Ag^+ binding to SRHA, SRFA, and PLFA

To investigate the effect of pH on Ag^+ binding to SRHA, SRFA, and PLFA, we studied Ag^+ complexation in three different pH buffers with pH = 6.0, 7.5, or 9.0 as representatives for acidic, neutral, and basic solutions. To keep the ionic strength constant, all pH buffers used in this study had an ionic strength of 0.1 M. To quantify the complexation of Ag^+ and NOM, fluorous-phase Ag^+ ISEs were placed in a solution of 1.0 μM $AgCH_3COO$ with a buffered pH (pH = 6.0, 7.5, and 9.0) and fixed ionic strength, aliquots of concentrated solutions of NOM were added to this solution, and the emf of the fluorous-phase Ag^+ ISE was monitored continuously. The results are depicted in Figure S5. When Ag^+ binds to NOM, the concentration of free Ag^+ is reduced. Consequently, a decrease in the emf is observed. Additions of aliquots of all the NOM types resulted in larger emf changes at higher pH than at lower pH (Figures S6A, B, and C). Stronger binding of Ag^+ to NOM resulted in a bigger change in $[Ag^+]$ (Figure S6D, E, and F) and, therefore, a greater decrease in the emf values. The effect of pH on Ag^+ and NOM complexation can be explained by the competition between Ag^+ and H^+ for binding to NOM;[232,224] increasing the pH lowers the H^+ concentration, and thus favors complexation with Ag^+. As expected from Le Châtelier's principle, increasing the concentration of NOM results in decreasing $[Ag^+]$ and an increasing concentration of Ag^+-NOM complexes;[232] the latter is observed for all NOM types in all three pH buffers (see Figure S6).

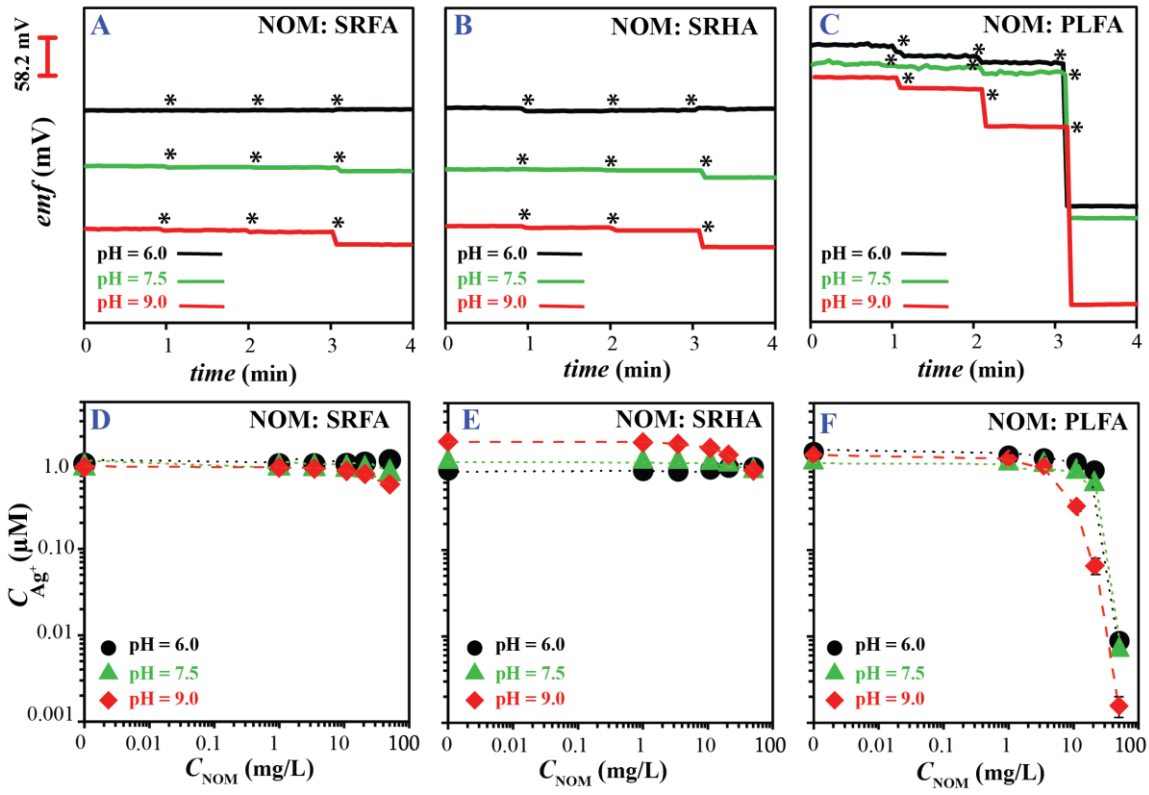

Figure S5. Effect of pH and NOM source on Ag^+ and NOM complexation: Shown are the emf values (at equilibrium) measured with fluorous-phase Ag^+ ISEs in 1.0 μM $AgCH_3COO$ with 0.0, 3.5, 11.0, and 51.0 mg/L (indicated by asterisks) SRFA (A), SRHA (B), and PLFA (C) for three pH buffers (pH = 6.0, black; pH= 7.5, green; pH= 9.0, red). The corresponding Ag^+ concentrations are shown in D, E, and F. For better visualization, the emf traces are shifted vertically relative to one another. Error bars are shown for three replicate measurements (in some cases the data label conceals the error bars.)

Interestingly, SRHA and SRFA bind Ag^+ only weakly. At pH = 6.0, no significant change in the free [Ag^+] can be detected (Figures S6 A, B, D, and E). At neutral pH, weak complexation can be observed for SRHA and SRFA. For example, at 51 mg/L SRHA, 20% of the silver ions in the 1.0 μM $AgCH_3COO$ solution is in the complexed

form whereas at the same concentration of SRFA, only 11% of the silver ions are in the complexed form. The difference in Ag^+ binding ability of SRHA and SRFA is also noticeable at higher pH. SRHA shows slightly stronger binding of Ag^+ than SRFA, i.e., a 55% decrease in concentration of Ag^+ at 51 mg/L SRHA at pH = 9.0 was observed, while a 38% decrease in concentration of Ag^+ was found for 51 mg/L SRFA at pH = 9.0.

Our data show limited Ag^+ binding to SRHA at pH 6.0, which is in agreement with findings by Z. Chen and co-workers, who used the ion exchange equilibrium and equilibrium dialysis techniques and found no significant binding of Ag^+ to SRHA at pH 5.5.[237] Weak binding of Ag^+ to SRHA also explains why SRHA had no significant effect on the toxicity of Ag^+ to *Pseudomonas fluorescens*,[230] *Chlamydomonas reinhardtii*,[237] and *Pseudokirchneriella subcapitata.*[237]

6.6.5 Confirmation of Ag NP Formation as a Result of Ag^+ Reduction by PLFA using Dark-field Microscopy with Hyperspectral Imaging and Transmission Electron Microscopy, TEM

To confirm that Ag^+ is reduced by PLFA, forming Ag NPs and changing the emf response over time, we used dark-field microscopy with hyperspectral imaging and also TEM. Dark-field micrographs of solutions containing either only Ag^+ or Ag^+ and PLFA were acquired using a modified Olympus microscope (vide infra). Then a visible-near infrared (VNIR) spectral map of the imaged area (consisting of spectra from each pixel within the imaged area and referred to here as a hyperspectral image) was acquired in each case. This was accomplished by recording the scattered light intensity across the VNIR using an in-line spectrophotometer and CCD camera as the sample was incrementally moved into the spectrograph's field of view on an automated sample stage. Assessment of Ag NP formation in solutions of Ag^+ or Ag^+ and PLFA was accomplished by comparing these hyperspectral images to those acquired from a reference solution of Ag NPs (see Figure S7). Areas of high spectral similarity between the solutions in

question and the reference solution of Ag NPs were identified using the Spectral Angle Mapping feature of ENVI 4.8 software (Exelis Visual Information Solutions, Boulder, CO), and were taken as evidence of Ag NP formation. A 3 µL aliquot was removed from each solution (1 µM Ag^+ or 1 µM Ag^+ with 51 mg/L PLFA in pH 7.5 buffer after 24 h incubation in the dark at room temperature), placed onto a glass slide, and covered with a glass coverslip. Dark-field micrographs were acquired on an Olympus BX43 microscope (Olympus America, Center Valley, PA) modified with a high signal-to-noise darkfield condenser unit from CytoViva (Auburn, AL), 150 W quartz-halogen lamp (Fiber-Lite DC-950, Dolan-Jenner Industries, Boxborough, MA), 100x 1.3 NA oil-immersion objective, and 12 bit CCD camera (pco.pixelfly, PCO, Kelheim, Germany). Hyperspectral images were acquired in the same field of view using the CytoViva hyperspectral imaging system consisting of a spectrophotometer (Specim, Oulu, Finland) with an integrated CCD (pco.pixelfly, PCO, Kelheim, Germany). Data were analyzed using the Spectral Angle Mapping feature of ENVI 4.8 software.

The dark-field images of 1.0 µM Ag^+ and 51 mg/L PLFA incubated for 24 h are shown in Figures S7A and S7B. Regions of these dark-field images identified to have significant spectral similarity to a reference solution of silver nanoparticles are indicated by bright pixels in Figure S7C and S7D. These images indicate that whereas a small number of Ag NPs were formed in a 1.0 µM Ag^+ lacking PLFA, the abundance of Ag NPs increased with PLFA addition.

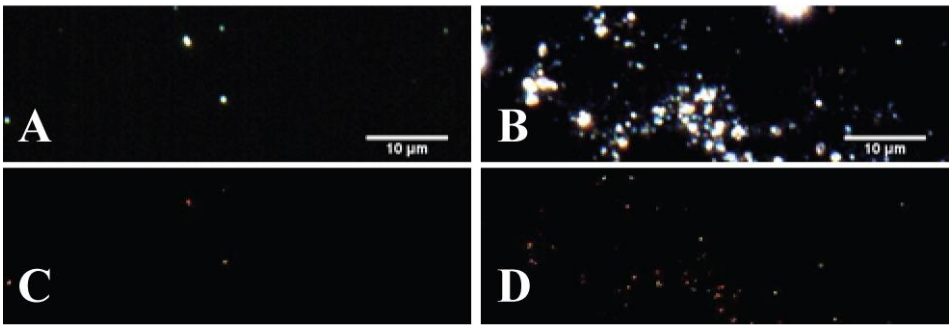

Figure S6. Dark-field microscopy and hyperspectral imaging show that silver nanoparticle formation in a 1.0 µM Ag^+ solution is greater in the presence of 51 mg/L PLFA (right) than in its absence (left). The top panels show dark-field micrographs of silver nanoparticles formed from a 1.0 µM Ag^+ solution in the absence (A) and presence (B) of 51 mg/L PLFA after 24 h incubation. The bright features in the bottom panels, C and D, indicate regions in the dark-field micrographs above that have high spectral similarity to a silver nanoparticle reference solution (not shown). This confirms the identity of the silver nanoparticles.

Further confirmation of Ag NP formation in solutions of Ag^+ with PLFA was obtained using transmission electron microscopy (TEM). Solutions of Ag^+ and PLFA incubated for 24 h, as well as controls consisting of pure buffer, Ag^+ alone, and PLFA alone, were loaded onto 200 mesh copper grids with Formvar and carbon supports (Ted Pella). Micrographs were then acquired using a JEOL 1200 EXII microscope operating at 120 kV. The higher electron density of Ag NPs relative to the background carbon grid results in lower electron transmission intensities and high contrast, facilitating detection of Ag NP formation in these solutions. As shown in Figure S8, Ag NP cluster formation was observed in a solution of Ag^+ with PLFA, but no Ag NPs were observed in the control solutions. Areas of high contrast observed in the pure buffer (Figure S8 D) and a solution of Ag^+ (Figure S8 E) that lacked the spherical form characteristic of Ag NPs were attributed to salt crystals.

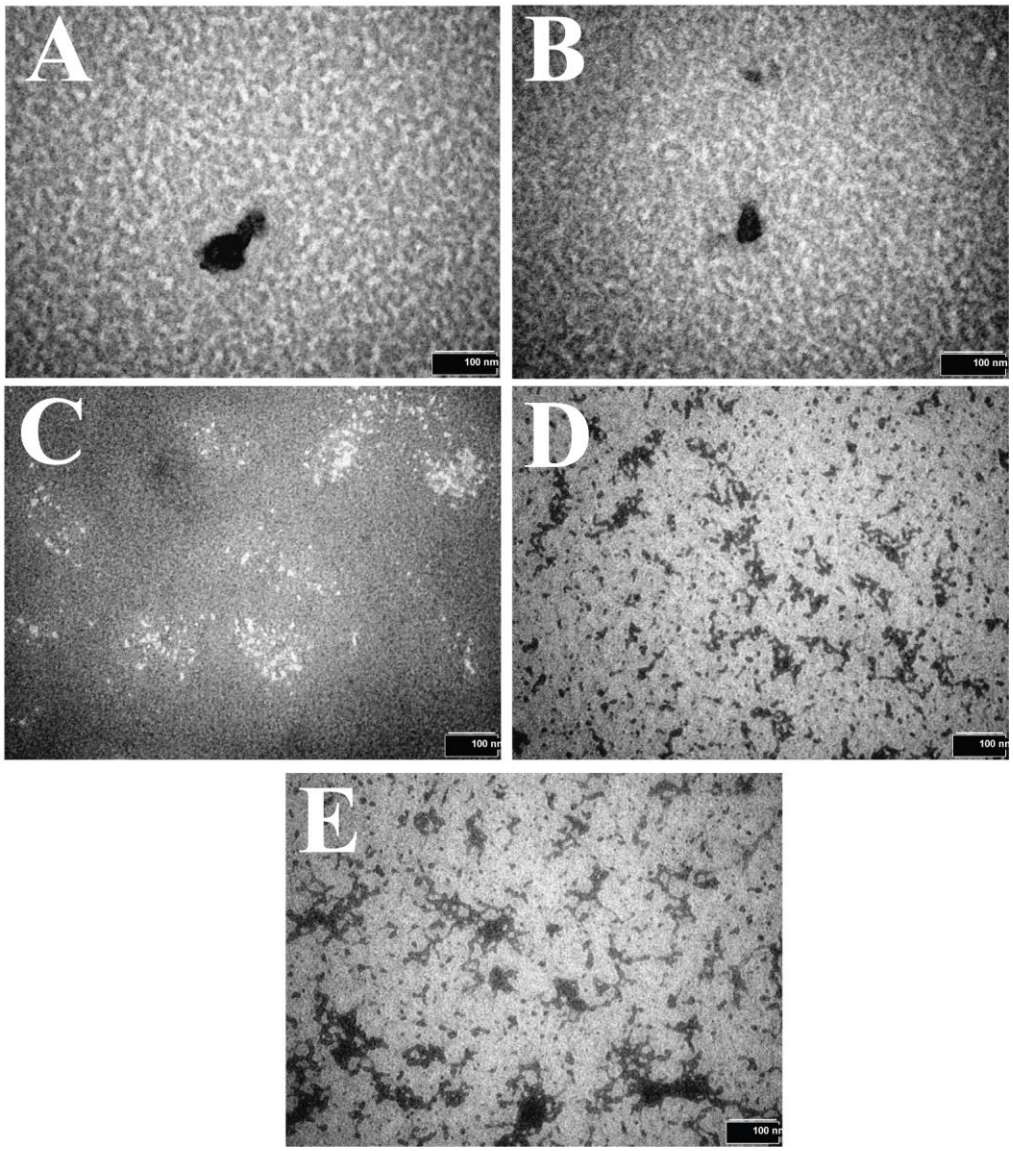

Figure S7. Confirmation of nanoparticle formation through Ag^+ reduction by PLFA. TEM images of 5 μM Ag^+ with 51 mg/L PLFA incubated for 24 h in A and B, only 51 mg/L PLFA in C, pure buffer in D, and 5.0 μM Ag^+ in E are shown. The distinctive dark spots in A and B represent the nanoparticles. In all images, the scale bar represents a length of 100 nanometers.

6.6.6 Silver Toxicity to Shewanella oneidensis

We evaluated bacterial membrane integrity after exposure to Ag^+ (using $AgNO_3$ as the source of Ag^+) using the LIVE/DEAD BacLight Viability Kit (Product L-7012, Life Technologies). *Shewanella oneidensis* MR-1 was cultured on LB agar plates over 24 h and was then inoculated into LB broth. After 1 h, cells were harvested by centrifugation at 2000 rcf (10 min) and resuspended in pH 7.5 phosphate buffer (cell concentration = 2 x 10^8 cells/mL). Then 1 mL aliquots of the cell suspension were mixed with $AgNO_3$ to achieve the desired Ag^+ exposure concentration. For experiments involving NOM, stock $AgNO_3$ solutions were incubated with NOM for 2 h in the dark prior to bacterial exposure. Cells were incubated with the $AgNO_3$ solutions for 30 min at room temperature and were then harvested by centrifugation at 2000 rcf (10 min). The cells were resuspended in pH 7.5 phosphate buffer after removing the supernatant. Then 100 µL of each cell suspension was mixed with 100 µL of a mixture of 3.34 mM Syto-9 and 20 mM propidium iodide in a 96 well plate. These reagents were provided in the BacLight Viability Kit described above.

Samples were incubated for 15 min at room temperature, and then the fluorescence emission intensities at 528/20 nm (Syto-9 emission) and 635/32 nm (propidium iodide emission) were measured on a Synergy 2 Multi-Mode Reader (BioTek, Winooski, VT) using an excitation wavelength of 485/20 nm. The ratio of the Syto-9 to propidium iodide emission intensities, representing the ratio of cells with intact membranes to those with damaged membranes, was then calculated. Exposing the bacteria to 2.5 µM Ag^+ reduced the live to dead cell ratio from 3.2 (0.0 µM Ag^+ control) to less than 2.5, confirming that Ag^+ is toxic to the bacteria at this dose.

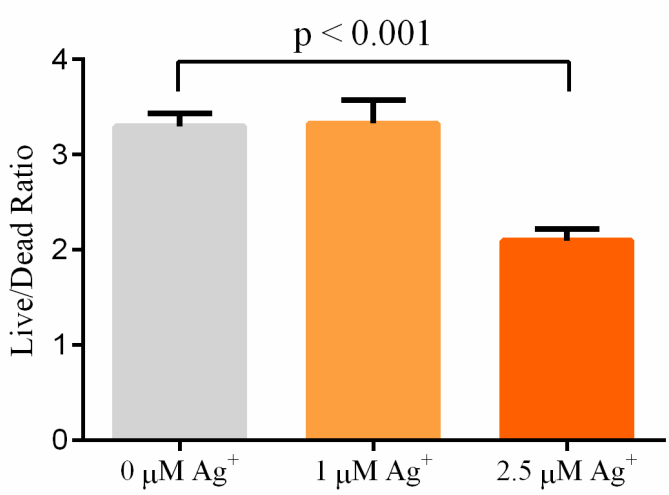

Figure S8. Toxicity of 1.0 μM and 2.5 μM Ag^{+} to *Shewanella oneidensis.*

7 CHAPTER SEVEN

Effect of Natural Organic Matter on the Toxicity and Speciation of Silver

Adapted from:

Gunsolus, I. L.; Mousavi, M. P. S.; Hussein, K.; Bühlmann, P.; Haynes, C. L., Effects of Humic and Fulvic Acids on Silver Nanoparticle Stability, Dissolution, and Toxicity. *Environ. Sci. Technol.* **2015,** *49* (13), 8078-8086.

.

This work was a joint effort by this author and Ian Gunsolus who carried out the synthesis and characterization of silver nanoparticle and toxicity assesments and Kadir Hussein (undergraduate student mentored by Ian Gunsolus) who assisted with toxicity experiments.

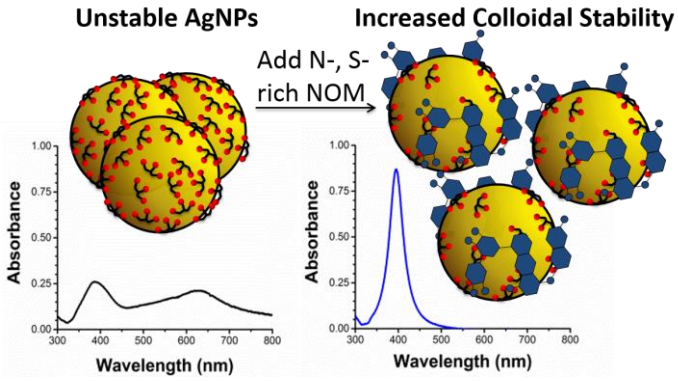

The colloidal stability of silver nanoparticles (AgNPs) in natural aquatic environments influences their transport and environmental persistence, while their dissolution to Ag^+ influences their toxicity to organisms. Here, we characterize the colloidal stability, dissolution behavior, and toxicity of two industrially relevant classes of AgNPs (i.e., AgNPs stabilized by citrate or polyvinylpyrrolidone) after exposure to natural organic matter (NOM), i.e., Suwannee River Humic and Fulvic Acid Standards and Pony Lake Fulvic Acid Reference. We show that NOM interaction with the nanoparticle surface depends on (i) the NOM's chemical composition, where sulfur- and nitrogen-rich NOM more significantly increases colloidal stability, and (ii) the affinity of the capping agent for the AgNP surface, where nanoparticles with loosely bound capping agents are more effectively stabilized by NOM. Adsorption of NOM is shown to have little effect on AgNP dissolution under most experimental conditions, the exception being when the NOM is rich in sulfur and nitrogen. Similarly, the toxicity of AgNPs to a bacterial model (*Shewanella oneidensis* MR-1) decreases most significantly in the presence of sulfur- and nitrogen-rich NOM. Our data suggest that the rate of AgNP aggregation and dissolution in aquatic environments containing NOM will depend on the chemical composition of the NOM, and that the toxicity of AgNPs to aquatic microorganisms is controlled primarily by the extent of nanoparticle dissolution.

7.1 Introduction

Silver nanoparticles (AgNPs) are the most commonly used engineered nanomaterial in consumer products, serving primarily as antimicrobial agents (e.g., in fabrics and ointments). Common product uses can result in leaching of AgNPs into water (e.g., through laundering or skin cleansing), which is expected to be the major route for AgNPs to enter the wastewater supply.[179,277] While a recent study demonstrated high removal efficiency of AgNPs in municipal waste water treatment plants,[278] AgNPs are also expected to enter natural environments through direct discharge from manufacturing and disposal of consumer and medical products that may circumvent wastewater treatment.[179,182,279] Given the potential for AgNP entry into environments and their known toxicity to microorganisms,[280] significant efforts are being made to identify the material and environmental parameters that control AgNP behavior and environmental impact.

AgNPs that enter natural aquatic environments encounter variable temperature, pH, light illumination, ionic strength, dissolved molecular oxygen concentration, and natural organic matter (NOM) concentration and composition. Each of these parameters has the potential to influence nanoparticle colloidal stability. These factors can also influence AgNP dissolution to give Ag^+ (a process that depends on proton and molecular oxygen concentration),[186] which is suggested to be the primary mode of AgNP toxicity to microorganisms.[181,183,281,282] Among the potential transformations of AgNPs entering natural aquatic environments, the least understood are those affected by NOM. A survey of the literature reveals variable effects of NOM on AgNP stability and dissolution, which appears to be caused by the high heterogeneity of NOM and the many AgNP models (in terms of size and surface chemistry) that have been employed.

Several studies demonstrated that addition of purified, naturally extracted NOM at low parts-per-million concentrations decreases homoaggregation rates (i.e., increases colloidal stability) of AgNPs; this applies to both AgNPs electrostatically stabilized with a citrate capping agent and sterically stabilized with polyvinylpyrrolidone (PVP) as

capping agent.[239,283,284] Similarly, increased stability of citrate-capped AgNPs in unpurified NOM suspensions was observed.[200] A few notable exceptions to this trend were reported. For example, fulvic acids isolated from a reference site in a Norwegian lake, despite having very similar elemental composition to Suwannee River fulvic acid models that were shown to stabilize AgNPs, had no effect on AgNP stability at equivalent or higher NOM concentrations.[188] Additionally, decreased colloidal stability of PVP-capped AgNPs following addition of cysteine (a simple model for protein-rich NOM) was observed in at least two studies.[187,285] Our current understanding of NOM's impact on AgNP colloidal stability is complicated by results obtained using a wide range of nanomaterial-stabilizing agents and NOM types, and the general notion that NOM, despite its high chemical heterogeneity, can be considered as a class of molecules to have common patterns of interaction with AgNPs. Here, we identify the characteristics of NOM that most significantly impact the colloidal stability of AgNPs by employing in a single study a series of NOM types with variable chemical composition and nanoparticle capping agents.

The kinetics of AgNP dissolution, the equilibrium concentration of released Ag^+, and complexation reactions of released Ag^+ have been studied under variable solution conditions and with variable AgNP types. Discrepancies exist in the literature regarding the effect of NOM (either macromolecular or small molecule NOM models) on the extent of AgNP dissolution. Liu et al. observed decreased AgNP dissolution in presence of thiol-containing species (e.g., cysteine and glutathione), which they attributed to a reduction in surface sites prone to oxidation.[286] In contrast, Gondikas et al. demonstrated increased dissolution of citrate- and PVP-capped AgNPs in the presence of cysteine.[187] The latter authors attributed the discrepancy between the two studies to differences in sample preparation (specifically, the possibility for analyte retention and loss when using centrifugal filter units).[187] Further studies employing other NOM models observed either significantly increased[287,288] or decreased[186,276] dissolution of AgNPs with increasing NOM concentration. We note that the majority of dissolution studies employ

measurements of total Ag concentration, without discriminating between free Ag^+ and Ag^+-NOM complexes, though our previous work demonstrated that Ag^+ binding to NOM can in some cases mitigate Ag^+ toxicity to bacteria.[289] In light of the important role of dissolved Ag^+ (and Ag^+-NOM complexes) to AgNP toxicity,[181,289] and to address existing discrepancies in the literature, we used fluorous-phase Ag^+ ion-selective electrodes (ISEs) for in situ detection of AgNP dissolution by monitoring the Ag^+ concentration. Fluorous-phase Ag^+ ISEs were previously shown to be powerful tools for dynamic monitoring of AgNP dissolution in complex media.[85]

Several studies observed reduced toxicity of AgNPs towards a number of organismal models in presence of NOM, but the mechanism of this effect remains unclear. Studies using bacterial models such as *Pseudomonas fluorescens*[243] and *Escherichia coli*[276] suggested the primary mechanism to be complexation of Ag^+ with NOM, reducing its bioavailability or bactericidal activity. Other studies using *Pseudomonas fluorescens*[230] and the nematode *Caenorhabditis elegans*[290] suggested that NOM adsorption to AgNP surfaces (possibly decreasing total Ag^+ release or modulating nanoparticle adsorption to or internalization by organisms) is the primary mechanism of toxicity mitigation. Through parallel measurements of Ag^+ concentration and AgNP toxicity to a bacterium (*Shewanella oneidensis* MR-1), this study provides a more direct means to evaluate the mechanism of NOM mitigation of AgNP toxicity than was previously possible. It seeks to provide new insight on the molecular interaction of NOM with commercially relevant AgNPs stabilized with citrate or PVP. By employing a series of NOM models to represent major NOM classes, we arrive at fundamental and generalizable conclusions about AgNP–NOM interactions. Using in situ characterization, we avoid sample preparation errors that may have contributed to conflicting interpretations of prior results.

7.2 Experimental

Citrate-capped AgNPs were prepared using a reported method.[200] PVP-capped AgNPs were prepared by incubating citrate-capped AgNPs with excess PVP-10 (average

molecular weight 10,000 g/mol, Sigma Aldrich), followed by purification. Ligand exchange was confirmed by zeta potential measurements, while particle size was determined using transmission electron microscopy. For details see the Supporting Information.

Stock solutions of 10 g/L NOM (Suwannee River Humic Acid Standard II, Suwannee River Fulvic Acid Standard II or Pony Lake Fulvic Acid Reference, International Humic Substances Society, St. Paul, MN) were prepared in deionized water and mixed with aliquots of purified and concentrated AgNP suspensions to achieve a 600 mg/L NOM concentration. Nanoparticles incubated with NOM in the dark without mixing for 18 h, followed by,redispersion in 0.1 M ionic strength potassium phosphate buffer (pH 7.5, 5 mg Ag/L, 10 mg/L of bulk NOM; acrylic cuvettes).

7.3 Results and Discussion

7.3.1 Impact of NOM and nanoparticle capping agents on AgNP colloidal stability

AgNPs were prepared with either a citrate or PVP-10 capping agent to represent two major classes of industrially relevant AgNPs. TEM micrographs (Supporting Information, Figure S1) reveal no appreciable change in AgNP morphology after exchanging citrate for PVP-10, demonstrating that nanoparticle surface functionalization can be varied independently from morphology. The average particle diameters of citrate- and PVP-capped AgNPs were calculated to be 12.1 ± 2.4 nm and 15.5 ± 4.1 nm, respectively, based on TEM analysis of 500 nanoparticles, indicating a statistically significant ($p < 0.001$) but minor difference in nanoparticle size. Replacement of citrate by PVP-10 was probed by measuring the nanoparticle zeta potential. The latter decreased significantly with exchange to PVP-10, from -32.8 ± 2.2 to -13.6 ± 3.6 mV. These values are consistent with at least partial replacement of negatively charged citrate with neutral PVP-10 (Figure S1), and are in agreement with literature values for PVP-capped AgNPs prepared directly.[186,291,292]

Initially, AgNPs were exposed to 10 mg/L NOM, chosen to fall within the concentration range of natural freshwaters (1-60 mg/L).[293] Three types of NOM were used: Suwannee River fulvic acid (SRFA) and Suwannee River humic acid (SRHA) have similar elemental compositions[235] (see Table S1) and represent NOM fractions derived primarily from decomposition of vegetation.[235] Pony Lake fulvic acid (PLFA) represents NOM rich in sites with high affinity for metallic silver and Ag^+ (due to high sulfur and nitrogen content,[235] a subset of which has a high affinity for silver and Ag^+;[289] see Table S1). It is derived exclusively from microbial matter decomposition.[235] None of these had a detectable effect on AgNP colloidal stability when present at a concentration of 10 mg/L, as determined by UV-visible extinction spectroscopy (Figure S2). This technique was used to demonstrate changes in AgNP aggregation by monitoring the intensity and position of size-dependent extinction peaks due to the localized surface plasmon resonance effect.

In subsequent experiments, AgNPs were exposed to a larger concentration of NOM (600 mg/L) prior to colloidal stability assessment to promote NOM interaction with the AgNP surface. This simulates, on an accelerated time-scale, particle acquisition of adsorbed NOM, which is expected to take place over longer time periods in natural aquatic environments containing lower NOM concentrations. Following redispersion in a high ionic strength (0.1 M) buffer, the bulk NOM concentration during colloidal stability assessment was 10 mg/L. The ionic strength was chosen to ensure that the interaction of NOM with the AgNP surface was not purely electrostatic while remaining representative of natural aquatic systems.[294] Nanoparticle colloidal stability was monitored over two days again using UV-visible extinction spectroscopy (Figure 1).

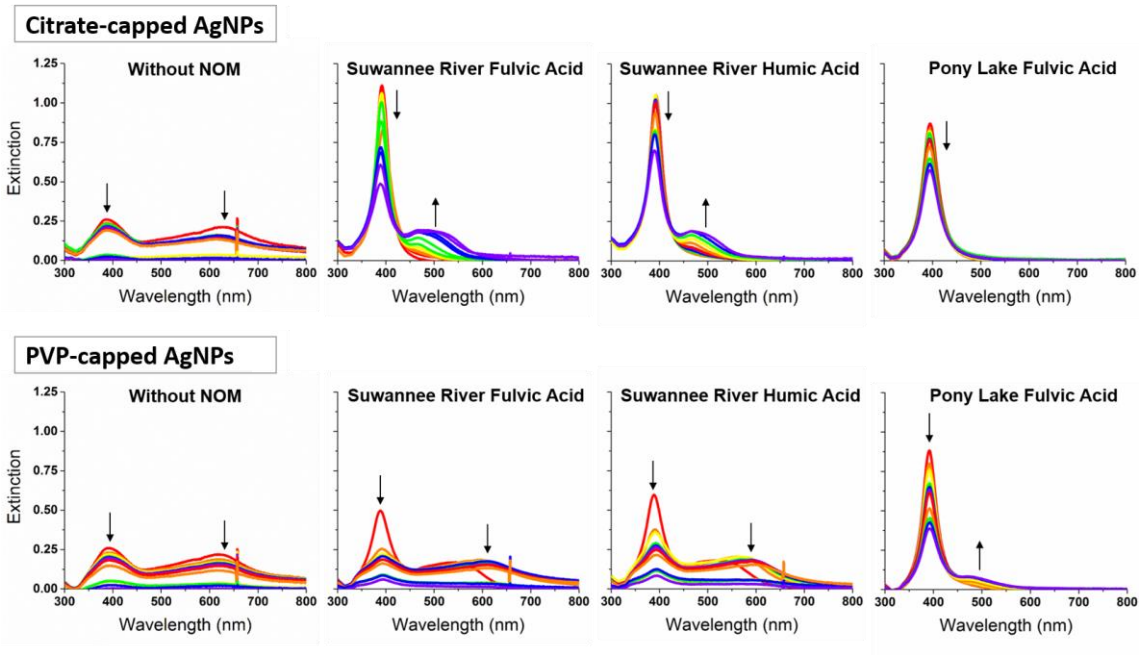

Figure 1. UV-visible extinction spectra show that NOM improves the colloidal stability of citrate-capped AgNPs more significantly than PVP-capped AgNPs, and that the degree of colloidal stabilization conferred by NOM for both particle types was SRFA < SRHA << PLFA. Spectra of citrate-capped (top) and PVP-capped (bottom) AgNPs in pH 7.5 phosphate buffer were collected after incubation of AgNPs with NOM type specified. Shown are spectra at 1-6 (red), 11, 20, 24, 30, and 46 h (violet) after particle redispersion; arrows indicate directions of peak intensity changes. The peak near 390 nm corresponds to extinction by the primary (12 nm-diameter) particle population and peaks at longer wavelengths correspond to aggregates. Agregate settling decreases peak intensities as it removes particles from the probed sample volume. The feature observed around 650 nm is an instrumental artifact. Results were duplicated in independent experiments.

The plasmon resonance of spherical metal nanoparticles causes light extinction features that are sensitive to inter-particle interactions.[295] Such interactions shift the particle plasmon extinction peak to higher wavelengths.[295] In our study, a primary extinction peak attributable to the plasmon resonance frequency of non-agglomerated 12 nm-diameter

AgNPs was observed at 391 and 394 nm for citrate- and PVP-capped AgNPs, respectively. The formation of variable-sized AgNP aggregates resulted in the appearance of a broader peak at longer wavelengths; larger aggregates produced broader and more red-shifted peaks. Similar observations of red-shifted UV-visible extinction spectra in response to AgNP aggregation were reported previously.[296] Nanoparticle aggregation was further characterized using dynamic light scattering (DLS) to track hydrodynamic particle diameter over time following dispersion in buffer (Figure 2).

Extinction spectroscopy and DLS demonstrate that incubation with NOM in a high ionic strength buffer (0.1 M) stabilized citrate- and PVP-capped AgNPs against homoaggregation relative to their pristine (no-NOM) counterparts. The aggregation behavior of AgNPs is known to depend on surface characteristics, where surface coatings that promote steric repulsion are typically more effective at maintaining AgNP colloidal stability in high ionic strength environments than their counterparts promoting only electrostatic repulsion.[297,298] However, surface coating-dependent behavior of AgNPs in the presence of NOM has not been studied thoroughly. It was observed that citrate- and PVP-capped AgNPs aggregated similarly with increasing ionic strength after addition of cysteine, which was used as a low molecular weight model for NOM.[187] However, higher molecular weight NOM, such as that used in our study, is expected to induce different effects, given its greater potential to increase steric repulsion between particles. In this study, the degree of AgNP stabilization conferred by NOM was dependent on both the NOM type and nanoparticle capping agent. Three primary effects were observed.

First, AgNPs exposed to high NOM concentrations had higher colloidal stability than pristine nanoparticles that were stabilized either electrostatically using citrate or sterically using PVP-10. Pristine citrate- and PVP-capped AgNPs aggregated immediately upon dispersion in phosphate buffer, as indicated by the low intensity of the primary extinction peak at 391 or 394 nm and the presence of a broad peak at longer wavelengths (Figure 1, left). The primary and secondary extinction peak intensities of citrate- and PVP-capped

AgNPs decayed over time as the nanoparticles aggregated and fell out of suspension; particle dissolution (which was observed using ISEs and is discussed in more detail below) likely also contributed to decreasing intensity of the primary extinction peak. Rapid increases in the hydrodynamic particle diameters were observed over the first three hours following dispersion (Figure 2), consistent with rapid formation of large aggregates. In contrast, citrate- and PVP-capped AgNPs that had been previously incubated with NOM showed a higher intensity primary extinction peak at early time-points, indicating a larger population of stable 12-nm nanoparticles. Appearance of a broader, secondary extinction peak at red-shifted wavelengths was also slower, suggesting slower aggregate formation. In most cases, the average hydrodynamic particle diameter increased following dispersion in buffer, but increases were dramatically slower than for pristine nanoparticles. This result suggests that ligand-stabilized AgNPs that encounter high concentrations of NOM have significantly higher colloidal stability than their pristine counterparts. While nanoparticle transport in natural aquatic environments depends not only on homoaggregation as evaluated here, but also on heteroaggregation and nanoparticle adsorption onto collector surfaces, our result suggests that AgNPs stabilized by NOM may be transported more efficiently through aquatic environments than their pristine counterparts, since homoaggregation and nanoparticle settling is reduced.

Second, the extent to which NOM increases AgNP colloidal stability depends on the affinity of the original organic capping agent for the nanoparticle surface. A fraction of PVP-capped AgNPs previously incubated with SRFA or SRHA aggregated immediately after dispersion in NOM-free buffer, resulting in a broad extinction peak between 500 and 750 nm (Figure 1, bottom). Equivalently prepared citrate-capped AgNPs aggregated more slowly and formed smaller aggregates, as indicated by slower growth of a narrower secondary extinction peak between 500 and 600 nm (Figure 1, top) and DLS measurement of hydrodynamic diameters (Figure 2). These results indicate that PVP-capped AgNPs are less effectively stabilized by NOM than citrate-capped AgNPs, which

may be caused by the higher affinity of PVP than citrate for the AgNP surface. Citrate is generally thought to be weakly bound to the AgNP surface,[296] and citrate-capping of AgNPs is widely used in industry to provide stable precursors for other functionalization schemes due to the labile nature of this agent. At the high NOM concentrations employed in the current study, NOM may displace citrate from the nanoparticle surface. In contrast, PVP coordinates with the AgNP surface through van der Waals interactions and direct bonding interactions with the Ag *d*-band.[299,300] Computational studies showed that the latter occurs through bonding orbitals of the 2-pyrrolidone subunit, localized on the oxygen (~60%) and nitrogen (~25%).[299,300] This is consistent with spectroscopic studies of PVP interaction with Ag, which suggested that direct bonding interactions occur through either only oxygen or a combination of oxygen and nitrogen.[301-303]

Due to direct bonding interactions with Ag, PVP is harder to displace than citrate, which may result in a greater barrier to NOM interaction with the nanoparticle surface. Alternatively, NOM might adsorb to either citrate or PVP on the AgNP surface, rather than displacing them. Under this assumption, our results suggest that more NOM binds to adsorbed citrate than to PVP since exposure to NOM induces a more significant increase in the colloidal stability of citrate- than PVP-capped AgNPs. However, at the pH of this system (pH 7.5), greater electrostatic repulsion exists between the negatively charged acidic residues of NOM and citrate (which carries three negative charges) than PVP (which is neutral). Based on our results, we conclude that AgNPs stabilized with easily displaceable organic capping agents will be more effectively stabilized by NOM.

Third, the extent to which NOM increases AgNP colloidal stability, regardless of the organic capping agent, depends on the concentration of sites with high affinity for metallic silver and Ag^+ (e.g., sulfur and nitrogen groups)[224] in the NOM. For both citrate- and PVP-capped AgNPs, the stabilizing power of NOM occurs in the order SRFA < SRHA << PLFA (Figures 1 and 2). Following dispersal of citrate-capped AgNPs exposed beforehand with SRFA or SRHA in NOM-free buffer (Figure 1, top middle), a

broad, secondary extinction peak between 500 and 600 nm (due to variable size aggregates) appeared. This suggests that AgNPs previously incubated with SRFA and SRHA aggregate significantly, although less than AgNPs not treated with NOM. In contrast, no secondary extinction peak was observed following dispersion of AgNPs exposed beforehand with PLFA (top right), suggesting that no significant aggregation occurs in this case. In the case of PVP-capped AgNPs, PLFA is the only NOM type that eliminates immediate formation of a broad aggregate peak (Figure 1, bottom right). Due to the presence of both primary (12 nm diameter) and variable-size nanoparticle aggregates in these samples, it was not possible to accurately determine the average hydrodynamic particle diameter by DLS using a single normal distribution model. Despite this limitation, the observed relative changes in estimated average hydrodynamic particle diameter were consistent with results of extinction spectroscopy. The estimated average hydrodynamic diameter of particles previously incubated with NOM increased most significantly over time when SRFA was used; this was true for both citrate- and PVP-capped AgNPs (Figure 2).

In the case of citrate-capped AgNPs, the SRHA and PLFA incubation had indistinguishable effects on hydrodynamic particle diameter, but PLFA was a more effective stabilizing agent than SRHA in the case of PVP-capped AgNPs. Visual evidence for the relative stabilizing power of SRFA, SRHA, and PLFA is provided in Figure S3, which shows dark-field images and spatially resolved light scattering spectra of pristine and NOM-stabilized citrate-capped AgNPs 24 hours after redispersion in buffer. These qualitative and semi-quantitative results, respectively, confirm that citrate-capped AgNPs are increasingly stable when exposed to NOM in the order SRFA < SRHA << PLFA.

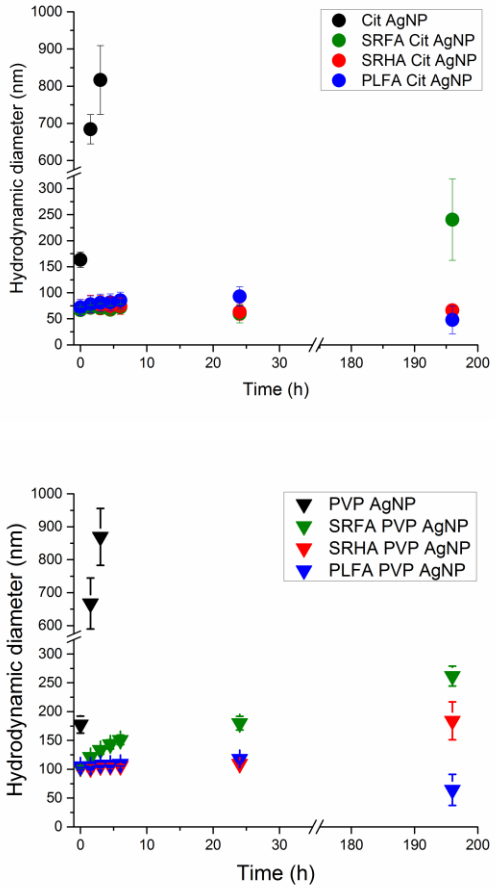

Figure 2. Average hydrodynamic diameters (Z-average particle size) of citrate-capped (top) and PVP-capped (bottom) AgNPs previously incubated with the NOM type specified after dispersion in buffer, as estimated with DLS. Error bars represent standard deviations of three independent replicates, each consisting of three analytical replicates.

The three NOM types used in the current study were chosen because they have similar average molecular weights (between 1300 and 1400 Da)[304] but differ in sulfur and nitrogen content. Sulfur-containing species such as thiols have strong bonding interactions with metallic silver, and electron donating groups like sulfur and nitrogen may act as Ag^{+}-coordinating sites[305] when in the form, e.g., of thiols and amines. PLFA has approximately five to six times more total sulfur than either SRHA or SRFA (see

Table S1),[235] with approximately twice the fractional exocyclic sulfur content (e.g., thiol) of SRHA and SRFA.[268] This results in an approximately eleven times higher thiol content of PLFA over SRHA and SRFA. Given the ability of thiols to form stable complexes with metals including silver and also with Ag^+ (which was shown to adsorb to the nanoparticle surface[186]), the observed NOM ranking (PLFA >> SRHA > SRFA) may be partly attributable to their relative thiol contents. PLFA also has five to ten times more total nitrogen than SRHA or SRFA.[235] This higher nitrogen content, present to a significant extent in the form of amides, amines, and heterocyclic nitrogens,[267] may also contribute to the greater stabilizing effect of PLFA.

This explanation is also consistent with the latter ranking (SRHA > SRFA), since SRHA has an approximately two times higher nitrogen content than SRFA but is otherwise chemically similar (see Table S1). Given the lower oxygen content of PLFA than SRFA or SRHA (see Table S1), the relative NOM ranking observed here suggests that electron donating groups containing oxygen (e.g., carboxylic acids and phenols) have less influence on AgNP colloidal stability than electron donating groups like sulfur and nitrogen. The relative NOM ranking observed here is consistent with that observed in our previous study considering Ag^+ only.[289]

We point out that while SRFA and SRHA have similar average molecular weights (1400 Da for SRHA, 1360 Da for SRFA),[306] their molecular weight distributions are different, with a larger fraction of higher molecular weight NOM in SRHA than SRFA.[307] A previous study of citrate-capped gold nanoparticle stability with NOM suggested that high molecular weight fractions have much larger effects on nanoparticle stability than low molecular weight fractions separated from the same NOM source.[308] Therefore, we suggest that preferential interaction of high molecular weight NOM fractions with AgNPs may also contribute to the increased colloidal stability of SRHA- over SRFA- stabilized AgNPs. PLFA has a similar molecular weight distribution as SRFA[309] yet has a much greater effect on AgNP colloidal stability than SRFA or SRHA, as described above.

Consequently, we suggest that sulfur and nitrogen content (i.e., sites with high affinity for metallic silver and Ag^+) plays a significant role in determining NOM's interaction with AgNPs in addition to molecular weight.

7.3.2 Impact of NOM on AgNP dissolution

The oxidative dissolution of AgNPs in natural aquatic environments is of interest due to the potential toxicity of released Ag^+ to microorganisms. In the absence of other oxidizing or reducing agents, AgNP dissolution proceeds with the following stoichiometry:[186]

$$2Ag_{(s)} + \frac{1}{2}O_{2(aq)} + 2H^+_{(aq)} \leftrightarrow 2Ag^+_{(aq)} + H_2O_{(l)}$$

The literature presents sometimes conflicting results regarding the effect of NOM on AgNP dissolution. For example, adsorption of thiol-containing species, such as cysteine, was shown to either inhibit[286,292] or increase[187] AgNP dissolution. Such discrepancies may result from errors introduced during separation of AgNPs from dissolved Ag^+ (e.g., from retention of Ag^+ on centrifugal filters).[187] A separation step is necessary when monitoring AgNP dissolution by spectroscopic or spectrometric techniques, as these techniques cannot discriminate between Ag^+ and AgNPs. In the current study, we employ fluorous-phase Ag^+ ISEs to monitor AgNP dissolution in situ, thereby eliminating the need for sample preparation and reducing potential sampling errors.[85]

We investigated the effect of NOM composition on the dissolution of 12-nm-diameter citrate-capped AgNPs under an environmentally relevant condition (pH 7.5 phosphate buffer, as used above, and 10 mg/L NOM concentration in the bulk solution). Citrate-capped AgNPs that had been previously incubated with a high concentration of NOM (600 mg/L) were added to the pH buffer, yielding a silver concentration of 5 mg/L and a bulk NOM concentration of 10 mg/L. (Experiments were also conducted using AgNPs

that had not been previously incubated with a high concentration of NOM, but the presence of 10 mg/L NOM in solution had no statistically significant effect on nanoparticle dissolution; see Figure S5.) Changes in the concentration of Ag^+ were then monitored by measuring the electromotive force, emf, of the fluorous-phase Ag^+ ISE with respect to a reference electrode placed into the same solution. At a constant temperature, the emf of fluorous-phase Ag^+ ISEs increases linearly with the logarithm of the Ag^+ activity. For example, at 20 °C a 10-fold increase in the activity of Ag^+ results in a 58.2 mV increase in emf.[42] The theoretical response and calibration of Ag^+ fluorous-phase ISEs are explained in the Supporting Information and illustrated with Figure S4.

Figure 3a shows the results of ISE monitoring of nanoparticle dissolution. A sudden increase in the emf after addition of the AgNPs is caused by NP dissolution to give Ag^+ ions. The emf becomes stable one hour after AgNP addition, indicating that the concentration of Ag^+ in solution reached a steady state. The gradual increase in emf represents an increase in free silver concentration and not a slow response time of the electrode, as shown by the nearly instantaneous (less than 1 s) response of the ISE to changes in Ag^+ concentration caused by hydrogen peroxide and NaCl additions. While hydrogen peroxide oxidizes AgNPs and increases the Ag^+ concentration in solution, chloride precipitates Ag^+, reducing the concentration of Ag^+ in solution. Both effects are detected by the ISE, illustrating the advantage of this sensor for dynamic in-situ detection.

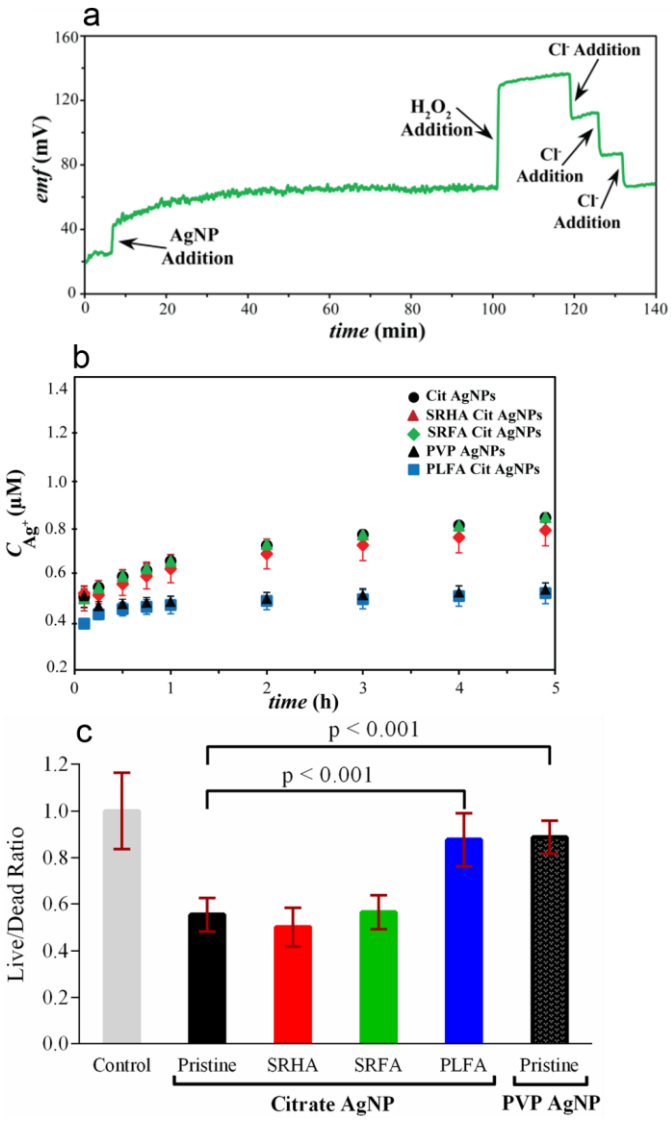

Figure 3. a: Continuous detection with fluorous-phase Ag^+ ISEs: 5 mg Ag/L citrate-capped AgNPs were added to pH = 7.5 buffer while monitoring the Ag^+ release. H_2O_2 was added to oxidize AgNPs, and Cl^- was added to reduce theAg^+ concentration. b: Dissolution of citrate-capped and PVP-capped AgNPs in pH 7.5 buffer (5 mg Ag/L) with or without prior incubation with NOM (non-surface bound NOM concentration 10 mg/L). Error bars represent standard deviations of three replicate measurements. c: Effect of AgNPs on *Shewanella* membrane integrity as a function of NOM type, as evaluated using

fluorescent dyes; shown is the ratio of fluorescence emission intensities for a membrane permeable dye (indicating live cells) and a membrane impermeable dye (indicating dead cells). Data collected from cells exposed to pristine nanoparticles (NP) and cells exposed to nanoparticles previously incubated with 600 mg/L NOM (PLFA-NP, SRFA-NP, and SRHA-NP) were normalized to a negative control from *Shewanella* not exposed to nanoparticles; values smaller than 1 indicate decreased membrane integrity following nanoparticle exposure. Error bars represent standard deviations of three biological replicates.

The effect of NOM with variable chemical composition on AgNP dissolution is presented in Figure 3b. SRHA- and SRFA-stabilized citrate-capped AgNPs showed equivalent Ag^+ release profiles over time to pristine nanoparticles (without NOM). Given the significantly increased colloidal stability of SRHA- and SRFA-stabilized AgNPs over pristine AgNPs, their similar dissolution profiles suggest that dissolution is relatively insensitive to nanoparticle aggregation state. This is consistent with previous reports, which suggested that AgNP aggregation only minimally decreases the surface area available for interaction with molecular oxygen.[186,204] In contrast to SRHA- and SRFA-stabilized AgNPs, PLFA-stabilized citrate-capped AgNPs released over five hours approximately one-half the Ag^+ content of pristine nanoparticles.

This result most likely reflects the high sulfur and nitrogen content of PLFA, as described above. Sulfur-containing functionalities, specifically thiol groups, have high affinities for silver surfaces, while thiolates and amines can form complexes with Ag^+. NOM bound to the AgNP surface (e.g., through interaction of thiol-containing species with metallic silver or thiolates and amines with surface-adsorbed Ag^+) may exclude molecular oxygen from active sites and thereby limit oxidative dissolution, as previously suggested in the case of thiols.[286] Our results demonstrate that even when AgNPs are exposed to a very high NOM concentration (600 mg/L), there is a minimal effect on Ag^+ release except when the NOM has a high concentration of strongly Ag-coordinating sites. Perhaps more

surprising is the observation that prior incubation with SRHA or SRFA, which significantly stabilizes AgNPs against homoaggregation (as shown in our colloidal stability experiments), had no effect on the rate and total amount of Ag^+ released.

We also compared the dissolution of citrate-capped and PVP-capped AgNPs. Exchanging a fraction of citrate for PVP-10 induced a significant decrease (~40%) in Ag^+ release over five hours. Previous reports suggested that PVP may have high affinity for not only Ag surfaces but also Ag^+,[310] an effect that could trap Ag^+ at the particle surface and buffer its release into solution.[286] To directly test this hypothesis, we used Ag^+-ISEs to monitor the concentration of free Ag^+ in solution after addition of PVP. We observed no detectable changes in free Ag^+ concentration after addition of up to 50 mg/L PVP (Figure S6), indicating that PVP has low affinity for Ag^+ and is unlikely to trap Ag^+ ions at the AgNP surface. An alternative mechanism to explain the observed PVP-induced decrease in AgNP dissolution is surface passivation. While it is beyond the scope of this work to directly assess the validity of this mechanism, we note Grubbs' suggestion that some polymer ligands can control access of molecular oxygen to the nanoparticle surface,[311] which would decrease the oxidative dissolution rate of AgNPs. We note that the total dissolved Ag^+ concentration in our experiments corresponds to approximately 1-2% (depending on the capping agent) of the total silver content present in the original AgNP suspension, consistent with previous dissolution studies using larger (39 nm) PVP-capped AgNPs.[292]

7.3.3 Impact of NOM on AgNP Toxicity to Bacteria

Previous work suggested that AgNP toxicity to bacteria can be fully attributed to the bioavailable Ag^+ concentration resulting from nanoparticle dissolution.[181] A recent report suggested that, while AgNPs and Ag^+ may have similar effects on bacterial survival, they have distinct mechanisms of antibacterial activity.[312] While questions remain regarding the relationship between AgNP dissolution and toxicity to bacteria, understanding AgNP

dissolution in environmental matrices remains a critical step towards understanding the implications of their release into natural aquatic environments. To this end, a few studies assessed the role of Ag^+-complexing agents, such as NOM, on resultant AgNP toxicity to bacteria. Fabrega et al. demonstrated reduced toxicity of citrate-capped AgNPs to *Pseudomonas fluorescens* with addition of 10 mg/L SRHA at pH 9.0, but no reduction of Ag^+ toxicity at an equivalent concentration.[230] They hypothesized that reduction of AgNP toxicity caused by SRHA may be due to its role as a physical barrier to cell-NP contact or as a ROS-scavenger (antioxidant), while its lack of effect on Ag^+ toxicity may be due to insignificant binding with Ag^+ or continued bioavailability of Ag^+ in the complexed form. Zhang et al. demonstrated reduced bacterial disinfection performance of PVP-capped AgNPs following addition of 5 mg/L SRHA, an effect that they attributed to an observed reduction in Ag^+ release under these conditions.[276]

As these examples demonstrate, disagreements persist regarding the effect of NOM on AgNP dissolution and toxicity to bacteria, perhaps in part due to the use of indirect measurements of AgNP dissolution and lack of Ag speciation information. Here, we coupled direct measurements of Ag^+ dissolution from AgNPs in the presence of NOM (described above) with an assessment of AgNP toxicity to *Shewanella oneidensis* MR-1 to provide novel insight into the mechanism of NOM's effect on AgNP bactericidal efficacy.

In these toxicity experiments, as in previously described nanoparticle colloidal stability experiments, AgNPs were initially exposed to a high concentration of NOM, and were then redispersed in NOM-free buffer. *Shewanella oneidensis* MR-1 was mixed with NOM-treated citrate- or PVP-capped AgNPs and cellular membrane integrity was evaluated as a function of NOM type. Nanoparticle-induced membrane damage, a known mechanism of AgNP bactericidal activity,[184,282] was observed by monitoring the relative fluorescence emission intensities of two nucleic acid probes, one of which is cell membrane-permeable, thus labeling all cells, and one which is cell membrane-

impermeable, thus labeling only membrane-compromised cells. The relative fraction of membrane-compromised cells in a sample was then determined by calculating the ratio of fluorescence emission intensity of these probes normalized to a sample receiving no nanoparticle treatment.

Our results (Figure 3c) demonstrate that the bactericidal efficacy of citrate-capped AgNPs was reduced after exposure to PLFA, while SRFA and SRHA had no effect. This is consistent with the results of our ISE dissolution studies, which indicated that PLFA was the only NOM type to significantly reduce Ag^+ release from AgNPs (Figure 3b). The relative impact of the NOM types used here on AgNP dissolution is also consistent with the results of our related study in which ISEs were used to measure Ag^+ binding to NOM in the absence of AgNPs.[289] Addition of PLFA to a Ag^+ solution significantly decreased the free Ag^+ concentration, indicating binding of NOM to Ag^+, while SRHA and SRFA induced smaller decreases. In the present study, PVP-capped AgNPs were also observed to be less toxic than citrate-capped AgNPs, consistent with their significantly lower release of Ag^+ (Figure 3b).

Complexation of Ag^+ with NOM on the nanoparticle surface or in the bulk may decrease its bulk concentration and lower the bactericidal efficacy of the nanoparticle. Passivation of the nanoparticle surface by adsorbed or covalently bound NOM may also suppress Ag^+ release in an analogous way to that described above for PVP. While direct evaluation of these proposed mechanisms is beyond the scope of this work, we note Liu et al.'s suggestion that both Ag^+ complexation with surface capping agents and AgNP surface passivation by ligands with high Ag-affinity are chemical approaches to control Ag^+ release from AgNPs.[286] Some studies suggested that NOM may reduce AgNP toxicity indirectly, that is, by influencing processes other than nanoparticle dissolution (e.g., AgNP interaction with the bacterial cell surface or scavenging of reactive oxygen species).[230] While our results do not exclude this possibility, they suggest that AgNP toxicity to bacteria is highly dependent on nanoparticle dissolution, a process that is in

turn dependent on the chemical composition of the nanoparticle capping agent and, if present, NOM.

The results of our AgNP colloidal stability, dissolution, and toxicity studies suggest that NOM with high affinity for Ag (i.e., NOM rich in some sulfur and nitrogen compounds) will induce the greatest increase in AgNP colloidal stability, the greatest decrease in nanoparticle release of Ag^+, and the greatest decrease in AgNP bactericidal efficacy. NOM with lower affinity for Ag (i.e., NOM lower in reduced sulfur and nitrogen) will increase AgNP colloidal stability but have limited impact on nanoparticle release of Ag^+ or bactericidal efficacy, potentially increasing the persistence and impact of AgNPs in natural aquatic environments. The magnitude of this effect is expected to depend on the relative concentrations of NOM in the bulk solution (where higher concentrations lead to greater complexation of NOM with Ag^+ and may in some cases reduce AgNP bactericidal efficacy),[289] and on the particle surface (where higher concentrations lead to greater colloidal stability but, in some cases, have no impact on Ag^+ release relative to less colloidally stable AgNPs).

In addition, our results indicate that exposure to NOM improves the colloidal stability of AgNPs by delaying the onset of aggregation rather than by eliminating it completely. We show that NOM can reduce the rate of AgNP aggregation over 1-8 days, but additional studies are needed to understand the longer-term aggregation behavior of AgNPs exposed to NOM. The present results and those of our previous study[289] suggest that the effect of NOM on the bactericidal efficacies of Ag^+ and AgNPs are not easily predicted by either the magnitude of NOM-Ag^+ complexation or the extent of NOM association with the AgNP surface. Therefore, the consequences of AgNP release into natural aquatic ecosystems containing NOM must be evaluated in an environment-specific context.

7.4 Acknowledgements

This work was supported by a UMN Doctoral Dissertation Fellowship to M.P.S.M., UMN Biotechnology Institute Training Grant and Torske Klubben Fellowship to I.L.G.; Heisig/Gleysteen Fellowship to KH., and NSF Award #CHE-1152931. Parts of this work were performed at the UMN Characterization Facility, which receives partial support from the MRSEC NSF program. Thanks to Katie Hurley and Samuel Egger for acquiring TEM images.

7.5 Supporting Information

7.5.1 Materials and Methods

7.5.1.1 Nanoparticle Synthesis

Citrate-capped AgNPs were synthesized according to the method used by Hackley and coworkers.[200] All glassware was washed with aqua regia (3:1 HCl: HNO_3) and rinsed three times with deionized water (18 MΩ·cm specific resistance, EMD Millipore, Burlington, MA, USA) prior to use. First, 100 mL deionized water was brought to a boil. Then 365 µL of 34 mM trisodium citrate dihydrate (Sigma Aldrich, St. Louis, MO, USA) and 211 µL of 58.8 mM $AgNO_3$ (Sigma Aldrich, St. Louis, MO, USA) were added with constant stirring. After 30 seconds, 250 µL of freshly prepared 100 mM aqueous $NaBH_4$ was added drop-wise, and the mixture was boiled with constant stirring for 15 minutes. The mixture was then removed from heat and allowed to cool to room temperature before beginning purification. To remove synthesis by-products and purify the nanoparticles, 15 mL aliquots of the mixture were loaded into regenerated cellulose (MWCO 50,000) centrifugal filter units (EMD Millipore, Carrigtwohill, Ireland), centrifuged 4 minutes at 1500 RCF, and then resuspended in 15 mL deionized water. Centrifugation and resuspension were repeated two more times. Following the final resuspension in deionized water, the mixture was centrifuged a final time to concentrate the nanoparticles. Nanoparticle concentration in units of silver mass per volume was determined by measuring the UV-visible extinction spectrum (USB2000, Ocean Optics,

Dunedin, FL, USA) using the nanoparticle extinction coefficient and silver atom number value reported by Maurer-Jones et al.[85]

Polyvinylpyrrolidone-capped AgNPs were prepared from the above citrate-capped AgNPs through ligand exchange, thus ensuring that nanoparticle core size and shape were preserved. Prior to centrifugal purification, a room temperature AgNP suspension, prepared as described above, was centrifuged for 30 minutes at 12500 RCF to pellet the nanoparticles. The supernatant was removed, replaced with 26 g/L PVP-10 (Sigma Aldrich, St. Louis, MO, USA), and incubated at room temperature in the dark with constant stirring for four days. The AgNP suspension was then purified using centrifugal filter units as described above.

7.5.1.2 Nanoparticle Characterization

Room temperature TEM images of AgNPs were acquired with a FEI Tecnai T12 microscope (FEI, Inc., Hillsboro, OR) operating at 120 kV. A 200 mesh copper grid with Formvar and carbon supports was dipped into a ~0.3 mg/mL NP suspension, then removed and allowed to dry before imaging. Image analysis was performed in ImageJ.[313]

The zeta potential of citrate- and PVP-capped AgNPs was measured using a Brookhaven ZetaPALS Zeta-Potential and Particle Sizing Analyzer (Holtsville, NY). Three independent samples were prepared by diluting the purified nanoparticle suspensions to 5 mg Ag/L in deionized water (pH 6).

7.5.1.3 Buffer Preparation:

The buffer used in all nanoparticle stability and dissolution experiments was prepared by combining 0.028 M K_2HPO_4 and 0.015 M KH_2PO_4 in deionized water and adjusting the pH to 7.5 by KOH additions.

7.5.1.4 UV-vis Extinction Spectroscopy:

The AgNP aggregation state was tracked over 46 hours at room temperature by monitoring light extinction in the UV-visible range caused by the localized surface plasmon resonance (LSPR) effect using an OceanOptics USB2000 spectrometer coupled to a MicroPack DH-2000 UV-vis-NIR light source. Deionized water or deionized water with 10 mg/L NOM served as the blank references, and measurements were performed on two independent samples.

7.5.1.5 Dynamic Light Scattering Measurement:

The Z-average particle size of citrate- and PVP-capped AgNPs was measured over 196 hours using a Brookhaven ZetaPALS Zeta-Potential and Particle Sizing Analyzer (Holtsville, NY). Three independent samples were analyzed using three analytical replicates per sample.

7.5.1.6 Dark-field Microscopy and Hyperspectral Imaging:

While dark-field microscopy provides only qualitative information regarding AgNP stability, when performed in conjunction with hyperspectral imaging, it offers a semi-quantitative method to assess particle stability. In this work, hyperspectral scans consisting of hundreds of visible-near-infrared spectra were acquired within the field of view of a given dark-field image. These spectra are generated exclusively from light scattered at the nanoparticle surface and not absorbed light, since oblique-angle illumination is used. Scattered light intensity is dependent on the resonance frequency of localized surface plasmons at the nanoparticle surface, which in turn is dependent on the material dielectric properties (or refractive index), size, shape, and interparticle spacing. Aggregation of AgNPs results in a significant change in the localized surface plasmon resonance frequency (see Figure 1 in the main text), leading to shifts in hyperspectral features.

Hyperspectral scans acquired within the field of view of a given dark-field image were pooled into spectral libraries characteristic of each AgNP type (i.e., with different types of NOM). Spectral libraries of different nanoparticle conditions were compared using Spectral Angle Mapping similarity analysis software (ENVI 4.8, Exelis Visual Information Solutions, Boulder, CO). This similarity analysis yields plots (see Figure S3, right-hand side) in which the x- and y-axes indicate position within a corresponding dark-field image, and the pixel brightness indicates spectral matches to a reference sample (here, AgNPs without NOM) above a defined threshold (here, 95% spectral similarity). No further normalization of these data are required, since the relative fraction of bright pixels (in the similarity plots) to total nanoparticles (in the dark-field images) indicates the degree of similarity between AgNPs exposed to NOM and pristine AgNPs in the reference sample.

Dark-field micrographs of AgNPs exposed to NOM were acquired on an Olympus BX43 microscope (Olympus America, Inc., Center Valley, PA) modified with a high signal-to-

noise darkfield condenser unit from CytoViva (Auburn, AL). A 3 µL sample aliquot was loaded onto a glass slide, covered with a coverslip, and imaged using a 150 W quartz-halogen lamp (Fiber-Lite DC-950, Dolan-Jenner Industries, Boxborough, MA), 100x 1.3 NA oil-immersion objective, and 12 bit CCD camera (pco.pixelfly, PCO, Kelheim, Germany). A hyperspectral imaging system consisting of a spectrophotometer (Specim, Oulu, Finland) and spectrophotometer-integrated CCD (pco.pixelfly, PCO, Kelheim, Germany) was then used to acquire hyperspectral images within the same field of view as the dark-field image.

7.5.1.7 Fabrication of Ag^+-Selective Electrodes with Fluorous Sensing Membranes

Ion-selective electrodes (ISEs) were fabricated as reported.[51] Sensing phases were prepared by adding 0.5 mM ionic sites (sodium tetrakis[3,5-bis(perfluorohexyl)phenyl]borate) and 1.5 mM ionophore (1,3-bis(perfluorooctyl-ethylthiomethyl)benzene)[80] into perfluoroperhydrophenanthrene (Alfa Aesar, Ward Hill, MA, USA). The mixture that resulted was stirred for at least a day to make sure that all the membrane components were completely dissolved. Fluoropore™ filters (porous poly(tetrafluoroethylene), 47 mm diameter, 0.45 µm pore size, 50 µm thickness, 85% porosity) from EMD Millipore (Bedford, MA, USA) were placed between two sheets of paper and cut with a 13-mm-diameter hole punch. This gave porous filter disks that were then used to mechanically support the sensing phase. Approximately 25 µL of this sensing phase was subsequently placed onto a stack of 2 porous filter disks. Complete penetration of the sensing phase into the porous supports was indicated by translucence of the filter disks.

The sensing membranes (i.e., the filter disks infiltrated with the fluorous sensing phase) were then mounted into custom-machined electrode bodies (prepared in house from poly(chlorotrifluoroethylene), as reported previously).[8] For this purpose, a cap with a hole (8.3 mm diameter) in its center was screwed onto the electrode body, which

positioned the sensing membrane between the cap and the electrode body but left all but the edge of the membrane exposed. Inner filling solution, 1 µM $AgCH_3CO_2$ (Sigma Aldrich, USA), was filled into the electrode bodies, and a AgCl-coated silver wire was inserted into this solution to act as the inner reference electrode. To replace the sodium ions in the thus prepared sensing membranes with silver ions, all electrodes were soaked prior to measurements for one day in 100 mL 0.1 mM $AgCH_3CO_2$ solution and then for another day in 100 mL 1.0 µM $AgCH_3CO_2$. This process is typically referred to as membrane conditioning.

7.5.1.8 Experimental Details of the Potentiometric Measurements

An EMF 16 potentiometer (Lawson Labs, Malvern, PA, USA) with EMF Suite 1.02 software (Lawson Labs) was used for all potentiometric measurements, which were performed at room temperature in stirred solutions. The external reference electrode (relative to which all measurements with fluorous membrane ISEs were performed) was a double-junction AgCl/Ag electrode with a AgCl saturated 3.0 M KCl reference electrolyte and 1.0 M LiOAc bridge electrolyte. All measurements were performed as at least 3 replicates. Successive addition of aliquots of 10 mM $AgCH_3CO_2$ solution to deionized water or the pH buffers was used to provide the data for calibration curves.

For the observation of nanoparticle dissolution, three ISEs were fabricated, calibrated, and inserted into 100 mL of the solution in which dissolution was going to take place. AgNPs were purified as described above and were added to the solution of interest to give AgNP concentrations of 5 mg Ag/L. Sensor monitoring was performed for 5 hours. All electrodes were calibrated once more after the NOM additions to confirm that the electrodes still exhibited stable responses to Ag^+.

7.5.1.9 Bacterial Membrane Integrity Assay

Bacterial membrane integrity was evaluated after AgNP exposure using the LIVE/DEAD Baclight Viability Kit (Product L-7012, Life Technologies). Cells cultured in LB broth

were centrifuged at 2000 rcf for 10 minutes and resuspended at a concentration of 2 x 10^8 cells/mL in pH 7.5 phosphate buffer. Then 1 mL of cell suspension was mixed with purified citrate- or PVP-capped AgNPs (5 mg Ag/L) that had been incubated overnight with or without NOM as described in the Materials and Methods. After 30 minutes of room temperature incubation, cells were centrifuged at 2000 rcf for 10 minutes, the supernatant was removed, and cells were resuspended in pH 7.5 phosphate buffer. Then 100 µL of each sample was mixed with 100 µL of a mixture of 3.34 mM Syto-9 and 20 mM propidium iodide provided in the Baclight Viability Kit in a 96 well plate. After a 15 minute room temperature incubation, fluorescence emission intensities at 528/20 nm (Syto-9 emission) and 635/32 nm (propidium iodide emission) were measured on a Synergy 2 Multi-Mode Reader (BioTek, Winooski, VT) using an excitation wavelength of 485/20 nm. The response of cells exposed to NOM in the absence of AgNPs (at a concentration matching that present in samples exposed to AgNPs pre-incubated with NOM) was not significantly different from that of the negative control (cells exposed to neither AgNPs nor NOM).

7.5.2 Characterization of AgNPs by TEM and Zeta-potential Measurements:

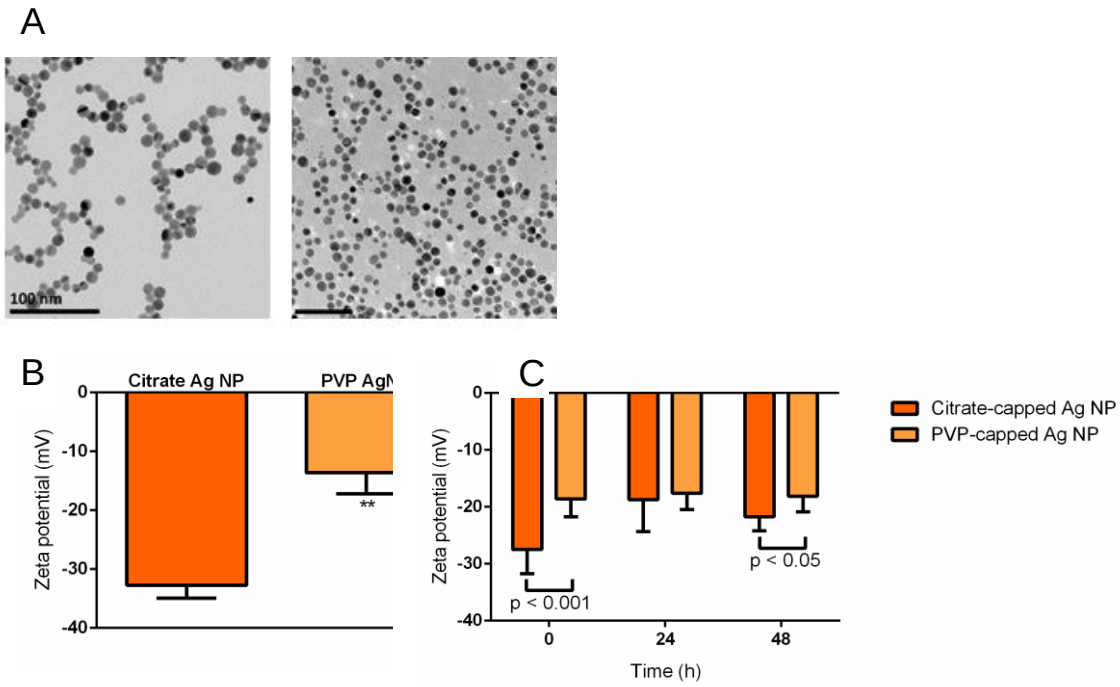

Figure S1. A: TEM micrographs of citrate-capped AgNPs (top left) and PVP-capped AgNPs (top right) reveal no change in nanoparticle size following exchange of the capping agent. B: Zeta potentials of freshly prepared AgNPs in deionized water (pH 6), where citrate- and PVP-capped AgNPs have average zeta potentials of -32.8 ± 2.2 mV and -13.6 ± 3.6 mV. Error bars represent the standard deviation of three independent replicates, each consisting of three zeta-potential measurements. Asterisks indicate $p < 0.01$ as calculated by the unpaired t-test. C: Stability of citrate- and PVP-capped AgNP zeta potentials over 48 h in deionized water (pH 6). P values shown were calculated by the unpaired t-test.

7.5.3 Aggregation of Citrate-capped AgNPs in a High Ionic Strength Buffer Containing 10 mg/L NOM Observed by UV-vis Extinction Spectroscopy

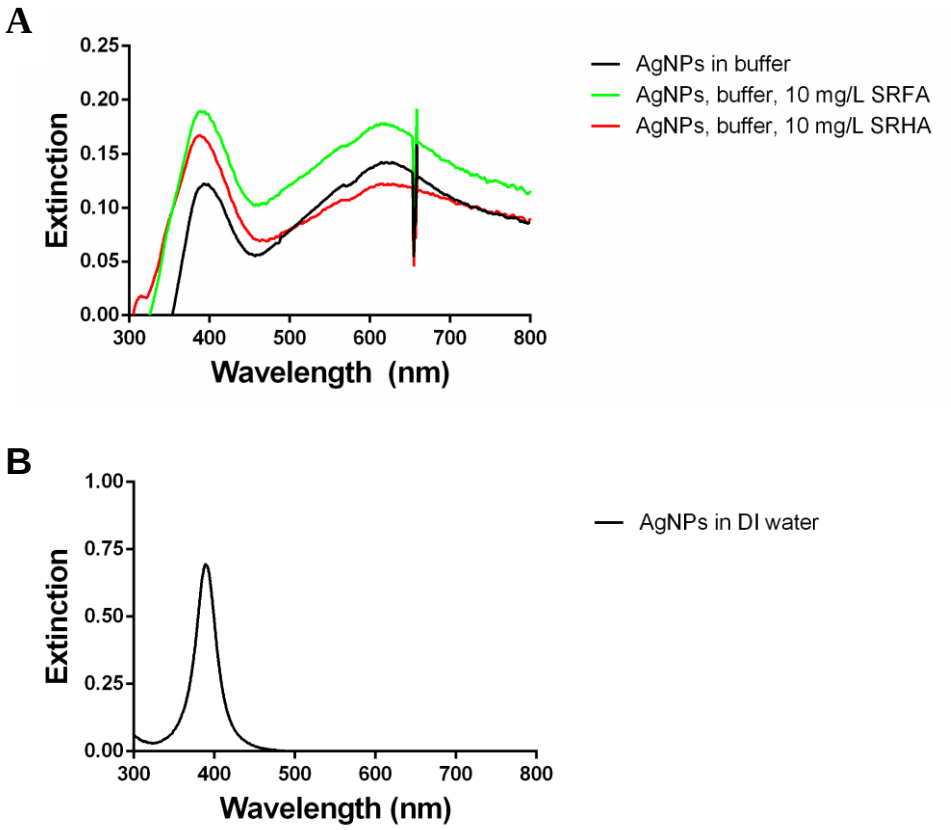

Figure S2. A: UV-vis extinction spectroscopy indicates that the addition of 10 mg/L NOM to a 0.1 M ionic strength phosphate buffer does not stabilize the AgNPs against homoaggregation, since the broad peak with maximum near 620 nm, attributable to variable-sized AgNP aggregates, is present in samples with and without NOM. Spectra of citrate-capped AgNPs exposed to no NOM, 10 mg/L Suwannee River Fulvic Acid (SRFA), or 10 mg/L Suwannee River Humic Acid (SRHA) in pH 7.5 phosphate buffer are shown. The feature observed near 670 nm is an instrumental artifact. B: Prior to AgNP introduction to the high ionic strength buffer with or without NOM, the extinction spectrum showed a single peak centered at 391 nm, indicative of a lack of aggregates and a relatively narrow particle size distribution. A representative spectrum is shown.

7.5.4 NOM Elemental Composition

Table S1. Elemental compositions of the three NOM models used in this study. Values shown are the percent (w/w) content of a dry, ash-free NOM sample.[235]

	C	H	O	N	S
Suwannee River Humic Acid Standard II	52.63	4.28	42.04	1.17	0.54
Suwannee River Fulvic Acid Standard II	52.34	4.36	42.98	0.67	0.46
Pony Lake Fulvic Acid Reference	52.47	5.39	31.38	6.51	3.03

7.5.5 Dark-field Microscopy and Hyperspectral Imaging Characterization of Citrate-capped AgNPs Exposed to NOM

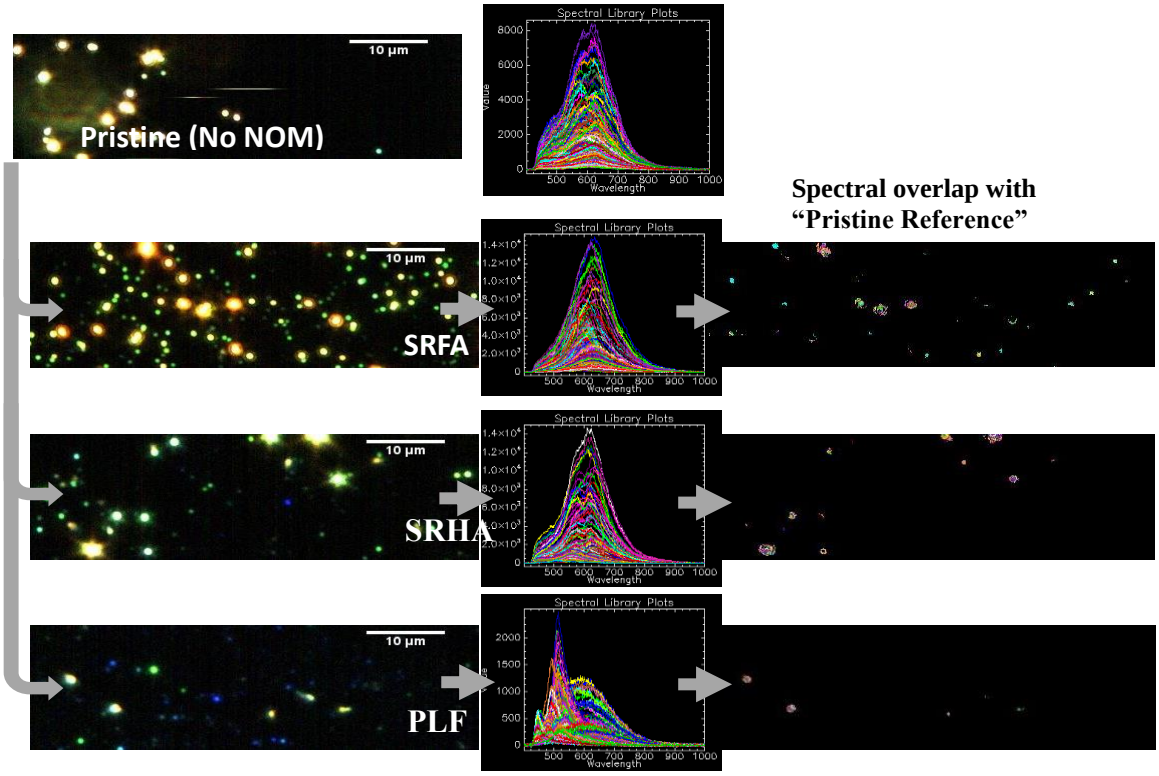

Figure S3. NOM-stabilized AgNPs are shown in order of increasing similarity (bottom to top on the right) to AgNPs without NOM (top left). Dark-field micrographs of citrate-capped AgNPs are shown on the left; these are stabilized with the NOM type indicated. In the images on the right, bright features correspond to areas within the micrographs on the left that have high spectral similarity to NOM-free nanoparticles. An increasing number of bright pixels indicates increasing similarity between the spectral features of the NOM-stabilized nanoparticle and those of NOM-free nanoparticles (i.e., increasing similarity to heavily aggregated AgNPs). Pixel colors represent distinct wavelengths (within the UV-visible region) at which spectral matches were recorded.

7.5.6 Theoretical Responses of Ag^+ ISEs

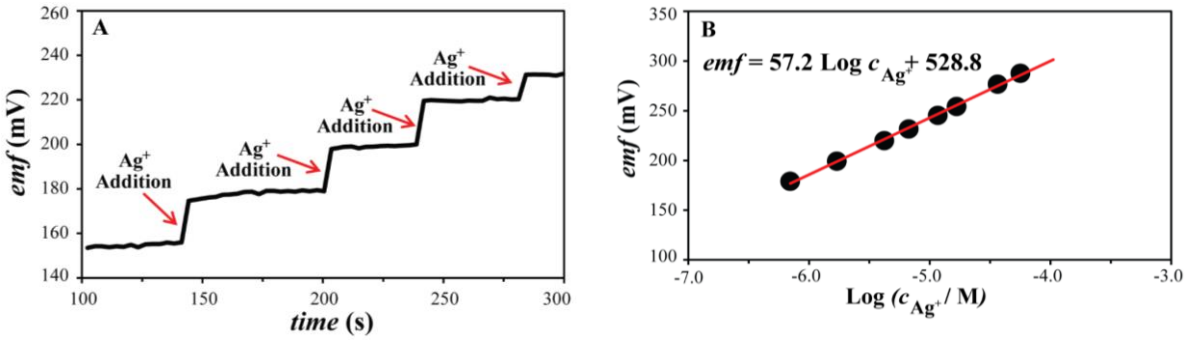

Figure S4: Representative calibration curve of a fluorous-phase Ag^+ ISE. (A) Red arrows indicate additions of aliquots of 10.0 mM $AgCH_3COO$ to the measuring solution. The emf of fluorous-phase Ag^+ ISEs increases after each Ag^+ addition. Only a portion of the calibration curve is shown for better visualization. (B) The linear relationship between the emf and Log c(Ag^+) can be used as the calibration equation for converting emf values to [Ag^+].

Potentiometric measurements are performed by the determination of the electrical potential (typically referred to as electromotive force, emf) between the measuring electrode (here the fluorous-phase Ag^+ ISE) and a reference electrode, which are both in contact with the sample of interest. Note that the reference electrode provides a constant, sample-independent contribution to the measured emf. Ideally, the emf gives a response that can be described with the Nernst equation, i.e., emf = E^o + (2.303 R T F^{-1}) Log a (Ag^+), where T represents the temperature in Kelvin, F is the Faraday constant, and R is the universal gas constant. For example, at 20 °C a tenfold increase in the Ag^+ activity results in a 58.2 mV increase in the measured emf.[42] Calibration of the ISEs to determine the constant E^o and check the prelogarithmic term (i.e., the response slope in a plot of emf vs Log a (Ag^+)) may be performed by addition of aliquots of concentrated $AgCH_3COO$ solution (*aq*) to a more dilute solution and measurement of the emf. The emf response of an electrode to Ag^+ addition provides the calibration curve resulting from that data. Note

that the activity of an ion is the product of the ion concentration and an activity coefficient, which depends, in general, on the ionic composition of the sample solution. However, in solutions with a fixed ionic strength, the activity coefficient of Ag^+ can be assumed to be constant and a plot of the emf vs Log *c* (Ag^+) exhibits the same linearity as the plot of the emf vs Log *a* (Ag^+). Therefore, emf data measured with a calibrated electrode can be converted to concentration using the calibration equation experimentally determined for that electrode. Figure S4 demonstrates the ISE-measured response to Ag^+ additions to buffer (panel A), and the corresponding calibration curve (panel B).

7.5.7 ISE-measured Dissolution of Citrate-capped AgNPs in pH Buffer Containing 10 mg/L NOM

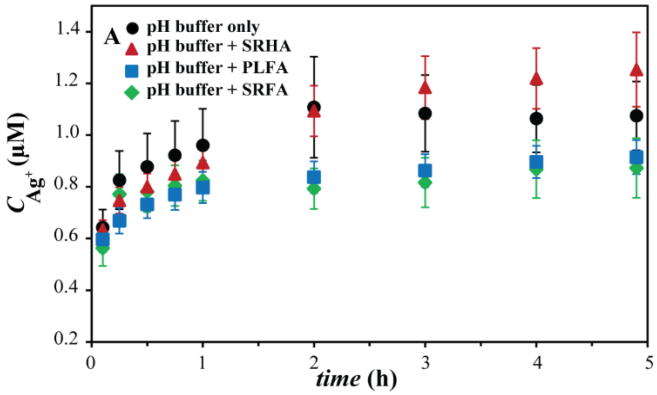

Figure S5. No significant effect of NOM on release of Ag^+ from 5 mg Ag/L citrate-capped AgNPs was observed at low NOM concentrations (10 mg/L) relative to NOM-free solutions. The Ag^+ released was measured with fluorous-phase Ag^+ ISEs in pH = 7.5 buffer with 10 mg/L SRHA, PLFA, or SRFA. Error bars represent the standard deviation of six replicate measurements.

7.5.8 ISE-measured Complexation of Ag^+ and Citrate or Polyvinylpyrrolidone

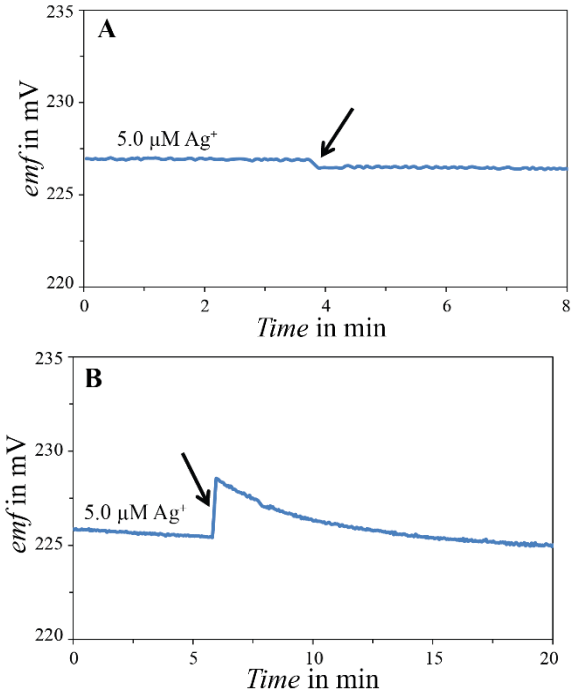

Figure S6. The emf of fluorous-phase Ag^+ ISEs in 5.0 µM $AgNO_3$ was monitored. (A) Addition of 50 mg/L trisodium citrate occurred at the time indicated by the black arrow and led to a 2% decrease in the Ag^+ concentration. (B) Addition of 50 mg/L polyvinylpyrrolidone (PVP-10) occurred at the time indicated by the black arrow, leading to an emf spike. After equilibration, no significant change in the Ag^+ concentration was observed.

8 CHAPTER EIGHT

Reference Electrodes with Salt Bridges Contained in Nanoporous Glass: An Underappreciated Source of Error

Adapted from:

Mousavi, M. P. S.; Buhlmann, P., Reference Electrodes with Salt Bridges Contained in Nanoporous Glass: An Underappreciated Source of Error. *Anal. Chem.* **2013,** *85* (19), 8895-8901.

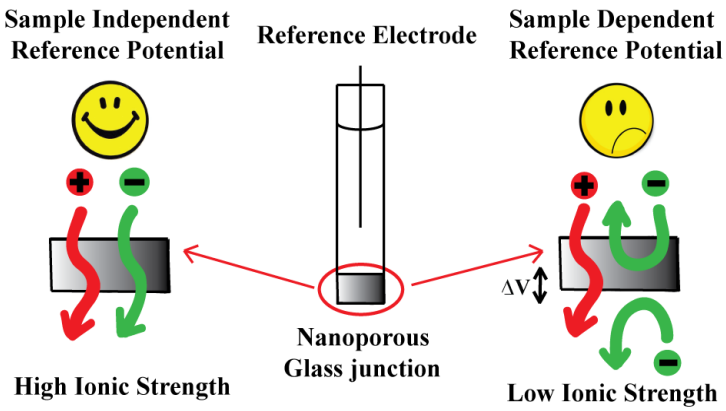

In electroanalytical measurements, nanoporous glass plugs are widely used to contain the electrolyte solution that forms a salt bridge between the sample and the reference electrode. Even though reference electrodes with plugs made of nanoporous glass (such as Vycor or CoralPor glass) are commercially available and are frequently used, the limits of their use have not been explored thoroughly. It is shown here that at ionic strengths lower than 100 mM, the half-cell potentials of reference electrodes with nanoporous glass plugs are not sample independent, as it would be desirable, but they depend on the ionic sample composition. Sample dependent shifts of more than 50 mV in the half cell potential were encountered. Reference potentials were found to be affected in aqueous solutions by HCl, NaCl, KCl, and $CaCl_2$, and in acetonitrile by CF_3COOH and the supporting electrolyte tetrabutylammonium perchlorate. These observations cannot be explained by the liquid junction potential between two mutually miscible electrolyte solutions, as commonly described with the Henderson equation. Instead, they result from the surface charge density on the glass surface and the resulting electrostatic screening of ion transfer into the glass pores when the latter have dimensions comparable to or smaller than the Debye length. Users of reference electrodes with nanoporous glass plugs need to be aware of these limitations to avoid substantial measurement errors.

8.1 Introduction

Reference electrodes are an inevitable part of almost every electrochemical measurement, be it potentiometry, amperometry, voltammetry, impedance spectroscopy, or another electroanalytical method. Most reference electrodes contact the reference solution and the sample through a salt bridge filled with an electrolyte solution.[2] Limiting factors for the use of these salt bridges are the loss of electrolyte into the sample and contamination of the salt bridge by sample components. To minimize these effects and to obtain low and stable junction potentials, porous plugs filled with electrolyte solution are often used, separating the reference from the sample solution while maintaining electrical contact between the two. These porous plugs must have a low electrical resistance while avoiding excessive transfer of electrolyte and sample components through the junction. In order to provide these characteristics, several materials with a high porosity and relatively small pores have been used both by academic researchers and commercial suppliers.[314]

Many studies investigated the properties of reference electrodes with microporous ceramic plugs,[2,315,316] which were reported to have pore diameters in the 0.1 to 3 μm range.[315,317] Nanoporous glass plugs commercially available under the brand names Vycor and (very recently) CoralPor have also been very popular for the fabrication of reference electrodes and offer the advantage of further restricting liquid flow.[314,318,319] The preparation of these glasses is based on the observation that ternary mixtures of silicon dioxide, boric acid, and alkali oxides may phase-separate on proper heat treatment, resulting in a porous skeleton rich in silica and surrounded by alkali and boric oxide.[320] The latter can be leached out with acids, leaving back a nanoporous and strongly hydrophilic glass, sometimes referred to as “thirsty glass”. The pore diameter can be controlled to some extent and has been reported to lie in the range of 4 to 20 of nanometers.[11]

Reference electrodes with nanoporous glass junctions are used widely for electrochemical measurements in both aqueous and organic media.[10] Since many publications from the

same time period described the use of reference electrodes of an unspecified nature, the actual number of studies for which reference electrodes with nanoporous glass plugs were used is likely much larger. However, even though the use of reference electrodes with nanoporous glass plugs was first proposed already in 1955,[12] the effect of nanoporous glass junctions on the performance of reference electrodes in water has to our knowledge not been reported in the literature, and limitations of their performance in organic solvents have been only associated with insolubility effects and mobility differences.[319]

This study critically probes the weaknesses of reference electrodes with nanoporous glass plugs and discusses the conditions that can lead to large measurement errors introduced by shifts in the reference potential. Even though limited variations in the potential of reference electrodes may not be a concern in some electrochemical measurements, many others require a highly reproducible reference electrode potential. For example, an error of 5 mV in the measurement of a monovalent ion with an ion-selective electrode results in an error of 18% in the determined ion activity.[42] In this study, we encountered discrepancies in reference potentials from reference electrodes with nanoporous glass plugs of more than 50 mV, and found a substantial dependence of reference potentials on the composition of the sample solutions.

Importantly, the largest errors that we observed cannot be explained by the well-known liquid junction potentials as they occur at the interface of two miscible electrolyte solutions. Instead, large errors were caused by electrostatic screening of ion transport through the nanopores of the porous glass plugs and the concomitant formation of a phase boundary potential at the interface of sample and plug. This phenomenon is not only analogous to the formation of a phase boundary potential at the surface of ion exchange resins[321] but has also been observed recently for a number of nanomaterials. White and coworkers demonstrated permselectivity for ion transport through chemically modified nanoporous opal films[322] and verified that permselectivity arises from restricted ion diffusion through the opal nanopores in contact with solutions with low pH and ionic

strength. Similarly, ionic strength and pore size were shown to control ion transport through single nanopores,[323-325] metal nanotubule membranes,[326] and chemically modified gold nanotubes.[327]

Surprisingly, it has not yet been reported in the literature that electrostatic screening also affects the popular reference electrodes with nanoporous glass plugs. This study shows how large such errors can be. It illustrates the effects of the ionic strength and the composition of aqueous and organic sample solutions, and describes how errors due to electrostatically induced permselectivity can be distinguished from those caused by liquid junction potentials at the interface of freely miscible electrolyte solutions. The understanding of these effects leads directly to procedures that avoid errors caused by inappropriate use of reference electrodes with nanoporous glass plugs.

8.2 Experimental

Cylindrical nanoporous glass plugs (porous Vycor tips, MF-2064; 3 mm diameter, 3 mm length) were purchased from Bioanalytical Systems (Mount Vernon, IN). A Vycor plug and a glass tube (5 cm long, 3 mm diameter) were placed in a Teflon heat shrink tube, followed by heating with a heat gun for 3 min to attach the plug to the glass tube. Aqueous reference electrodes with nanoporous glass plugs were then prepared by inserting an AgCl/Ag electrode into the glass tube equipped with the Vycor glass plug at one end and filling of the tube from the other end with a solution that contained 1.0 mM KCl and 1.0 M lithium acetate (LiOAc). Note that KCl and LiOAc are both equitransferrent salts, i.e., salts composed of a cation and an anion with equal mobility. In order to completely fill the nanoporous glass plugs with 1.0 M LiOAc, the electrodes were then stored in stirred 1.0 M LiOAc solutions for at least one week. Calibration curves were measured by successive dilution or addition of aliquots of concentrated solutions of NaCl, KCl, $CaCl_2$, or HCl.

A 1255B frequency response analyzer and a SI 1287 electrochemical interface from Solartron (Farnborough, Hampshire, UK) with a three-electrode system were used to determine the electrical resistance of the nanoporous glass plugs. A Pt wire and a free flow double-junction AgCl/Ag electrode with a 1.0 M lithium acetate (LiOAc) bridge electrolyte were used as counter and reference electrodes, respectively. Resistances were obtained by fitting of impedance spectra with ZPlot software (Scribner Associates, Southern Pines, NC) in the 10^4 to 10^5 Hz range.

All electromotive force (emf) values for measurements with a free-flow liquid-junction were corrected for liquid junction potentials using the mobility of the ions[45,328] and the Henderson equation,[329] except for the measurements with trifluoroacetic acid, CF_3COOH (Figure 7). Ionic activities were calculated using a two-parameter Debye-Huckel approximation.[330] To obtain free flow salt bridge junctions, glass pipettes were pulled in a flame to give tip diameters of ≈ 20 μm and filled with either aqueous LiOAc solutions (1.0 M) or acetonitrile solutions of NBu_4ClO_4 (100 mM). In all free flow experiments, reference electrodes with nanoporous glass plugs were placed into these pipettes filled with electrolyte solution, and a small flow of solution out of the pipette into the sample was confirmed. These measurements were then repeated in the same sample solutions but without the electrolyte solution filled pipette, i.e., with direct contact of the nanoporous glass plugs and the sample solution.

8.2.1 Measurements in aqueous media

All potential measurements were performed in stirred aqueous solution at room temperature (25 °C) with an EMF 16 channel potentiometer (Lawson Labs, Malvern, PA) controlled with EMF Suite 1.02 software (Lawson Labs). For comparison, external reference electrodes (DX-200; Mettler Toledo, Columbus, OH) with a free flow double-junction AgCl/Ag electrode, a 1.0 M lithium acetate (LiOAc) bridge electrolyte (movable ground glass sleeve junction), and a 3.0 M KCl reference electrolyte were used. All the

solutions were prepared with deionized purified water (18.2 MΩcm specific resistance, EMD Millipore, Philadelphia, PA), and all measurements were performed in triplicate. The pH measurements were performed with a pH half-cell electrode from Mettler Toledo.

8.2.2 Measurements in organic solutions

Reference electrodes with nanoporous glass plugs for use in organic solutions were prepared by inserting an Ag wire into a glass tube equipped with a Vycor glass plug at one end, filling of the tube from the other end with an acetonitrile solution that contained 10.0 mM $AgNO_3$ and 100 mM tetrabutylammonium perchlorate (NBu_4ClO_4), and inserting the thus prepared electrodes into a stirred solution of identical composition at least for one week prior to measurements. Cyclic voltammograms of bis(pentamethylcyclopentadienyl)iron, $Me_{10}Fc$, (97%; Aldrich, Milwaukee, WI) were measured with a CHI600C potentiostat (CH Instruments, Austin, TX). All electrochemical measurements were carried out with a scan rate of 100 mV/s, using a three electrode setup with a 3.0 mm-diameter gold disk as working electrode (BAS, West Lafayette, IN), a 0.25 mm Pt wire coil (99.998%, Alfa Aesar, Ward Hill, MA) as auxiliary electrode (total surface area $\approx$ 0.5 cm^2), and the reference electrodes with nanoporous glass plugs prepared in house. The working electrode was polished on Microcloth polishing pads using 5.0 μm Micropolish II deagglomerated alumina, both from Buehler (Lake Bluff, IL). After polishing, the working electrode was rinsed thoroughly with deionized water and then ethanol, followed by drying under a stream of argon. Prior to measurements, all solutions were purged with argon for 15 min while stirring vigorously to remove dissolved oxygen. All potentials are reported with respect to 10 mM Ag^+/Ag reference electrodes with nanoporous glass plugs.

8.3 Results and discussion

In an ideal electroanalytical measurement, the salt bridge that connects the sample and reference half cells does not contribute to the measured cell potential. To achieve near ideality, salt bridges typically contain an equitransferrent salt in high concentration, minimizing the liquid junction potential at the interface of the salt bridge and the sample. This work shows that, when used in samples of moderate or low ionic strength, reference electrodes with nanoporous glass plugs exhibit far from ideal behavior. Quite to the contrary, these reference electrodes exhibited near Nernstian responses to several ions, both in aqueous media and organic solvents.

As shown in Figure 1, reference electrodes with nanoporous glass plugs and aqueous 1.0 M LiOAc/1.0 mM KCl inner electrolyte solutions respond potentiometrically to aqueous HCl solutions. To investigate whether the measured emf responses were due to entrapment of previously measured samples in the plug pores, as well known for reference electrodes with conventional porous ceramic plugs when there is small or negligible flow of salt bridge electrolyte into the sample,[5] the response to HCl was measured in 4 sequential steps. At first, the HCl solution was diluted to raise the pH, then HCl was added into the diluted solution to lower the pH again, then a second dilution was performed, and finally HCl was added a second time. If indeed occurring, low diffusive or convective mass transfer into and out of the porous plug would be expected to result in a substantial memory effect. However, Figure 1 shows only a very small hysteresis effect. The four pH response curves from the two dilutions and two HCl additions deviate from one another by only a few millivolts, i.e., much less than the nearly 100 mV of emf response between pH 2 and 5.

This clearly shows that sample entrapment in the porous plug and ensuing hysteresis have only a minor effect on the observed potentiometric response. Interestingly, the pH response is not limited to the region of lowest ionic strength but is largest from pH 4 all the way down to pH 2, where the ionic strength is 10 mM. Indeed, in this region the pH

response has a slope of approximately 30 mV/decade, which is roughly half of the Nernstian response slope of 58 mV/decade as exhibited by a pH glass electrode.

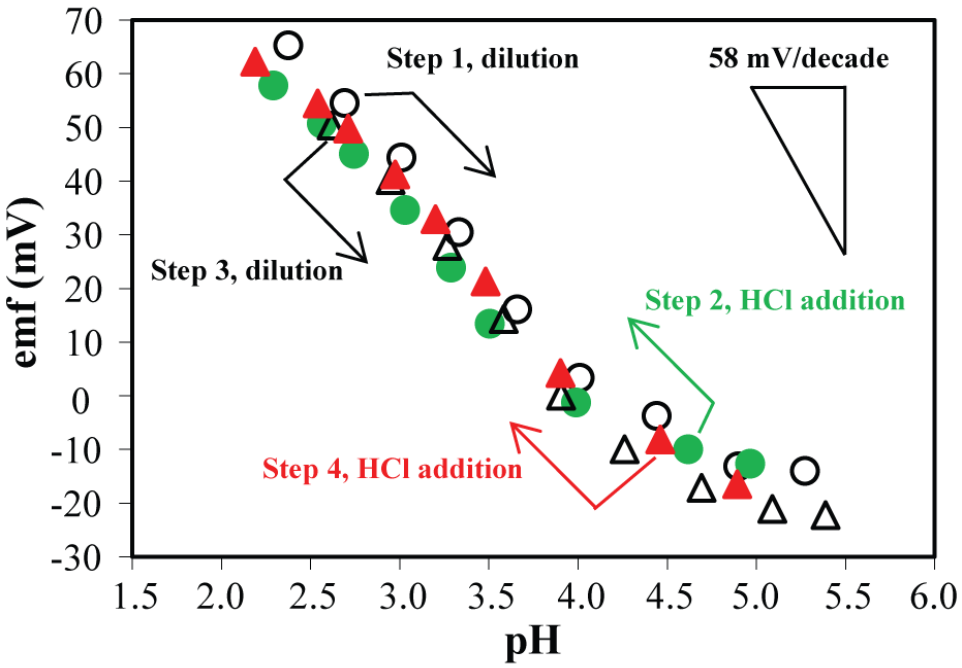

Figure 1. Potentiometric response to HCl of a reference electrode with a nanoporous glass plug, relative to a conventional free-flow double-junction reference electrode. To assess possible hysteresis, the emf was measured in sequential steps, i.e., (1) starting by stepwise dilution of a HCl solution of low pH (empty black circles), then (2) adding aliquots of concentrated HCl to lower the pH (filled green circles), followed by (3) a second sequence of dilutions (empty black triangles), and finally (4) adding once more concentrated HCl to return to the original pH (filled red triangles). The triangle in the top right corner illustrates for comparison the ideal Nernstian response slope of an ion selective electrode to a monocation.

Figure 2 illustrates how the potentiometric response of the reference electrode with the nanoporous plug depends on the ionic strength of the sample. In HCl solutions with a background of high ionic strength (50 mM $CaCl_2$), the observed emf changes less than 2

mV upon a thousandfold change in the concentration of HCl (filled triangles), whereas similar measurements without the $CaCl_2$ background yielded emf changes of more than 100 mV (filled circles). Note that the difference in the potentiometric responses cannot be explained by liquid junction potentials between the sample and the adjacent bridge electrolyte solution, as illustrated by the lack of a potentiometric response to HCl in solutions without the $CaCl_2$ background when a free-flow double-junction reference electrode was used (open circles).

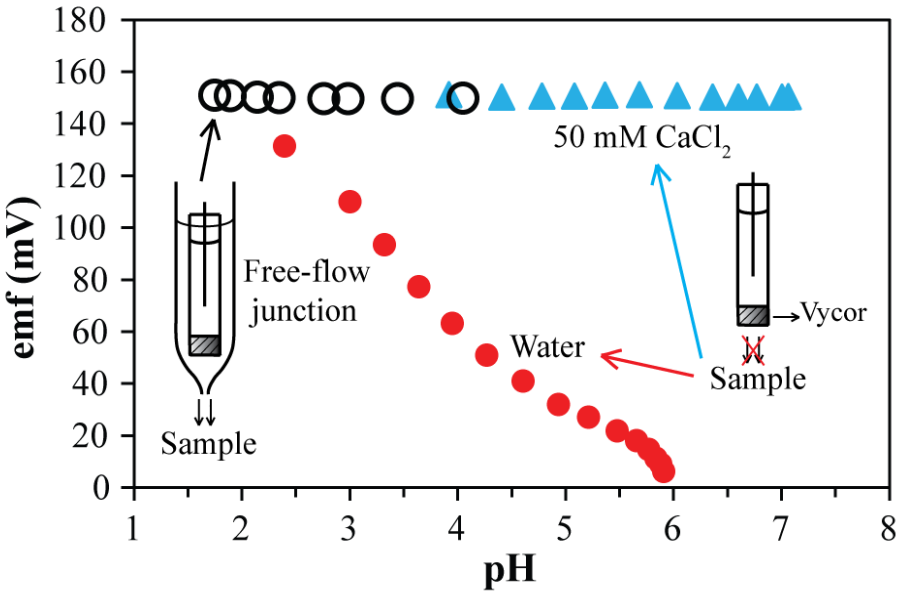

Figure 2. Potentiometric response to HCl of a reference electrode with a nanoporous glass plug, relative to a conventional free-flow double-junction reference electrode. Filled circles and triangles: responses of the nanoporous plug reference electrode in direct contact with HCl samples, sample with a background of 0 and 50 mM $CaCl_2$, respectively. Empty circles: response of a free-flow double-junction reference electrode consisting of the above reference electrode with a nanoporous glass plug inserted into a pipette filled with 1.0 M LiOAc. A small flow of the LiOAc solution from the pipette into the sample solution was ensured.

These potentiometric responses are all consistent with electrostatic screening of ion access into the pores of the nanoporous glass plugs, as it is similarly known, e.g., for ion exchange resins,[321] nanoporous opal films,[322] nanopores,[331] and nanotubes.[327] Access of ions into and diffusive transport of ions through porous materials may be affected by electrostatic forces if the surface of these materials exhibit a surface charge due to electrically charged surface functional groups or adsorbed ions.[323] If the sum of the Debye screening length of the electric field within the pores and the ion radius is much smaller than the pore size, ionic diffusion through the porous material is not significantly affected by electrostatic forces. However, when the pore size approaches the nanometer range, electrostatic interactions with the surface charge start to affect the presence of cations and anions with opposite effects. This results in partial or even complete exclusion of ions of one sign from the porous material, an effect that is referred to as permselectivity. Since the electrochemical potential of any type of ion in the pores has to equal its electrochemical potential in the bulk of a solution in equilibrium with this porous material, it can be shown readily that an electrical phase boundary potential must develop at the interface between the bulk solution and the porous material.[321]

A lower pH reduces the surface charge and weakens electrostatic screening, while at higher pH, the negative surface charge on the glass surface due to deprotonation of silanol groups[332] results in partial exclusion of anions from the glass nanopores. This is consistent with the effect of the ionic strength on the potentiometric response. Since the Debye screening length decreases with the ionic strength,[13,333] the permselectivity of nanoporous materials is lost at high ionic strengths.[322,323,327,331,334,335] This explains the different potentiometric pH responses in absence and presence of a $CaCl_2$ background, as shown in Figure 2.

To further test the consistency of this model with experimental observations, the potentiometric responses of reference electrodes with nanoporous glass plugs to solutions of different metal chlorides were determined. Figure 3 shows that the KCl and NaCl

responses are identical within error, giving no evidence for specific interactions of the monovalent cations K^+ and Na^+ with the glass surface. In an intermediate range from 1.0 mM to 30 mM, the KCl and NaCl responses are close to the theoretical (Nernstian) response that is expected for the permselective population of the nanopores with monocations. Also, as expected for an increasingly shorter Debye screening length at high ionic strength, the measured emf reaches a plateau at high KCl and NaCl concentrations. Similar observations were made for the $CaCl_2$, but the response slope in the 1.0 mM to 30 mM range was only half as large as for NaCl and KCl. This is indeed expected in the case of permselective cation transfer into the glass nanopores considering the inverse relationship of the phase boundary potential change and the charge number of the cation.

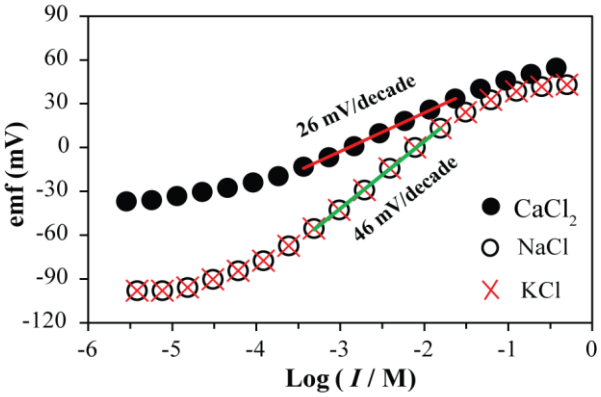

Figure 3. Effect of $CaCl_2$, NaCl, and KCl on the potentiometric response of reference electrodes with nanoporous glass plugs as a function of the ionic strength.

As for the HCl response shown in Figure 2 too, the high ionic strength provided by a 1.0 M LiOAc background eliminated the responses to NaCl, KCl, and $CaCl_2$ (Figure 4A), which is again consistent with the electrostatic screening model. Use of a more dilute ionic background of 1.0 mM LiOAc to provide a well-defined phase boundary potential restores the response to NaCl, KCl, and $CaCl_2$ but again confirms the overall low level of

ion selectivity (Figure 4B). However, the H^+ response stands apart from the responses to the two monovalent cations Na^+ and K^+, which is not surprising given the specific interaction of H^+ with deprotonated surface groups on glass.

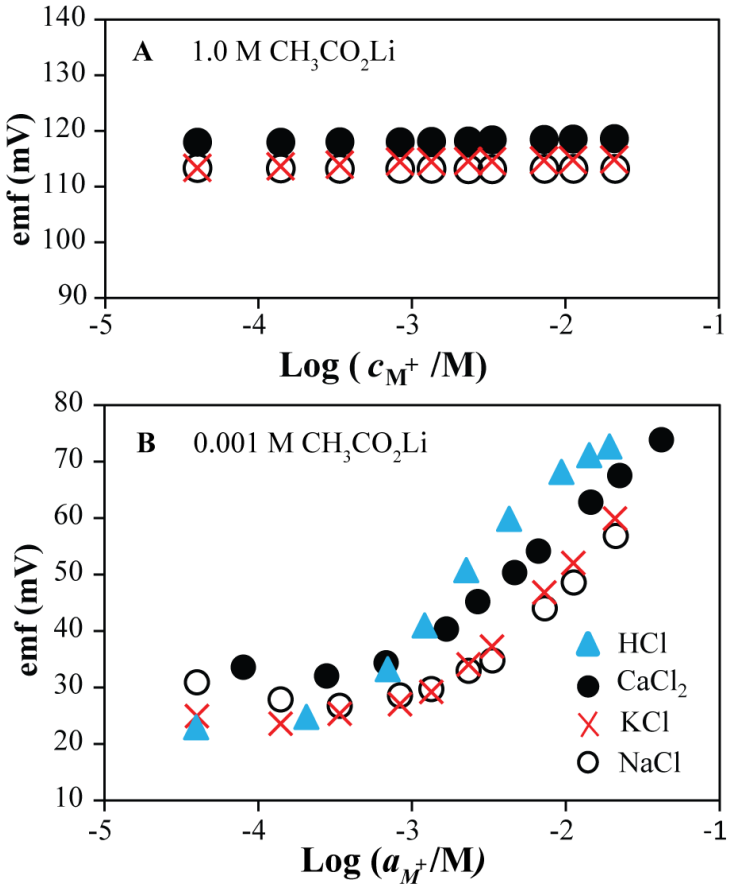

Figure 4. Ion selectivity of the HCl, $CaCl_2$, KCl, and NaCl responses of reference electrodes with a nanoporous glass plug in a background of (A) 1.0 M LiOAc and (B) 1.0 mM LiOAc.

Electrostatic screening effects at the interface between sample solutions and the nanoporous salt bridge plugs are consistent with the dimensions of the nanopores. The Debye lengths in 0.001 and 1.0 M LiOAc are 9.6 and 0.30 nm,[13,333] respectively. The

former is much larger than the ionic radii of H^+, Na^+, K^+, Ca^{2+}, and Cl^-, which are all less than 1.0 nm.[336] Moreover, the Debye length in the 0.001 M LiOAc solutions is also substantially larger than the average pore size of the porous glass plugs used in this study, which was 4.0 nm.[11] Consequently, electrostatic screening effects are to be expected.

Further insight into the effect of electrostatic screening on the ion transport through the nanoporous glass plugs was gained from electrical resistance measurements. For this purpose, a reference electrode with a nanoporous glass plug filled with 1.0 M LiOAc/1.0 mM LiCl and an inner filling solution of the same composition was inserted into a stirred solution with a much lower ionic concentration (1.0 mM LiOAc/1.0 mM LiCl). As Figure 5 shows, the electrical resistance of the nanoporous glass plug remained steady over 24 h at 5.8 ± 0.8 kΩ. Note that if free ion transport from the plug into the 1.0 mM LiOAc solution had gradually depleted the LiOAc in the nanoporous plug, the electrical resistance should have gradually increased over the timeframe of several hours that is necessary for diffusion through a plug of 3 mm thickness. Moreover, the measured value of the electrical resistance in this experiment is much closer to the 2.1 ± 0.1 kΩ resistance of a nanoporous glass plug filled with 1.0 M LiOAc/1.0 mM LiCl solution when in contact on both sides with 1.0 M LiOAc/1.0 mM LiCl, than to the 166 ± 6 kΩ resistance of a nanoporous glass plug filled with 1.0 mM LiOAc/1.0 mM LiCl in contact on both sides with 1.0 mM LiOAc/1.0 mM LiCl. This suggests that even after 24 hours of exposure on one side to 1.0 mM LiOAc/1.0 mM LiCl, the plug that was filled originally 1.0 M LiOAc/1.0 mM LiCl is still filled predominantly with this solution of much higher concentration. This is consistent with an interfacial layer at the water/porous glass interface that inhibits anion transfer to a large extent by electrostatic screening.

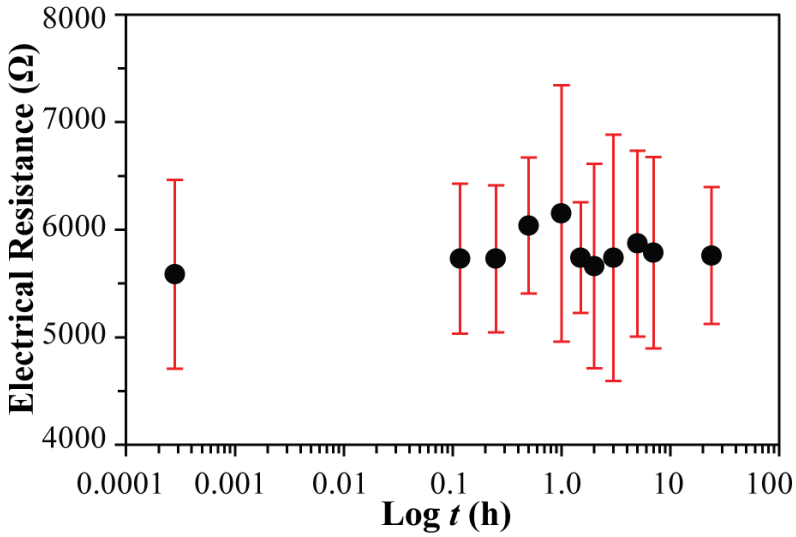

Figure 5. Electrical resistance of a nanoporous glass plug that was initially filled with 1.0 M LiOAc/1.0 mM LiCl and stored in contact on both sides with 1.0 M LiOAc/1.0 mM LiCl for at least 12 h, and then brought at t = 0 h on one side in contact with 1.0 mM LiOAc/1.0 mM LiCl while keeping the same 1.0 M LiOAc/1.0 mM LiCl solution on the other side. Error bars represent results from 3 separate measurements.

A look at the recently published literature shows that reference electrodes with nanoporous glass plugs are not only used frequently for measurements with aqueous samples but are also very popular for measurements in organic solvents such as acetonitrile,[337] propylenecarbonate,[17,163] methanol,[338] dichloromethane,[339] and ionic liquids.[340] This prompted us to investigate the performance of reference electrodes with nanoporous glass plugs also with acetonitrile as a representative organic solvent. To assess the potential contribution of the nanoporous glass plugs, the peak potential in the oxidation of decamethylferrocene, $Me_{10}Fc$, in a cyclic voltammogram (CV) was measured with respect to a reference electrode with a nanoporous plug and an inner filling solution containing 10.0 mM $AgNO_3$ and 100.0 mM tetrabutylammonium perchlorate (NBu_4ClO_4) in acetonitrile. The $Me_{10}Fc^+/Me_{10}Fc$ couple was chosen because

it is known to be minimally affected by the sample composition.[341,342] For comparison, and analogous to the aqueous experiments performed for Figure 2, the peak potential of the $Me_{10}Fc$ oxidation was also determined with respect to a free-flow double junction electrode, for which only a conventional liquid junction potential is expected at the interface to the sample. For the latter purpose, a reference electrode with a nanoporous plug was placed into a pipette filled with an acetonitrile solution containing 100 mM NBu_4ClO_4 as electrolyte solution. When the thus prepared double junction electrode was placed into samples, it was ensured that a very small flow of the 100 mM NBu_4ClO_4 into the sample occurred.

As expected, in the free flow set up, the potential of the reference electrode was only minimally affected by the concentration of the supporting electrolyte (Figure 6, empty circles). However, when the nanoporous plugs were directly contacted with the sample, a change in the peak potential of the $Me_{10}Fc$ oxidation of 20 mV was observed upon stepwise dilution of the supporting electrolyte from 100 to 6.25 mM. This finding confirms electrostatic screening also in acetonitrile solution, despite the fact that the pK_a values are well known to be much higher in acetonitrile than in water,[343] making it harder to ionize the glass surface in this solvent.

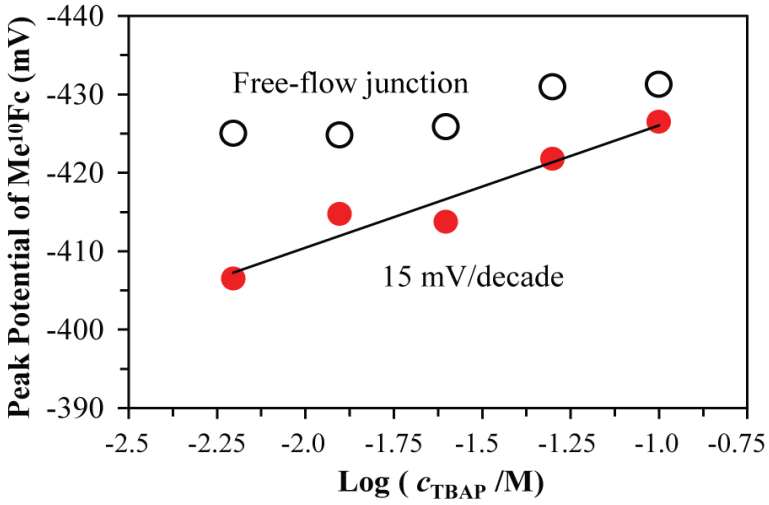

Figure 6. Effect of concentration of NBu_4ClO_4 supporting electrolyte (6.25–100 mM) on the potential of reference electrodes. Shown is the peak potential of the $Me_{10}Fc$ (0.1 mM) oxidation as determined from CVs. Filled circles: reference electrode with a nanoporous glass plug in direct contact with the sample. Empty circles: free-flow double-junction reference electrode with a 100 mM NBu_4ClO_4 solution flowing into the sample.

The effect of CF_3COOH, on the potential of reference electrodes was investigated as well. CF_3COOH is commonly used to change the pH of organic solutions in order to probe the pH dependence of redox potentials and elucidate the mechanism of electron transfer reactions.[344-346] Such studies would be seriously compromised if the potential contribution of the reference electrode were affected by addition of CF_3COOH but changes observed in the CVs were mistakenly interpreted as changes in the redox potentials of an electroactive species caused by the involvement of protons in the electron transfer step.

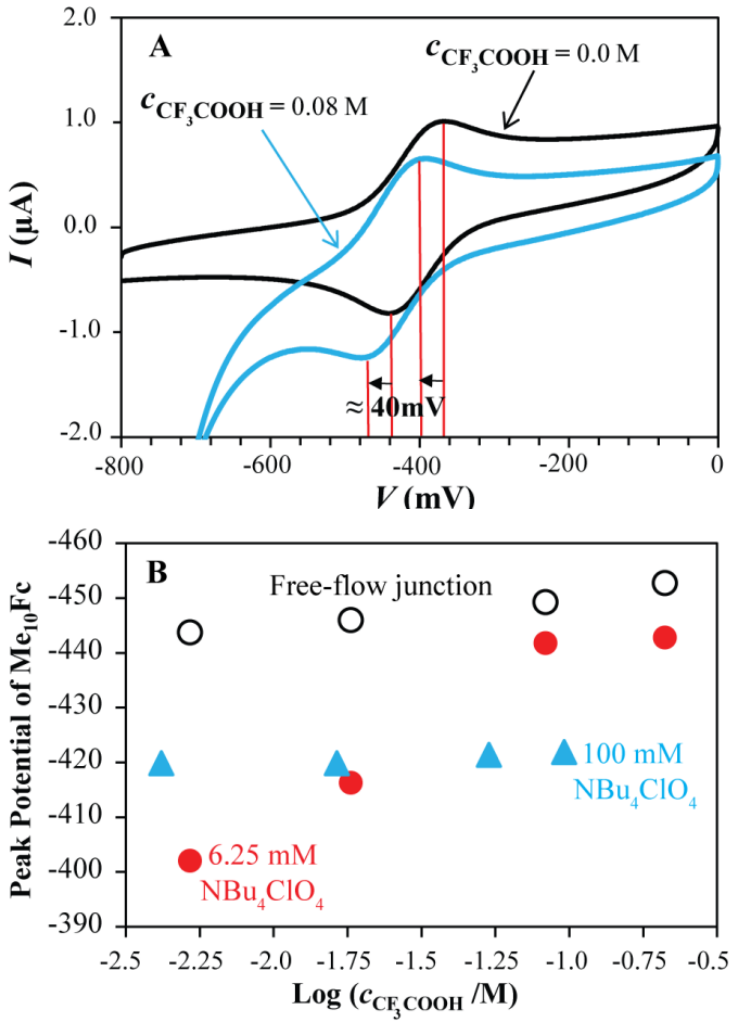

Figure 7. Effect of CF_3COOH on the potential of reference electrodes with nanoporous glass plugs. (A) CVs of 0.1 mM $Me_{10}Fc$ in 6.25 mM NBu_4ClO_4 in absence and presence of CF_3COOH. (B) Dependence of potential of $Me_{10}Fc$ (0.1 mM) oxidation on the CF_3COOH concentration. Filled circles and triangles show results for a reference electrode with a porous plug in direct contact to samples with an electrolyte concentration of 6.25 and 100 mM NBu_4ClO_4, respectively. Empty circles: sample with a 6.25 mM NBu_4ClO_4 electrolyte and a free-flow double-junction reference electrode (100mM NBu_4ClO_4 solution flowing into the sample).

As can be seen from Figure 7, the reference electrodes with nanoporous glass plugs show permselectivity for CF_3COOH at low ionic strength. Addition of CF_3COOH to a solution that does not have a sufficiently high concentration of supporting electrolyte (6.25 mM) causes significant undesirable changes in the reference potential (Figure 7A). However, by increasing the concentration of supporting electrolyte or avoiding direct contact between the porous plug and the sample, the changes in the reference potential during the measurement can be minimized (Figure 7B). As in the case of the experiments with aqueous solutions, the potential changes at low ionic strengths can be explained by anion exclusion and formation of a charge separation layer at the interface of the sample and the nanoporous glass plug.

8.4 Conclusions

In this work, we demonstrated that the porous glass plugs frequently used to provide an interface between reference electrodes and samples can cause unwanted variations in reference potentials. Repulsion forces between freely dissolved anions and the negative charges of the nanopore surfaces have been recognized as the source of error. Not only at low but even at moderately high ionic strengths, the Debye length exceeds the radius of the pores, resulting in anion exclusion from the porous plugs and formation of a charge separation layer at the interface of the porous glass and the sample. This effect occurs both with aqueous and organic solutions. The potential of the reference electrodes with nanoporous glass plugs is sample independent only in solutions with comparatively high ionic strength, and the use of a highly concentrated salt bridge electrolyte alone does not prevent measurement errors. In situations where modifying the sample composition to achieve a high ionic strength is not possible, the free-flow double-junction set up is preferable. Electrostatic theory suggests that, alternatively, micro- rather than nanoporous plugs may be used to avoid unwanted sample dependencies of the reference potential.

While we emphasize here the problems that can arise when using reference electrodes with nanoporous *glass* plugs, it is evident that reference electrodes with nanoporous plugs prepared from other materials may also be affected by the same problem if they have surfaces with ionizable groups. For example, some of the problems observed by Illingworth[5] with a selection of porous ceramic plugs may have had similar origins, although this has apparently never been investigated in detail. With a broader point of view, our results also add a new example for the still relatively small number of examples for electrostatic screening at nanoporous materials.[322,327,331] Implications of this effect go beyond electroanalytical chemistry, and should also be important to the development of, e.g., battery materials and nanoporous supercapacitors.

8.5 Acknowledgments

This project was partially supported by grant RL-0012-12 from the Initiative for Renewable Energy and the Environment of the University of Minnesota. We acknowledge Jon Thompson for interesting discussions about porous glasses.

9 CHAPTER NINE

Avoiding Errors in Electrochemical Measurements: Effect of Frit Material on the Performance of Reference Electrodes with Porous Frits

This work was a joint effort by this author and Stacey Saba (who carried out the characterization of polymer frits), and Evan Anderson (who assisted with voltammetry experiments).

Reference electrodes are designed to provide a constant and sample-independent reference potential and are used in almost every electrochemical measurement. In many commercially available and in-house-prepared reference electrodes, nanoporous glass plugs (often of a brand named Vycor) contain the electrolyte solution that forms a salt bridge between the sample and the reference solution. Recently, we showed that in samples with low ionic strength the half-cell potentials of reference electrodes containing nanoporous Vycor frits are affected by the sample composition and can shift by more than 50 mV (which can cause up to 900% error in the measurement). It was confirmed that the large potential variations result from electrostatic screening of ion transfer due to the negatively charged surfaces of the glass nanopores. Since Vycor glass was recently discontinued from the production line, new materials have been used as porous frits in commercially available reference electrodes, namely two porous glasses sold under the brand names of CoralPor and Electro-porous KT and porous Teflon and polyethylene polymers. In this work, we studied the effect of frit material on the performance of the reference electrodes, and show that the unwanted changes in the reference potential are not unique to electrodes with Vycor frits. However, increasing the pore size in the glass frits or switching to porous polymeric frits nearly eliminates the potential variations caused by screening of ion transport through the pores of the frit. Unfortunately, bigger frit pores result in larger flow rates of the reference solution through the pores, which can result in the contamination of test solutions. This contribution quantitatively describes the sample dependence of reference potentials and solution flow rates through the frits, allowing users to appropriately choose the frit material that suits their application.

9.1 Introduction

Reference electrodes designed to provide a constant and sample-independent reference potential are used for measurements with almost every electrochemical method (e.g., potentiometry, amperometry, voltammetry).[1,3] A constant potential is achieved by employing a half cell comprising a redox couple with buffered concentrations for all the participating reactants of the redox reaction. The most common redox systems for reference electrodes used in aqueous media is $Ag/AgCl/Cl^-$, where the metal is in contact with the AgCl precipitate and is immersed in an aqueous solution of potassium chloride (usually 1-3 M).[1-3] Reference electrodes for organic media usually apply a Ag/Ag^+ redox system, i.e., a Ag wire is immersed in a $AgNO_3$ solution of an organic solvent.[1,3]

To allow an accurate electrical measurement, reference and sample solutions should be brought into contact using a junction with low electrical resistance.[2,7] To avoid the cross-contamination of sample and reference solutions, intermixing of these solutions at the junction should be minimized.[2] A common approach for satisfying both of these criteria is separating the reference and sample solutions by a porous material filled with an electrolyte (usually the same electrolyte as used in the reference solution).[10] First reported in 1955, porous glass plugs with a high density of nanopores (4.0 nm average pore size),[11] were made commercially available under the brand name Vycor and were recommended for use in reference electrodes.[12] Nanoporous Vycor offered the advantage of restricting excessive mass transfer of reference and sample components across a stable and low-resistance junction.[7,12] Since then, Vycor has been widely used for fabrication of both in house-prepared and commercial reference electrodes.[7,10-12] Unfortunately, until very recently, there have been no systematic studies investigating the performance and limitations of these reference electrodes.

In 2013, we reported about systematic errors in measurements made with reference electrodes that contain nanoporous Vycor frits.[10] We showed that the reference potential

of these electrodes depends on the sample composition and can shift by as much as 50 mV.[10] While some electrochemical measurements are less affected by the potential of reference electrodes, a 50 mV change in reference potential can cause substantial errors in others, e.g., causing up to 900% error in potentiometric determination of monovalent ions.[42] The variations in the reference potential were shown to be caused by the surface charge density on the glass surface of the nanoporous Vycor, and to be highly affected by the ionic strength of the sample solution.[10,13] When the sample has low ionic strength, the Debye length (the length by which electrostatic forces persist in an electrolyte solution, which is inversely proportional to the square root of ionic strength)[13,333] approaches dimensions greater than the pore size of the frit. This results in electrostatic screening and prevents ion transport from the sample into the nanoporous frit.[10] For example, the Debye length in a 1.0 mM KCl solution is 9.6 nm, which is substantially larger than the 4.0 nm average pore size of the Vycor glass frits.[333] This phenomenon was also reported for several other nanostructured materials, including chemically modified nanoporous opal films, metal nanotubule membranes, chemically modified gold nanotubes, and single nanopores.[322-327,347]

Ion screening causes a sample-dependent phase boundary potential at the interface of the sample and the porous frit, which adds to the constant and sample-independent potential provided by the reference redox system, resulting in an overall sample-dependent potential of the reference electrode. Our work demonstrated this inherent disadvantage of reference electrodes with nanoporous frits and showed that variations in their reference potential.[10] Recently, nanoporous Vycor glass was discontinued from the production line, leaving suppliers of electrochemical equipment and and researchers in search of alternative materials to be used as porous frits for reference electrodes. This chapter reports on different readily available glass and polymeric monoliths of varied pore size and composition that have been reported as alternatives to Vycor. The performance of reference electrodes incorporating these frits is described, allowing for identification of the material that provides the most reliable reference electrode for particular applications.

9.2 Experimental

All cylindrical porous plugs had dimensions of approximately 3 mm diameter and 3 mm length. The porous Vycor was purchased from Koslow Scientific (Englewood, NJ). Electro-porous KT Glass (G0300) and porous polyethylene (G0194) plugs were purchased from Princeton Applied Research (Oak Ridge, TN). CoralPor 1000 glass was provided by SCHOTT (Duryea, PA). Glass tubing with pre-attached porous Teflon tips were purchased from CH Instruments (Austin, TX). The porous plugs were attached to glass tubes (7 cm long, 3 mm diameter) using Teflon heat shrink tubing. Aqueous reference electrodes were prepared by inserting a AgCl/Ag electrode into the glass tube attached to the porous plug, and filling the tube from the other end with 3.0 M aqueous KCl solution. The electrodes were then stored in 3.0 M aqueous KCl solution for at least one week prior to measurements. Reference electrodes for use in organic solutions were prepared by inserting an Ag wire into the glass tube with the porous plug and subsequently filling the tube with acetonitrile containing 10.0 mM $AgNO_3$ and 100 mM tetrabutylammonium perchlorate (NBu_4ClO_4). These electrodes were stored in an acetonitrile solution of 100 mM NBu_4ClO_4.

9.2.1 Measurements in Aqueous Media

Potential measurements were performed in stirred solutions at room temperature (25 °C) with an EMF 16 channel potentiometer (Lawson Labs, Malvern, PA) controlled with EMF Suite 1.02 software (Lawson Labs). A free-flow double-junction AgCl/Ag electrode with a movable ground glass sleeve junction (no porous plug) and with a 3.0 M KCl bridge electrolyte and reference electrolyte purchased from Mettler Toledo (Columbus, OH) was used as external reference electrodes in measurements.[2] All of the solutions were prepared with deionized purified water (18.2 MΩ cm specific resistance, EMD Millipore, Philadelphia, PA), and all measurements were performed in triplicate. The pH

measurements were performed with a pH half-cell electrode from Mettler Toledo (Columbus, OH).

9.2.2 Measurements in Organic Solutions

Electrochemical measurements were performed with a CHI600C potentiostat (CH Instruments, Austin, TX), a scan rate of 100 mV/s, and a three electrode setup. Gold disk electrodes (BAS, West Lafayette, IN) of 3.0 mm diameter were used as the working electrode; 0.25 mm Pt wire coil (99.998%, Alfa Aesar, Ward Hill, MA) was used as the auxiliary electrode. The working electrode was polished on Microcloth polishing pads using 5.0 μm Micropolish II deagglomerated alumina and was rinsed thoroughly with deionized water and then ethanol, followed by drying under a stream of argon. Prior to measurements, all solutions were purged with argon for 15 min while stirring vigorously to remove dissolved oxygen. All potentials are reported with respect to 10 mM Ag^+/Ag reference electrodes with porous plugs. Bis(pentamethylcyclopentadienyl)iron, $Me_{10}Fc$, (97%) was purchased from Aldrich (Milwaukee, WI).

9.2.3 Resistance Measurements

The resistance of the porous plugs were determined by impedance spectroscopy as reported previously[10,348] with a 1255B frequency response analyzer and a SI 1287 electrochemical interface from Solartron (Farnborough, Hampshire, UK) in aqueous 3.0 M KCl solution or 100 mM NBu_4ClO_4 acetonitrile solution (for frits filled with aqueous and organic electrolyte solutions, respectively). A two-electrode system was used with AgCl-coated Ag wires as electrodes for aqueous measurements and Ag wires for organic measurements. Resistances were obtained by fitting impedance spectra with ZView software (Scribner Associates, Southern Pines, NC) in the 10^4 to 10^5 Hz range. The plugs were characterized by scanning electron microscopy (SEM) and nitrogen sorption

measurements. Experimental details, and measurements of solution flow through the plugs, are described in the supporting information.

9.3 Result and Discussion

The mechanism of ion screening phenomenon (Figure 1), as observed in porous Vycor glass, suggests smaller errors in the potential of reference electrodes equipped with porous glass frits with larger pore diameters or porous frits that bear no surface charges (i.e., porous polymeric frits).[10] Two new porous glasses with the brand names of CoralPor and Electro-porous KT, and two porous polymers of different chemical identity (Teflon and polyethylene) have recently been used as replacements of Vycor for the fabrication of reference electrodes.[349-354] The effect of the frit material on the performance of each reference electrode was carefully investigated in this work.

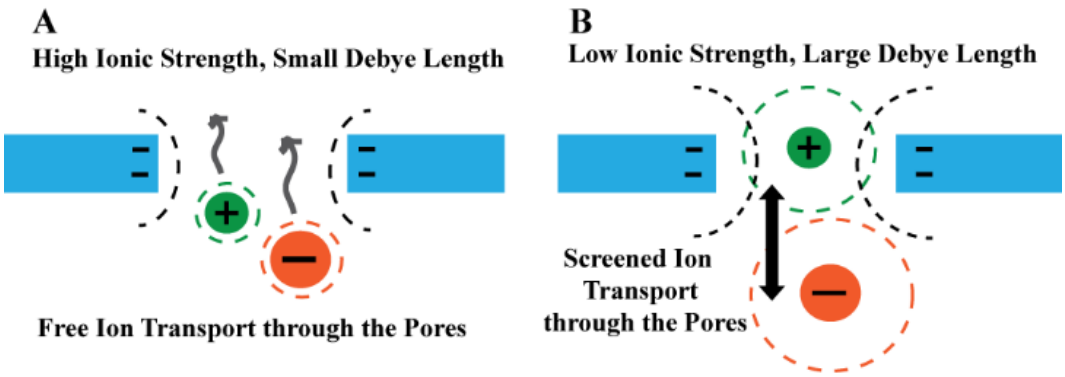

Figure 1. Two-dimensional representation of a pore in the porous glass network. The blue rectangles represent the glass structure, negative signs show the surface charge density on the pore wall, and the dashed lines show the Debye length. (A) A sample with high ionic strength, where the Debye length is smaller than the diameter of the pore, and ion transport occurs freely through the pores. (B) Sample with low ionic strength, where the Debye length is larger or comparable to the pore diameter and ion transport is affected by electrostatic forces. Scales are adjusted for easy visualization.

9.3.1 Porous Glass Frits

We prepared reference electrodes with Vycor, CoralPor, and Electro-porous KT glass frits (triplicate of each) using 3.0 M KCl as the inner filling solution for pictures of the experimental set-up see Figure S1).[1] The electrodes were stored in 3 M KCl, and impedance spectroscopy was used to verify the wettability of the frits. The low resistance of the frits (< 150 Ω, Table 1) confirmed that the pores were completely filled with 3 M KCl. The pH dependence of the potentials of aqueous reference electrodes with porous frits prepared with the Vycor, CoralPor, and Electro-porous KT glasses were measured is shown in Figure 2. Note that the potentials were measured with respect to an external free-flow sleeve-junction reference electrode (Figure S2), which does not contain a porous frit (3 M KCl inner filling electrolyte) and it is not biased by screening of ion transport at the salt bridge junction, as shown previously.[2,85,289,355,356]

Table 1. Properties of the porous frits used in this work.

	Vycor	CoralPor	Electro-Porous KT	Teflon	Polyethylene
Color	Clear	Clear	White	White	White
Average Pore Size[a]	4-6 nm	4-10 nm	500-1000 nm	1 μm	10 μLm
Resistance in 3.0 M KCl	69 ± 17 Ω	139 ± 53 Ω	71 ± 27 Ω	222 ± 195 Ω	424 ± 341 Ω
Resistance in 0.1 M NBu_4ClO_4	3.2 ± 0.5 kΩ	5.1 ± 0.9 kΩ	10.1 ± 0.5 kΩ	22.3 ± 0.4 kΩ	-----
Flow(aq) (μL/h)[b]	0.004 ± 0.002	0.005 ± 0.003	3.838 ± 1.317	29.307 ± 3.626	318.197 ± 279.331
Flow(org) (μL/h)[c]	0.003 ± 0.001	0.003 ± 0.001	2.442 ± 0.604	47.100 ± 15.700	----
Potential drift (mV over 48 h)[d]	7.1 ± 0.8	7.7 ± 7.6	8.1 ± 4.5	-2.2 ± 1.3	-5.8 ± 7.6

Standard deviations are based on measurements on three separate, but identically prepared electrodes.

[a]Pore size was estimated from N_2 sorption experiments for Vycor and CoralPor and from SEM micrographs for Electro-porous KT glass, Teflon, and polyethylene.

[b]Flow of 3.0 M KCl through the porous frits in an environment with 100% humidity, measured at 0.99 bar.

[c]Flow of acetonitrile solution of 10 mM $AgNO_3$ and 100 mM NBu_4ClO_4 through the porous frits in an acetonitrile saturated environ-ment, measured at 0.99 bar.

[d]Potentials of reference electrodes with aqueous inner filling solutions and the specified porous frit were monitored for 48 h in 0.10 M KCl at 25 °C with respect to an external free-flow sleeve junction reference electrode.

Figures 2A and 2B show the pH dependence of potentials of reference electrodes with porous Vycor frits at the two background concentrations of 0.01 and 0.30 M $KCl_{(aq)}$. With a background of 0.01 M KCl, increasing the pH from 2 to 12 resulted in potential shift greater than 40 mV. For comparison, the potential of a reference electrode with a large-pore junction is expected to be affected by a change in the liquid-junction potential (a non-equilibrium potential formed at the interface of two miscible solutions with different electrolyte concentrations or different cation and anion mobilities[1-3]) of less than 2.0 mV, as predicted by the Henderson equation.[1] Increasing the background electrolyte concentration to 0.30 M KCl nearly eliminates the shift in the potential of the reference electrode. Figures 1C and 1D demonstrate that the electrodes with CoralPor frits behave similarly to electrodes with Vycor frits (≈40 mV change in reference potential over 10 pH units), however there is much less variation (≈5 mV) in the potential of reference electrodes with glass frits made of Electro-porous KT glass.

SEM micrographs of the glass plugs show that Vycor and CoralPor glass have similar disordered network pore structures (Figures 3A and 3B). Nitrogen sorption experiments reveal that the pore size distributions of these two glass materials are also similar (4–16 nm based on a nonlocal density functional theory, NLDFT, kernel for nitrogen on silica applied to the adsorption branch)[357] and the materials have comparable Brunauer–Emmett–Teller specific surface areas of 112 and 129 $m^2\ g^{-1}$ for Vycor and CoralPor, respectively (see Figure 3C).[358] However, the SEM micrograph of Electro-porous KT glass shows a dramatically different structure with much larger pores on the order of a micrometer in size (Figure 3D). Since this pore size is much larger than the Debye length even in low ionic strength solutions (i.e., 9.6 nm in 1.0 mM aqueous KCl), electrodes containing electro-porous KT glass are less affected by changes in the sample composition.

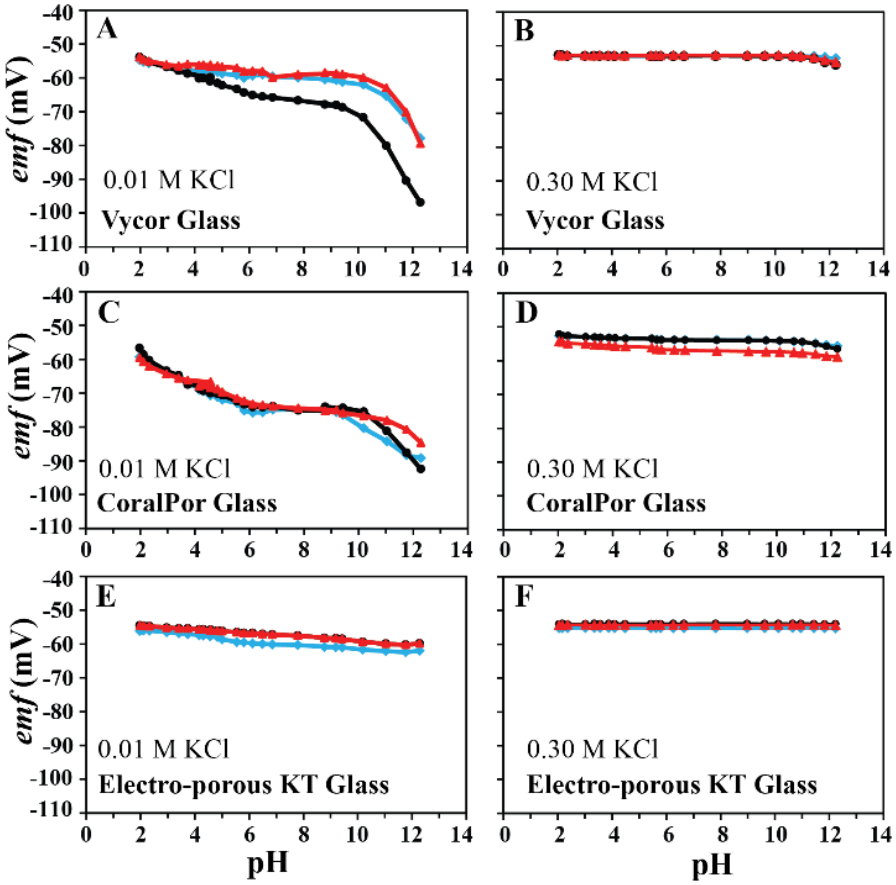

Figure 2. Dependence of the potential of reference electrodes with porous glass frits on pH at background KCl concentrations of 0.01 M (A, C, E) and 0.3 M (B, D, F). The type of glass frit is specified in each panel. The starting solution was 0.01 M HCl (with 0.01 M or 0.3 M background KCl), and the pH was increased by successive additions of 10.0 M NaOH solution. Measurements were made with three separate but identically prepared electrodes, as indicated by the black, red, and blue markers.

Changes in the reference potential are not only caused by varying pH, but also by changes in electrolyte concentration. To show the effect of a few representative electrolytes, the potentials of reference electrodes with porous glass frits are shown with respect to the concentration of KCl, $NaNO_3$, Na_2SO_4, or NBu_4Cl (Figure 4). Electrodes

with Vycor and CoralPor frits were affected quite strongly by changes in the concentration of these electrolytes (≈50 mV; see Figures 4A and 4B) while the electrodes with KT glass frits were affected to a lesser extent (≈10 mV). Only the potentiometric response of one electrode for each frit material is shown in Figure 4, but similar responses were observed for triplicate electrodes (see Figures S3–S6). As expected, the effect of different electrolytes on the reference potential is very similar, and only limited ion selectivity can be observed in the response curves. Because the sizes of all tested ions are much smaller than the Debye length (dictated by ionic strength of solution), the ion screening phenomenon is controlled by the ionic strength of the solutions rather than the character of particular types of ions.

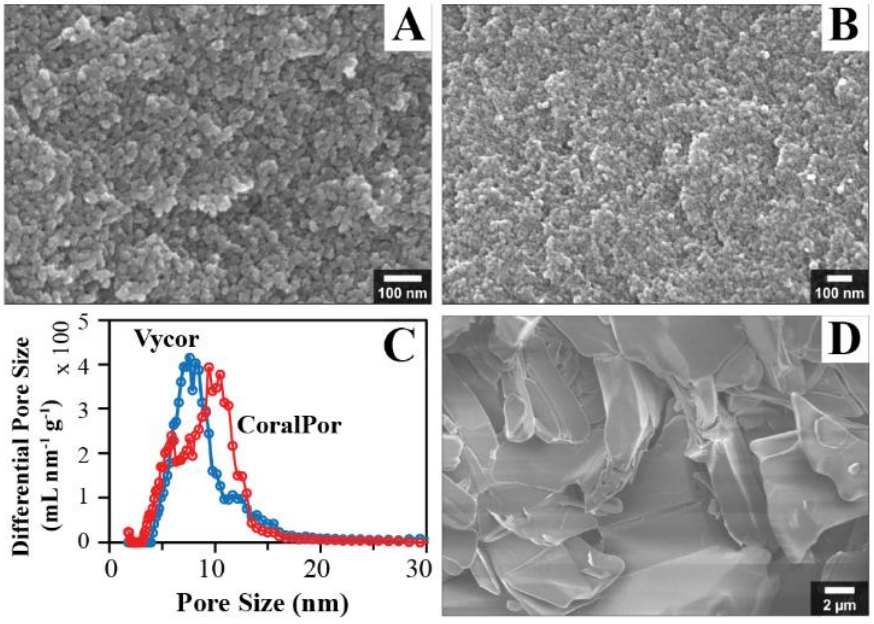

Figure 3. Characterization of commercially available porous plugs. SEM micrographs of Vycor (A), CoralPor (B), and the pore size distributions of each based on the NLDFT method applied to the desorption branch (C). SEM micrographs of electro-porous KT (D).

Evidently, increasing the pore size of the glass frit can substantially decrease the sample dependence of the potential and improve the performance of the electrode. However, the biggest disadvantage of larger pores is a more rapid intermixing of the reference and sample solutions due to higher flow rates through the porous plug. The Hagen–Poiseuille equation, which describes flow through a cylindrical pore, predicts that the flow velocity scales with the square of pore diameter. suggesting much larger flow rates for frits with larger pores, causing significant contamination of samples by bridge electrolyte.[359] Measurements show that solution flow through Electro-porous KT glass (3.8 ± 1.3 μL/h at ~ 0.99 bar) is at least three orders of magnitude larger than through Vycor and CoralPor glass, (Table 1). Considering the large flow of solution through the Electro-porous KT glass to the sample, the suitability of these electrodes must be assessed based on the time scale of the experiment and the test solutions' sensitivity to chloride contamination. The potential stabilities of the electrodes were monitored over 48 h in 0.1 M KCl at 25 °C, and all electrodes had potential drifts of less than 10 mV (see Table 1 and Figure S16).

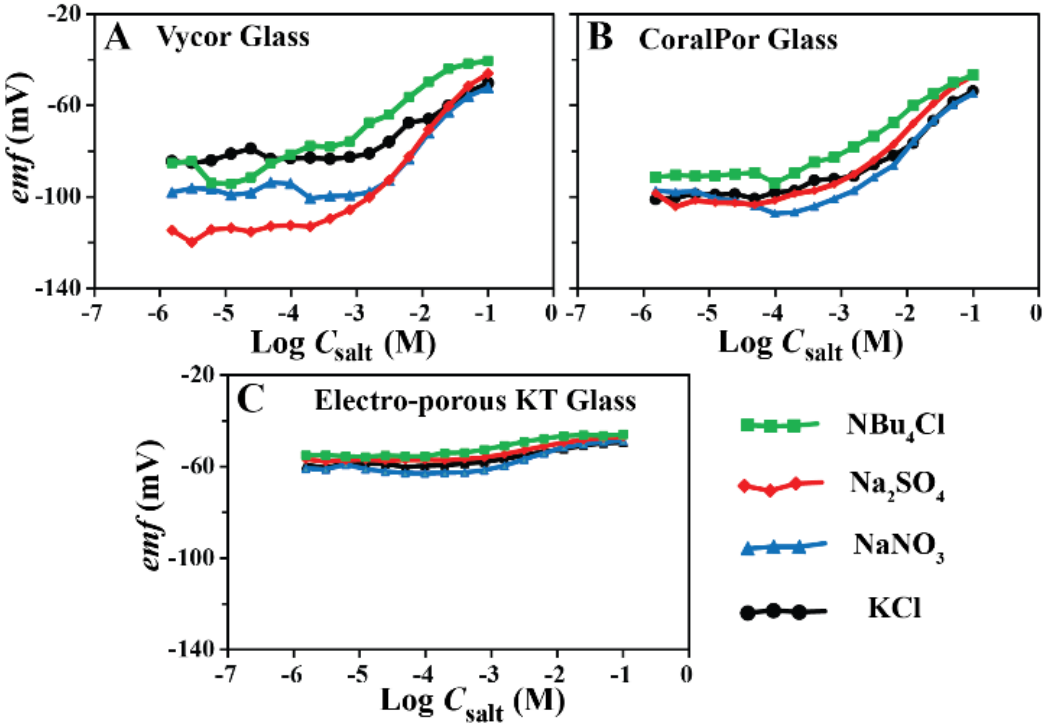

Figure 4. Effect of NBu_4Cl, Na_2SO_4, $NaNO_3$, and KCl on the potentiometric response of reference electrodes with nanoporous glass plugs made of Vycor (A), CoralPor (B), and Electro-porous KT (C) glass, as a function of salt concentration. Response curves of only one electrode for each frit material are shown.

9.3.2 Porous Polymer Plugs

In addition to porous glass, porous Teflon and polyethylene plugs have been reported as alternatives to Vycor frits.[353,354] SEM micrographs show that the pore sizes in these polymers are large (≈10 μm for polyethylene and ≈1 μm for Teflon) in comparison to those in porous glass frits (Figures 5A and 5B). Electrodes were fabricated with polyethylene and Teflon frits by filling the reference electrode tube with 3.0 M KCl. Due to the hydrophobic nature of both Teflon and polyethylene, we anticipated that the pores might not be readily wettable by aqueous solutions. Thus the electrodes were preconditioned in 3.0 M KCl for at least one week in attempts to facilitate the filling of

the pores with electrolyte solution. Notwithstanding impedance measurements showed very high resistances for these polymer frits (>1.0 GΩ vs. ≈100 Ω for the glass frits). We attribute this to incomplete wetting of the frits, preventing a proper junction from being formed between the inner filling and test solutions. Therefore, wetting of the frit was subsequently facilitated by applying pressure (~ 40 psi) to the inner filling solution, thereby filling the pores of the plug. Indeed, the frit resistance decreased by many orders of magnitude to < 500 Ω.

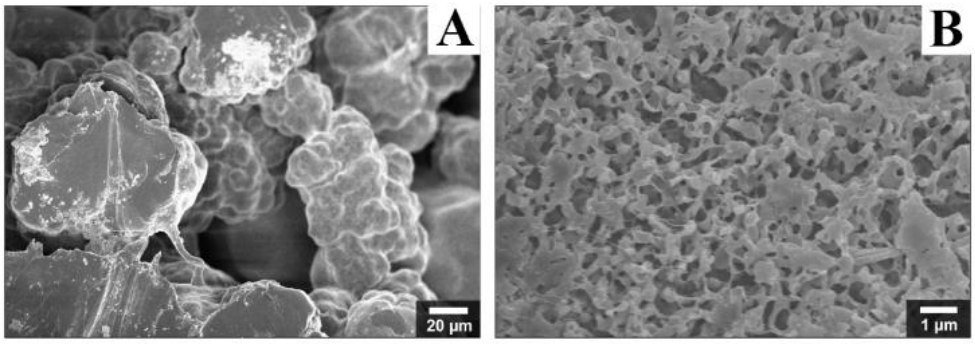

Figure 5. Characterization of commercially available polymeric plugs. SEM micrographs of polyethylene (A), and Teflon (B).

The effects of pH and the sample concentrations of NBu_4Cl, Na_2SO_4, $NaNO_3$, and KCl on the reference potential were tested as for the glass frits. As Figure 6 shows, the variations and sample dependence of the reference potentials were minimal (see also S10–S13). In most cases, there are only minimal changes in the potential of the electrodes upon changes in pH and the concentration of NBu_4Cl. However, in some of the electrodes, abrupt changes in the potential or regions where the potential appeared to be sample-dependent were observed. These potential changes were caused by entrapment of air bubbles in the porous frits, which was confirmed by frit resistances larger than 1.0 GΩ. The entrapment of air bubbles occurred during sample changes, when the frits were temporarily exposed to air. Examples for this erratic behavior of the reference electrodes are illustrated by the potential jumps at 0.001 M NBu_4Cl in Figures 6A and 6B and at pH

10 in Figure 6D. To minimize such effects, when an abnormal behavior of the electrodes was observed, experiments were paused, and air bubbles were removed by applying pressure on the inner filling solution. This resulted in an improved performance of the electrodes.

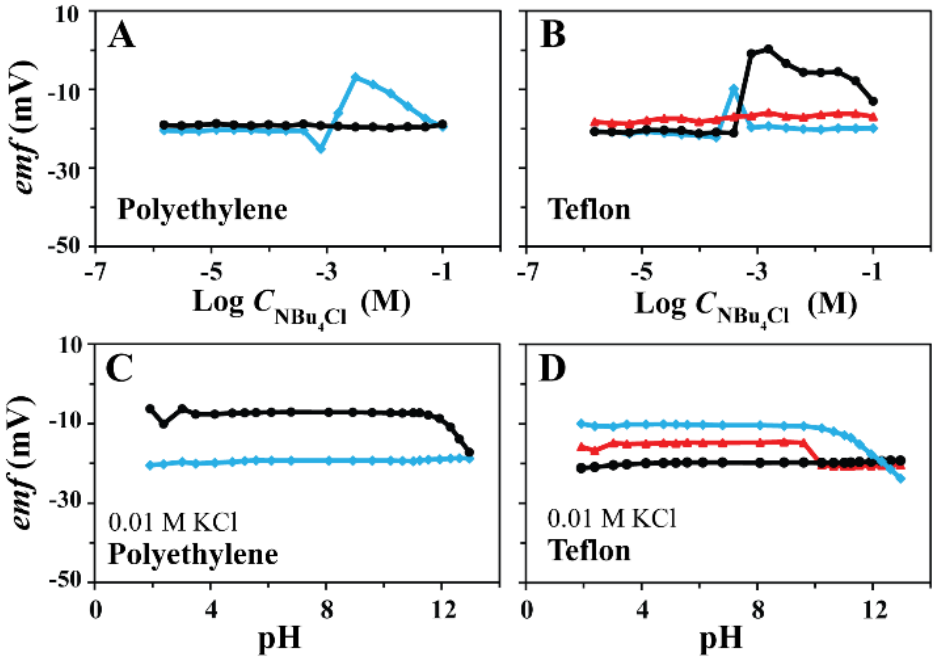

Figure 6. Effect of NBu_4Cl and pH on the potential of reference electrodes with porous frits made of polyethylene (A and C), and Teflon (B and D). The black, red, and blue traces show results for three separate, but identically prepared electrodes. Only two replicates are shown for electrodes with polyethylene frits; the flow of inner filling solution to the sample was so rapid for the third electrode (> 1000 µL/h) that the electrode could not be used within the timeframe of the experiment. The large flow was possibly caused by a crack in the frit.

In summary, reference electrodes with porous polyethylene and Teflon frits provide constant and sample-independent potential and, unlike reference electrodes with nanoporous glass frits, are not biased by ion screening effects. However, due to the

hydrophobic nature of these polymers, special attention and care must be paid to wetting of the frits during electrode fabrication and use. Also, due to larger pore sizes, solution flow rates through these polymeric frits are much larger than observed for Vycor and CoralPor (see Table 1). Therefore, even though reference electrodes with Teflon and polyethylene frits have good potential stability (≈5 mV for 48 h), they are not recommended for long term experiments due to contamination of samples with reference solution. The performance of reference electrodes comprising polymeric frits could be significantly improved by employing hydrophilic porous polymeric plugs with smaller pore sizes. We are currently investigating the applicability of new hydrophilic nanoporous polymer plugs for use as reference electrodes.

9.3.3 Reference Electrodes for Organic Media

Reference electrodes with nanoporous Vycor glass frits have also been widely used for measurements in organic media such as acetonitrile, propylenecarbonate, dimethylforamide, dichloromethane, and ionic liquids.[41,94,163,344,346,360,361] In this section, we compare reference electrodes with porous Vycor frits to electrodes with frits made of Vycor substitutes (CoralPor,[349] Electro-porous KT glass,[354] and porous Teflon[353]) in view of uses in organic solvents. Our previous work showed that the potential of reference electrodes with porous Vycor frits is affected by ion-screening effects at the surface of their nanopores, but that the potential variations are much smaller than what is observed in aqueous systems.[10] Electrodes were fabricated by immersing an Ag wire into a 10 mM $AgNO_3$/100 mM NBu_4ClO_4 acetonitrile solution that was separated from the sample by the porous frit, and were stored in an acetonitrile solution of the same composition. The Vycor, CoralPor, Electro-porous KT, and Teflon frits had similar resistances in 100 mM NBu_4ClO_4 (3-25 kΩ, Table 1), confirming complete infiltration of the acetonitrile solution into the pores of the frits.

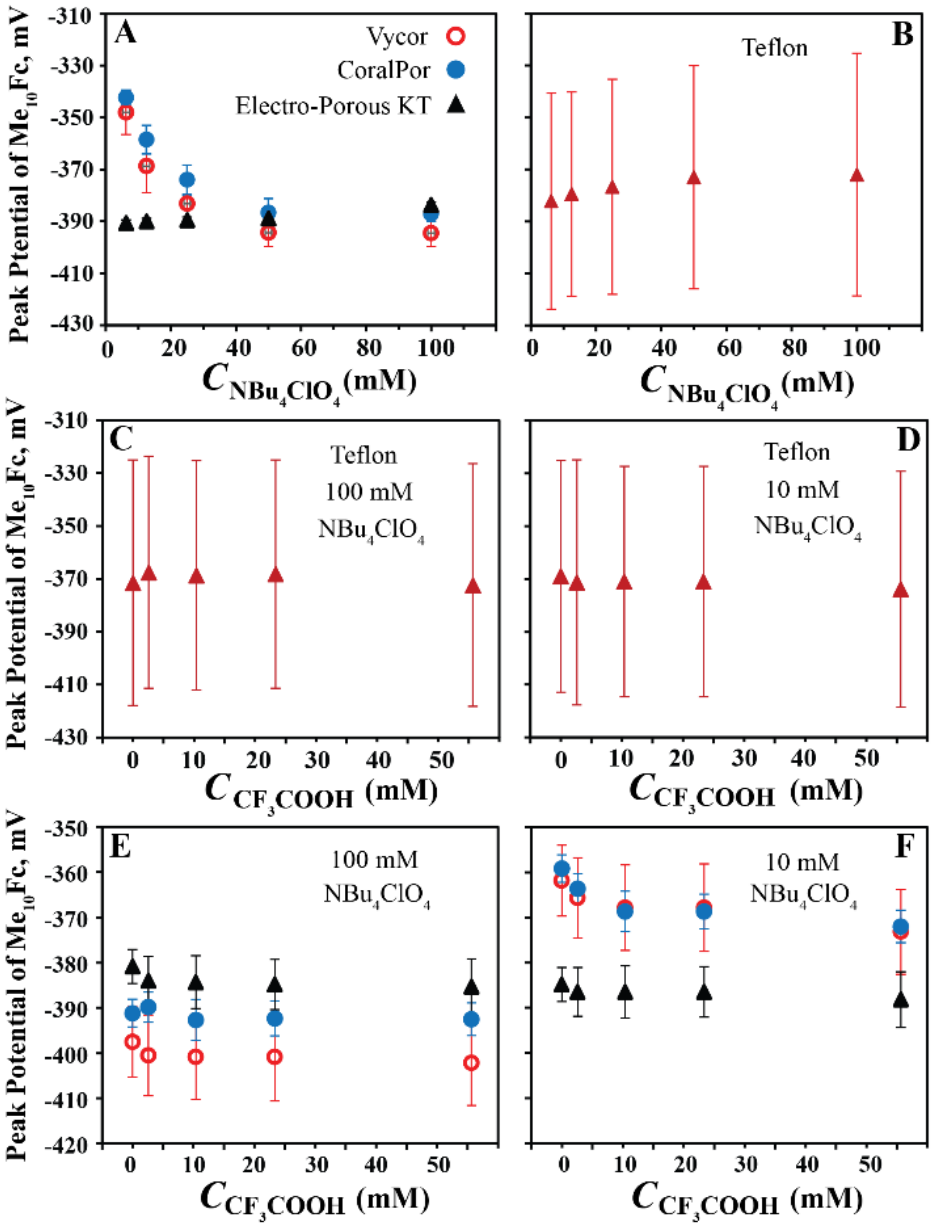

Figure 7. Effect of the concentration of the supporting electrolyte (NBu_4ClO_4) and CF_3COOH on the potential of reference electrodes with porous Vycor (empty red circles), CoralPor (solid blue circles) and KT glass (black triangles) (A), and porous Teflon (solid red triangles) frits (B). The peak potential of $Me_{10}Fc$ (0.1 mM) was determined from cyclic voltammograms measured with each reference electrode.

CF_3COOH was added to a background of 100 mM NBu_4ClO_4 (C and E) or a background of 10 mM NBu_4ClO_4 (D and F).

The effects of supporting electrolyte and trifluoroacetic acid (CF_3COOH) on the reference potential of the electrodes were quantified. The supporting electrolyte concentration was investigated because the majority of electrochemical analyses in organic solvents are carried out in presence of a background electrolyte, e.g., NBu_4ClO_4.[1] CF_3COOH was chosen because it is often used to adjust the pH of organic solutions in order to probe the pH dependence of redox potentials and electron transfer mechanisms.[344,346] It should be noted that if CF_3COOH result in changes in the reference potential, this may be interpreted wrongly as a change in the formal redox potential and could be mistakenly attributed to the involvement of protons in the redox reaction, causing significant errors in the study of electron transfer mechanisms. Therefore, to evaluate changes in the reference potential, we determined the peak potential from the oxidation of decamethylferrocene ($Me_{10}Fc$) in a cyclic voltammogram with respect to the reference electrode with the porous frit. Acetonitrile was used as a representative organic solvent. The $Me_{10}Fc^+/Me_{10}Fc$ couple was chosen because the effects of sample composition on the redox potential of this redox couple are minimal; therefore, a change in the observed peak potential of this redox couple can indicate changes in the reference potential caused by the type of frit used.[10,342]

Figures 7A and 7B show that decreasing the concentration of supporting electrolyte from 100 mM to 6.25 mM causes an up to 45 mV shift in potential of reference electrodes with Vycor and CoralPor frits, while electrodes with Electro-porous KT glass and Teflon frits are minimally affected (<10 mV, which can be explained by the liquid junction potential between the 100 mM NBu_4ClO_4 bridge electrolyte and the test solution[1,328]). This observation is consistent with predictions from ion-screening theory, and also the performance of these electrodes in aqueous systems. Larger standard deviations for electrodes with Teflon frits compared to those with glass frits are noticeable (determined

by measurements performed on identically prepared electrodes with three separate frits). This is attributed to a greater variability in the pore structure of the Teflon frit, compared to the glass frits, resulting in a greater frit-to-frit variability for Teflon. Addition of 50 mM CF_3COOH to two test solutions with high (100 mM NBu_4ClO_4) and low (10 mM NBu_4ClO_4) ionic strength had minimal effects on the potential of electrodes with Teflon frits (< 5 mV) (Figures 7C and 7D). The same behavior was observed for electrodes with Electro-porous KT glass frits (Figures 7E and 7F). The effect of CF_3COOH on the potential of electrodes with Vycor and CoralPor frits depended on the ionic strength of the solution, and the magnitude of potential change was greater at 10 mM (≈10 mV) compared to 100 mM (≈3 mV) NBu_4ClO_4. Similar as for electrodes for aqueous systems, the flow rate of electrolyte solution through the porous frits is much larger for Electro-porous KT glass and Teflon frits than for Vycor and CoralPor frits (Table 1).

9.4 Conclusions

Our earlier work showed that the nanoporous frits that are frequently used in reference electrodes can cause an unwanted sample dependence of the liquid junction potential to these electrodes. The potential changes are caused by electrostatic screening of ion transfer into the negatively charged pores of the glass frit when the Debye length in the sample solution has dimensions comparable to or greater than the pore diameter. This effect occurs both in aqueous and organic solutions, and can be minimized by employing a high ionic strength background in the test solution. This work showed that the potential of electrodes with glass frits with larger pore sizes (e.g., Electro-porous KT, which has been recently introduced as a replacement for Vycor, which is no longer produced commercially) is less affected by the ion screening phenomenon. However, solution flow through the frits increases as the pore sizes increases, which can cause significant contamination of test solutions by the reference solution in electrodes with frits with larger pore sizes in long-term measurements. The application of porous polymers that bear no surface charges as frits eliminates the potential variations caused by the ion

screening phenomenon, but large pore sizes and decreased wettability of the currently commercially available frit materials (Teflon and polyethylene) limits their application in reference electrodes suitable for real-life analyses. The development of more hydrophilic polymers with smaller pores is desirable for this purpose. To avoid unwanted errors in electrochemical measurements, we recommend the use of reference electrodes that do not have nanoporous frits. If an alternative reference electrode is not accessible, we recommend using Vycor and CoralPor frits (with the smallest pores) in samples with high ionic strength, and Electro-porous KT glass and Teflon frits in low ionic strength solutions.

9.5 Acknowledgments

This project was partially supported by a Graham N. Gleysteen Excellence Fellowship and a University of Minnesota Doctoral Dissertation Fellowship to M. P. S. M., a NSF Graduate Research Fellowship to S.A.S., and Grant RL-0012-12 from the Initiative for Renewable Energy and the Environment of the University of Minnesota. Parts of this work were carried out in the Characterization Facility, University of Minnesota, which receives partial sup-port from NSF through the MRSEC program.

9.6 Supporting Information

9.6.1 Measurement of Solution Flow through the Frits

Solution flow through the porous frits was measured at a pressure of 0.99 bar (pressure caused by 5 cm height of 3.0 M KCl added to the atmospheric pressure at the altitude of Minneapolis, MN). The aqueous reference electrodes were kept in a water-saturated environment (to minimize evaporation of the inner filling solution) and the changes in the height of the inner filling solution were measured over a period of 60 days for Vycor and CoralPor frits, and 1 day for Electro-porous KT glass, Teflon, and polyethylene frits. Similar measurements were performed for reference electrodes with organic reference and bridge electrolyte solutions except that the electrodes were stored in an acetonitrile-

saturated environment, and that the inner filling solution contained 10 mM $AgNO_3$ and 100 mM NBu_4ClO_4 in acetonitrile.

9.6.2 Potentiometric Response of Reference Electrodes with Porous Glass Frits

Electrodes with Vycor, CoralPor, and Electro-porous KT glass frits (triplicate of each) were prepared using 3.0 M KCl as the inner filling solution; see Figure S1 for a representative electrode. The potentials were measured with respect to an external free-flow sleeve-junction reference electrode (3.0 M KCl inner filling and bridge electrolyte solution), which did not contain a porous frit (see Figure S2). To evaluate the sample dependence of the potential of reference electrodes with porous glass frits, electrodes were placed in 0.1 M solutions of the electrolyte (KCl, $NaNO_3$, Na_2SO_4, and NBu_4ClO_4), and the electrolyte concentration was altered by successive dilutions of the test solution with deionized water, while monitoring the potential. Results of these experiments are shown in Figures S3–S6.

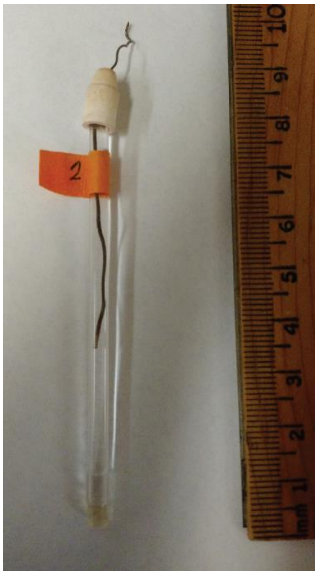

Figure S1. An electrode with a porous CoralPor frit, with an inner AgCl/Ag reference electrode and a 3.0 M KCl inner filling solution. The porous plugs were attached to glass tubes (7 cm long, 3 mm outer diameter) using heat shrink tubing.

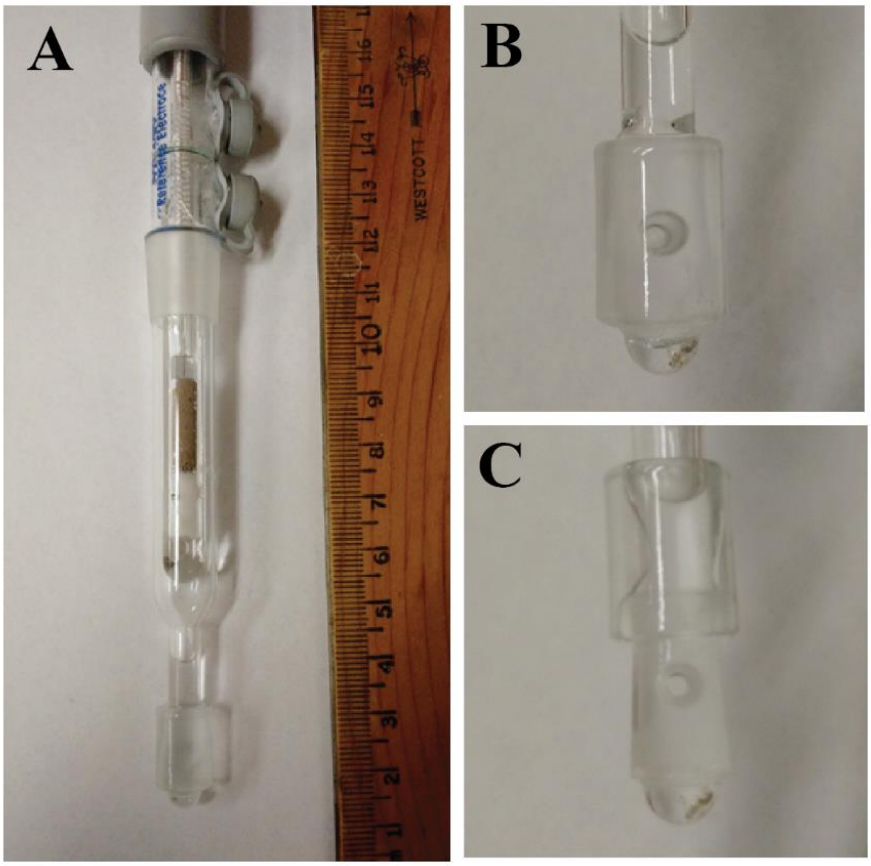

Figure S2. A free-flow double-junction AgCl/Ag electrode with movable ground glass sleeve junction (no porous plug) with 3.0 M KCl bridge electrolyte and reference electrolyte solutions (purchased from Mettler Toledo, Columbus, OH) that was used as external reference electrodes for all potentiometric measurements (A). Zoomed-in view of the sleeve junction of this electrode (B and C).

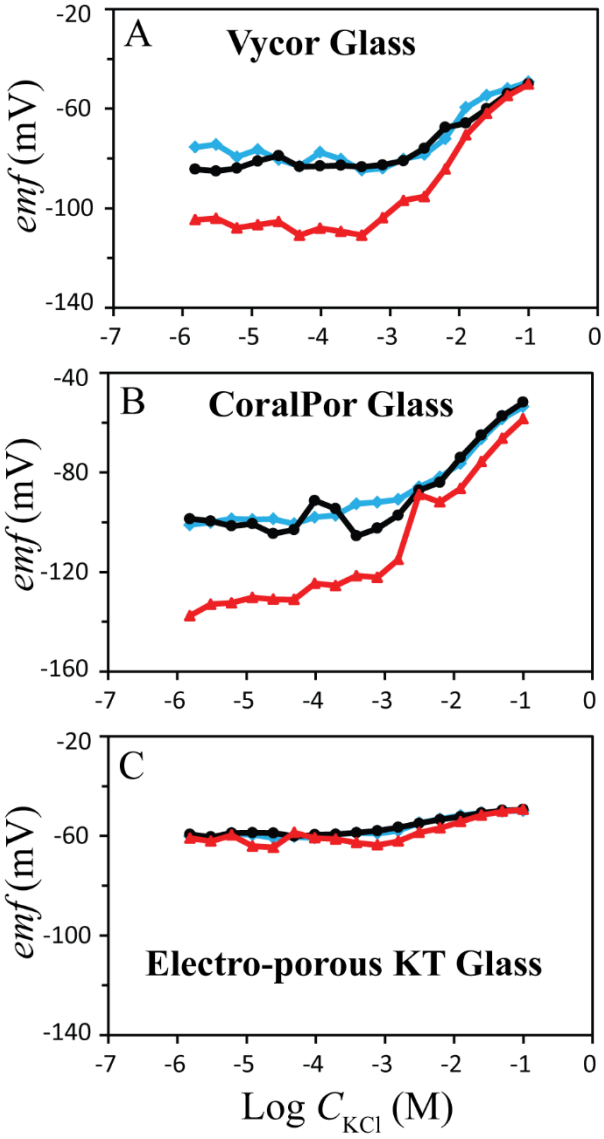

Figure S3. Effect of KCl concentration on the potential of reference electrodes with Vycor (A), CoralPor (B), and electro-porous KT (C) glass frits. The black, red, and blue traces show results for three separate, but identically prepared electrodes.

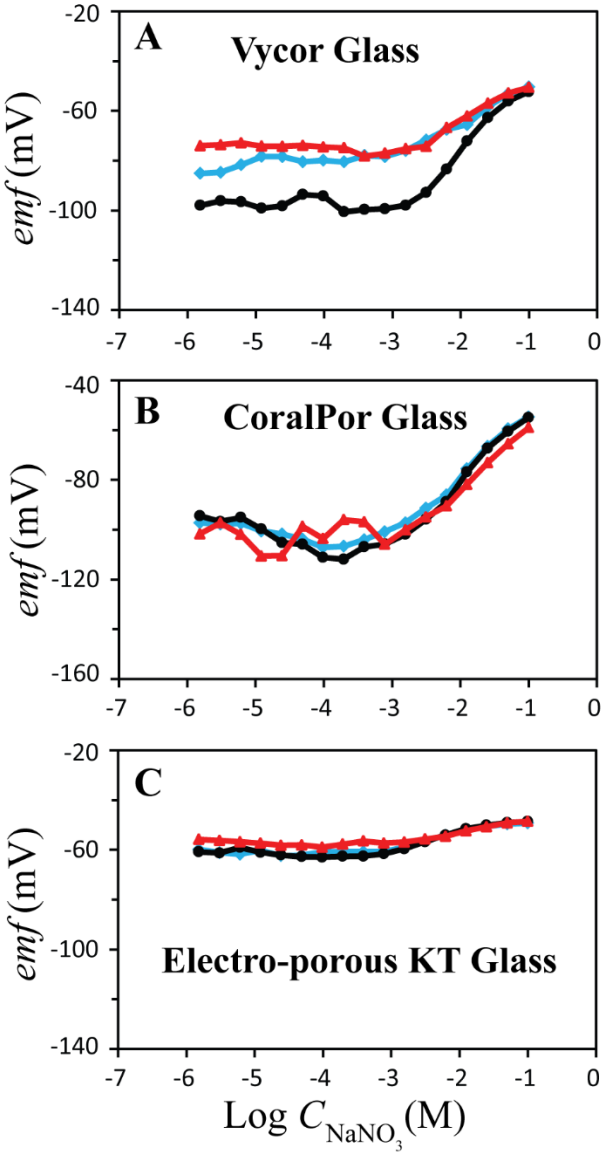

Figure S4. Effect of $NaNO_3$ concentration on the potential of reference electrodes with Vycor (A), CoralPor (B), and electro-porous KT (C) glass frits. The black, red, and blue traces show results for three separate, but identically prepared electrodes.

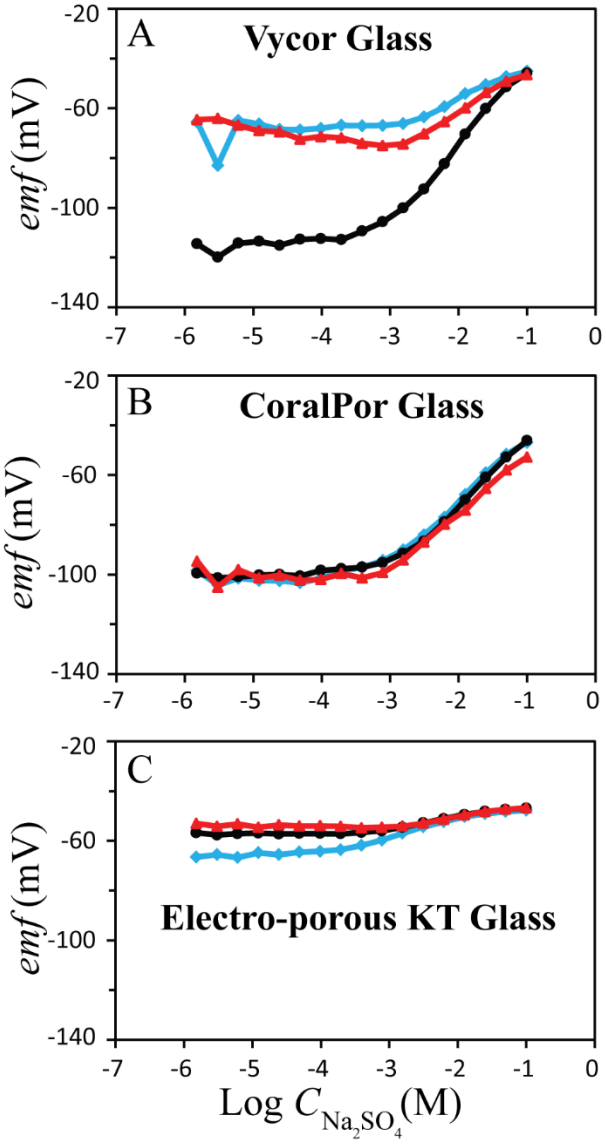

Figure S5. Effect of Na_2SO_4 concentration on the potential of reference electrodes with Vycor (A), CoralPor (B), and electro-porous KT (C) glass frits. The black, red, and blue traces show results for three separate, but identically prepared electrodes.

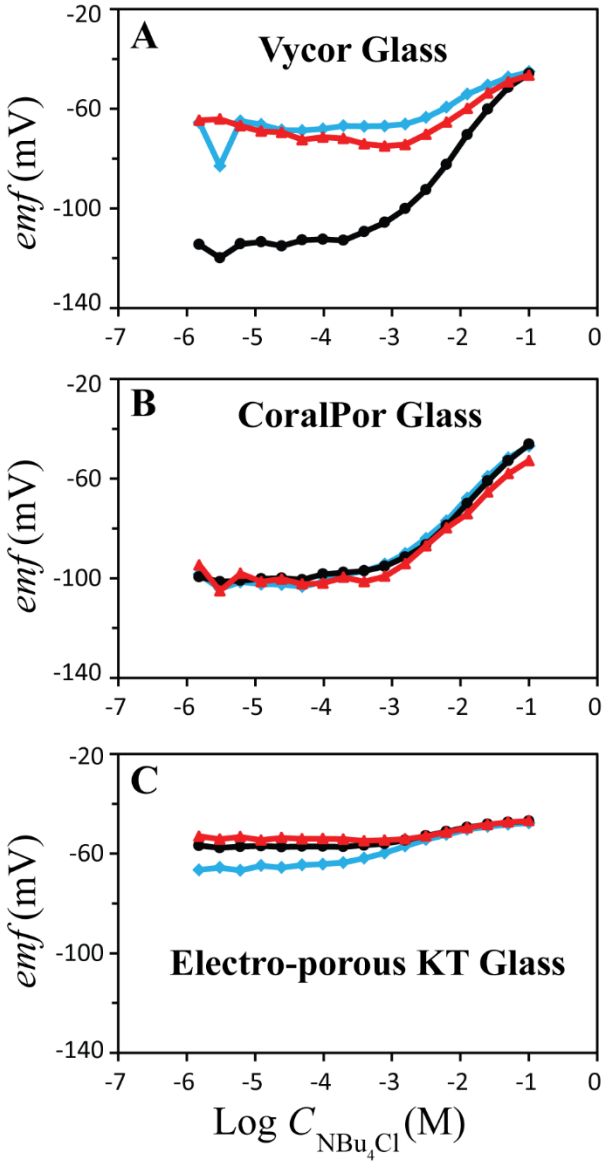

Figure S6. Effect of NBu_4Cl concentration on the potential of reference electrodes with Vycor (A), CoralPor (B), and electro-porous KT (C) glass frits. The black, red, and blue traces show results for three separate, but identically prepared electrodes.

9.6.3 Half Cell Potentials of of Reference Electrodes with Porous Polymer Frits

Electrodes with porous Teflon or polyethylene plugs were filled with 3.0 M KCl and equilibrated for at least one week. The potentials were measured with respect to an external free-flow sleeve-junction reference electrode (see Figure S2). To evaluate the sample dependence of the potential of the reference electrodes with porous polymeric frits, electrodes were placed in 0.1 M test solutions of the electrolyte (KCl, $NaNO_3$, Na_2SO_4, and NBu_4ClO_4) and the electrolyte concentration was altered by successive dilutions of the test solution with deionized water while monitoring the potential. Response to pH, KCl, $NaNO_3$, Na_2SO_4, and NBu_4Cl are shown in Figures S4–S8.

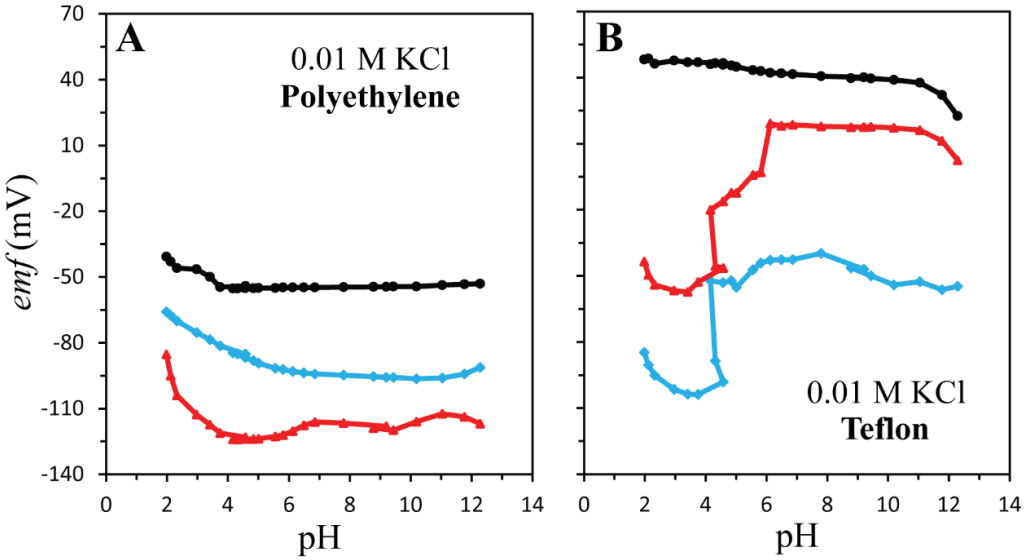

Figure S7**.** pH dependence of the potential of reference electrodes with porous polymeric frits in aqueous solutions with a 0.01 M KCl background. The type of the polymer frit is specified in each panel. The starting solution was 0.01 M HCl (with 0.01 M or 0.3 M background KCl), and the pH was increased by successive additions of aqueous 10.0 M NaOH solution. Measurements were performed in triplicate using identically prepared electrodes. The black, red, and blue traces represent individual electrodes.

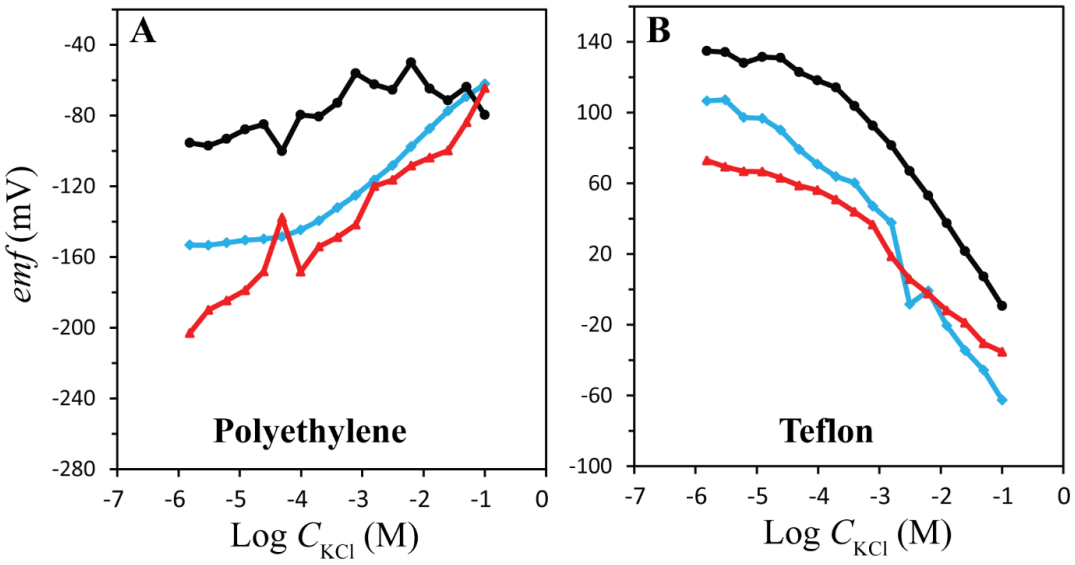

Figure S8. Effect of KCl concentration on the potential of reference electrodes with Teflon and polyethylene frits. Measurements were performed in triplicate using identically prepared electrodes. The black, red, and blue traces represent individual electrodes.

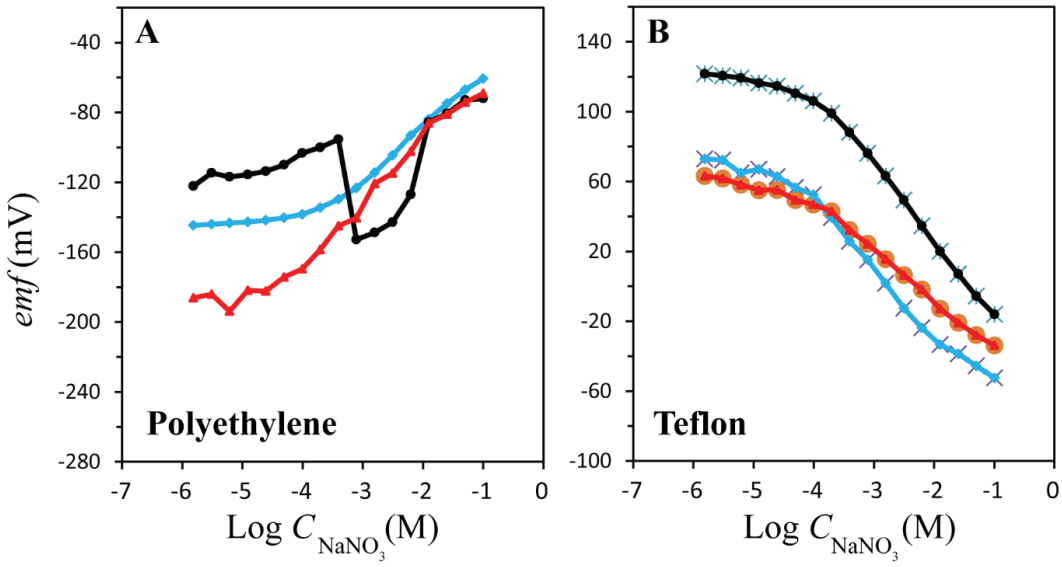

Figure S9. Effect of $NaNO_3$ concentration on the potential of reference electrodes with Teflon and polyethylene frits. Measurements were performed in triplicate using identically prepared electrodes. The black, red, and blue traces represent individual electrodes.

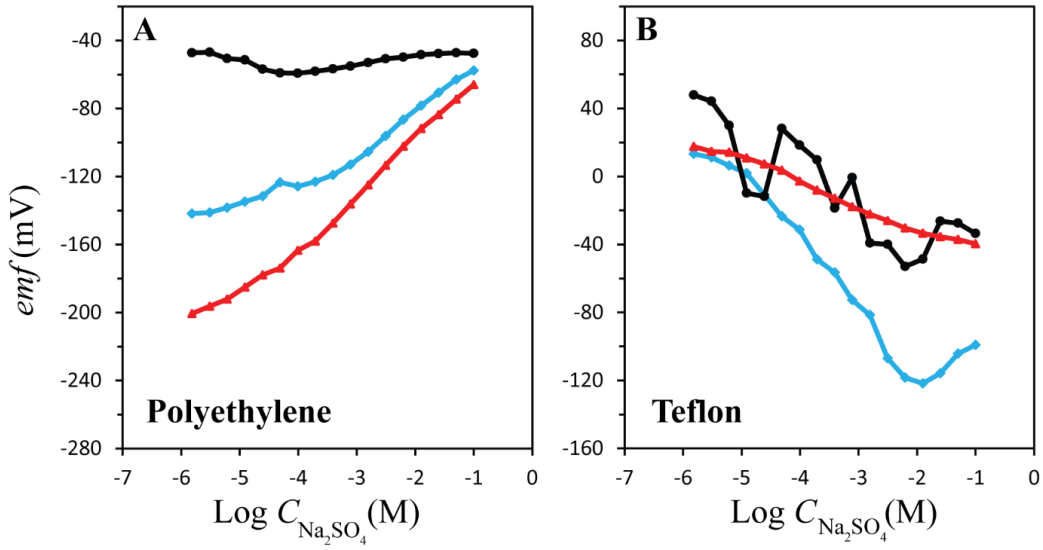

Figure S10. Effect of Na_2SO_4 on the potential of reference electrodes with Teflon and polyethylene frits. Measurements were performed in triplicate using identically prepared electrodes. The black, red, and blue traces represent individual electrodes.

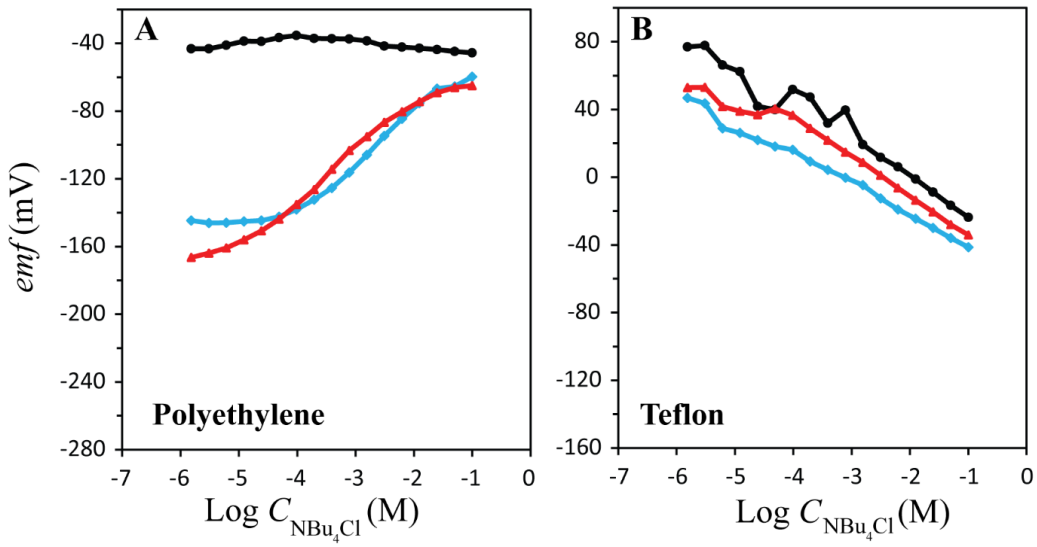

Figure S11. Effect of NBu_4Cl concentration on the potential of reference electrodes with Teflon and polyethylene frits. Measurements were performed in triplicate using identically prepared electrodes. The black, red, and blue traces represent individual electrodes.

To improve the signal stability of the reference electrodes with porous polymeric frits and facilitate wetting of the polymer plugs, a stream of air was pointed at the top of the inner filling solution of the electrode. The pressure caused by the air stream (≈40 psi) facilitated filling the pores with 3.0 M KCl, as confirmed by measuring the resistance of the frits (<500 Ω). The improved wetting minimized the electrode-to-electrode variations of the emf and reduced the sample dependence of the reference potential. The effects of the concentration of KCl, $NaNO_3$, Na_2SO4, NBu_4Cl, and pH are shown in Figures S10–S15. In some cases, during the measurement or during the preparation steps, air bubbles got trapped in the polymeric frit, which resulted in changes and a sample-dependence of the reference electrode potential. Entrapment of air bubbles resulted in increased resistance of the plugs, as confirmed by impedance spectroscopy. Pausing the experiment and applying a stream of air (producing an approximate pressure of 40 psi) on top of the

inner filling solution restored the previous condition and improved the performance of reference electrodes.

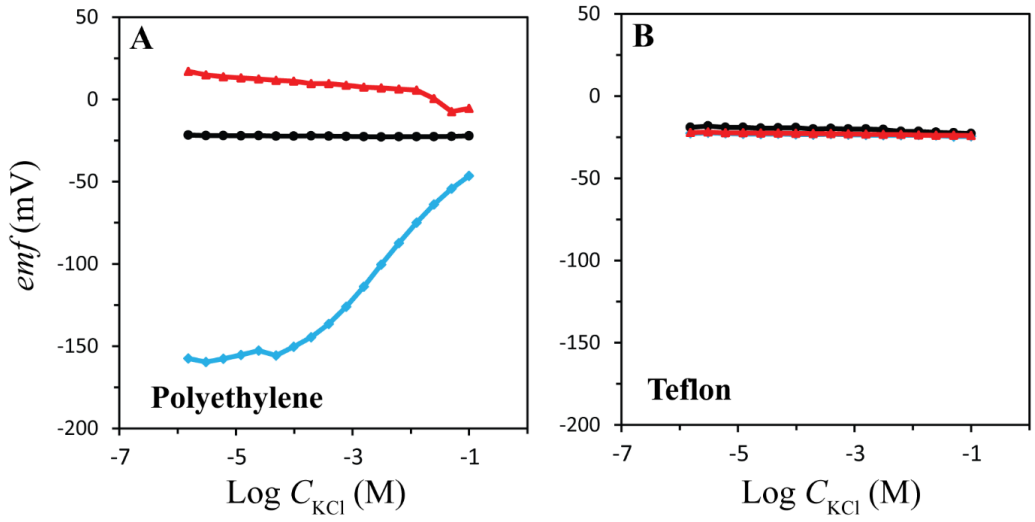

Figure S12. Effect of KCl concentration on the potential of reference electrodes with Teflon and polyethylene frits. Measurements were performed in triplicate using identically prepared electrodes. The black, red, and blue traces represent individual electrodes. The type of the polymer frit is specified in each panel. Wetting of the plug was facilitated by applying pressure on the inner filling solution, thereby filling the pores of the porous plug.

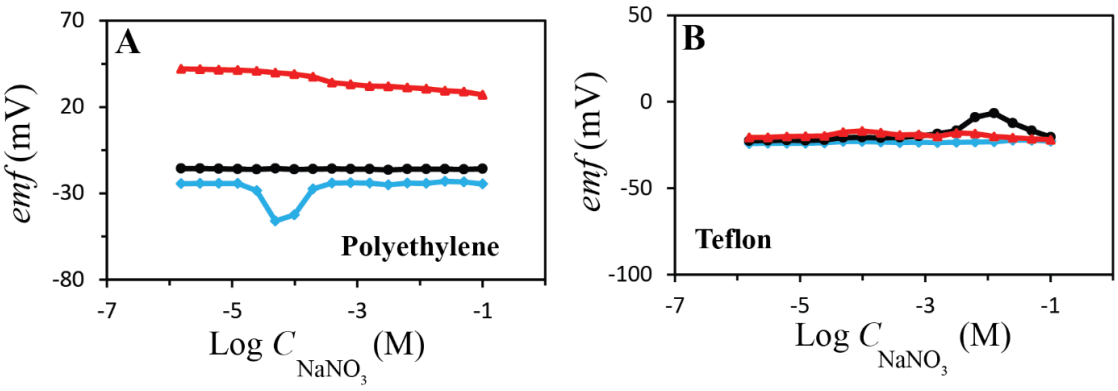

Figure S13. Effect of $NaNO_3$ concentration on the potential of reference electrodes with polyethylene (A) and Teflon (B) frits. Wetting of the plug was facilitated by applying pressure on the inner filling solution, thereby filling the pores of the plug. Measurements were performed in triplicate using identically prepared electrodes. The black, red, and blue traces represent individual electrodes.

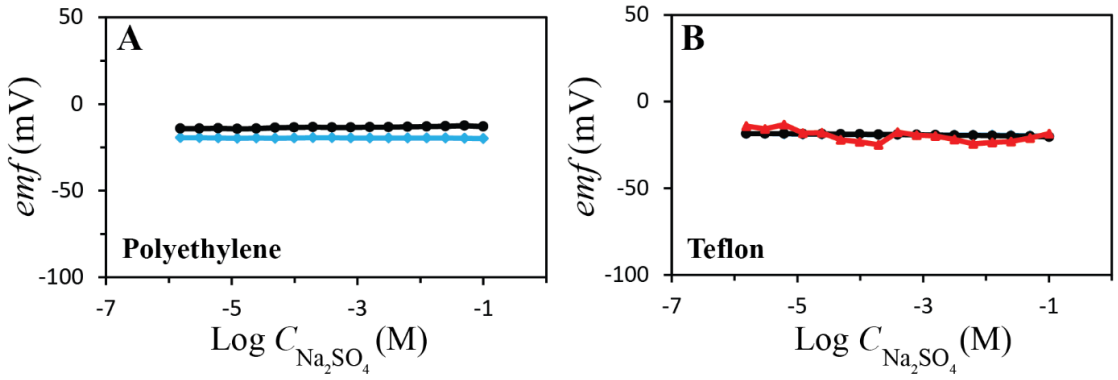

Figure S14. Effect of Na_2SO_4 concentration on the potential of reference electrodes with polyethylene (A) and Teflon (B) frits. Wetting of the plug was facilitated by applying pressure on the inner filling solution, thereby filling the pores of the plug. Measurements were performed in triplicate using identically prepared electrodes. The black, red, and blue traces represent individual electrodes. Only two replicates are shown for electrodes with polyethylene frits; the flow of inner filling solution to the sample was so rapid for the third electrode (> 1000 μL/h) that the electrode could not be used within the time frame of the experiment. The large flow was possibly caused by a crack in the frit.

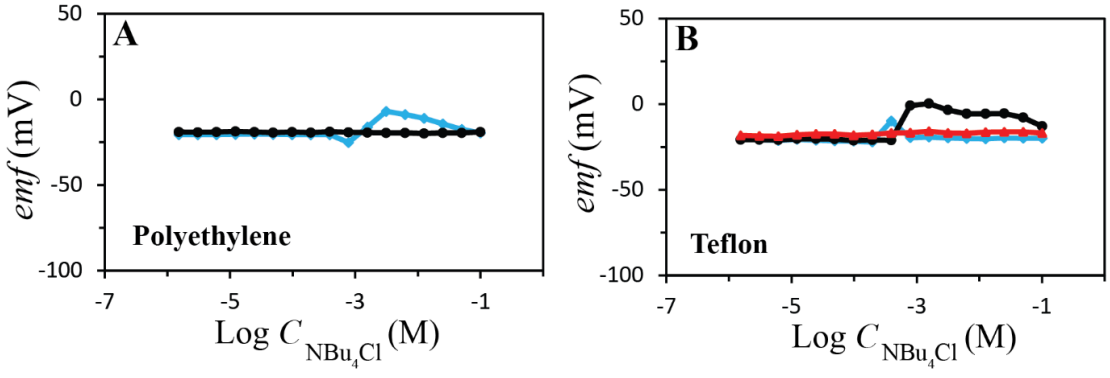

Figure S15. Effect of NBu_4Cl concentration on the potential of reference electrodes with polyethylene (A) and Teflon (B) frits. Wetting of the plug was facilitated by applying pressure on the inner filling solution, thereby wetting the pores of the plug. Measurements were performed in triplicate using identically prepared electrodes. The black, red, and blue traces represent individual electrodes. Only two replicates are shown for electrodes with polyethylene frits; the flow of inner filling solution to the sample was so large for the third electrode (> 1000 μL/h) that the electrode could not be used within the time frame of the experiment. The large flow was possibly caused by a crack in the frit.

9.6.4 Potential Stability

Potentials of reference electrodes with porous Vycor glass, CoralPor glass, Electro-porous KT glass, Teflon, and polyethylene frits (reference solution 3.00 M KCl) were monitored for 48 hours in a temperature-controlled (25 °C) 0.10 M KCl solution with respect to an external free-flow sleeve-junction reference electrode (see Figure S2). Potential of electrodes with respect to time are shown in Figure S16.

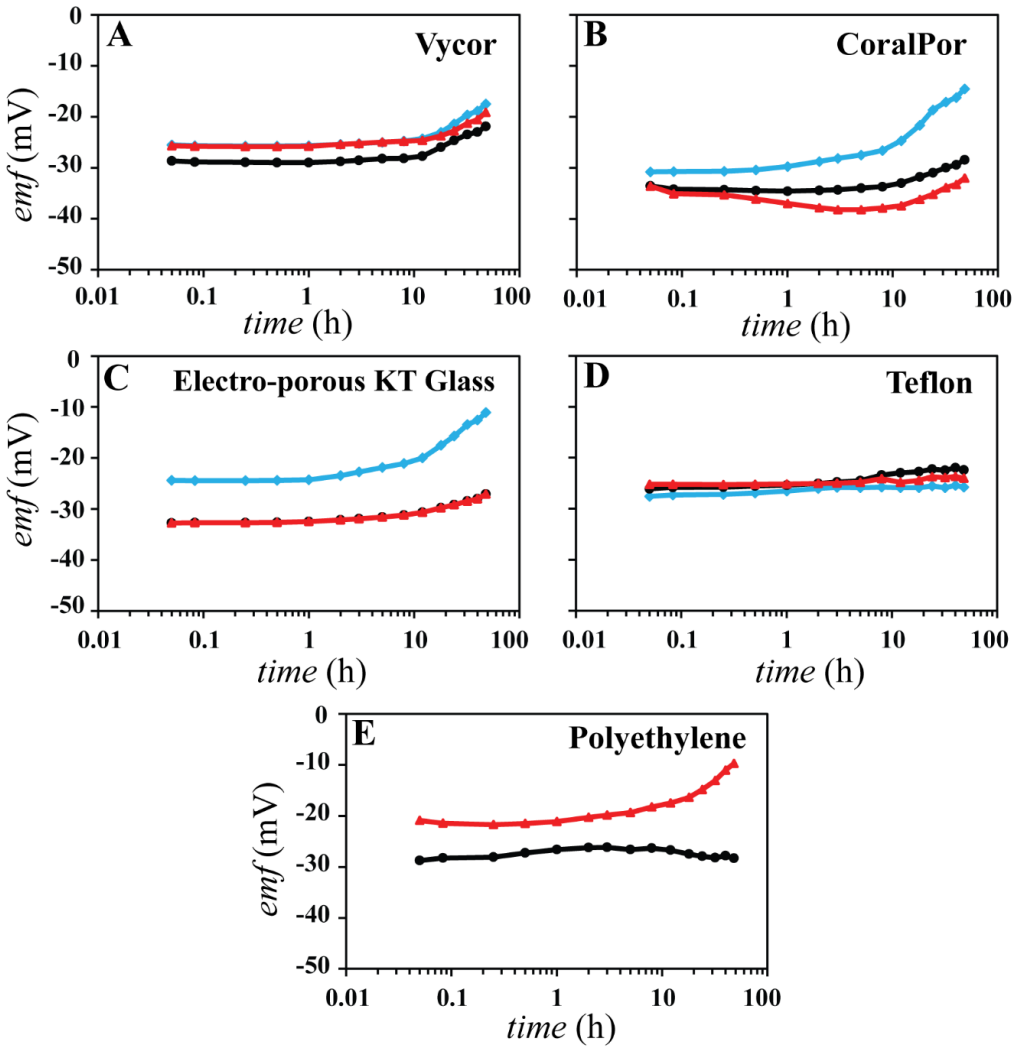

Figure S16. Signal stability of reference electrodes with Vycor (A), CoralPor (B), Electro-porous KT (C), Teflon (D), and polyethylene (E) frits in a 0.10 M KCl at 25 °C. Measurements were performed in triplicate using identically prepared electrodes. The black, red, and blue traces represent individual electrodes. Only two replicates are shown for electrodes with polyethylene frits; the flow of inner filling solution to the sample was so large for the third electrode (> 1000 µL/h) that the electrode could not be used within the time-frame of the experiment. The large flow was possibly caused by a crack in the frit.

9.6.5 Scanning Electron Microscopy and Nitrogen Sorption Measurements

Scanning electron microscopy micrographs were obtained on a Hitachi S-4700 cold field emission gun scanning electron miscroscope with an accelerating voltage of 3–5 kV. Before imaging, the plugs were cryo-fractured and coated with ca. 3 nm of Pt via sputtering using either a VCR Group IBS TM200S Ion Beam Sputterer or a Balzers Union MED 010. Nitrogen sorption isotherms were collected on a Quantachrome Autosorb iQ^2-MP at liquid nitrogen temperature (77 K). Prior to measurement, samples were outgassed at 200 °C for 2 h, followed by 50 °C for 6 h using a turbomolecular vacuum pump. Brunauer-Emmett-Teller (BET) specific surface areas were obtained from the adsorption branch from P/P_0 = 0.05–0.35.[358] Mesopore size distributions were estimated using a nonlocal density functional theory kernel for nitrogen on silica with cylindrical pores applied to the adsorption branch.[357]

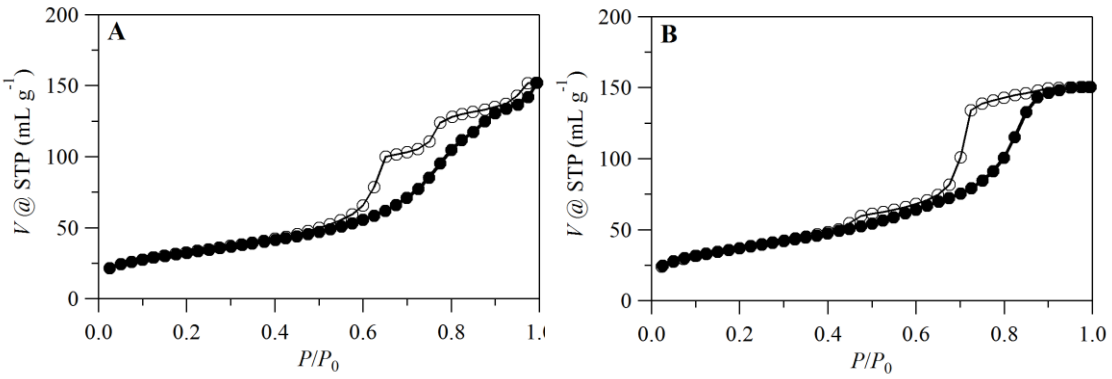

Figure S17. Nitrogen sorption isotherms for Vycor (A) and CoralPor (B) glass. Filled circles indicate adsorption and empty circles indicate desorption.

10 CHAPTER TEN

Fluorophilic Electrolytes and Ionophores

This work was a joint effort by this author and Evan Anderson (who assisted with conductivity measurements and synthesis of fluorophilic anionic sites), and Xin Sean Chen (who assisted with potentiometric measurements on fluorous-phase pH ISEs).

10.1 Development of Fluorophilic Electrolytes

Application of fluorous phases to sensing membranes of ISEs resulted in development of a new generation of ISEs with much wider response ranges, increased selectivities, and higher resistances to biofouling in real-life analyses.[77,80,82,85,87,289,356] These characteristics are achieved because of the extremely low polarity and polarizability of fluorous environments; however, the low polarity and poor coordinating properties of fluorous media also causes poor ion solubility in these phases. As a result, fluorous-phase ISEs generally have resistances much larger than the conventional PVC-based ISEs (the resistance of ISEs are generally determined by the resistance of the sensing membrane).[82] To avoid any potential gradients across the membrane, there should be proper ion conductance in the ISE sensing membrane. Morover, for an accurate potential measurement, the resistance of the ISE must be much lower than the input resistance of the potentiostat used for electrical measurements. For example, for a potentiostat with an input resistance of 1.00 TΩ, a membrane resistance of 10.00 GΩ will result in 1% error in the determination of emf of ISEs.

The electrical resistance of ISE membranes can be lowered by dissolving an electrolyte consisting of two lipophilic ions.[67,362] The same strategy can be adapted for fluorous-phase ISEs, however, it is very challenging to find electrolytes that have sufficient solubilities in fluorous phases. A fluorophilic electrolyte can be developed by pairing a highly fluorophilic cation (e.g., cationic sites used in fluorous-phase ISEs) with a fluorophilic anion (e.g., anionic sites used in fluorous-phase ISEs).[82]

10.1.1 Anionic Site for Fluorous-Phase ISEs

Highly hydrophobic tetraphenylborate salts commonly used in conventional ISEs are insufficiently soluble in fluorous phases. To increase the solubility of the salt, the anion structure was modified by addition of perfluorinated alkyl groups to the meta positions of the phenyl rings of tetraphenylborate. This resulted in development of the first

fluorophilic anionic site, tetrakis[3,5-bis(perfluorohexyl)phenyl]borate, which was successfully used in cation-selective fluorous-phase ISEs, see Figure 1.[77] The eight perfluorohexyl groups of the anionic site result in fluorine content of 67.5% (w/w) and cause the high solubility of this salt in the fluorous matrix. This electrolyte was synthesized according to a modified literature procedure in two steps from 1,3,5-tribromobenzene.[363,364]

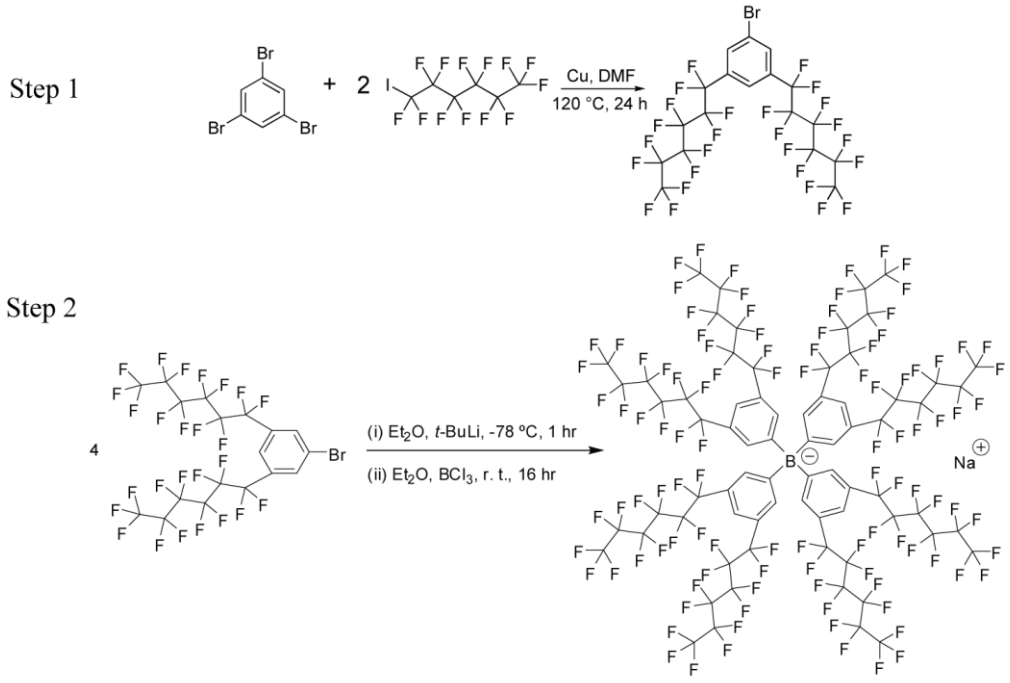

Figure 1. Synthesis of tetrakis[3,5-bis(perfluorohexyl)phenyl]borate.

10.1.2 Cationic Sites for Fluorous-Phase ISEs

In order to extend sensing with fluorous-phase ISEs, development of a highly fluorophilic cationic site which is soluble in a fluorous matrix even when paired with highly hydrophilic ions such as Cl^-, F^-, or HPO_4^{2-} is needed.[365] Several cations based on ammonium, phosphonium, and bisphosphineiminium structures were reported as fluorophilic cations with application in fluorous-phase ISEs. Examples of these

structures are shown in Figure 2. Cation 1 did not show sufficient solubility in fluorous solvents when paired with hydrophilic anion of chloride.[82] Cation 5, developed by Maruoka and co-workers was found to be soluble in perfluorohexanes when paired with Br^-.[366] Unfortunately, the 11-step synthesis required to prepare this salt (overall yield approximately 19%) inhibits its widespread application.

A fluorophilic phosphonium electrolyte bearing six fluorous ponytails (number 4 in Figure 2) was developed by P.G. Boswell and coworkers.[82] High solubilities (at least 14 mM) for this electrolyte in fluorous solvents of perfluoromethylcyclohexane, perfluorohexanes, and perfluoroperhydrophenanthrene was reported. This electrolyte was used as a cationic site in the first reported fluorous-phase anion-exchanger membrane electrodes.[82] The anion-selective fluorous-membrane sensors exhibited Nernstian responses and fast response times (less than 1 min) when measuring NO_3^-, I^-, and Br^-. However, when measuring the ions F^-, OAc^-, NO_2^-, OH^-, and HCO_3^-, ISEs exhibited noisy responses, and in some cases response times increased to over 30 min. For these ions, the response was strongly dependent on the rate of sample stirring. An explanation for the unusual stir rate dependence is that the phosphonium salt is unstable and degrades in the presence of those anions that cause the noisy, stir rate dependent responses. This hypothesis was confirmed by the authors by stirring the perfluoro-(perhydrophenanthrene) solution of the fluorophilic phosphonium salt at room temperature for 24 hours in the presence of an aqueous 1.0 M NaOH solution. ^{31}P NMR spectroscopy was used to observe decomposition of fluorophilic phosphonium cations to a phosphine oxide.

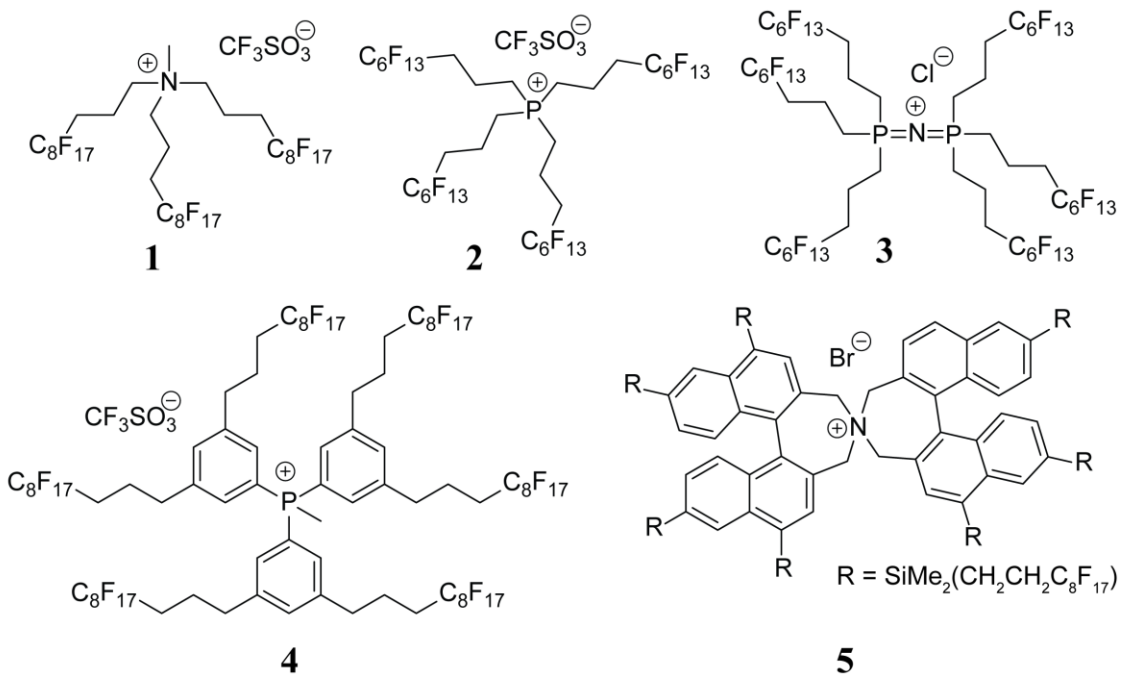

Figure 2. Structures of fluorophilic electrolytes with application as cationic exchangers for fluorous-phase ISEs.

A more stable fluorophilic cationic site (compound 2 in Figure 2) with a similar structure was reported by Chen and coworkers soon after.[365] Loss of response of fluorous-phase anion exchanger ISEs based on this compound was observed only upon exposure to highly alkaline solutions. Unlike the membranes doped with the methyltriarylphosphonium derivative, the membranes containing cation 2 did not exhibit a stir rate dependence of the F^- response and short-term drifts in the responses to hydroxide and basic anions. A loss of sensor response was only observed when the fluorous membranes were exposed to 0.1 M hydroxide solutions for 24 hours which was attributed to decomposition of the phosphine to a phosphine oxide according to the data obtained from ^{31}P NMR spectroscopy. It has been hypothesized by the authors that in extremely alkaline conditions, the phosphonium cation slowly decomposes to form two

phosphine oxides, i.e., $(Rf_8(CH_2)_2)(Rf_6(CH_2)_2)_2PO$ and $(Rf_6(CH_2)_2)_3PO$.[365] This hypothesis was confirmed by high resolution mass spectrometry.

The resistance of the prepared fluorous anion-exchanger membranes (2.0 mM tetraalkylphosphonium salt in perfluoroperhydrophenanthrene) was measured to be 5.6 ± 0.3 GΩ, which is sufficiently low to permit potentiometric measurements without complications.[365] Interestingly, this resistance was much lower than that of the fluorous anion selective membranes with the same concentration of the methyltriarylphosphonium salt (2 mM) in the same fluorous solvent.[365] Indeed, sensing membranes containing the latter could only be used when a fluorophilic electrolyte salt was added to lower the electrical resistance. Charge delocalization in the methyltriarylphosphonium unit would be expected to disfavor ion pair formation, which is just the opposite of the observed trend. Therefore, it appears likely that steric effects dominate, favoring ion pairs of the sterically only poorly shielded methyltriarylphosphonium ion. Evidently, the tendency to form electrically neutral ion aggregates can limit the usefulness of a fluorophilic salt just as much as a limited solubility.[365]

The fluorophilic salt bis(tris[(perfluorohexyl)propyl]-phosphine)iminium chloride (compound 3 , Figure 2) was used to provide cationic sites in a highly selective carbonate ISE.[86] In comparison to salts of fluorophilic cations used in previous potentiometric studies, the bis(triphenylphosphoranylidene)ammonium cation has the advantage of a higher chemical stability in the presence of OH^-.[86] Fluorous membranes doped with cationic site 3 did not show any sign of deterioration even when exposed to strongly alkaline solutions, such as 0.1 M NaOH, and exhibited no more interference from OH^- than expected for a nonspecific ionophore-free ion exchanger membrane. The resistance of the ion exchanger ISE membrane with 2 mM cationic site 3 in perfluoroperhydrophenanthrene as the solvent was reported to be 20.1± 1.5 GΩ which is higher than cationic sites 2 and 4 with the same concentration and solvent.[86]

10.1.3 Imidazolium and Ammonium Based Fluorophilic Cations

The bis(phosphine)iminium cation provided excellent chemical stability, but poor conductivity, contrary to the tetralkylphosphonium cation with high conductivity, but low relatively chemical stability. Low chemical stability of this cation is likely caused by coordination of the accessible d-orbitals in the valence shell of the cation to strong bases such as OH^-. Therefore, it is crucial to develop of a new class of fluorophilic cations with higher chemical stability, higher solubility, and also higher electrical conductivity. The tetralkylammonium cations could possibly be less affected by OH^- in the sample solution, but their limited solubilities in the fluorous phases restricted their application as cationic sites. The proposed solution for improving solubility of fluorophilic tetraalkylammonium cations is incorporating four perfluorinated alkyl ponytails in the cation structure rather than three fluorinated ponytails and a methyl group. The synthesis of the following cation shown in Figure 3 was proposed.

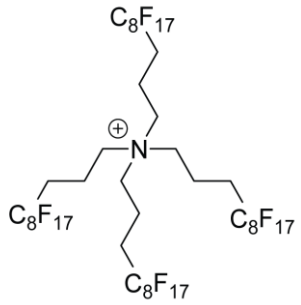

Figure 3. Fluorophilic tetraalkylammonium cations with four perfluorinated alky ponytails.

This synthesis was designed based on a modified literature, using 3-(perfluorooctyl)propyl iodide as starting material, shown in Figure 4.[367]

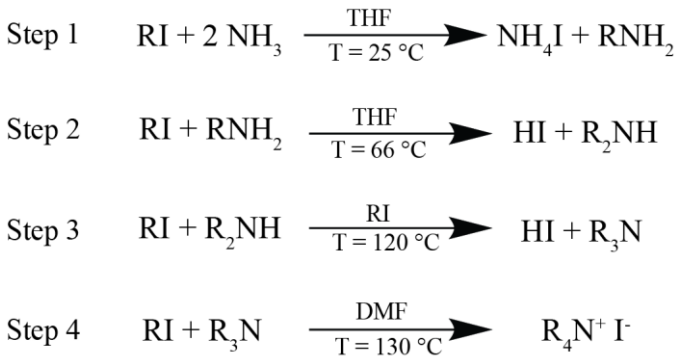

Figure 4. Synthetic scheme of synthesis of fluorophilic amines and quaternary ammoniums from fluorophilic alkyl iodides.

The synthesis was carried out successfully to obtain the tertiary amine of tris(4,4,5,5,6,6,7,7,8,8,9,9,10,10,11,11,11-heptadecafluoroundecyl)amine, confirmed by ^{1}H NMR and ^{13}C NMR spectroscopy and mass spectrometry. Unfortunately, step 4 of the synthesis, which was the quaternarization of this amine, did not proceed successfully. Increasing the reaction temperature resulted in degradation of the amine. This phenomenon can be explained by reduced nucleophilicity of nitrogen at each step, caused by high electron withdrawing characteristics of perfluoroalkyl groups.[87] A strategy to overcome this issue could be increasing the number of CH_2 spacers between the nitrogen and perfluorinated alkyl groups. Increasing the number of CH_2 spacers from three to four could mitigate the reduced nucleophilic activity of nitrogen caused by multiple perfluorinated alkyl groups, therefore, synthesis of cation shown in Figure 5 was proposed. To date, the synthesis of the tertiary amine, tris(5,5,6,6,7,7,8,8,9,9,10,10,11,11,12,12,12-heptadecafluorododecyl)amine, has been carried out successfully.

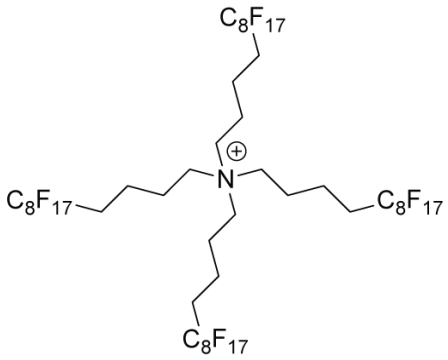

Figure 5. Tuning the number of CH_2 spacers to develop fluorophilic quaternary ammonium cations.

Despite the ammonium, phosphonium, and bis(phosphine)iminium core structures which have been studied for development of fluorophilic cations, imidazolium based cations have not been considered as potential cationic sites for fluorous-phase ISEs. Imidazolium cations have many interesting properties including high conductivity, high chemical stability, and high solubilities in organic solvent, indeed, many ionic liquids developed to date, use imidazolium core structure for their cations.[106,153,164,166] Synthesis of fluorophilic imidazolium cations was carried out based a published procedure, see Figure 6.[368-370] Structures were confirmed by ^{1}H NMR and ^{13}C NMR spectroscopy and mass spectrometry. Number of CH_2 spacers, and the length of perfluorinated alkyl group was varied to understand the effect of each parameter on solubility, fluorophilicity, and conductivity of the resulting cations. The imidazolium cation with perfluoroether substituent was generously provided by Professor Jaroslav Kvíčala, Department of Organic Chemistry, Institute of Chemical Technology, Prague, Czech Republic.

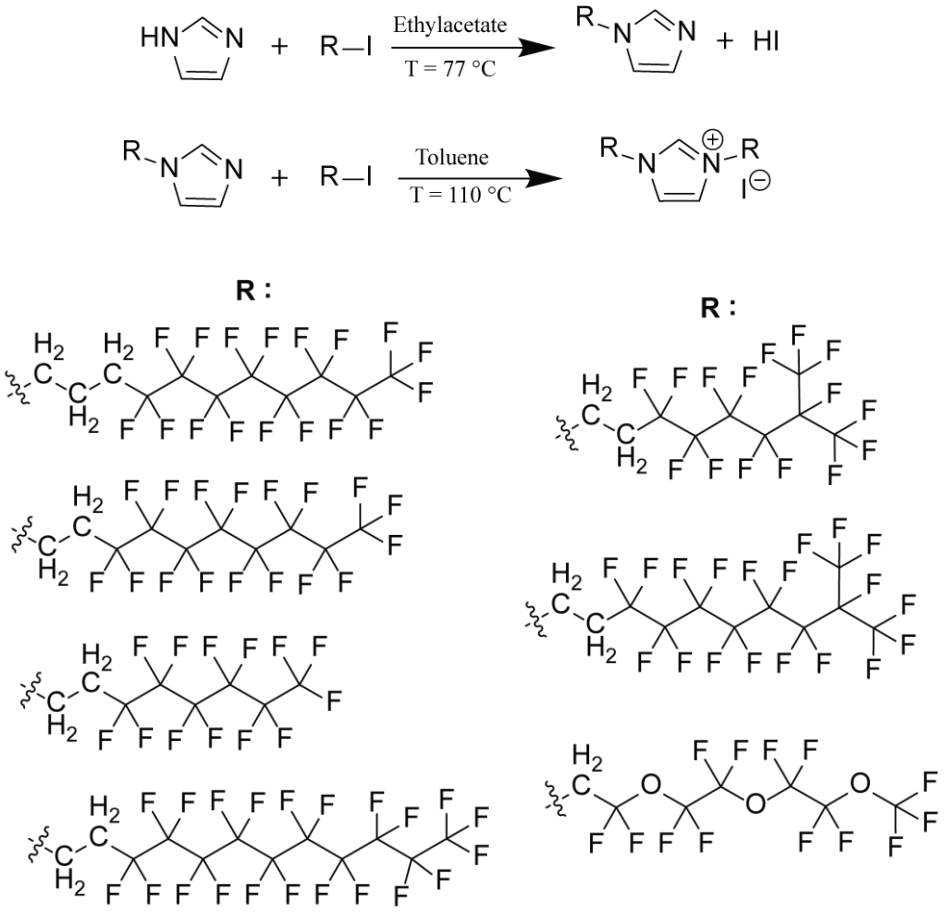

Figure 6. Synthesis of fluorophilic imidazolium iodides from perfluorinated alkyl iodides.

10.1.4 Fluorophilic Electrolytes Based on Dialkylimidazolium Cation and Tetraalkylborate Anion

The fluorophilic electrolyte, shown in Figure 7, was obtained from metathesis of previously synthesized [1,3-bis(4,4,5,5,6,6,7,7,8,8,9,9,10,10,11,11,11-heptadecafluoroundecyl)-1H-imidazol-3-ium] iodide and sodium [tetrakis[3,5-bis-(perfluorohexyl)phenyl]borate]. This electrolyte was confirmed to be soluble in most

fluorous solvents. It is soluble in perfluorohexanes up to 10 mM and in perfluoroperhydrophenanthrene up to 5 mM.

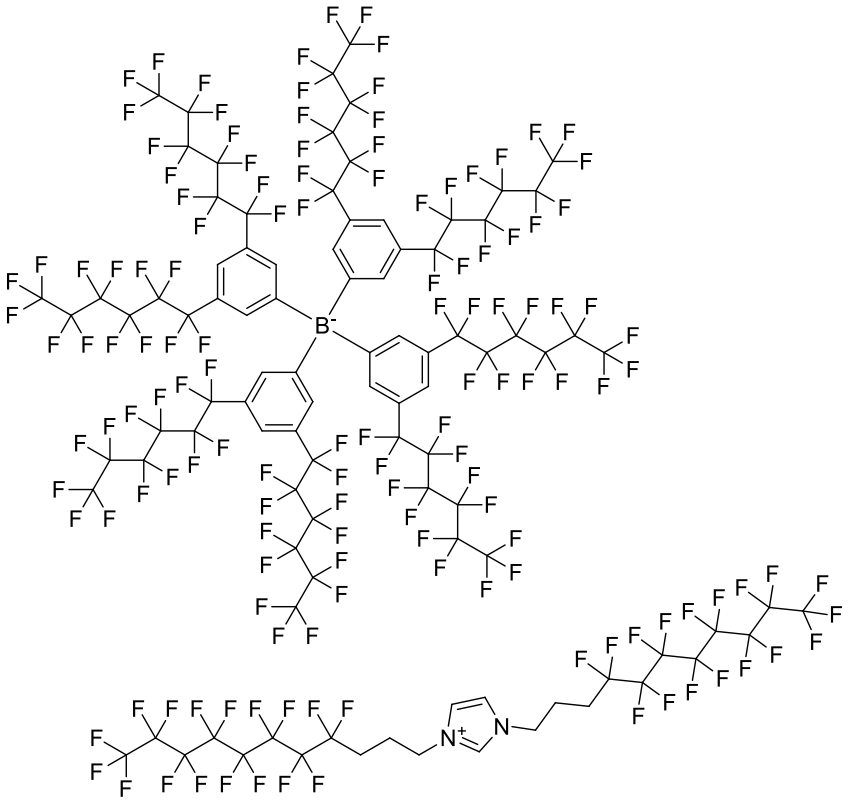

Figure 7. Structure of developed fluorophilic electrolyte.

The specific conductivity of the electrolyte was measured (5 mM in perfluoroperhydrophenanthrene) by impedance spectroscopy using a homemade conductivity cell (calibrated with a 500 µS/cm KCl conductivity standard obtained from Fluka). The specific conductivity was determined to be 38.47 ± 0.02 µS/cm. In summary, the developed fluorophilic electrolyte provided good solubilities in fluorous environments, resulting in lowering the resistance of fluorous phases by at least three orders of magnitude. In addition to potentiometry, this electrolyte can have applications in voltammetric techniques for fluorous media, e.g., ion transfer voltammetry. Future direction of this development focuses on how conductivity, solubility, and fluorophilicity

of dialkylimidazolium based electrolytes are affected by the structure of perfluorinated alkyl substituents. Also, studying fundamentals of ionic behaviors of fluorophilic electrolytes in the low polarity fluorous media could shed light on better design of this class of electrolytes.

10.2 Development of Proton Ionophores for Fluorous-Phase ISEs

Fluorophilic tertiary amines have been previously used as proton ionophores to develop fluorous-phase pH ISEs that are more adaptable to biological and environmental conditions.[87] Compared to conventional nonfluorous ISEs with hydrophobic amine ionophores, the authors showed enhancement in proton selectivity in the fluorous-phase ISEs. The authors investigated a variety of structures for fluorouphilic pH ionophore, including the number of CH_2 spacers and the length of perfluorinated alkyl substituents, see I, II, III, and V in Figure 8. It was shown that the basicity of nitrogen, and the performance of the ISE is strongly dependent on the length of the hydrocarbon spacers separating the perfluoroalkyl substituents from the amino groups.

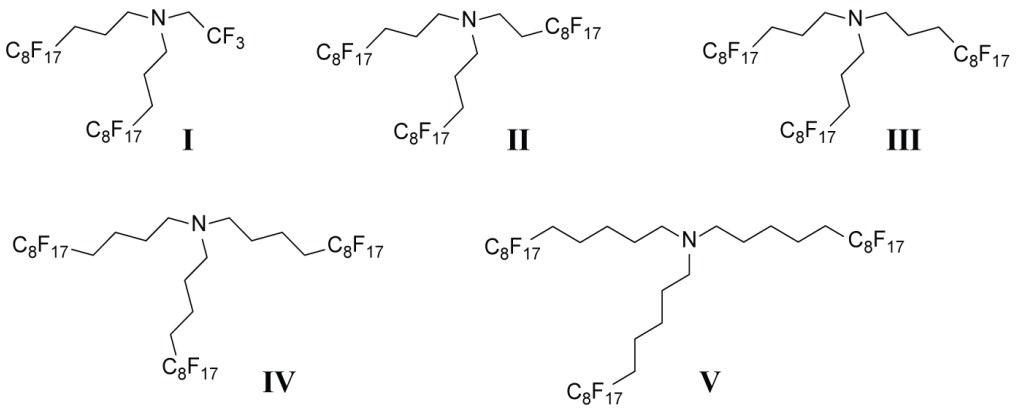

Figure 8. Structures of fluorophilic amines used as ionophores in fluorous-phase pH ISEs.

Due to their low basicity, ISEs with ionophores I and II responded in only a limited pH range of 0 to 3. ISE with ionophore III (three CH_2 spacers) responded over a wider pH

range of 2 to 8, however, the limiting upper range of pH 8 limited application of this ISE for real-life analyses. ISE with ionophore V (five CH_2 spacers) provided a much wider detection range on basic pH values, yet the detection range was limited on the acidic solutions (response range of pH 4 to 14). Moreover, high basicity of amine V and its strong binding to protons resulted in early Donan failure of the ISEs and super-Nerstian responses in the acidic range.[87] Utilizing four CH_2 spacers separating the perfluoroalkyl substituents from the amino groups (IV in Figure 8), rather than three in ionophore III, and five in ionophore V, could result in a more applicable response range in both acidic and basic regions. This ionophore was synthesized according to a previously published procedure, shown in Figure 4.[367] Fluorous-phase ISEs with pH ionophore IV were prepared and characterized based on the procedure published by Boswel and coworkers.[87] Indeed, initial experiments showed Nernstian responses for these ISEs from starting pH of 3 to 10 which provides a desirable detection range for many real-life analyses. The responses of two ISEs with ionophores of III and IV are compared to Figure 9. Future research will focus on quantifying selectivity of this ionophore over common interfering ions such as K^+, Na^+, and Ca^{2+}. The lower detection range in the acidic regions needs to be determined and Donan failure and resistance to biofouling of flurous-phase ISEs with pH ionophore IV will be investigated.

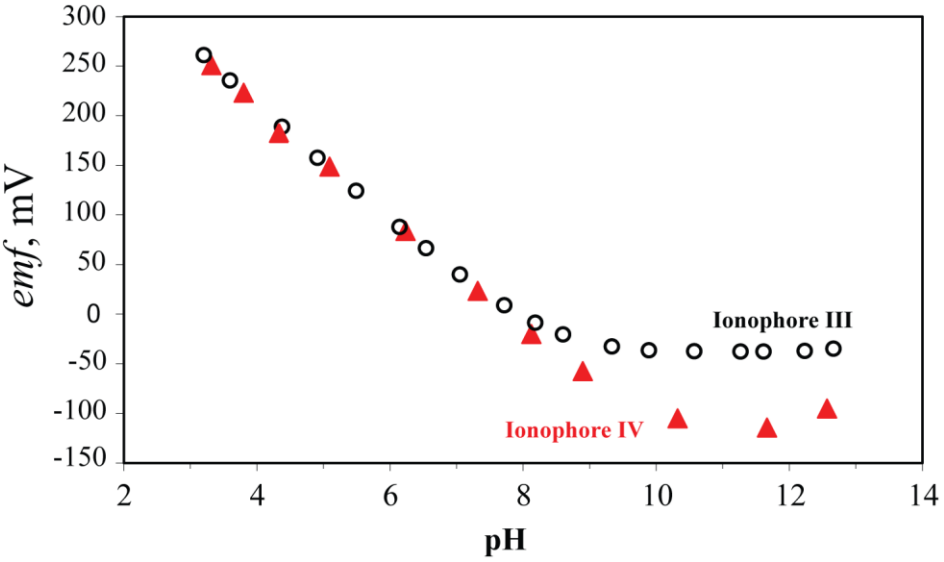

Figure 9. Potentiometric responses of fluorous-phase ISEs with ISEs with ionophores of III and IV.

11 CHAPTER ELEVEN

Conclusions and Research Outlook

11.1 Summary of Results

In this thesis research, two main categories of electrochemical devices that have application in sensing and energy storage (ion-selective electrodes and electrochemical double-layer capacitors) were studied. Chapters 1 provides the theoretical concepts and principles behind the techniques presented in Chapters 2 to 10. Electrochemical double-layer capacitors and strategies for improving their energy density are discussed in Chapters 2 to 4. Applications of fluorous sensing membranes in ISEs and the reliability of detection with fluorous-phase ISEs are laid out in Chapters 5, 6, and 7. Chapters 8 and 9 discuss proper usage of reference electrodes and possible errors that can be introduced in the measurement with reference electrodes. Strategies for eliminating and minimizing these errors are presented and methods for development of more robust reference electrodes are discussed. Chapter 10 covers current limitations of sensing with fluorous-phase ISEs, provided suggestions for overcoming the existing limitations, and mentioned the unpublished results and findings on this topic.

11.1.1 Highlights from Chapters 2, 3, and 4

With the increasing global demand for energy, improving the existing energy storage technologies is as critical as developing more efficient methods for energy production. Among electrical energy storage devices, batteries, electrochemical and hybrid battery/capacitor systems are the prevalent options. Even though batteries have low power, long charging times, limited cycling life times, and require maintenance, consumers adapted to the limitations of these devices due to lack of an alternative with comparable energy density. Recent advances in the design of nanostructured materials have resulted in improvements of the energy density of electrochemical capacitors, making them more compelling for energy storage applications. With this motivation, part of my graduate research investigated strategies for improving the energy density of electrochemical double-layer capacitors.[14,15]

Electrochemical capacitors store electrical charge in a double layer at the interface of electrolyte and electrode. The energy density of such a capacitor is determined by ½ CV^2, where V is the potential difference between the plates of a capacitor and C is the capacitance density.[90] The operational voltage of such devices is limited by the electrochemical window of the electrolyte, which is the potential range in which the electrolyte does not get reduced or oxidized as a result of the applied potential. The energy density of double-layer capacitors can be maximized by modifying the electrode material to increase the capacitance density, C, and by tuning the structure of the electrolyte to improve its electrochemical stability, and thus the accessible electrochemical window.

As the first step in developing electrolytes with wider electrochemical windows, different approaches for quantifying the electrochemical stability of electrolytes were explored and it was realized that the determination of the electrochemical window of the electrolytes has not been well defined in the past. Usually, a linear sweep current-voltage curve is measured, and the potentials at which specific current densities are reached are identified as the electrochemical limits, see Figure 1.[17,41] The choice of the cut-off current density, $J_{\text{cut-off}}$, is quite arbitrary and it strongly affects the determined electrochemical stability limit. Unfortunately, different standards have been applied in the literature, and as a result, electrochemical windows that differ by as much as 0.9 V are reported for the same electrolytes.[17,24] Therefore, the comparison of data from studies that used different $J_{\text{cut-off}}$ values is not readily possibly, making it difficult to gain a collective understanding of the effect of the electrolyte structure on its electrochemical stability. This thesis research showed that parameters such as electrolyte concentration, scan rate, and electrode surface area can bias the electrochemical limits by as much as 0.5 V.[41] To address this issue, a series of numerical simulations was performed to identify the parameters that affect the electrochemical degradation of electrolytes, and based on these findings, an improved method for the quantification of electrochemical stability limits was suggested.[41] The proposed method is based on linear fits of the current–voltage curve at potentials below

and above the onset of the cathodic or anodic decomposition, where the intercept of the two fits is defined as the electrochemical limit of the electrolyte (see Figure 1). This method minimizes the effect of electrolyte concentration, scan rate, and electrode surface area, and it eliminates discrepancies that result from the choice of an arbitrary value of $J_{\text{cut-off}}$, therefore, providing a more reliable method for the assessment of electrochemical stability limits.[41]

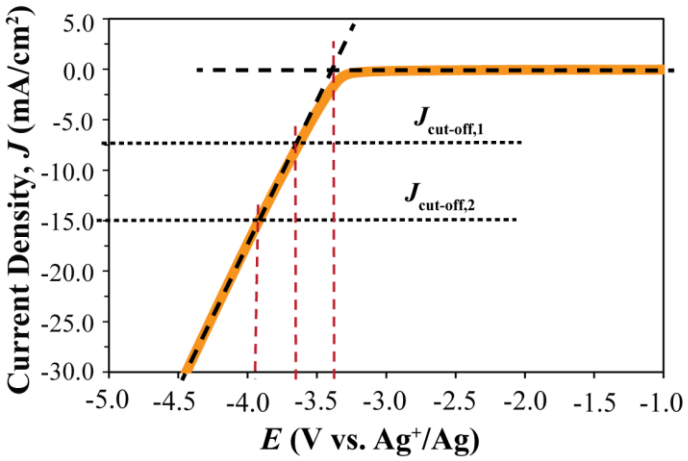

Figure 1. Determination of the electrochemical stability of electrolytes using the $J_{\text{cut-off}}$ and linear fit methods.

Using this more reliable assessment criterion, the effect of electrolyte structure on the electrochemical stability was studied, and electrochemical windows of a variety of electrolytes and ionic liquids were measured. Results indicate that the cation part that carries the positive charge has a significant effect on the stability towards reduction. Quaternary ammonium ions with alkyl substituents generally provide the highest cathodic stabilities, whereas cations with aromatic substituents are less stable towards reduction. To further improve the cathodic stability of quaternary ammonium cations and to investigate the effect of cation structure on the electrochemical stability, several tetraalkylammonium cations were designed and synthesized. It was shown that the chain

length, type of branching, size, and steric hindrance of the substituents have only a minimal effect on the electrochemical stability.[163]

Investigations of the electrochemical stability of ionic liquids show a higher stability of the bis(trifluoromethane)sulfonamide anion towards oxidation than for the tetrafluoroborate and triflate anions. Unlike suggested in several previous reports, it was shown that increasing the length of the alkyl substituents in dialkylimidazolium bis(trifluoromethane)sulfonamide ionic liquids does not improve electrochemical stability. It was shown that previous observations were artifacts of the $J_{\text{cut-off}}$ method used for the quantification of electrochemical stability. For fabrication of high energy density electrochemical capacitors, ionic liquids were used as electrolytes to maximize the ion concentration and increase the capacitance density. Mesoporous carbon with a high accessible surface area (three-dimensionally ordered mesoporous carbon) was used as electrode material to further improve the capacitance density, and develop high energy density double-layer capacitors. It was demonstrated that while ionic liquids based on a quaternary ammonium cation offer wider potential windows than imidazolium based ones, they yield much lower specific capacitance values in electrochemical capacitors. This research highlighted the importance of balancing both the electrochemical stability and the specific capacitance of ionic liquid-carbon systems for obtaining optimized energy densities. The findings of this research can provide insight into choosing the best ionic liquids for the desired application.

11.1.2 Highlights from Chapters 5, 6, and 7

Ion-selective electrodes, ISEs, are electrochemical sensors that are used to determine the concentration of a wide range of ions and are used for billions of measurements in clinical, environmental, and chemical process analyses every year.[42] A critical element in ISEs that enables detection of ions is the hydrophobic ion-selective membrane; see Figure 2. The components of the ion-selective membrane are specifically designed to selectively

bind to the ion of interest and develop a concentration-dependent phase boundary potential at the interface of the membrane and sample.[42] This measured potential is referred to as the electromotive force, emf, and is measured with respect to an additional electrode that provides a constant and sample independent potential, known as the reference electrode; see Figure 2. ISEs offer sensitive, selective, label-free, and non-destructive detection in complex media, and, therefore, are appealing tools for in situ analysis and measurements in complex biological media.[42] However, two factors limit the application of ISEs in biological analyses: (1) Interference from biological molecules: Due to the hydrophobicity of many biological molecules, such molecules can get extracted into the hydrophobic sensing membranes of ISEs or adsorb onto these sensing membrane, thereby decreasing the life-time of ISEs. This phenomenon is referred to as the biofouling of ISEs. (2) Large sample volumes required for ISE measurements with conventional macro-sized electrodes makes potentiometry with ISEs inapplicable to many biological samples, e.g., samples containing enzymes and antibodies. The thesis research presented in Chapters 5 to 10 described approaches to address these two limiting factors of ISEs and discusses the development of sensors that are more suitable for analyses in biological environments.

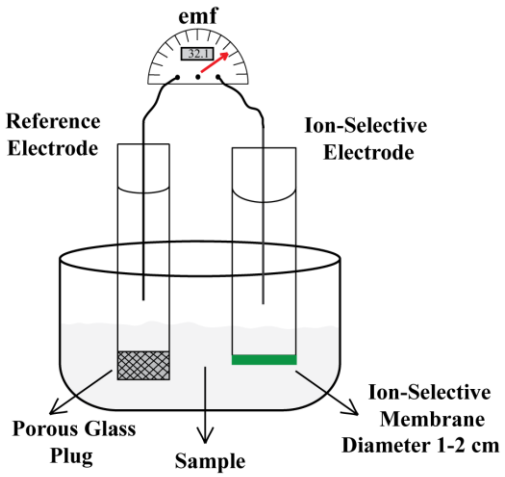

Figure 2. Conventional Experimental Setup an Ion-Selective Electrode.

A strategy for limiting biofouling of ISEs is incorporation of fluorous compounds into the ISE sensing membrane.[77] Fluorous compounds have a high content of fluorine atoms within their structures and, consequently, exhibit a much lower hydrophobicity compared to that of biological molecules;[78] therefore, ISEs with fluorous sensing membranes can be less susceptible to biofouling.[77] (Fluorous compounds are both hydrophobic and lipophobic; thus, they are immiscible with non-fluorinated organic substances such as hexane, toluene, alcohols, water, etc.) Recently, fluorous-phase receptor doped silver-selective ISEs were developed in our group and were shown to provide an exceptionally high selectivity and low limit of detection for silver.[51] In order to investigate the reliability of detection with these sensors in environmental and biological samples, the application of fluorous-phase receptor doped silver-selective ISEs in studying toxicity of silver nanoparticles was evaluated.

The widespread use of silver nanoparticles, AgNPs, in consumer products has raised concerns about their impact on the environment. AgNPs are known to be toxic to the bacteria. The toxicity is mainly imparted through ionization and release of Ag^+.[181] Therefore, understanding the dynamics of Ag^+ release from AgNPs is critical for a correct AgNP risk assessment and a better design of these nanomaterials. It was shown that silver-selective fluorous-phase ISEs can be used to monitor the extent and kinetics of Ag^+ release from AgNPs in the presence of the bacterium, *Shewanella oneidensis*, and in the cell growth media where the sensors are exposed to a variety of interfering biological molecules.[85] Fluorous-phase silver selective ISEs were also successfully used for Ag^+ detection in the presence of Natural Organic Matter, NOM, which is a product of the decomposition of living organisms and consists of large biological molecules.[289] NOM is present in water, soil, and sediments, and NOM can interact with Ag^+ released from AgNPs, resulting in silver ion speciation, decreased bioavailability, and altered toxicity. The extent of Ag^+ speciation and toxicity and AgNP ionization were fully quantified, providing critical information for the correct assessment of AgNP toxicity.[85,289,356]

Fast kinetics for Ag^+ binding to NOM and slow kinetics for the reduction of Ag^+ by certain types of NOM in environmentally relevant conditions were confirmed, providing the first report on the kinetics of Ag^+ binding to NOM with time resolution of less than a second. It was shown that pH affects the extent of Ag^+ binding to NOM, where higher pH results in stronger binding. Studies of Ag^+ speciation must ensure that buffer components are selected that avoid unwanted complexation with Ag^+. Buffer compounds such as HEPES and MOPS, which are commonly used in bacterial culture environments, should be excluded from Ag^+ speciation studies since they form stable complexes with Ag^+ and interfere with NOM binding to Ag^+. Lastly, the correlation between the ability of NOM to protect against Ag^+ toxicity with the extent of Ag^+ binding to NOM was discussed. This work demonstrated successful ion sensing with fluorous-phase ISEs under various environmentally and biologically relevant conditions.

11.1.3 Highlights from Chapters 8, 9, and 10

Even though ISE biofouling was addressed by using fluorous-phase ISEs, the large sample volumes required are still a drawback for the use of these sensors. This issue can be resolved by decreasing the size of both the ISE and the reference electrode. The tip diameter of ISEs (1-2 cm) can be decreased by more than one thousand fold by developing ion-selective microelectrodes, µ-ISEs (tip diameter 1-5 µm).[42] However, in µ-ISEs, the increased thickness and decreased surface area of the ion-selective membrane drastically increases the electrical resistance of the electrode, which will result in inaccurate measurements of the emf.

In conventional µ-ISEs, a highly lipophilic electrolyte salt is added to the µ-ISE membrane to decrease the membrane resistance. Unfortunately, the available electrolytes did not have sufficient solubility in fluorous phases to allow development of fluorous-phase µ-ISEs. Therefore, several structures for this electrolyte were designed (1,3-dialkylimidazolium or tetraalkylammonium cations paired with tetrakis[3,5-bis-

(alkyl)phenyl]borates, where the alkyl groups are partially fluorinated hydrocarbon chains chains of the type $(CH_2)_nC_mF_{2m+1}$ with $0 \leq n \leq 4$, and $6 \leq m \leq 10$) and the synthesis was carried out. Results show that the designed electrolytes have good solubilities in fluorous phases and can decrease the membrane resistance by more than six orders of magnitude.

In addition to miniaturizing the fluorous-phase ISEs, the dimensions of the reference electrode should also be modified to allow sensing with fluorous-phase ISEs in small volumes. A common strategy for decreasing the size of reference electrodes is separating the reference and sample solutions by a nanoporous glass plug with small dimensions (1-2 mm), see Figure 2. The nanoporous glass plugs minimize intermixing and contamination of sample and reference solutions, while still providing enough ion conduction to allow a reliable potential measurement. Therefore, miniaturizing the size of the reference electrodes was attempted using this approach. However, the characterization of the developed reference electrodes showed sample-independent potentials in solutions with low ionic strength (as a result, errors up to 900% could be introduced in the determination of analyte concentration).[10] Surprisingly, even though nanoporous glass plugs have been used in commercially available reference electrodes for more than two decades, no studies had systematically assessed their limitations.[10] The research findings presented in Chapter 8 showed that due to the negative surface charge of glass at intermediate and high pH, electrostatic forces and ion screening contribute to the deficiency of these reference electrodes.[10] Realizing the impact of porous frits on the performance of reference electrodes, alternative frit materials to Vycor glass and the advantages and disadvantages of each material were developed, as discussed in Chaper 9. It was revealed that porous polymeric materials are appealing candidates for frit materials in reference electrodes because the pore size and surface chemistry can be well controlled and designed.

11.2 Future Work

The longterm goal of this research on ion-selective electrodes was the development of platforms that allow potentiometric detection in complex media with small volumes (μL). Fluorous-phase ISEs were shown to be excellent tools for measurements in real-life environments; yet, the large volumes required for the detection with these sensors still needs to be addressed. The current progress in the development of fluorophilic electrolytes, which are used for lowering membrane resistances and allowing the development of microelectrodes, lays the foundation to a better understanding of ionic aggregation and conductivities in fluorous phases. In my opinion, future research should focus on completing the study of the conductivity of fluorophilic electrolyte solutions and the fluorophilicity of these electrolytes. Effects of the center carrying the positive charge in cations and the length of perfluoroalkyl ponytail substituents on the characteristics of fluorophilic electrolytes should be quantified. The obtained knowledge can guide the design of new generations of fluorophilic electrolytes if the existing options are not suitable for application in ISEs. This will allow the fabrication of fluorous-phase μ-ISEs using the new fluorophilic electrolytes.

11.2.1 Conductivity of Fluorophilic Electrolytes

Conductivities of electrolytes are usually measured by means of commercially available conductivity probes. However, the currently available conductivity probes have limited application for the analysis of conductivities of fluorophilic electrolytes; mainly, because they require large sample volumes and are designed for solutions with high and moderate specific conductivities. Development of a custom-made conductivity cell, made of two temperature-controlled stainless steel plates and a Teflon spacer to hold the sample is recommended, see Figure 3. The thickness and diameter of the cavity in the Teflon spacer can be adjusted to allow measurement of conductivity of electrolyte solutions with low specific conductivities and in volumes of less than 100 μL.

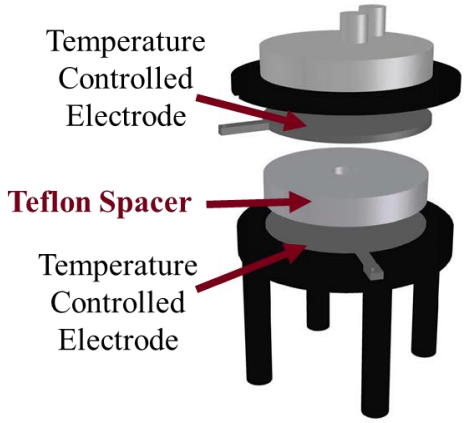

Figure 3. Diagram of conductivity cell with low sample volumes.

The molar conductivity of strong electrolytes increases by decreasing the electrolyte concentration and is generally described by the Debye-Huckel-Onsager equation shown below:

$$\Lambda = \Lambda^{\circ} - \beta\, C^{\frac{1}{2}} \qquad (1)$$

Where Λ is the molar conductivity of the electrolyte, Λ° is the molar conductivity of the electrolyte at infinite dilution, C is the electrolyte concentration, and β is a constant value which is dependent on ion charge, viscosity of the solvent, temperature, and the dielectric permeability of solvent.[1] Because Equation 1 does not consider formation of ion pairs, it fails to accurately predict the effect of electrolyte concentration on conductivity of electrolyte in low polarity solvents, e.g., fluorous solvents. A modified model that considers both ion pair and triple ion formation is recommended for conductivity measurements in fluorous media, see Equation 2:

$$\Lambda = \frac{\Lambda_s^{\infty}}{K_{ip}^{\frac{1}{2}}\, C^{\frac{1}{2}}} + \frac{2\,\Lambda_s^{\infty} K_t C^{\frac{1}{2}}}{3\,K_{ip}^{\frac{1}{2}}} \qquad (2)$$

Where Λ is the molar conductivity of the electrolyte, Λ°_s is the limiting molar conductivity of the undissociated electrolyte, C is the electrolyte concentration, and K_{ip}

and K_t are the ion pair and triple ion formation constants.[87,371] This model allows a better understanding of the effect of structure of fluorophilic electrolytes on their conductivity and the degree of ion pair formation in fluorous solvents.

11.2.2 Development of Fluorous-Phase μ-ISEs

After overcoming the challenges associated to high resistivity of fluorous sensing phases, fluorous-phase μ-ISEs can be developed. Glass μ-pipettes are commonly used to develop μ-ISEs with fine tip diameters.[42,214,372] A critical step in development of μ-ISEs is modification of the glass surface to improve contact of ISE sensing membrane and the glass wall. The hydrophilic surface of glass is modified by introduction of hydrophobic alkyl chains to the silicate groups at the glass surface. The common synthetic approaches for creating glasses with hydrophobic surfaces are shown in Figure 4. Similar strategy can be applied to develop glass surfaces that are both hydrophobic and lipophobic; the R group in Figure 4 can be replaced with highly perfluorinated alkyl groups. Indeed, successful modification of glass surface by perfluorinated silane coupling agents was reported, confirmed by measurements of contact angles of water and oleic acid on the modified glass plate surface. The authors reported an increase in the contact angle by increasing the length of the perfluorinated polytails of the silane coupling agent, indicating that length of the perfluorinated alkl ponytails must be tunned to achieve good coverage of glass surface.[373]

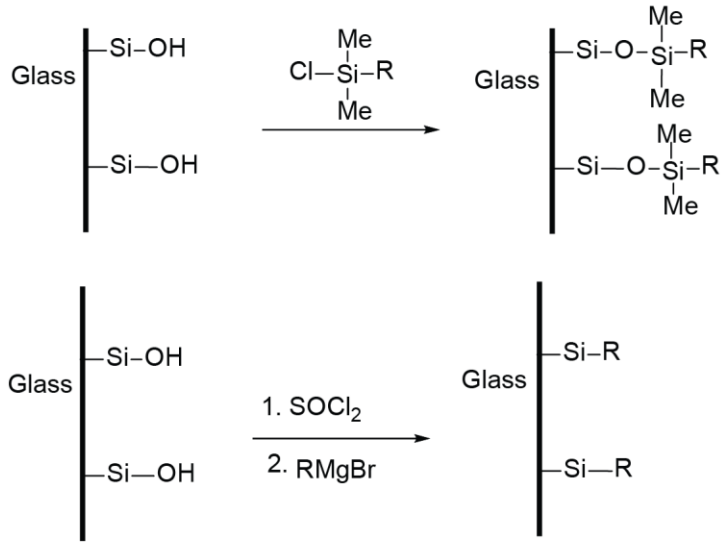

Figure 4. Modification of glass surface for development of μ-ISEs. R represents a hydrophobic alkyl group.

References

(1) Bard, A. J.; Faulkner, L. R. *Electrochemical Methods Fundamentals and Applications*, 2nd ed.; John Wiley and sons: New York, 2009.
(2) Dohner, R. E.; Wegmann, D.; Morf, W. E.; Simon, W. *Anal. Chem.* **1986**, *58*, 2585-2589.
(3) G. Inzelt; Lewenstam, A.; Scholz, F. *Handbook of Reference Electrodes*; Springer-Verlag Berlin Heidelberg: New York, 2013.
(4) Zhang, T.; Lai, C.-Z.; Fierke, M. A.; Stein, A.; Bühlmann, P. *Anal. Chem.* **2012**, *84*, 7771-7778.
(5) Brezinski, D. P. *Analyst* **1983**, *108*, 425-442.
(6) Bard, A. J.; Inzelt, G.; Scholz, F. *Electrochemical Dictionary*; Springer: Berlin, 2008.
(7) Brezinski, D. P. *Anal. Chim. Acta* **1982**, *134*, 247-262.
(8) Zou, X. U.; Buehlmann, P. *Anal. Chem.* **2013**, *85*, 3817-3821.
(9) Payne, R. B.; Buckley, B. M.; Rawson, K. M. *Ann. Clin. Biochem.* **1991**, *28*, 68-72.
(10) Mousavi, M. P. S.; Buhlmann, P. *Anal. Chem.* **2013**, *85*, 8895-8901.
(11) VYCOR® Brand Porous Glass 7930, Corning Inc. http://www.corning.com/docs/specialtymaterials/pisheets/Vycor%207930.pdf. , Accessed May 5th 2013.
(12) Carson, W. N.; Michelron, C. E.; Koyama, K.; Atomic, H. *Anal. Chem.* **1955**, *27*, 472-476.
(13) Israelachvili, J. *Intermolecular and Surface Forces*, 1 st ed.; Academic Press Inc.: London, 1985.
(14) Barbieri, O.; Hahn, M.; Herzog, A.; Kotz, R. *Carbon* **2005**, *43*, 1303-1310.
(15) Kotz, R.; Carlen, M. *Electrochim. Acta* **2000**, *45*, 2483-2498.
(16) Sharma, P.; Bhatti, T. S. *Energy Convers. Manage.* **2010**, *51*, 2901-2912.
(17) Olson, E. J.; Buhlmann, P. *J. Electrochem. Soc.* **2013**, *160*, A320-A323.
(18) Wu, H.; Wang, X.; Jiang, L.; Wu, C.; Zhao, Q.; Liu, X.; Hu, B. a.; Yi, L. *J. Power Sources* **2013**, *226*, 202-209.
(19) Wang, Y.; Zheng, C.; Qi, L.; Yoshio, M.; Yoshizuka, K.; Wang, H. *J. Power Sources* **2011**, *196*, 10507-10510.
(20) Lewandowski, A.; Swiderska, A. *Solid State Ionics* **2003**, *161*, 243-249.
(21) Galiński, M.; Lewandowski, A.; Stępniak, I. *Electrochim. Acta* **2006**, *51*, 5567-5580.
(22) Arbizzani, C.; Biso, M.; Cericola, D.; Lazzari, M.; Soavi, F.; Mastragostino, M. *J. Power Sources* **2008**, *185*, 1575-1579.
(23) Wei, D.; Ivaska, A. *Anal. Chim. Acta* **2008**, *607*, 126-135.

(24) De Vos, N.; Maton, C.; Stevens, C. V. *ChemElectroChem* **2014**, *1*, 1258-1270.
(25) Xu, K.; Ding, M. S.; Jow, T. R. *J. Electrochem. Soc.* **2001**, *148*, A267.
(26) Ue, M.; Ida, K.; Mori, S. *J. Electrochem. Soc.* **1994**, *141*, 2989-2996.
(27) Le, M. L. P.; Alloin, F.; Strobel, P.; Lepretre, J. C.; Cointeaux, L.; del Valle, C. P. *Ionics* **2012**, *18*, 817-827.
(28) Appetecchi, G. B.; Montanino, M.; Zane, D.; Carewska, M.; Alessandrini, F.; Passerini, S. *Electrochim. Acta* **2009**, *54*, 1325-1332.
(29) Fang, S.; Jin, Y.; Yang, L.; Hirano, S.-i.; Tachibana, K.; Katayama, S. *Electrochim. Acta* **2011**, *56*, 4663-4671.
(30) Reiter, J.; Jeremias, S.; Paillard, E.; Winter, M.; Passerini, S. *Phys. Chem. Chem. Phys.* **2013**, *15*, 2565-2571.
(31) Jin, Y.; Fang, S.; Chai, M.; Yang, L.; Tachibana, K.; Hirano, S.-i. *J. Power Sources* **2013**, *226*, 210-218.
(32) Moganty, S. S.; Baltus, R. E.; Roy, D. *Chem. Phys. Lett.* **2009**, *483*, 90-94.
(33) Morita, M.; Goto, M.; Matsuda, Y. *J. Appl. Electrochem.* **1992**, *22*, 901-908.
(34) Lang, C. M.; Kim, K.; Guerra, L.; Kohl, P. A. *J. Phys. Chem. B* **2005**, *109*, 19454-19462.
(35) Zhou, Z. B.; Matsumoto, H.; Tatsumi, K. *Chemistry* **2005**, *11*, 752-766.
(36) Fu, S.; Gong, S.; Liu, C.; Zheng, L.; Feng, W.; Nie, J.; Zhou, Z. *Electrochim. Acta* **2013**, *94*, 229-237.
(37) Liu, C.; Xu, F.; Feng, S.; Zheng, L.; Zhang, H.; Feng, W.; Huang, X.; Armand, M.; Nie, J.; Zhou, Z. *Electrochim. Acta* **2013**, *99*, 262-272.
(38) Zhou, Z. B.; Matsumoto, H.; Tatsumi, K. *Chemistry* **2006**, *12*, 2196-2212.
(39) O'Mahony, A. M.; Silvester, D. S.; Aldous, L.; Hardacre, C.; Compton, R. G. *J. Chem. Eng. Data* **2008**, *53*, 2884-2891.
(40) Lang, C. M.; Kohl, P. A. *J. Electrochem. Soc.* **2007**, *154*, F106.
(41) Mousavi, M. P. S.; Dittmer, A. J.; Wilson, B.; Hu, J.; Stein, A.; Buhlmann, P. *J. Electrochem. Soc.* **2015**, *162*, A2250-A2258.
(42) Buhlmann, P.; Chen, L. D. In *Supramolecular Chemistry: From Molecules to Nanomaterials*, Steed, J. W.; Gale, P. A., Eds.; John Wiley & Sons Ltd: Chichester, UK, 2012.
(43) Buhlmann, P.; Pretsch, E.; Bakker, E. *Chem. Rev.* **1998**, *98*, 1593-1687.
(44) Gunaratna, P. C.; Koch, W. F.; Paule, R. C.; Cormier, A. D.; Dorazio, P.; Greenberg, N.; Oconnell, K. M.; Malenfant, A.; Okorodudu, A. O.; Miller, R.; Kus, D. M.; Bowers, G. N. *Clin. Chem.* **1992**, *38*, 1459-1465.
(45) Morf, W. E. *Studies in Analytical Chemistry, Vol. 2: The Principles of Ion-Selective Electrodes and of Membrane Transport*; Elsevier, 1981, p 420 pp.

(46) Moore, C.; Pressman, B. C. *Biochem. Biophys. Res. Commun.* **1964**, *15*, 562-567.
(47) Frant, M. S. *J. Chem. Educ.* **1997**, *74*, 159.
(48) Štefanac, Z.; Simon, W. *Microchem. J.* **1967**, *12*, 125-132.
(49) Hu, J.; Ho, K. T.; Zou, X. U.; Smyrl, W. H.; Stein, A.; Bühlmann, P. *Anal. Chem.* **2015**, *87*, 2981-2987.
(50) Lan, W.-J.; Zou, X. U.; Hamedi, M. M.; Hu, J.; Parolo, C.; Maxwell, E. J.; Bühlmann, P.; Whitesides, G. M. *Anal. Chem.* **2014**, *86*, 9548-9553.
(51) Lai, C. Z.; Fierke, M. A.; da Costa, R. C.; Gladysz, J. A.; Stein, A.; Buhlmann, P. *Anal. Chem.* **2010**, *82*, 7634-7640.
(52) Radomska, A.; Bodenszac, E.; Głb, S.; Koncki, R. *Talanta* **2004**, *64*, 603-608.
(53) Bühlmann, P.; Hayakawa, M.; Ohshiro, T.; Amemiya, S.; Umezawa, Y. *Anal. Chem.* **2001**, *73*, 3199-3205.
(54) Buhlmann, P.; Amemiya, S.; Yajima, S.; Umezawa, Y. *Anal. Chem.* **1998**, *70*, 4291-4303.
(55) Qin, Y.; Peper, S.; Bakker, E. *Electroanal* **2002**, *14*, 1375-1381.
(56) Kazarjan, N. A.; Pungor, E. *Anal. Chim. Acta* **1970**, *51*, 213-220.
(57) Lindfors, T.; Szücs, J.; Sundfors, F.; Gyurcsányi, R. E. *Anal. Chem.* **2010**, *82*, 9425-9432.
(58) Malinowska, E.; Niedziółka, J.; Meyerhoff, M. E. *Anal. Chim. Acta* **2001**, *432*, 67-78.
(59) Bakker, E.; Bühlmann, P.; Pretsch, E. *Chemical Reviews* **1997**, *97*, 3083-3132.
(60) Bakker, E.; Pretsch, E.; Buhlmann, P. *Anal. Chem.* **2000**, *72*, 1127-1133.
(61) Ammann, D.; Pretsch, E.; Simon, W.; Lindner, E.; Bezegh, A.; Pungor, E. *Anal. Chim. Acta* **1985**, *171*, 119-129.
(62) Ammann, D. *Ion-selective Microelectrodes Principles Design and Application*, 1986, p XV+346P-XV+346P.
(63) Nann, A.; Pretsch, E. *J. Chromatogr. A* **1994**, *676*, 437-442.
(64) Oehme, M.; Simon, W. *Anal. Chim. Acta* **1976**, *86*, 21-25.
(65) Ammann, D.; Lanter, F.; Steiner, R. A.; Schulthess, P.; Shijo, Y.; Simon, W. *Anal. Chem.* **1981**, *53*, 2267-2269.
(66) Messerli, M. A.; Kurtz, I.; Smith, P. J. S. *Anal Bioanal Chem* **2008**, *390*, 1355-1359.
(67) Ammann, D.; Chao, P.; Simon, W. *Neuroscience Letters* **1987**, *74*, 221-226.
(68) Tohda, K.; Umezawa, Y.; Yoshiyagawa, S.; Hashimoto, S.; Kawasaki, M. *Anal. Chem.* **1995**, *67*, 570-577.
(69) Frost, M. C.; Meyerhoff, M. E. *Curr. Opin. Chem. Biol.* **2002**, *6*, 633-641.
(70) Ward, W. K.; Casey, H. M.; Quinn, M. J.; Federiuk, I. F.; Wood, M. D. *Diabetes Technology & Therapeutics* **2003**, *5*, 943-952.

(71) Oesch, U.; Simon, W. *Anal. Chem.* **1980**, *52*, 692-700.
(72) Dinten, O.; Spichiger, U. E.; Chaniotakis, N.; Gehrig, P.; Rusterholz, B.; Morf, W. E.; Simon, W. *Anal. Chem.* **1991**, *63*, 596-603.
(73) Bühlmann, P.; Umezawa, Y.; Rondinini, S.; Vertova, A.; Pigliucci, A.; Bertesago, L. *Anal. Chem.* **2000**, *72*, 1843-1852.
(74) Lee, Y.; Oh, B. K.; Meyerhoff, M. E. *Anal. Chem.* **2004**, *76*, 536-544.
(75) Reynolds, M. M.; Frost, M. C.; Meyerhoff, M. E. *Free Radical Biol. Med.* **2004**, *37*, 926-936.
(76) Upreti, P.; Metzger, L. E.; Bühlmann, P. *Talanta* **2004**, *63*, 139-148.
(77) Boswell, P. G.; Buhlmann, P. *J. Am. Chem. Soc.* **2005**, *127*, 8958-8959.
(78) Brady, J. E.; Carr, P. W. *Anal. Chem.* **1982**, *54*, 1751-1757.
(79) Grec, J. J.; Riess, J. G.; Devallez, B. *Nouveau Journal De Chimie* **1985**, *2*, 109-117.
(80) Boswell, P. G.; Lugert, E. C.; Rabai, J.; Amin, E. A.; Buhlmann, P. *J. Am. Chem. Soc.* **2005**, *127*, 16976-16984.
(81) Lai, C. Z.; Reardon, M. E.; Boswell, P. G.; Buhlmann, P. *J. Fluorine Chem.* **2010**, *131*, 42-46.
(82) Boswell, P. G.; Anfang, A. C.; Buhlmann, P. *J. Fluorine Chem.* **2008**, *129*, 961-967.
(83) Olson, E. J.; Boswell, P. G.; Givot, B. L.; Yao, L. J.; Buhlmann, P. *J. Electroanal. Chem.* **2010**, *639*, 154-160.
(84) Chen, L. D.; Lai, C. Z.; Granda, L. P.; Fierke, M. A.; Mandal, D.; Stein, A.; Gladysz, J. A.; Buhlmann, P. *Anal. Chem.* **2013**, *85*, 7471-7477.
(85) Maurer-Jones, M. A.; Mousavi, M. P. S.; Chen, L. D.; Buhlmann, P.; Haynes, C. L. *Chem. Sci.* **2013**, *4*, 2564-2572.
(86) Chen, L. D.; Mandal, D.; Pozzi, G.; Gladysz, J. A.; Buhlmann, P. *J. Am. Chem. Soc.* **2011**, *133*, 20869-20877.
(87) Boswell, P. G.; Szíjjártó, C.; Jurisch, M.; Gladysz, J. A.; Rábai, J.; Bühlmann, P. *Anal. Chem.* **2008**, *80*, 2084-2090.
(88) Ue, M.; Takeda, M.; Takehara, M.; Mori, S. *J. Electrochem. Soc.* **1997**, *144*, 2684-2688.
(89) Xu, K.; Ding, M. S.; Jow, T. R. *Electrochim. Acta* **2001**, *46*, 1823-1827.
(90) Lewandowski, A.; Galinski, M. *J. Phys. Chem. Solids* **2004**, *65*, 281-286.
(91) Vu, A.; Li, X. Y.; Phillips, J.; Han, A. J.; Smyrl, W. H.; Buhlmann, P.; Stein, A. *Chem. Mater.* **2013**, *25*, 4137-4148.
(92) Xu, K.; Ding, S. P.; Jow, T. R. *J. Electrochem. Soc.* **1999**, *146*, 4172-4178.
(93) Li, Z. J.; Jaroniec, M. *J. Am. Chem. Soc.* **2001**, *123*, 9208-9209.
(94) Hu, J. B.; Zou, X. U.; Stein, A.; Buhlmann, P. *Anal. Chem.* **2014**, *86*, 7111-7118.

(95) Yoshimura, M.; Honda, K.; Kondo, T.; Uchikado, R.; Einaga, Y.; Rao, T. N.; Tryk, D. A.; Fujishima, A. *Diamond Relat. Mater.* **2002**, *11*, 67-74.
(96) Klug, C. L.; Bridges, N. J.; Visser, A. E.; Crump, S. L.; Villa-Aleman, E. *New J. Chem.* **2014**, *38*, 3879-3884.
(97) Pan, Y. F.; Boyd, L. E.; Kruplak, J. F.; Cleland, W. E.; Wilkes, J. S.; Hussey, C. L. *J. Electrochem. Soc.* **2011**, *158*, F1-F9.
(98) Sato, T.; Masuda, G.; Takagi, K. *Electrochim. Acta* **2004**, *49*, 3603-3611.
(99) Ue, M. *Electrochemistry* **2007**, *75*, 565-572.
(100) Belding, S. R.; Compton, R. G. *J. Electroanal. Chem.* **2012**, *683*, 1-13.
(101) Chen, P. Y.; Hussey, C. L. *Electrochim. Acta* **2004**, *49*, 5125-5138.
(102) Largeot, C.; Portet, C.; Chmiola, J.; Taberna, P. L.; Gogotsi, Y.; Simon, P. *J. Am. Chem. Soc.* **2008**, *130*.
(103) Chen, L. F.; Zhang, X. D.; Liang, H. W.; Kong, M. G.; Guan, Q. F.; Chen, P.; Wu, Z. Y.; Yu, S. H. *Acs Nano* **2012**, *6*, 7092-7102.
(104) Weingarth, D.; Noh, H.; Foelske-Schmitz, A.; Wokaun, A.; Kotz, R. *Electrochim. Acta* **2013**, *103*, 119-124.
(105) Moosbauer, D.; Jordan, S.; Wudy, F.; Zhang, S. S.; Schmidt, M.; Gores, H. J. *Acta Chim Slov* **2009**, *56*, 218-224.
(106) Jin, Y.; Fang, S.; Zhang, J.; Zhang, Z.; Yu, K.; Song, J.; Yang, L.; Hirano, S.-i. *Industrial & Engineering Chemistry Research* **2014**, *53*, 2860-2871.
(107) Finkelstein, M.; Petersen, R. C.; S.D. Ross. *J. Am. Chem. Soc.* **1959**, *81*, 2361–2364
(108) Mayell, J. S.; Bard, A. J. *J. Am. Chem. Soc.* **1963**, *85*.
(109) Kroon, M. C.; Buijs, W.; Peters, C. J.; Witkamp, G. J. *Green Chemistry* **2006**, *8*, 241-245.
(110) Kim, K.; Lang, C.; Moulton, R.; Kohl, P. A. *J. Electrochem. Soc.* **2004**, *151*, A1168-A1172.
(111) Fletcher, S.; Black, V. J.; Kirkpatrick, I.; Varley, T. S. *J. Solid State Electrochem.* **2013**, *17*, 327-337.
(112) Runge, E.; Gross, E. K. U. *Phys. Rev. Lett.* **1984**, *52*, 997-1000.
(113) Bauernschmitt, R.; Ahlrichs, R. *Chem. Phys. Lett.* **1996**, *256*, 454-464.
(114) Casida, M. E. *Time-Dependent Density Functional Theory for Molecules*; World Scientific: Singapore, 1995; Vol. 1.
(115) Mousavi, M. P. S.; Buhlmann, P. *Meeting Abstracts* **2014**, *MA2014-01*, 1099.
(116) Sears, P. G.; Caruso, J. A.; Popov, A. I. *J. Phys. Chem.* **1967**, *71*, 905-909.
(117) Daggett, H. M.; Bair, E. J.; Kraus, C. A. *J. Am. Chem. Soc.* **1951**, *73*, 799-803.

(118) Goga, S. T.; Lebed, A. V.; McHedlov-Petrossyan, N. O. *Journal of Chemical & Engineering Data* **2010**, *55*, 1887-1892.
(119) Zhang, G.; Musgrave, C. B. *J. Phys. Chem. A* **2007**, *111*, 1554-1561.
(120) Devlin, F. J.; Finley, J. W.; Stephens, P. J.; Frisch, M. J. *J. Phys. Chem.* **1995**, *99*, 16883-16902.
(121) Becke, A. D. *J. Chem. Phys.* **1993**, *98*, 5648-5652.
(122) Becke, A. D. *Phys Rev A* **1988**, *38*, 3098-3100.
(123) Lee, C. T.; Yang, W. T.; Parr, R. G. *Phys Rev B* **1988**, *37*, 785-789.
(124) Cances, E.; Mennucci, B.; Tomasi, J. *J. Chem. Phys.* **1997**, *107*, 3032-3041.
(125) Mennucci, B.; Cances, E.; Tomasi, J. *J. Phys. Chem. B* **1997**, *101*, 10506-10517.
(126) Tomasi, J.; Mennucci, B.; Cances, E. *J Mol Struc-Theochem* **1999**, *464*, 211-226.
(127) Miertuš, S.; Scrocco, E.; Tomasi, J. *Chem. Phys.* **1981**, *55*, 117-129.
(128) Miertus, S.; Tomasi, J. *Chem. Phys.* **1982**, *65*, 239-245.
(129) Hohenberg, P.; Kohn, W. *Physical Review* **1964**, *136*, B864-B871.
(130) Kohn, W.; Sham, L. J. *Physical Review* **1965**, *140*, A1133-A1138.
(131) Frisch, M. J. T., G. W.; Schlegel, H. B.; Scuseria, G. E.; Robb, M. A.; Cheeseman, J. R.; Montgomery, Jr., J. A.; Vreven, T.; Kudin, K. N.; Burant, J. C.; Millam, J. M.; Iyengar, S. S.; Tomasi, J.; Barone, V.; Mennucci, B.; Cossi, M.; Scalmani, G.; Rega, N.; Petersson, G. A.; Nakatsuji, H.; Hada, M.; Ehara, M.; Toyota, K.; Fukuda, R.; Hasegawa, J.; Ishida, M.; Nakajima, T.; Honda, Y.; Kitao, O.; Nakai, H.; Klene, M.; Li, X.; Knox, J. E.; Hratchian, H. P.; Cross, J. B.; Bakken, V.; Adamo, C.; Jaramillo, J.; Gomperts, R.; Stratmann, R. E.; Yazyev, O.; Austin, A. J.; Cammi, R.; Pomelli, C.; Ochterski, J. W.; Ayala, P. Y.; Morokuma, K.; Voth, G. A.; Salvador, P.; Dannenberg, J. J.; Zakrzewski, V. G.; Dapprich, S.; Daniels, A. D.; Strain, M. C.; Farkas, O.; Malick, D. K.; Rabuck, A. D.; Raghavachari, K.; Foresman, J. B.; Ortiz, J. V.; Cui, Q.; Baboul, A. G.; Clifford, S.; Cioslowski, J.; Stefanov, B. B.; Liu, G.; Liashenko, A.; Piskorz, P.; Komaromi, I.; Martin, R. L.; Fox, D. J.; Keith, T.; Al-Laham, M. A.; Peng, C. Y.; Nanayakkara, A.; Challacombe, M.; Gill, P. M. W.; Johnson, B.; Chen, W.; Wong, M. W.; Gonzalez, C.; Pople, J. A.; Gaussian 03, Revision C.02, Gaussian Inc.: Wallingford CT, 2004.
(132) Lu, Y. C.; Gasteiger, H. A.; Crumlin, E.; McGuire, R.; Shao-Horn, Y. *J. Electrochem. Soc.* **2010**, *157*, A1016-A1025.
(133) Ong, S. P.; Andreussi, O.; Wu, Y. B.; Marzari, N.; Ceder, G. *Chem. Mater.* **2011**, *23*, 2979-2986.
(134) Tian, Y. H.; Goff, G. S.; Runde, W. H.; Batista, E. R. *J. Phys. Chem. B* **2012**, *116*, 11943-11952.
(135) Mendez-Hernandez, D. D.; Tarakeshwar, P.; Gust, D.; Moore, T. A.; Moore, A. L.; Mujica, V. *J. Mol. Model.* **2013**, *19*, 2845-2848.

(136) Maeshima, H.; Moriwake, H.; Kuwabara, A.; Fisher, C. A. J. *J. Electrochem. Soc.* **2010**, *157*, A696-A701.
(137) Maeshima, H.; Moriwake, H.; Kuwabara, A.; Fisher, C. A. J.; Tanaka, I. *J. Electrochem. Soc.* **2014**, *161*, G7-G14.
(138) Marenich, A. V.; Cramer, C. J.; Truhlar, D. G. *J. Chem. Theory Comput.* **2010**, *6*, 2829-2844.
(139) West, W. C.; Whitacre, J. F.; Leifer, N.; Greenbaum, S.; Smart, M.; Bugga, R.; Blanco, M.; Narayanan, S. R. *J. Electrochem. Soc.* **2007**, *154*, A929-A936.
(140) Roy, R. N.; Vernon, W.; Gibbons, J. J.; Bothwell, A. L. M. *J. Chem. Soc. A: Inorganic, Physical, Theoretical* **1971**, 3589-3592.
(141) Barone, V.; Cossi, M.; Tomasi, J. *J. Chem. Phys.* **1997**, *107*, 3210-3221.
(142) Marenich, A. V.; Cramer, C. J.; Truhlar, D. G.; Guido, C. A.; Mennucci, B.; Scalmani, G.; Frisch, M. J. *Chem. Sci.* **2011**, *2*, 2143-2161.
(143) Walcarius, A. *Chem. Soc. Rev.* **2013**, *42*, 4098-4140.
(144) Zhai, Y. P.; Dou, Y. Q.; Zhao, D. Y.; Fulvio, P. F.; Mayes, R. T.; Dai, S. *Adv. Mater.* **2011**, *23*, 4828-4850.
(145) Conte, M. *Fuel Cells* **2010**, *10*, 806-818.
(146) MacFarlane, D. R.; Tachikawa, N.; Forsyth, M.; Pringle, J. M.; Howlett, P. C.; Elliott, G. D.; Davis, J. H.; Watanabe, M.; Simon, P.; Angell, C. A. *Energ Environ Sci* **2014**, *7*, 232-250.
(147) Stoller, M. D.; Park, S. J.; Zhu, Y. W.; An, J. H.; Ruoff, R. S. *Nano Lett.* **2008**, *8*, 3498-3502.
(148) Xing, W.; Qiao, S. Z.; Ding, R. G.; Li, F.; Lu, G. Q.; Yan, Z. F.; Cheng, H. M. *Carbon* **2006**, *44*, 216-224.
(149) Jeong, H. M.; Lee, J. W.; Shin, W. H.; Choi, Y. J.; Shin, H. J.; Kang, J. K.; Choi, J. W. *Nano Lett.* **2011**, *11*, 2472-2477.
(150) Yuyama, K.; Masuda, G.; Yoshida, H.; Sato, T. *J. Power Sources* **2006**, *162*, 1401-1408.
(151) Ue, M.; Takeda, M.; Toriumi, A.; Kominato, A.; Hagiwara, R.; Ito, Y. *J. Electrochem. Soc.* **2003**, *150*, A499-A502.
(152) Montanino, M.; Carewska, M.; Alessandrini, F.; Passerini, S.; Appetecchi, G. B. *Electrochim. Acta* **2011**, *57*, 153-159.
(153) Fitchett, B. D.; Knepp, T. N.; Conboy, J. C. *J. Electrochem. Soc.* **2004**, *151*, E219-E225.
(154) Lockett, V.; Sedev, R.; Ralston, J.; Horne, M.; Rodopoulos, T. *J. Phys. Chem. C* **2008**, *112*, 7486-7495.
(155) Liu, H.; Zhu, G. *J. Power Sources* **2007**, *171*, 1054-1061.

(156) Bedrov, D.; Vatamanu, J.; Hu, Z. *J. Non-Cryst. Solids* **2015**, *407*, 339-348.
(157) Gryglewicz, G.; Machnikowski, J.; Lorenc-Grabowska, E.; Lota, G.; Frackowiak, E. *Electrochim. Acta* **2005**, *50*, 1197-1206.
(158) Vu, A.; Li, X.; Phillips, J.; Han, A.; Smyrl, W. H.; Bühlmann, P.; Stein, A. *Chem. Mater.* **2013**, *25*, 4137-4148.
(159) Lee, C.; Yang, W.; Parr, R. G. *Phys Rev B* **1988**, *37*, 785-789.
(160) Stephens, P. J.; Devlin, F. J.; Chabalowski, C. F.; Frisch, M. J. *J. Phys. Chem.* **1994**, *98*, 11623-11627.
(161) Lu, T.; Chen, F. *J. Comput. Chem.* **2012**, *33*, 580-592.
(162) Zhang, Y.; Shi, C.; Brennecke, J. F.; Maginn, E. J. *J. Phys. Chem. B* **2014**, *118*, 6250-6255.
(163) Mousavi, M. P. S.; Kashefolgheta, S.; Stein, A.; Buhlmann, P. *J. Elec. Soc.* **2016**, *163*, H74-H80.
(164) Zhou, Z. B.; Matsumoto, H.; Tatsumi, K. *Chem-Eur J* **2004**, *10*, 6581-6591.
(165) Tsuzuki, S.; Shinoda, W.; Miran, M. S.; Kinoshita, H.; Yasuda, T.; Watanabe, M. *The Journal of Chemical Physics* **2013**, *139*, 174504.
(166) Hunt, P. A.; Gould, I. R.; Kirchner, B. *Aust. J. Chem.* **2007**, *60*, 9-14.
(167) Singh, H.; Mukherjee, U. *J. Mol. Model.* **2013**, *19*, 2317-2327.
(168) Handy, S. T.; Okello, M. *The Journal of Organic Chemistry* **2005**, *70*, 1915-1918.
(169) Holloczki, O.; Nyulaszi, L. *Organic & Biomolecular Chemistry* **2011**, *9*, 2634-2640.
(170) Sakaebe, H.; Matsumoto, H. *Electrochem. Commun.* **2003**, *5*, 594-598.
(171) MacFarlane, D.; Meakin, P.; Sun, J.; Amini, N.; Forsyth, M. *J. Phys. Chem. B* **1999**, *103*, 4164-4170.
(172) Wilson, B. E.; He, S. Y.; Buffington, K.; Rudisill, S.; Smyrl, W. H.; Stein, A. *J. Power Sources* **2015**, *298*, 193-202.
(173) Gor, G. Y.; Thommes, M.; Cychosz, K. A.; Neimark, A. V. *Carbon* **2012**, *50*, 1583-1590.
(174) Fierke, M. A.; Lai, C. Z.; Buhlmann, P.; Stein, A. *Anal. Chem.* **2010**, *82*, 680-688.
(175) Yokoi, T.; Sakamoto, Y.; Terasaki, O.; Kubota, Y.; Okubo, T.; Tatsumi, T. *J. Am. Chem. Soc.* **2006**, *128*, 13664-13665.
(176) Meng, Y.; Gu, D.; Zhang, F.; Shi, Y.; Yang, H.; Li, Z.; Yu, C.; Tu, B.; Zhao, D. *Angew. Chem. Int. Ed.* **2005**, *44*, 7053-7059.
(177) Cornelis, G.; Doolette, C.; Thomas, M.; McLaughlin, M. J.; Kirby, J. K.; Beak, D. G.; Chittleborough, D. *Soil Science Society of America Journal* **2012**, *76*, 891-902.
(178) Lowry, G. V.; Espinasse, B. P.; Badireddy, A. R.; Richardson, C. J.; Reinsch, B. C.; Bryant, L. D.; Bone, A. J.; Deonarine, A.; Chae, S.; Therezien, M.; Colman, B. P.;

Hsu-Kim, H.; Bernhardt, E. S.; Matson, C. W.; Wiesner, M. R. *Environ. Sci. Technol.* **2012**, *46*, 7027-7036.
(179) Benn, T. M.; Westerhoff, P. *Environ. Sci. Technol.* **2008**, *42*, 4133-4139.
(180) Stensberg, M. C.; Wei, Q.; McLamore, E. S.; Porterfield, D. M.; Wei, A.; Sepúlveda, M. S. *Nanomedicine* **2011**, *6*, 879-898.
(181) Xiu, Z. M.; Zhang, Q. B.; Puppala, H. L.; Colvin, V. L.; Alvarez, P. J. J. *Nano Lett.* **2012**, *12*, 4271-4275.
(182) Marambio-Jones, C.; Hoek, E. V. *J. Nanopart. Res.* **2010**, *12*, 1531-1551.
(183) Jung, W. K.; Koo, H. C.; Kim, K. W.; Shin, S.; Kim, S. H.; Park, Y. H. *Applied and Environmental Microbiology* **2008**, *74*, 2171-2178.
(184) Sondi, I.; Salopek-Sondi, B. *J. Colloid Interface Sci.* **2004**, *275*, 177-182.
(185) Elzey, S.; Grassian, V. *J. Nanopart. Res.* **2010**, *12*, 1945-1958.
(186) Liu, J.; Hurt, R. H. *Environ. Sci. Technol.* **2010**, *44*, 2169-2175.
(187) Gondikas, A. P.; Morris, A.; Reinsch, B. C.; Marinakos, S. M.; Lowry, G. V.; Hsu-Kim, H. *Environ. Sci. Technol.* **2012**, *46*, 7037-7045.
(188) Li, X.; Lenhart, J. J.; Walker, H. W. *Langmuir* **2012**, *28*, 1095-1104.
(189) Zook, J.; Long, S.; Cleveland, D.; Geronimo, C.; MacCuspie, R. *Anal Bioanal Chem* **2011**, *401*, 1993-2002.
(190) Koch, M.; Kiefer, S.; Cavelius, C.; Kraegeloh, A. *J. Nanopart. Res.* **2012**, *14*, 1-11.
(191) Reinsch, B. C.; Levard, C.; Li, Z.; Ma, R.; Wise, A.; Gregory, K. B.; Brown, G. E.; Lowry, G. V. *Environ. Sci. Technol.* **2012**, *46*, 6992-7000.
(192) Choi, O.; Deng, K. K.; Kim, N.-J.; Ross Jr, L.; Surampalli, R. Y.; Hu, Z. *Water Res.* **2008**, *42*, 3066-3074.
(193) Boswell, P. G.; Bühlmann, P. *Journal of the American Chemical Society* **2005**, *127*, 8958–8959.
(194) Riess, J. G. *Tetrahedron* **2002**, *58*, 4113-4131.
(195) Riess, J. G.; Leblanc, M. *Pure Appl. Chem.* **1982**, *54*, 2383-2406.
(196) Fierke, M. A.; Lai, C.-Z.; Bühlmann, P.; Stein, A. *Analytical Chemistry* **2010**, *82*, 680-688.
(197) Hau, H. H.; Gralnick, J. A. In *Annual Review of Microbiology*, 2007, pp 237-258.
(198) Wu, B.; Huang, R.; Sahu, M.; Feng, X.; Biswas, P.; Tang, Y. J. *Sci. Total Environ.* **2010**, *408*, 1755-1758.
(199) Wu, B.; Zhuang, W.-Q.; Sahu, M.; Biswas, P.; Tang, Y. J. *Sci. Total Environ.* **2011**, *409*, 4635-4639.
(200) Chinnapongse, S. L.; MacCuspie, R. I.; Hackley, V. A. *Sci. Total Environ.* **2011**, *409*, 2443-2450.

(201) El Badawy, A. M.; Scheckel, K. G.; Suidan, M.; Tolaymat, T. *Sci. Total Environ.* **2012**, *429*, 325-331.
(202) Gottschalk, F.; Sonderer, T.; Scholz, R. W.; Nowack, B. *Environ. Sci. Technol.* **2009**, *43*, 9216-9222.
(203) Blaser, S. A.; Scheringer, M.; MacLeod, M.; Hungerbühler, K. *Sci. Total Environ.* **2008**, *390*, 396-409.
(204) Zhang, W.; Yao, Y.; Sullivan, N.; Chen, Y. *Environ. Sci. Technol.* **2011**, *45*, 4422-4428.
(205) Atlas, R. M. *Handbook of Microbiological Media*, Third ed.; CRC Press, 2004.
(206) Dasari, T. P.; Hwang, H.-M. *Sci. Total Environ.* **2010**, *408*, 5817-5823.
(207) Kim, S.; Baek, Y.-W.; An, Y.-J. *Appl. Microbiol. Biotechnol.* **2011**, *92*, 1045-1052.
(208) Suresh, A. K.; Pelletier, D. A.; Wang, W.; Moon, J.-W.; Gu, B.; Mortensen, N. P.; Allison, D. P.; Joy, D. C.; Phelps, T. J.; Doktycz, M. J. *Environ. Sci. Technol.* **2010**, *44*, 5210-5215.
(209) Pokhrel, L. R.; Silva, T.; Dubey, B.; El Badawy, A. M.; Tolaymat, T. M.; Scheuerman, P. R. *Sci. Total Environ.* **2012**, *426*, 414-422.
(210) Marquis, B. J.; Maurer-Jones, M. A.; Braun, K. L.; Haynes, C. L. *Analyst* **2009**, *134*, 2293-2300.
(211) Maurer-Jones, M. A.; Lin, Y.-S.; Haynes, C. L. *Acs Nano* **2010**, *4*, 3363-3373.
(212) Balch, W. E.; Fox, G. E.; Magrum, L. J.; Woese, C. R.; Wolfe, R. S. *Microbiol. Rev.* **1979**, *43*, 260-296.
(213) Dean, J. A. *Lange's Handbook of Chemistry, Fourteenth Edition*; McGraw-Hill, 1992, p Unpaged.
(214) Decker, U. P. *Zeitschrift für Chemie* **1983**, *23*, 315-316.
(215) Rubinson, J. F.; Rubinson, K. *Contemporary Chemical Analysis*: Upper Saddle River, NJ, 1998.
(216) Ratte, H. T. *Environ. Toxicol. Chem.* **1999**, *18*, 89-108.
(217) Hogstrand, C.; Galvez, F.; Wood, C. M. *Environ. Toxicol. Chem.* **1996**, *15*, 1102-1108.
(218) Leblanc, G. A.; Mastone, J. D.; Paradice, A. P.; Wilson, B. F.; Lockhart, H. B.; Robillard, K. A. *Environ. Toxicol. Chem.* **1984**, *3*, 37-46.
(219) Janes, N.; Playle, R. C. *Environ. Toxicol. Chem.* **1995**, *14*, 1847-1858.
(220) Rose-Janes, N. G.; Playle, R. C. *Aquat. Toxicol.* **2000**, *51*, 1-18.
(221) Hering, J. G.; Morel, F. M. M. *Environ. Sci. Technol.* **1988**, *22*, 1234-1237.
(222) Di Toro, D. M.; Allen, H. E.; Bergman, H. L.; Meyer, J. S.; Paquin, P. R.; Santore, R. C. *Environ. Toxicol. Chem.* **2001**, *20*, 2383-2396.
(223) Hayes, M. *Nature* **1983**, *303*, 835-836.

(224) Sikora, F. J.; Stevenson, F. J. *Geoderma* **1988**, *42*, 353-363.
(225) Ma, H. Z.; Kim, S. D.; Cha, D. K.; Allen, H. E. *Abstr. Pap. Am. Chem. S.* **1998**, *216*, U785-U785.
(226) Glover, C. N.; Wood, C. M. *Aquat. Toxicol.* **2005**, *73*, 406-417.
(227) Pagenkopf, G. K. *Environ. Sci. Technol.* **1983**, *17*, 342-347.
(228) Unrine, J. M.; Colman, B. P.; Bone, A. J.; Gondikas, A. P.; Matson, C. W. *Environ. Sci. Technol.* **2012**, *46*, 6915-6924.
(229) Bone, A. J.; Colman, B. P.; Gondikas, A. P.; Newton, K. M.; Harrold, K. H.; Cory, R. M.; Unrine, J. M.; Klaine, S. J.; Matson, C. W.; Di Giulio, R. T. *Environ. Sci. Technol.* **2012**, *46*, 6925-6933.
(230) Fabrega, J.; Fawcett, S. R.; Renshaw, J. C.; Lead, J. R. *Environ. Sci. Technol.* **2009**, *43*, 7285-7290.
(231) Benoit, R.; Wilkinson, K. J.; Sauve, S. *Chem. Cent. J.* **2013**, *7*.
(232) Boggs, S.; Livermore, D.; Seitz, M. G., Humic substances in natural waters andtheir complexation with trace metals and radionuclides: a review, in: TechnicalReport ANL-84-78; Argonne National Laboratory: Lemont, IL, 1985.
(233) Gatselou, V. A.; Giokas, D. L.; Vlessidis, A. G. *Anal. Chim. Acta* **2014**, *812*, 121-128.
(234) Maurer-Jones, M. A.; Gunsolus, I. L.; Murphy, C. J.; Haynes, C. L. *Anal. Chem.* **2013**, *85*, 3036-3049.
(235) International Humic Substances Society. 2014.
(236) Cumberland, S. A.; Lead, J. R. *J. Chromatogr. A* **2009**, *1216*, 9099-9105.
(237) Chen, Z.; Porcher, C.; Campbell, P. G.; Fortin, C. *Environ. Sci. Technol.* **2013**, *47*, 8835-8842.
(238) Chen, Z.; Campbell, P. G.; Fortin, C. *J. Phys. Chem. A* **2012**, *116*, 6532-6539.
(239) Angel, B. M.; Batley, G. E.; Jarolimek, C. V.; Rogers, N. J. *Chemosphere* **2013**, *93*, 359-365.
(240) Hou, W. C.; Stuart, B.; Howes, R.; Zepp, R. G. *Environ. Sci. Technol.* **2013**, *47*, 7713-7721.
(241) Maurer, F.; Christl, I.; Hoffmann, M.; Kretzschmar, R. *Environ. Sci. Technol.* **2012**, *46*, 8808-8816.
(242) Gunsolus, I. L.; Mousavi, M. P. S.; Hussein, K.; Buhlmann, P.; Haynes, C. L. *Environ. Sci. Technol.* **2015**.
(243) Wirth, S. M.; Lowry, G. V.; Tilton, R. D. *Environ. Sci. Technol.* **2012**, *46*, 12687-12696.
(244) Gao, J.; Powers, K.; Wang, Y.; Zhou, H.; Roberts, S. M.; Moudgil, B. M.; Koopman, B.; Barber, D. S. *Chemosphere* **2012**, *89*, 96-101.

(245) Glover, C. N.; Playle, R. C.; Wood, C. M. *Environ. Toxicol. Chem.* **2005**, *24*, 2934-2940.
(246) Brauner, C. J.; Wood, C. M. *Comp. Biochem. Physiol., C: Comp. Pharmacol. Toxicol.* **2002**, *133*, 161-173.
(247) Kim, J. Y.; Kim, K. T.; Lee, B. G.; Lim, B. J.; Kim, S. D. *Ecotoxicol. Environ. Saf.* **2013**, *92*, 57-63.
(248) VanGenderen, E. J.; Ryan, A. C.; Tomasso, J. R.; Klaine, S. J. *Environ. Toxicol. Chem.* **2003**, *22*, 2746-2751.
(249) Peretyazhko, T. S.; Zhang, Q. B.; Colvin, V. L. *Environ. Sci. Technol.* **2014**, *48*, 11954-11961.
(250) Kulpmann, W. R. *J Clin Chem Clin Bio* **1989**, *27*, 815-824.
(251) Park, S. B.; Matuszewski, W.; Meyerhoff, M. E.; Liu, Y. H.; Kadish, K. M. *Electroanal* **1991**, *3*, 909-916.
(252) Chang, Q.; Park, S. B.; Kliza, D.; Cha, G. S.; Yim, H.; Meyerhoff, M. E. *Am Biotechnol Lab* **1990**, *8*, 10-&.
(253) Yajima, S.; Tohda, K.; Buhlmann, P.; Umezawa, Y. *Anal. Chem.* **1997**, *69*, 1919-1924.
(254) Lindner, E.; Toth, K.; Pungor, E. *Bunseki Kagaku* **1981**, *30*, S67-S92.
(255) Piccapietra, F.; Sigg, L.; Behra, R. *Environ. Sci. Technol.* **2012**, *46*, 818-825.
(256) Mumper, C. K.; Ostermeyer, A. K.; Semprini, L.; Radniecki, T. S. *Chemosphere* **2013**, *93*, 2493-2498.
(257) Sun, R. W. Y.; Chen, R.; Chung, N. P. Y.; Ho, C. M.; Lin, C. L. S.; Che, C. M. *Chem. Commun.* **2005**, 5059-5061.
(258) Choi, C.; Cui, Y. *Bioresour. Technol.* **2012**, *107*, 522-525.
(259) Zhan, D.; Li, X.; Zhan, W.; Fan, F.-R. F.; Bard, A. J. *Anal. Chem.* **2007**, *79*, 5225-5231.
(260) Mash, H. E.; Chin, Y. P.; Sigg, L.; Hari, R.; Xue, H. B. *Anal. Chem.* **2003**, *75*, 671-677.
(261) Poulson, S. R.; Drever, J. I. *Talanta* **1996**, *43*, 1975-1981.
(262) Soares, H.; Conde, P.; Almeida, A. A. N.; Vasconcelos, M. *Anal. Chim. Acta* **1999**, *394*, 325-335.
(263) Hem, J. D.; Geological Survey (U.S.). *Study and interpretation of the chemical characteristics of natural water*, 3rd ed.; UNITED STATES GOVERNMENT PRINTING OFFICE Alexandria, VA, 1985, p xii, 263 p.
(264) Nagao, S.; Matsunaga, T.; Suzuki, Y.; Ueno, T.; Amano, H. *Water Res.* **2003**, *37*, 4159-4170.

(265) Robards, K.; Mckelvie, I. D.; Benson, R. L.; Worsfold, P. J.; Blundell, N. J.; Casey, H. *Anal. Chim. Acta* **1994**, *287*, 147-190.
(266) McDonald, S.; Bishop, A. G.; Prenzler, P. D.; Robards, K. *Anal. Chim. Acta* **2004**, *527*, 105-124.
(267) Thorn, K. A.; Cox, L. G. *Org. Geochem.* **2009**, *40*, 484-499.
(268) Manceau, A.; Nagy, K. L. *Geochim. Cosmochim. Acta* **2012**, *99*, 206-223.
(269) Glover, C. N.; Sharma, S. K.; Wood, C. M. *Environ. Toxicol. Chem.* **2005**, *24*, 2941-2947.
(270) Harris, D. C. *Quantitative Chemical Analysis*, Six ed.; Michelle Russel Julet: United States of America, 2003.
(271) Skoog, D. A.; West, D. M.; Holler, F. J. *Fundamentals of Analytical Chemistry*, Seventh ed.; Harcourt College Publisher: United States of America, 1997.
(272) Boudou, J. P.; Schimmelmann, A.; Ader, M.; Mastalerz, M.; Sebilo, M.; Gengembre, L. *Geochim. Cosmochim. Acta* **2008**, *72*, 1199-1221.
(273) Akaighe, N.; Maccuspie, R. I.; Navarro, D. A.; Aga, D. S.; Banerjee, S.; Sohn, M.; Sharma, V. K. *Environ. Sci. Technol.* **2011**, *45*, 3895-3901.
(274) Baalousha, M.; Motelica-Heino, M.; Le Coustumer, P. *Colloid Surface A* **2006**, *272*, 48-55.
(275) Nuzzo, A.; Sanchez, A.; Fontaine, B.; Piccolo, A. *J Geochem Explor* **2013**, *129*, 1-5.
(276) Zhang, H.; Smith, J. A.; Oyanedel-Craver, V. *Water Res.* **2012**, *46*, 691-699.
(277) Kaegi, R.; Voegelin, A.; Sinnet, B.; Zuleeg, S.; Hagendorfer, H.; Burkhardt, M.; Siegrist, H. *Environ. Sci. Technol.* **2011**, *45*, 3902-3908.
(278) Li, L.; Hartmann, G.; Döblinger, M.; Schuster, M. *Environ. Sci. Technol.* **2013**, *47*, 7317-7323.
(279) Mueller, N. C.; Nowack, B. *Environ. Sci. Technol.* **2008**, *42*, 4447-4453.
(280) Rai, M.; Yadav, A.; Gade, A. *Biotechnol. Adv.* **2009**, *27*, 76-83.
(281) Xiu, Z.-M.; Ma, J.; Alvarez, P. J. J. *Environ. Sci. Technol.* **2011**, *45*, 9003-9008.
(282) Hwang, E. T.; Lee, J. H.; Chae, Y. J.; Kim, Y. S.; Kim, B. C.; Sang, B. I.; Gu, M. B. *Small* **2008**, *4*, 746-750.
(283) Huynh, K. A.; Chen, K. L. *Environ. Sci. Technol.* **2011**, *45*, 5564-5571.
(284) Yu, S. J.; Yin, Y. G.; Chao, J. B.; Shen, M. H.; Liu, J. F. *Environ. Sci. Technol.* **2014**, *48*, 403-411.
(285) Yang, X. Y.; Lin, S. H.; Wiesner, M. R. *J. Hazard. Mater.* **2014**, *264*, 161-168.
(286) Liu, J. Y.; Sonshine, D. A.; Shervani, S.; Hurt, R. H. *Acs Nano* **2010**, *4*, 6903-6913.
(287) Pokhrel, L. R.; Dubey, B.; Scheuerman, P. R. *Environmental Science-Nano* **2014**, *1*, 45-54.

(288) Pokhrel, L. R.; Dubey, B.; Scheuerman, P. R. *Environ. Sci. Technol.* **2013**, *47*, 12877-12885.
(289) Mousavi, M. P. S.; Gunsolus, I. L.; Pérez De Jesús, C. E.; Lancaster, M.; Hussein, K.; Haynes, C. L.; Bühlmann, P. *Sci. Total Environ.* **2015**, *537*, 453-461.
(290) Yang, X. Y.; Jiang, C. J.; Hsu-Kim, H.; Badireddy, A. R.; Dykstra, M.; Wiesner, M.; Hinton, D. E.; Meyer, J. N. *Environ. Sci. Technol.* **2014**, *48*, 3486-3495.
(291) Kittler, S.; Greulich, C.; Diendorf, J.; Koller, M.; Epple, M. *Chem. Mater.* **2010**, *22*, 4548-4554.
(292) Levard, C.; Reinsch, B. C.; Michel, F. M.; Oumahi, C.; Lowry, G. V.; Brown, G. E. *Environ. Sci. Technol.* **2011**, *45*, 5260-5266.
(293) Robertson, A. I.; Bunn, S. E.; Boon, P. I.; Walker, K. F. *Marine and Freshwater Research* **1999**, *50*, 813-829.
(294) Millero, F. J. *Pure Appl. Chem.* **1985**, *57*, 1015-1024.
(295) Zeman, E. J.; Schatz, G. C. *J. Phys. Chem.* **1987**, *91*, 634-643.
(296) Tejamaya, M.; Römer, I.; Merrifield, R. C.; Lead, J. R. *Environ. Sci. Technol.* **2012**, *46*, 7011-7017.
(297) Li, Y.; Zhang, W.; Niu, J.; Chen, Y. *Environ. Sci. Technol.* **2013**, *47*, 10293-10301.
(298) El Badawy, A. M.; Luxton, T. P.; Silva, R. G.; Scheckel, K. G.; Suidan, M. T.; Tolaymat, T. M. *Environ. Sci. Technol.* **2010**, *44*, 1260-1266.
(299) Al-Saidi, W. A.; Feng, H.; Fichthorn, K. A. *Nano Lett.* **2012**, *12*, 997-1001.
(300) Saidi, W. A.; Feng, H.; Fichthorn, K. A. *J. Phys. Chem. C* **2013**, *117*, 1163-1171.
(301) Huang, H. H.; Ni, X. P.; Loy, G. L.; Chew, C. H.; Tan, K. L.; Loh, F. C.; Deng, J. F.; Xu, G. Q. *Langmuir* **1996**, *12*, 909-912.
(302) Wang, H. S.; Qiao, X. L.; Chen, J. G.; Wang, X. J.; Ding, S. Y. *Mater. Chem. Phys.* **2005**, *94*, 449-453.
(303) Zhang, Z. T.; Zhao, B.; Hu, L. M. *J. Solid State Chem.* **1996**, *121*, 105-110.
(304) Deonarine, A.; Lau, B. L. T.; Aiken, G. R.; Ryan, J. N.; Hsu-Kim, H. *Environ. Sci. Technol.* **2011**, *45*, 3217-3223.
(305) Gordon, O.; Slenters, T. V.; Brunetto, P. S.; Villaruz, A. E.; Sturdevant, D. E.; Otto, M.; Landmann, R.; Fromm, K. M. *Antimicrob. Agents Chemother.* **2010**, *54*, 4208-4218.
(306) Waples, J. S.; Nagy, K. L.; Aiken, G. R.; Ryan, J. N. *Geochim. Cosmochim. Acta* **2005**, *69*, 1575-1588.
(307) Hyung, H.; Kim, J.-H. *Environ. Sci. Technol.* **2008**, *42*, 4416-4421.
(308) Louie, S. M.; Tilton, R. D.; Lowry, G. V. *Environ. Sci. Technol.* **2013**, *47*, 4245-4254.
(309) Duarte, R.; Barros, A. C.; Duarte, A. C. *J. Chromatogr. A* **2012**, *1249*, 138-146.

(310) Chen, D. P.; Qiao, X. L.; Qiu, X. L.; Chen, J. G. *Journal of Materials Science* **2009**, *44*, 1076-1081.
(311) Grubbs, R. B. *Polymer Reviews* **2007**, *47*, 197-215.
(312) Ivask, A.; ElBadawy, A.; Kaweeteerawat, C.; Boren, D.; Fischer, H.; Ji, Z. X.; Chang, C. H.; Liu, R.; Tolaymat, T.; Telesca, D.; Zink, J. I.; Cohen, Y.; Holden, P. A.; Godwin, H. A. *Acs Nano* **2014**, *8*, 374-386.
(313) Schneider, C. A.; Rasband, W. S.; Eliceiri, K. W. *Nature Methods* **2012**, *9*, 671-675.
(314) BASi Reference Electrodes. http://www.basinc.com/products/ec/ref.php. Accessed May 3rd 2013.
(315) Bosch, R. W.; Straetmans, S.; Dyck, S. V. *Journal of Materials Science* **2002**, *37*, 3973-3979.
(316) Illingworth, J. A. *Biochem. J* **1981**, *195*, 259-262.
(317) Ito, S.; Kobayashi, F.; Baba, K.; Asano, Y.; Wada, H. *Talanta* **1996**, *43*, 135-142.
(318) BioLogic Science Instruments Reference Electrodes, http://www.bio-logic.info/potentiostat/accessories/ReferenceElectrodes.html. Accessed May 25th 2013, 2013.
(319) Carano, M.; Colonna, B.; Echegoyen, L.; Le Derf, F.; Levillain, E.; Salle, M. *Supramol. Chem.* **2003**, *15*, 83-85.
(321) Helfferich, F. G. *Ion Exchange*; McGraw-Hill: New York, 1962.
(322) Newton, M. R.; Bohaty, A. K.; White, H. S.; Zharov, I. *J. Am. Chem. Soc.* **2005**, *127*, 7268-7269.
(323) Wang, G.; Zhang, B.; Wayment, J. R.; Harris, J. M.; White, H. S. *J. Am. Chem. Soc.* **2006**, *128*, 7679-7686.
(324) Zhang, Y.; Zhang, B.; White, H. S. *J. Phys. Chem. B* **2006**, *110*, 1768-1774.
(325) Lan, W.-J.; Holden, D. A.; White, H. S. *J. Am. Chem. Soc.* **2011**, *133*, 13300-13303.
(326) Nishizawa, M.; Menon, V. P.; Martin, C. R. *Science* **1995**, *268*, 700-702.
(327) Jágerszki, G.; Gyurcsányi, R. E.; Höfler, L.; Pretsch, E. *Nano Lett.* **2007**, *7*, 1609-1612.
(328) Springer, C. H.; Coetzee, J. F.; Kay, R. L. *J. Phys. Chem.* **1969**, *73*, 471-476.
(329) Bard, A. J.; Faulkner, L. R. *Electrochemical Methods: Fundamentals and Applications*, 2nd ed.; Wiley: New York, 2001.
(330) Meier, P. C. *Anal. Chim. Acta* **1982**, *136*, 363-368.
(331) Gyurcsányi, R. E. *TrAC, Trends Anal. Chem.* **2008**, *27*, 627-639.
(332) Behrens, S. H.; Grier, D. G. *J. Chem. Phys.* **2001**, *115*, 6716-6721.

(333) Russel, W. B.; Saville, D. A.; Schowalter, W. R. *Colloidal Dispersion*; Cambridge University Press: Cambridge, U. K., 1989.
(334) Newton, M. R.; Bohaty, A. K.; Zhang, Y. H.; White, H. S.; Zharov, I. *Langmuir* **2006**, *22*, 4429-4432.
(335) Fernandez, J. L.; White, J. M.; Sun, Y. M.; Tang, W. J.; Henkelman, G.; Bard, A. J. *Langmuir* **2006**, *22*, 10426-10431.
(336) Harris, D. C. *Exploring Chemical Analysis, 3rd ed.*; W. H. Freeman and Company: New York, 2005.
(337) Rickert, P. G.; Antonio, M. R.; Firestone, M. A.; Kubatko, K.-A.; Szreder, T.; Wishart, J. F.; Dietz, M. L. *Dalton Transactions* **2007**, 529-531.
(338) Aşangil, D.; Hüdai Taşdemir, İ.; Kılıç, E. *Journal of Pharmaceutical Analysis* **2012**, *2*, 193-199.
(339) Do, K.; Kim, C.; Song, K.; Yun, S. J.; Lee, J. K.; Ko, J. *Sol. Energy Mater. Sol. Cells* **2013**, *115*, 52-57.
(340) Xu, M.; Ivey, D. G.; Xie, Z.; Qu, W. *Electrochim. Acta* **2013**, *89*, 756-762.
(341) Ruiz, J.; Astruc, D. *Comptes Rendus de l'Académie des Sciences - Series IIC - Chemistry* **1998**, *1*, 21-27.
(342) Noviandri, I.; Brown, K. N.; Fleming, D. S.; Gulyas, P. T.; Lay, P. A.; Masters, A. F.; Phillips, L. *J. Phys. Chem. B* **1999**, *103*, 6713-6722.
(343) Raamat, E.; Kaupmees, K.; Ovsjannikov, G.; Trummal, A.; Kuett, A.; Saame, J.; Koppel, I.; Kaljurand, I.; Lipping, L.; Rodima, T.; Pihl, V.; Koppel, I. A.; Leito, I. *J. Phys. Org. Chem.* **2013**, *26*, 162-170.
(344) Le, T. H.; Nafady, A.; Qu, X.; Martin, L. L.; Bond, A. M. *Anal. Chem.* **2011**, *83*, 6731-6737.
(345) Ou, Z.; Khoury, T.; Fang, Y.; Zhu, W.; Sintic, P. J.; Crossley, M. J.; Kadish, K. M. *Inorg. Chem.* **2013**, *52*, 2474-2483.
(346) Wang, D.; Zhang, M.; Buehlmann, P.; Que, L., Jr. *J. Am. Chem. Soc.* **2010**, *132*, 7638-7644.
(347) Perera, R. T.; Johnson, R. P.; Edwards, M. A.; White, H. S. *J. Phys. Chem. C* **2015**, *119*, 24299-24306.
(348) Saba, S. A.; Mousavi, M. P. S.; Bühlmann, P.; Hillmyer, M. A. *J. Am. Chem. Soc.* **2015**, *137*, 8896-8899.
(349) BASi Reference Electrodes, Bioanalytical Systems Inc. https://www.basinc.com/products/ec/ref.php , Accessed October 30th 2015.
(350) Koslow Scientific Testing Instruments, Silver/Silver Sulfate Reference Electrode 1003, http://www.koslow.com/silver-silver-sulfate-reference-electrode-1003.html, Accessed October 30th 2015.

(351) GAMRY Instruments, Reference Electrode Overview and Care, http://www.gamry.com/support/technical-support/frequently-asked-questions/care-of-reference-electrodes, Accessed October 30th 2015.
(352) Princeton Applied Research, Reference Electrodes, http://www.princetonappliedresearch.com/Our-Products/Accessories/Reference-Electrodes.aspx, Accessed October 30th 2015. .
(353) CH Instruments, Accessories, http://www.chinstruments.com/accessories.shtml, Accessed September 27 2015.
(354) Princton Applied Research, Reference Electrodes, http://www.princetonappliedresearch.com/Our-Products/Accessories/Reference-Electrodes.aspx, Accessed September 30 2015.
(355) Ceresa, A.; Sokalski, T.; Pretsch, E. *J. Electroanal. Chem.* **2001**, *501*, 70-76.
(356) Gunsolus, I. L.; Mousavi, M. P. S.; Hussein, K.; Bühlmann, P.; Haynes, C. L. *Environ. Sci. Technol.* **2015**, *49*, 8078-8086.
(357) Thommes, M.; Smarsly, B.; Groenewolt, M.; Ravikovitch, P. I.; Neimark, A. V. *Langmuir* **2006**, *22*, 756-764.
(358) Brunauer, S.; Emmett, P. H.; Teller, E. *J. Am. Chem. Soc.* **1938**, *60*, 309-319.
(359) Cussler, E. L. *Diffusion, Mass Transfer in Fluid Systems*, 3rd ed.; Cambridge University Press: Cambridge, UK, 2009.
(360) Hall, J. L.; Jennings, P. W. *Anal. Chem.* **1976**, *48*, 2026-2027.
(361) Manning, C. W.; Purdy, W. C. *Anal. Chim. Acta* **1970**, *51*, 124-126.
(362) Nieman, T. A.; Horvai, G. *Anal. Chim. Acta* **1985**, *170*, 359-363.
(363) van den Broeke, J.; de Wolf, E.; Deelman, B.-J.; van Koten, G. *Adv. Synth. Catal.* **2003**, *345*, 625-634.
(364) van den Broeke, J.; Deelman, B.-J.; van Koten, G. *Tetrahedron Lett.* **2001**, *42*, 8085-8087.
(365) Chen, L. D.; Mandal, D.; Gladysz, J. A.; Buhlmann, P. *New J. Chem.* **2010**, *34*, 1867-1874.
(366) Shirakawa, S.; Tanaka, Y.; Maruoka, K. *Org. Lett.* **2004**, *6*, 1429-1431.
(367) Szlavik, Z.; Tarkanyi, G.; Gomory, A.; Tarczay, G.; Rabai, J. *J. Fluorine Chem.* **2001**, *108*, 7-14.
(368) Skalický, M.; Skalická, V.; Paterová, J.; Rybáčková, M.; Kvíčalová, M.; Cvačka, J.; Březinová, A.; Kvíčala, J. *Organometallics* **2012**, *31*, 1524-1532.
(369) Kysilka, O.; Rybackova, M.; Skalicky, M.; Kvicalova, M.; Cvacka, J.; Kvicala, J. *Collect. Czech. Chem. Commun.* **2008**, *73*, 1799-1813.
(370) Skalický, M.; Rybáčková, M.; Kysilka, O.; Kvíčalová, M.; Cvačka, J.; Čejka, J.; Kvíčala, J. *J. Fluorine Chem.* **2009**, *130*, 966-973.

(371) Kraus, C. A.; Fuoss, R. M. *J. Am. Chem. Soc.* **1933**, *55*, 21-36.
(372) Haemmerli, A.; Janata, J.; Brown, H. M. *Anal. Chem.* **1980**, *52*, 1179-1182.
(373) Yoshino, N.; Sasaki, A.; Seto, T. *J. Fluorine Chem.* **1995**, *71*, 21-29.